DETERMINING THE IMPACT OF CONCRETE ROADWAYS ON GAMMA RAY BACKGROUND READINGS FOR RADIATION PORTAL MONITORING SYSTEMS

A Thesis

by

CHRISTOPHER MICHAEL RYAN

Submitted to the Office of Graduate Studies of
Texas A&M University
in partial fulfillment of the requirements for the degree of

MASTER OF SCIENCE

May 2011

Major Subject: Nuclear Engineering

DETERMINING THE IMPACT OF CONCRETE ROADWAYS ON GAMMA RAY BACKGROUND READINGS FOR RADIATION PORTAL MONITORING SYSTEMS

A Thesis

by

CHRISTOPHER MICHAEL RYAN

Submitted to the Office of Graduate Studies of
Texas A&M University
in partial fulfillment of the requirements for the degree of

MASTER OF SCIENCE

Approved by:

Chair of Committee,	Craig M. Marianno
Committee Members,	William S. Charlton
	Gwan S. Choi
Head of Department,	Raymond J. Juzaitis

May 2011

Major Subject: Nuclear Engineering

ABSTRACT

Determining the Impact of Concrete Roadways on Gamma Ray Background Readings for Radiation Portal Monitoring Systems. (May 2011)

Christopher Michael Ryan, B.S., Texas A&M University

Chair of Advisory Committee: Dr. Craig M. Marianno

The dissolution of the Soviet Union coupled with the growing sophistication of international terror organizations has brought about a desire to ensure that a sound infrastructure exists to interdict smuggled nuclear material prior to leaving its country of origin. To combat the threat of nuclear trafficking, radiation portal monitors (RPMs) are deployed around the world to intercept illicit material while in transit by passively detecting gamma and neutron radiation. Portal monitors in some locations have reported abnormally high gamma background count rates. The higher background data has been attributed, in part, to the concrete surrounding the portal monitors. Higher background can ultimately lead to more material passing through the RPMs undetected.

This work is focused on understanding the influence of the concrete surrounding the monitors on the total gamma ray background for the system. This research employed a combination of destructive and nondestructive analytical techniques with computer simulations to form a model that may be adapted to any RPM configuration. Six samples were taken from three different composition concrete slabs. The natural

radiological background of these samples was determined using a high-purity germanium (HPGe) detector in conjunction with the Canberra In-Situ Object Counting System (ISOCS™) and Genie™ 2000 software packages. The composition of each sample was determined using thermal and fast neutron activation analysis (NAA) techniques. The results from these experiments were incorporated into a Monte Carlo N-Particle (MNCP) photon transport simulation to determine the expected gamma ray count rate in the RPM due to the concrete.

The results indicate that a quantitative estimate may be possible if the experimental conditions are optimized to eliminate sources of uncertainty. Comparisons of actual and simulated count rate data for ^{137}Cs check sources showed that the model was accurate to within 15%. A comparison of estimated and simulated count rates in one concrete slab showed that the model was accurate to within 4%. Subsequent sensitivity analysis showed that if the elemental concentrations are well known, the carbon and hydrogen content could be easily estimated. Another sensitivity analysis revealed that the small fluctuations in density have a minimal impact on the gamma count rate.

DEDICATION

This thesis is dedicated to my parents, James and Michele Ryan, and to my brother, Zachary Ryan. Thank you for your love and support over the years. Mom and Dad, no words could ever do justice to everything you have taught me. Thanks for always being there, whether it seemed like I was listening to you or not. You may not understand most of what lies beyond this page, but it was possible only because you taught me to put my heart into every endeavor. I can only hope you are as proud of me as I am of both of you. Zach – "fair winds and following seas" – you will never know just how proud I am of everything you have accomplished.

~ Isaiah 40:31 ~

ACKNOWLEDGEMENTS

This thesis and the research it details could not have been completed without the assistance of several individuals. I would like to thank the chair of my advisory committee, Dr. Craig M. Marianno, for providing me with a foundation of knowledge in the field of radiation detection, and being available to answer my myriad of questions about gamma rays and their interactions. I would also like to thank the other members of my committee, Drs. William S. Charlton and Gwan S. Choi, for their comments on the work and suggestions along the way to its completion. In addition, Dr. Charlton deserves special thanks for first introducing me to the field of nuclear nonproliferation and arms control during my years as an undergraduate. What started as a simple curiosity has now become a career endeavor.

I would also like to thank Dr. Alexander A. Solodov of Oak Ridge National Laboratory for being available to answer my questions about radiation portal monitors and his willingness to suffer with me while trying to make sense of the results.

Dr. William D. James and Mr. Michael Raulerson from the Center for Chemical Characterization and Analysis at Texas A&M University were valuable assets when it came time to complete the neutron activation analysis experiments. I want to thank them for allowing me to use their equipment, time, and expertise. Without their assistance, a large portion of this research could not have been completed.

Mr. Braden Goddard, a doctoral student with the Department of Nuclear Engineering, was always willing to help me make sense of my results, provide a critique

of the work, and offer suggestions to improve my methods. I hope you can eventually make sense of all those neutrons we found in Italy, buddy.

I want to thank my family for being supportive over the past several years. My life has taken many unexpected twists and turns, but they have always been there to lift my spirits and give me strength.

Last but certainly not least, a very special thanks to my beautiful fiancée, Alexis Crawley. I never could have imagined that I would be so blessed by two technical fouls. Thank you for your love and your faith in me. Who knows where we will end up, but it is sure to be one amazing ride.

NOMENCLATURE

B_4C	Boron Carbide
BDL	Below Detectable Limits
BF_3	Boron Triflouride
BN	Boron Nitride
CCCA	Center for Chemical Characterization and Analysis
CT	Cadmium Telluride
CZT	Cadmium Zinc Telluride
DOD	Department of Defense
DOE	Department of Energy
DTRA	Defense Threat Reduction Agency
ENAA	Epithermal Neutron Activation Analysis
EXBS	Export Control and Related Border Security
FNAA	Fast Neutron Activation Analysis
FSU	Former Soviet Union
FWHM	Full-Width at Half-Maximum
FY	Fiscal Year
Ge(Li)	Lithium-Drifted Germanium
HgI_2	Mercury Iodide
HPGe	High-Purity Germanium
ICP	International Counterproliferation Program

INAA	Instrumental Neutron Activation Analysis
IND	Improvised Nuclear Device
ISN	Bureau of International Security and Nonproliferation
ISOCS	In-Situ Object Counting System
KHP	Potassium Hydrogen Phthalate
LANL	Los Alamos National Laboratory
MCA	Multichannel Analyzer
MCS	Multichannel Scaling
MCNP	Monte Carlo N-Particle
MDA	Minimum Detectable Activity
NAA	Neutron Activation Analysis
NaI(Tl)	Thallium-Doped Sodium Iodide
NBS	National Bureau of Standards
NIST	National Institute of Standards and Technology
NNSA	National Nuclear Security Administration
NSC	Nuclear Science Center
ORNL	Oak Ridge National Laboratory
PGNAA	Prompt Gamma Neutron Activation Analysis
PLC	Programmable Logic Controller
PMMA	Polymethyl Methacrylate
PMT	Photomultiplier Tube
POE	Port of Entry

POEs	Ports of Entry
PVT	Polyvinyl Toluene
RDD	Radiological Dispersal Device
RN	Radiological and Nuclear
RNAA	Radiochemical Neutron Activation Analysis
RPM	Radiation Portal Monitor
RPMs	Radiation Portal Monitors
RSICC	Radiation Safety Information Computational Center
SLD	Second Line of Defense
SRM	Standard Reference Material
TRIGA	Training, Research, Isotopes, General Atomics
TSCA	Timing Single Channel Analyzer
USG	United States Government
USGS	United States Geological Survey
WMD	Weapons of Mass Destruction

TABLE OF CONTENTS

CHAPTER Page

LIST OF FIGURES

FIGURE Page

LIST OF TABLES

CHAPTER I

INTRODUCTION

I.A. Interdicting nuclear smuggling

Since the dissolution of the Soviet Union in 1991, there has been a general unease about the ability of the Russian Federation along with the other countries of the Former Soviet Union (FSU) to adequately protect their radiological and nuclear (RN) materials and prevent the illicit transfer of these materials across international boundaries.[1] In addition, the 11 September 2001 terrorist attacks against the United States highlighted the unconventional nature of modern terror groups and their desire to inflict mass casualties on civilian targets. This combination of unsecured RN material, porous borders throughout the FSU, and terrorist organizations seeking to acquire such material, makes radiation detection at ports of entry (POEs) a vital step in combating nuclear smuggling.

The United States Government (USG) has engaged in multiple partnerships around the world and invested a significant amount of money to ensure that stolen or diverted nuclear material is not allowed to cross international boundaries. The Departments of Energy (DOE), State, and Defense (DOD) provide the majority of USG assistance.[2] Each department has specialized programs that are responsible for providing radiation detection equipment, training, and support to customs officials and border security personnel at international POEs.

This thesis follows the style of *Nuclear Technology*.

The DOE's National Nuclear Security Administration (NNSA) is responsible for the Second Line of Defense (SLD) program, which is tasked with cooperating with foreign governments to strengthen their ability to deter, detect, and interdict illicit trafficking in RN material.[3] SLD consists of two programs: 1) SLD-Core, which is responsible for installing radiation detection equipment at POEs in Russia and other FSU states; and 2) the Megaports Initiative, which is responsible for providing detection equipment to international seaports. The fiscal year (FY) 2009 budget estimate for SLD was $212.7 million.[4]

The DOD's Defense Threat Reduction Agency (DTRA) is responsible for the International Counterproliferation Program (ICP), which is tasked with engaging law enforcement, investigators, and border security officials to ensure that components of weapons of mass destruction (WMD) are not transported to terrorists or hostile states.[5] The program provides handheld radiation detectors and RPMs to countries in Central and Eastern Europe, the Baltic States, and the FSU. The FY 2009 budget estimate for the ICP was $10.5 million.[6]

The State Department's Bureau of International Security and Nonproliferation (ISN) is responsible for the Export Control and Related Border Security Assistance (EXBS) program, which is designed to prevent the proliferation of WMD, delivery systems, and conventional weapons by working with other countries to strengthen their export control systems. The EXBS program has provided training and radiation detection equipment to assist in apprehending illicit nuclear material.[7] The FY 2009 budget estimate for EXBS was $41.3 million.[4]

I.B. Problem explanation

Since more than 40% of illicit nuclear material trafficking cases between 1991 and 2006 had a nexus in Russia and the former Soviet Republics, there is a pressing need for reliable detection equipment along the borders at the POEs of these countries.[8] A distribution of these cases by the country of origin for the material seized is shown in Figure 1. Stolen RN material may be used to create an improvised nuclear device (IND) or a radiological dispersal device (RDD). Inadequate or improperly maintained detection equipment increases the possibility of these materials or devices being smuggled out of the country of origin and transported to the desired target location.

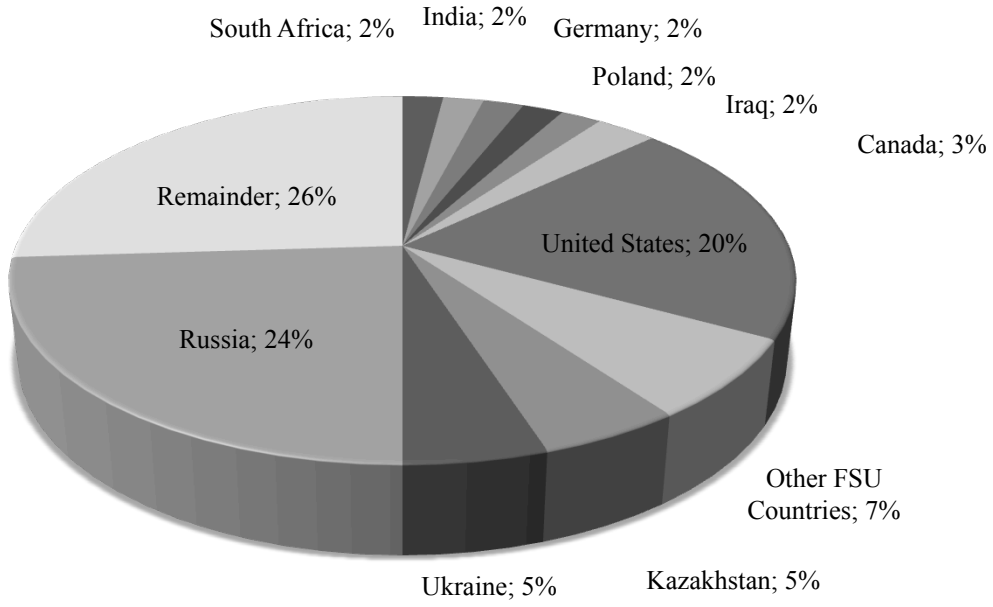

Figure 1. Distribution of nuclear trafficking cases by country of origin for material seized (1991-2006).[8]

Many USG assistance programs provide RPMs for use at POEs to intercept smuggled nuclear material. RPMs are designed for vehicular, rail, or pedestrian traffic, but in each case they are used to passively detect gamma and/or neutron radiation. Gammas are detected in the RPMs using polyvinyl toluene (PVT) scintillators, thallium-doped sodium iodide [NaI(Tl)] scintillators, or high-purity germanium (HPGe) semiconductor detectors. Neutrons are detected using ^{3}He or BF_3 gas-filled proportional counters, or ^{6}Li glass scintillators. The research described in this thesis specifically focuses on gamma detection in vehicle RPMs containing PVT scintillation detectors; however, the methods described may be adapted for any type of RPM containing any variety of detectors.

The RPMs continuously measure the background radiation in the surrounding area and adjust alarm thresholds accordingly. In some locations, the RPMs have reported abnormally high background data with little or no consistency. It is possible that the natural background radiation in the concrete roadway beneath the portal monitors may be contributing to this anomalous data.[9] Higher background levels will increase the minimum detectable activity (MDA) of the RPMs, thereby raising the threshold for alarms and the likelihood that RN material may pass through the monitors undetected. An example of a deployed vehicle RPM is shown in Figure 2.

Figure 2. An example of a deployed vehicular RPM.[10]

The current method for reducing high background at some RPM locations involves removing the roadway beneath the monitors and replacing it with new material. Not only is this an expensive proposition – especially in countries with poor economies and little established infrastructure – but also the new material can be of unknown origin and composition.[9] Not only could this lead to the same abnormality, but it may also introduce new problems if the concrete is fabricated in a location with large uranium ore deposits or in close proximity to previous nuclear weapon test sites.

I.C. Overview of research

The primary objective of this research is to develop a method for determining the natural radiological background and elemental composition of the concrete underneath an RPM in order to estimate its contribution to the overall gamma ray background. This

method was developed using a combination of established analytical methods and photon transport simulations.

A set of six core-drilled concrete samples from three different composition parent slabs was acquired from Oak Ridge National Laboratory (ORNL). The natural radiological background activity of each sample was determined using a HPGe detector. Each of the samples was modeled using the In-Situ Object Counting System (ISOCS™) software from Canberra Industries to generate efficiency calibration files for the detector. The spectrum and calibration files were used to identify the activity of radioisotopes present in each sample using the Genie™ 2000 gamma spectroscopy software package from Canberra Industries.

The elemental composition of the concrete was determined using a combination of fast and instrumental neutron activation analysis (NAA). The neutron sources used for the fast and instrumental NAA were a Kaman Sciences Corporation A-711 sealed tube neutron generator and 1 MW Training, Research, Isotopes, General Atomics (TRIGA) research reactor, respectively. A comparator standard was incorporated into these experiments so the weight fraction of the identified elements could be determined using the relative method. Quality control samples were also used to ensure the integrity of the experiments and subsequent calculations.

The photon transport calculations were done using the Monte Carlo N-Particle (MCNP) version 5 code.[11] The elemental composition from the NAA experiments was used to define the MCNP material card for concrete. The radiation source term was made using the results from the gamma spectroscopy analysis and distributed throughout

the concrete slab. The RPM configuration was modeled in MCNP to reflect a TSA Systems, Ltd. VM-250AG gamma portal monitor located at ORNL. Pulse tallies were used to determine the total gamma ray count rate for the RPM. The MCNP model was validated by measuring the count rate of a ^{137}Cs check source with the RPM and comparing it to the count rate obtained by modeling the source with MCNP. The validity of the method was checked by comparing simulated count rate data for the concrete slab to count rate data for the parent slab obtained from the RPM. Finally, sensitivity analyses were conducted with minor fluctuations in density and major fluctuations in carbon and hydrogen concentration to determine the impact on the final results and verify critical assumptions.

CHAPTER II

BACKGROUND

II.A. Radiation portal monitors

Threat detection for high-impact, low-probability events – such as the detonation of an IND or RDD – is a challenging task. In order to combat this threat, RPMs are deployed at border crossings, airports, seaports and other locations of interest around the world to detect RN material.[12] Portal monitoring systems passively detect gamma and neutron radiation emitted from cargo or pedestrian traffic. A RPM may contain any variety of detection equipment depending on the specific requirements of the customer. Portal monitors are available in multiple configurations from several different manufacturers all over the world. Typically, vendors provide data sheets outlining the physical size of the RPM, its suggested purpose, operational conditions, and detection capabilities. This section will provide an overview of portal monitors as it relates to the TSA Systems, Ltd. model VM-AG250 vehicle gamma monitor. The experimental methods described in this research are adaptable for any RPM configuration. Readers desiring a more exact description of a particular model are encouraged to request the relevant data sheets and user manuals from their vendor of choice.

A deployed RPM may consist of one or two self-contained pillars located on the side of a roadway. The pillars contain radiation detectors, an occupancy sensor, and amplification electronics. In a two-pillar system, the master pillar will also contain a battery, a battery charger, a single channel analyzer, and the system control circuitry.[13]

Monitors are also equipped with communications ports (e.g., RS-232, Ethernet, USB, etc.) to facilitate data transfer between the pillars and a control center. The pillars are typically bolted to a concrete footing.

While the RPM is unoccupied, it continuously monitors the background and updates the display reading in 5 sec increments. At any point, the background count rate is the average number of counts over the collection time. The system alarm algorithm is dependent upon a rolling average of the background count rate over a user-defined time period.[13] When the unit is occupied, it will begin collecting data at shorter time intervals. The monitor calculates a rolling average count rate for each detector based on the count for the interval and a user-defined number of intervals to count during occupancy. The number of intervals should be based on the expected amount of time it will take a vehicle to pass through the monitor at a given rate of speed. The system count rate is determined by summing the rolling average count rate of all relevant detectors in the pillars.[13] If the user is interested in the count rate over a certain energy region, upper and lower level discriminators can be applied to the detectors. The RPM used in this research was discriminated between 40 and 140 keV at the request of the research sponsor. Most monitors also have a "look back" and "hold in" capability to protect against hidden sources in the front or rear of a vehicle. During "look back" the system will make an alarm comparison immediately after occupancy using count data for a specified amount of time preceding occupancy. During "hold in", the monitor will continue to make alarm comparisons for a specified amount of time after the vehicle has vacated the RPM.

The alarm threshold is the count rate above background required to trigger a radiation alarm. A typical alarm algorithm is given by:

$$A_{\text{th}} = B_{\text{avg}} + N\sigma_{B_{\text{avg}}} \tag{1}$$

where A_{th} is the alarm threshold, B_{avg} is the rolling average background count rate, N is a user-defined variable, and $\sigma_{B_{\text{avg}}}$ is the standard deviation of the rolling average background count rate.[13] The selection of N is important since it directly impacts the detection capabilities of the monitor. If N is set too low, the number of false alarms may increase, conversely, if N is set too high, the system may not alarm at all. In order to prevent artificially raising and lowering the background, some monitors include high and low gamma faults. If the count rate ever surpasses the high fault point, or dips below the low fault point, the monitor will give a fault alarm and cease to operate until the problem is corrected.[13]

When considering the impact of background radiation on a RPM, it should also be noted that higher background increases the MDA of the system, which may lead to more material being undetected during transit. The method of calculating detection limits is largely based on the technique developed by Currie.[14] The Currie Equation is used to calculate the minimum count rate – or number of counts – required to ensure false-positive alarm rates less than a given .[15] The Currie Equation is given by the following:

$$N_D = 4.653\sigma_B + 2.706 \tag{2}$$

where N_D is the minimum number of counts required to achieve false-positive rates less than 5% and σ_B is the standard deviation of the counts attributable to background.[15] The Currie Equation may be adapted to determine the MDA for a particular radioisotope of interest using the following:

$$A_{\mathrm{MD}} = \frac{N_D}{y\varepsilon t} \tag{3}$$

where A_{MD} is the MDA of a specific nuclide, y is the gamma yield per decay for that nuclide, ε is the absolute efficiency of the detector, and t is the counting time.[15]

Since both the alarm threshold and MDA for a RPM are dependent on the background count, it is important to highlight what constitutes background radiation. Most natural gamma radiation comes from members of the ^{238}U or ^{232}Th decay chains or ^{40}K. The radionuclides formed in these decay series were of primary concern during the course of this research. In addition to natural sources, there are man-made and cosmic sources of background radiation. Man-made sources are caused by nuclear weapons testing and use, nuclear accidents, and nuclear reactors.[16] Cosmic radiation refers to energetic particles of extraterrestrial origin that interact with the Earth's atmosphere. These particles may be either galactic or solar in origin.

Concrete is typically made up aggregate materials and a binding paste. The aggregates comprise between 60 and 70 percent of the total volume of concrete and may be made of any granular material available to the mixer, such as: sand, gravel, glass, or crushed quarry stone.[17] The uranium and thorium concentration in the aggregate materials varies widely across the world. Natural gamma ray emitters contained in the concrete surrounding portal monitors can contribute significantly to the background of the detectors.[18]

II.B. Gamma ray interactions

While there are more than 3,000 known nuclides, only about 270 of them are stable.[19] The rest are radioactive and decay into other nuclides by emitting radiation. There are at least nine different decay modes that provide a path for an unstable nuclide to attain stability. A nuclide may attain stability through energy loss caused by either the emission of ionizing particles or electromagnetic radiation. Typically, most radioactive decay processes consist of one or a combination of the most common modes: alpha, beta, and gamma.[19] The number of emitted particles and their respective energies can be quantified through interactions with a radiation detector.

The methods described in this thesis focus entirely on detection of emitted gamma rays. They are a form of high-energy, short-wavelength electromagnetic radiation with an energy range typically between 10 keV and 10 MeV.[20] When an unstable nuclide undergoes alpha or beta decay, the daughter nuclide is left in an excited state in which it possesses more energy than its ground state. The daughter nuclide must

return to its ground state by casting off the excess energy. This is primarily done through the emission of a gamma ray. In most cases, the daughter nuclide will have more than one excited state, requiring the emission of multiple gamma rays to successfully transition to its ground state.

In order to be detected, a gamma ray must undergo at least one of three possible interactions with the detector material: 1) photoelectric absorption, 2) Compton scattering, or 3) pair production. In photoelectric absorption, a photon collides with a bound electron of a target atom. This photoelectron is subsequently ejected from its shell with kinetic energy given by:

$$T_e = E_\gamma - E_b \tag{4}$$

where T_e is the kinetic energy of the photoelectron, E_γ is the energy of the incident gamma, and E_b is the binding energy of the electron in its shell.[21] After this event, the target atom is left in an excited state and will release its excess energy either by redistributing it between the remaining electrons or through x-ray fluorescence coupled with subsequent photoelectric absorptions.[19] In most cases, the result of photoelectric absorption is an ejected photoelectron which carries off a majority of the initial gamma energy coupled with one or more lower-energy electrons corresponding to the original binding energy of the photoelectron. If none of the characteristic x-rays escape the detector, the sum of the kinetic energies of the electrons created during this process will equal the energy of the incident photon.[15]

In Compton scattering, an incident gamma undergoes an elastic collision with a free electron, resulting in a recoil electron and a scattered gamma. The kinetic energies of the recoil electron and scattered gamma are given by Eqs. (5) and (6), respectively.

$$T_e = E_\gamma - E'_\gamma \tag{5}$$

$$E'_\gamma = \frac{E_\gamma}{1 + \left(\frac{E_\gamma}{m_o c^2}\right)(1 - \cos\theta)} \tag{6}$$

Where T_e is the kinetic energy of the recoil electron, E'_γ is the kinetic energy of the scattered gamma, E_γ is the energy of the incident gamma, $m_o c^2$ is the rest mass energy of an electron (511 keV), and θ is the scattering angle.[21] All scattering angles from 0 to π will occur within a detector. This allows a continuum of energies to be transferred to the free electron between the minimum and maximum scattering angles.

During pair production, an incident photon interacts with the electric field around the target nucleus and is completely absorbed, resulting in the creation of a positron-electron pair. Since an energy of twice the rest mass of an electron is required to create the pair, the incident gamma must have an initial energy of at least 1.022 MeV for the process to occur.[15] If the incident gamma energy is above 1.022 MeV, the excess energy is shared between the positron-electron pair. The kinetic energy of the positron-electron pair is given by:

$$T_{e-} + T_{e+} = E_\gamma - 2m_o c^2 \tag{7}$$

where T_{e-} is the kinetic energy of the electron, T_{e+} is the kinetic energy of the positron, E_γ is the energy of the incident gamma, $m_o c^2$ is the rest mass energy of an electron.[21] Additionally during pair production, when the kinetic energy of the positron becomes low, the positron will combine with a normal electron in the target medium and create two annihilation photons,[15] each with an energy of $m_o c^2$. Both the positron and the electron are destroyed during this process and the energy from the annihilation may be absorbed in the detector material.

The three processes can all occur within a detector; however, their dominance varies with energy of the incident gamma ray and the atomic number of the absorption medium. The photoelectric effect is dominant at low energies (<100 keV), pair production at high energies (>5 MeV), and Compton at energies between these regions. The three photon interaction processes and their corresponding regions of dominance are shown in Figure 3.

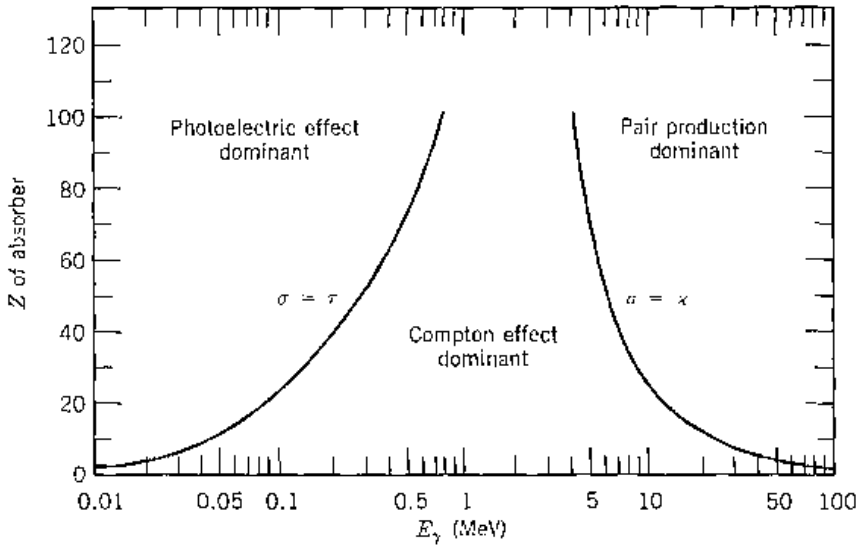

Figure 3. The three primary gamma ray interaction processes and their corresponding regions of dominance.[21]

II.C. Characteristics of gamma ray detectors

In order for a gamma ray to be detected, it must interact with some material, and that interaction must be recorded. While there are several different types of gamma ray detectors, two are of particular importance to this research: scintillation and semiconductor – or solid-state – detectors. Information on other types of gamma ray detectors may be found in *Radiation Detection and Measurement* by Knoll or *Passive Nondestructive Assay of Nuclear Materials* by Reilly, et. al.[15,22] One characteristic of interest for both solid scintillators and semiconductor detectors is the electronic band structure. For an individual atom, electrons are arrayed in precise energy levels; however, when a collection of atoms is combined to form a solid these energy levels are broadened into energy bands, each of which can contain a fixed number of electrons.[15] Between the bands are energy regions that are forbidden to an electron. The highest

occupied energy band is called the valence band. The next available energy states are in a higher band called the conduction band. It is separated from the valence band by the forbidden region.[20] In order for an electron to migrate through a material, it must be able to move out of its current energy state and into another so that it can move from one atom to another. Applying an external electric field will allow a current to flow if electrons are able to move into suitable energy levels.[20]

There are three types of material: insulators, conductors, and semiconductors. A schematic of the electronic band gap structures for these materials is shown in Figure 4. In an insulator, the valence band is full and the next available energy states are in the conduction band. An electron must have sufficient energy to traverse the forbidden region from the valence band to the conduction band in to order to migrate through the material. For an insulator, this gap may be between 5 and 10 eV or larger, which is usually more than can be attained through thermal excitation.[20] In a conductor, the conduction band is continuous with the valence band, and the valence band is not full. Thermal excitation will ensure that the conduction band is always populated and the application of any electric field will cause a current to flow.[20] In a semiconductor, the valence band is full, but the forbidden region is much smaller than for an insulator. This gap is typically around 1 eV, which is achievable through thermal excitation. In a normal environment there will always be a small electron population in the conduction band and the material will exhibit some degree of conductivity.[20]

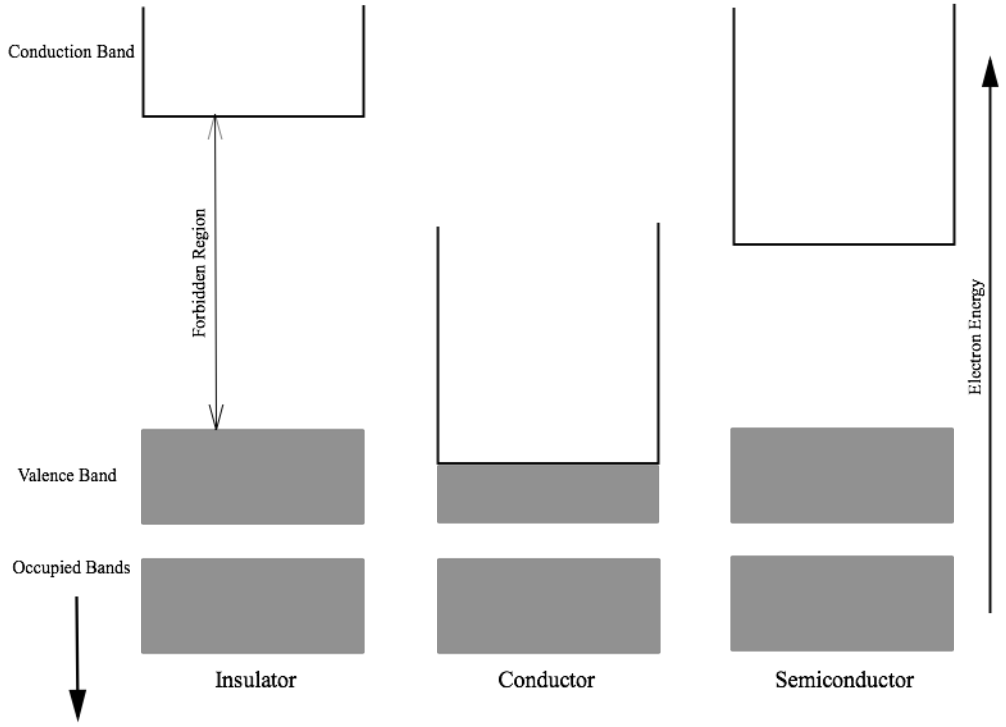

Figure 4. A schematic of the electronic band gap structure of insulators, conductors, and semiconductors.

Scintillation detectors are one of the oldest methods for detecting ionizing radiation. A scintillation detector consists of a solid, liquid, or gas luminescent material coupled with a photomultiplier tube (PMT), which is capable of detecting emitted light. The scintillator may be organic (e.g., liquid or plastic) or inorganic (e.g., sodium iodide or cesium iodide); however, it must be capable of proportionally converting the kinetic energy of charged particles into visible light at a high efficiency, be transparent to the wavelength of its own emission, and have a short decay time for the induced luminescence.[15]

In a scintillator, an incoming gamma ray excites an electron from the valence band to the conduction band. In some cases, the energy imparted to the electron may not be sufficient to raise it to the conduction band, thus it remains electrostatically attracted to the hole in the valence band. If the electron de-excites by returning to the valence band, it will emit electromagnetic radiation in the form of a photon.[20] In a pure inorganic scintillator, the de-excitation of the electron and emission of a photon is an inefficient process, and the size of the forbidden region is such that the emitted photon would be of too high an energy to be in the visible spectrum.[15] These problems are solved by adding a small amount of impurity material, called an activator. Thallium is added as an activator material in most sodium iodide detectors. The addition of the activator creates defects in the lattice where the normal electronic band structure is different from that of the pure crystal.[15] These defects give rise to additional energy states in the forbidden region where the electron may de-excite back to the valence band. If the appropriate activator is used, this transition will give rise to a visible photon, which serves as the foundation for the scintillation process.[15]

When an incident gamma ray undergoes photoelectric absorption in the scintillator, the elevation of secondary electrons from the valence band to the conduction band will cause the emergent photoelectron passing through the medium to create a large number of electron-hole pairs. The positive hole will drift to the location of an activator site and ionize it, since the ionization energy of the impurity is less than that of a lattice site.[15] The electron will continue to move through the crystal until it encounters an ionized activator site. At this point, the electron will drop into the activator site and

create a neutral configuration with its own excited energy states. If the excited configuration has an allowed transition to the activator ground state, it will de-excite and emit a photon in the visible range.[15]

The emitted photons from the scintillator must be collected and converted into an electrical pulse in order to form a useful detector. Generally, this is done using a PMT, which is optically coupled to the scintillation crystal. Incident photons in the visible range strike the photocathode of the PMT, where they undergo the photoelectric effect. An electrical field then accelerates the ejected photoelectrons through the PMT. As they are accelerated, they collide with dynodes in the tube and release additional electrons. The electrons are then further accelerated to collide with succeeding dynodes, resulting in a multiplication of the electron flux from the initial state at the photocathode.[22] An amplified charge arrives at the anode of the tube where magnitude of the electrical pulse is proportional to the amount of energy deposited in the scintillator. A drawing of the components of a typical scintillation detector is shown in Figure 5.

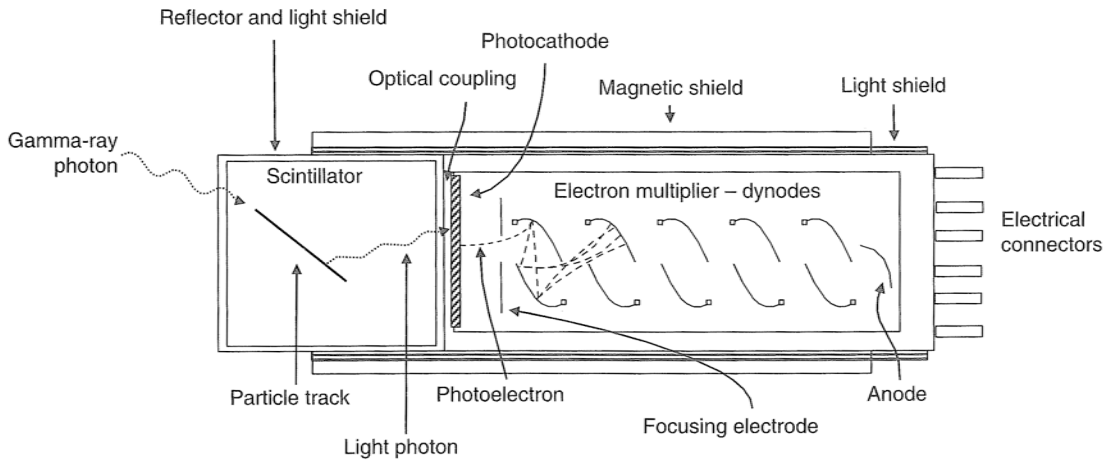

Figure 5. A drawing of the components of a scintillation detector.[20]

Unlike scintillation detectors, semiconductor detectors collect the charge created by gamma ray interactions directly by applying voltage across the material and sweeping the charge carriers to the electrodes.[22] For any temperature greater than 0 K, the electrons in the semiconductor crystal will share some thermal energy. When a valence electron achieves sufficient thermal energy to cross the forbidden region into the conduction band, a vacancy in the valence band is left behind. This combination is referred to as an electron-hole pair. When a voltage is applied to the material, the electron in the conduction band and the hole in the valence band will move in opposite directions, contributing to the observed conductivity of the semiconductor.[15] The probability that an electron-hole pair is generated in the material is dependent upon the temperature of the material, as shown by the following:

$$p(t) = CT^{\left(3/2\right)} e^{-\left(\frac{E_f}{2kT}\right)} \tag{8}$$

where $p(t)$ is the probability per unit time that an electron hole pair is produced, C is a proportionality constant characteristic to the semiconductor material, T is absolute temperature, E_f is the energy required to cross the forbidden region, and k is the Boltzmann constant.[15] The number of electrons in the conduction band can be reduced by cooling the semiconductor. This reduces the amount of current flowing across the surface of the detector and makes it easier to detect the extra excitation induced by the gamma ray interactions.[20]

After an incident gamma ray interacts with the detector material, primary electrons are produced with greater than thermal energies. Subsequent interactions of the primary electrons can raise secondary electrons from occupied energy bands well below the valence band to energy levels well above the base of the conduction band.[20] The excited electron and embedded hole will redistribute themselves within available energy bands until they arrive at the base of the conduction band and the top of the valence band, respectively. The migration of the electron-hole pair through the material creates additional excitations, leading to an electron-hole pair cascade for each primary electron interaction.[20] In the presence of an electric field, the electrons and holes will move up and down the field gradient, respectively, to the electrodes. The collected charge is then converted into a voltage pulse by a preamplifier.[22] The number of electron-hole pairs produced is directly related to the absorbed energy of the incident gamma ray, as shown by the following:

$$n = \frac{E_\gamma}{\varepsilon} \tag{9}$$

where n is the number of electron-hole pairs produced, E_γ is the absorbed energy of the incident gamma ray, and ε is the average energy required to create an electron-hole pair in the detector.[20]

In a perfect semiconductor, the electrons promoted to the conduction band would leave behind an equal number of holes in the valence band. This is referred to as an

intrinsic semiconductor. It is impossible to create a material free of impurities. The impurities found in semiconductor materials can have a significant impact on their thermal conductivity.[15] As an example, germanium has a valency of +4 and in a crystal lattice it is surrounded by four other germanium atoms. If an impurity atom with a different valency is present, it will disturb the electronic balance of the lattice. If the impurity atom has a lower valency than the germanium, there will be holes in the electronic configuration.[20] When these impurities are distributed throughout the semiconductor, extra energy states – called acceptor states – are created above the valence band. Germanium with this type of impurity is called P-type. If an impurity atom had a higher valency than the germanium, there will be an excess of electrons in the lattice structure.[20] This gives rise to extra energy states – called donor states – just below the conduction band. Germanium with this type of impurity is called N-type. In each case, the effect of the extra energy states is a narrowing of the forbidden region and a higher conductivity than in an intrinsic semiconductor. A deeper explanation on the solid-state physics of semiconductors and its impact on radiation detection is beyond the scope of this thesis; however, additional discussion may be found in *Practical Gamma-ray Spectrometry* by Gilmore.[20]

The choice of detector is primarily dependent on the objectives of the measurement. In cases where spectral resolution is of the utmost importance, such as in the measurement of spent fuel or background radiation, a semiconductor detector offers superior resolution to that of a scintillator, thus allowing easier differentiation of gamma ray energy peaks. If a small number of nuclides are being measured with energies

sufficiently far apart to reduce overlap between peaks, a scintillator is an efficient, low-cost option.[20] A semiconductor detector made with germanium or silicon will require cryogenic cooling to operate; however, a scintillator may be used at room temperature. While some semiconductor detectors such as cadmium telluride (CT), cadmium zinc telluride (CZT), or mercury iodide (HgI_2) will operate at room temperature, they are limited in size and ideally suited for low-energy gamma ray measurements.[20] An entire semiconductor detector apparatus consisting of the semiconductor crystal, housing, amplification electronics, cryogenic components, and a liquid nitrogen dewar or mechanical cooling system can cost over an order of magnitude more than a scintillation unit coupled to a PMT.

II.D. Neutron activation analysis

NAA is primarily used to determine trace elements in a sample; however, in some cases – such as this research – it may also be used for determination of minor and major elemental concentrations. This method of analysis was first proposed by Hevesy and Levi in 1936 while observing the consequences of neutron bombardment of rare earth elements.[23,24] It did not become a practical method of analysis until the advent of the nuclear reactor as a source of neutrons. The introduction of NaI(Tl), lithium-drifted germanium [Ge(Li)], and HPGe gamma ray detectors over the years made NAA the preeminent method for determination of trace materials.[25]

In practice, NAA references a group of analytical techniques that use neutrons to induce a nuclear reaction in a target atom. The decay properties of the product nuclides

are detected and used to quantify the elemental concentration of the target. Neutron bombardment of the target atoms may induce several different reactions, such as: (n, γ), (n, p), (n, α), (n, 2n), or even (n, n). The probability of one incident particle interacting with a target nucleus to induce a reaction is referred to as the microscopic cross-section.[21] There is a microscopic cross-section for each specific reaction a target nuclide is capable of undergoing. A plot of select microscopic cross-sections for ^{28}Si is shown in Figure 6.

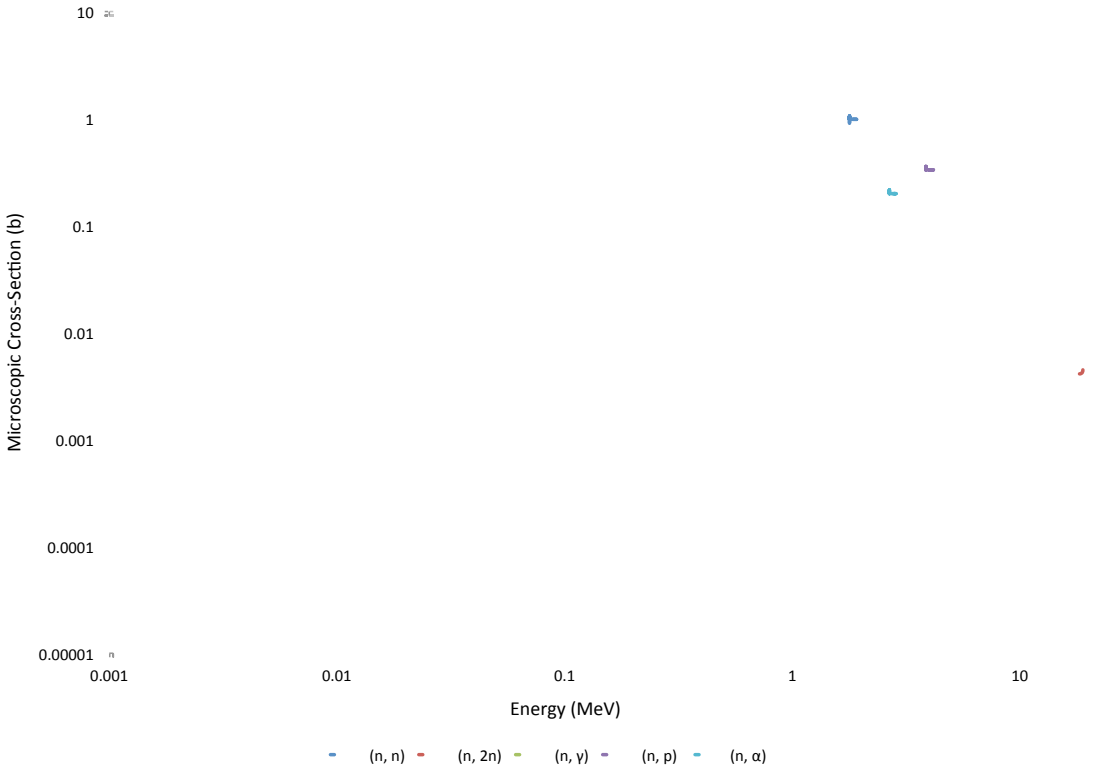

Figure 6. A plot of microscopic cross section data for select reactions in ^{28}Si.[26]

NAA is generally divided into two categories: instrumental neutron activation analysis (INAA) and radiochemical neutron activation analysis (RNAA). In RNAA, the desired nuclide is chemically separated from the elemental matrix prior to measuring the gamma spectrum of the irradiated sample. While this allows for lower detection limits, it is too time-consuming to be used for routine analysis.[25,27] This research described in this thesis involved only INAA. A discussion of the theory, process, and application of RNAA can be found in *Neutron Activation Analysis* by De Soete.[28]

While the field of INAA encompasses several different analytical methods, it is primarily associated with activation of a sample with thermal neutrons. For some trace or minor elements, measurement by thermal neutron activation may be insufficient because the reaction probability is too low, their half-lives are too short (< 1 sec) or excessively long (> 100 yrs), or the production nuclides do not emit gamma rays.[25] In these cases epithermal NAA (ENAA), prompt gamma NAA (PGNAA) or fast NAA (FNAA) may be used to determine material composition. In ENAA, a sample is irradiated in a vial designed to filter out thermal neutrons through the use of strong absorbers such as cadmium, boron carbide (B_4C), or boron nitride (BN).[25] In PGNAA, the prompt capture gamma rays are measured rather than the radioactive product using a collimated neutron beam.[25] In FNAA, a sample is irradiated with fast neutrons from a generator in order to determine material concentrations through the use of reactions with high threshold energies. While ENAA and PGNAA have several useful applications, the research described in this thesis incorporates only INAA with thermal neutrons and FNAA.

In INAA, a sample is bombarded with thermal neutrons, the source of which is generally nuclear fission in a reactor. In most cases, this induces a (n, γ) reaction in the target nuclide. The resultant gamma rays from the subsequent decay processes are then quantified using a suitable detector. Since all samples will contain more than one type of nuclide, there is a possibility that several hundreds of different gamma rays will be produced during irradiation. Modern detectors coupled with a multichannel analyzer (MCA) have the ability to differentiate and analyze multiple gamma ray interactions with the detector at one time, thereby making INAA well suited for multi-element analysis. Detection limits of INAA vary widely between elements because the sensitivity of the method for a given nuclide is a function of properties of its nuclear structure, such as the microscopic cross-section for a given reaction and the half-life.[25] Approximate detection limits for elements characterized by INAA are given in Table I. In addition, there has been research regarding a theoretical relationship between detector characteristics and INAA detection limits.[29]

Table I. Detection limits for elements characterized by INAA.[30]

Element	Limit (ng)	Element	Limit (ng)	Element	Limit (ng)
Ba	3,000	As	20	Sb	5
Sr	3,000	W	20	Sm	5
K	2,000	Br	10	Ag	3
Fe	500	Ce	10	Se	3
Rb	500	Co	10	Eu	2
Cd	200	Cs	10	Ta	1
Na	200	Th	10	Tb	1
Nd	100	U	10	Tm	1
Zn	100	Hf	5	Yb	1
Cr	50	La	5	Ir	0.5
Gd	50	Lu	5	Sc	0.5

There are several advantages to using INAA as a method of multi-element analysis. The major advantage of the method is the ability to analyze elements in a variety of matrices. INAA is generally independent of matrix interference because nuclear reactions and subsequent decay processes are not influenced by the physical and chemical composition of the sample pre- and post-irradiation.[25,31] Another advantage of INAA is the relatively small amount of sample preparation required prior to irradiation. In many cases, preparation only involves packaging the material in the appropriate vial whereas in competing techniques, such as mass spectrometry, the sample must normally be in a solution.[25] Since INAA is capable of discerning several elements from a single sample, it is also more cost-effective on a per-element basis. The large number of elements that can be determined from a single experiment offsets the costs of more precise analytical services for a single element.[31] In some instances, INAA may be used as a method of nondestructive analysis; however, recovery of the sample in some cases may be difficult or impossible due to the amount of emitted radioactivity from long half-

life nuclides that are produced during irradiation.[31] The recovery of the sample may also be impossible depending on the preparation required to conduct the experiment.

While INAA has several advantages, there are a few disadvantages to using the method. The major disadvantage is that it requires access to a nuclear reactor and the ability to conduct work in a radiation environment.[25,31] In most cases, radiation work requires a license from a government authority or regulatory body. This may be overcome by contracting the work to a facility. Another disadvantage of INAA is that it is incapable of determining the speciation or oxidation state information for a particular element.[25,31] This is due to the fact that INAA is a nuclear process and thereby independent of the chemical state of the sample. Speciation information may be obtained through chemical separation prior to irradiation.[25] Establishing and maintaining a counting laboratory for INAA is an expensive endeavor since the method is best performed with high-resolution semiconductor detectors that require cryogenic cooling to function properly.[31] Less expensive scintillation detectors may be used, but their poor resolution compared with semiconductor detectors make them a non-ideal solution for discerning multiple elements within a sample.

In cases where the microscopic cross-section for the (n, γ) reaction is too low, the (n, γ) reaction does not produce a radioactive species, or the half-lives of the product nuclide are too short to be measured using thermal neutron INAA, FNAA may be used to induce a nuclear reaction.[25] In FNAA, fast neutrons are produced by a generator for the purpose of inducing a threshold reaction in the target. A threshold reaction is a reaction in which the incident neutron must have a minimum amount of energy in order

to occur. Examples of threshold reactions include (n, p), (n, α) or (n, 2n) reactions. The energy required for a particular threshold reaction to occur is as follows:

$$E_{\text{th}} = -Q\frac{m_a + m_X}{m_X} \tag{10}$$

where E_{th} is the threshold energy of the reaction, Q is the rest mass energy difference between the target nucleus and incident particle and the product nucleus and ejected particle, m_a is the relative atomic mass of the incident particle, and m_X is the relative atomic mass of the target nuclide.[32] The value of Q is calculated by:

$$Q = \left(m_X + m_a - m_Y + m_b\right)c^2 \tag{11}$$

where m_Y is the relative atomic mass of the product nuclide, m_b is the relative atomic mass of the ejected particle, and c is the speed of the light.[21] Additional information on nuclear reactions and reaction kinematics may be found in any nuclear or modern physics text such as: *Introductory Nuclear Physics* by Krane, *Modern Physics* by Tipler and Llewellyn, or *Modern Physics for Engineers* by Oldenberg and Rasmussen.[19,21,32]

In this research, FNAA was used to determine oxygen and silicon content in the samples through the ^{16}O(n, p)^{16}N and ^{28}Si(n, p)^{28}Al reactions, respectively. These reactions were induced by 14.7 MeV neutrons resulting from the ^{3}H(^{2}H, n)^{4}He fusion reaction in a sealed tube neutron generator. The fusion reaction caused by an impinging

beam of deuterons on a tritium-coated target leads to an isotropic emission of product neutrons. Once the neutrons strike the target nuclide in a sample, it is possible to use gamma rays emitted from the subsequent decay processes of the product nuclide to quantify the concentration of the target. In the case of silicon determination, ^{28}Al decays to ^{28}Si by beta emission with a half-life of 135 sec. The detected gamma ray from this process has an emission rate of 100% and energy of 1.78 MeV. In the case of oxygen determination, ^{16}N decays to ^{16}O by beta emission with a half-life of 7.13 sec. The detected gamma rays from this process have energies of 6.13 MeV and 7.12 MeV, with emission rates of 67% and 5%, respectively.[33] An exhaustive discussion on the operational characteristics of neutron generators is beyond the scope of this thesis; however, an excellent description and analysis of pumped and sealed tube neutron generator systems may be found in *Activation Analysis with Neutron Generators* by Nargolwalla and Przybylowicz.[34]

It should be noted that there are two distinct methods for conducting FNAA measurements. A common method is to use a dual-axis rotator assembly to irradiate the unknown sample and the comparator standard at the same time and then count them simultaneously on two different detectors. Another method involves conducting single-pass or cyclic irradiations of the samples and comparator standard. This requires the neutron count be normalized to account for flux variations between irradiations. The normalization technique used in this research has been outlined previously by Ehmann and James.[35-37] In this technique, a boron trifluoride (BF_3) gas-filled proportional counter is used as the neutron detector. During irradiation, the signal from neutron

interactions in the BF_3 tube is passed to a multichannel scalar (MCS). The MCS has a user-defined number of channels with a preset dwell time per channel. Neutron counts during the dwell time are recorded in one channel. Once the dwell time is complete, the MCS moves to the next channel and the process repeats. The total neutron count is then obtained by integrating with respect to the collection time of the BF_3 tube. Comparison of total counts between samples allows for normalization of the neutrons generated between sample irradiations.

There are many advantages to using FNAA for compositional analysis. One of the major advantages of the method is the ability to automate the process. Most isotopes used for analysis with FNAA have short half-lives, thus the irradiation and counting time are small compared to INAA. Automation allows a computer to control the generator operation, sample transfer, counting sequence, detector spectrometry, and data analysis. This allows for higher accuracy in measurements, especially when nuclides with short half-lives are counted.[34] Another advantage of FNAA is that the technique is highly selective, allowing the experimenter the to use nuclear properties (e.g., half-life, reaction cross-section, decay properties) to differentiate elements in a matrix through a choice of irradiation, decay, and counting times.[34] Neutron energy may be adjusted by adding moderating media or changing the target material. Additionally, the type of gamma ray detector may be selected to coincide with the experimental requirements. Typically, NaI(Tl) scintillation detectors are more than adequate for FNAA analysis. In some cases, Ge(Li) or HPGe detectors are employed when higher resolution is needed, but the low efficiency of these detectors limits their usefulness.[34]

There are limitations of the FNAA method when compared to other analytical methods. The largest limitation is the lack of sufficient neutron flux from generators to attain the desired sensitivity for some elements.[34] In addition, microscopic cross-sections for fast neutron induced reactions are around one to three orders of magnitude smaller than the (n, γ) reaction for thermal neutrons. This fact, coupled with a typical neutron output from a tritium target of 10^{10} to 10^{11} sec^{-1}, results in detection limits between 0.1 mg and 10 mg for most elements.[34] Another limitation of FNAA is the cost associated with establishing a facility capable of conducting the measurements. At a minimum, a neutron generator, multichannel analyzer, gamma ray detector, and shielding will be required. Adding the necessary computer or logic control systems to automate the process will also increase the cost.[34] As with INAA, this may be overcome by contracting the work to an existing facility.

II.E. Principles of radioactive decay and the relative method

Knowledge of the basic principles of radioactive decay is necessary in order to understand the methods used to calculate elemental concentration from INAA and FNAA data. Disintegration of an atom is one of the true random events in nature. It is impossible to predict when one nuclide will decay; however, the rate of decay of a group of nuclei is directly proportional to the number of atoms present. The probability per unit time that a nucleus will decay is called the decay constant. The decay constant is expressed by the following:

$$\lambda = -\frac{dN/dt}{N} \tag{12}$$

where λ is the decay constant, N is the number of radioactive nuclide present, and dN is the number of nuclides that decay in time, dt.[21] Integrating this equation gives the following:

$$N(t) = N_o e^{-\lambda t} \tag{13}$$

where $N(t)$ is the number of nuclides present at time, t, and N_o is the initial number of nuclides present.[21] The decay constant may be expressed in terms of the half-life of the nuclide, or the amount of time required for half of the nuclei to decay. The decay constant is given by:

$$\lambda = \frac{\ln(2)}{t_{1/2}} \tag{14}$$

where $t_{1/2}$ is the half-life of the nuclide. The activity is defined as the rate at which decays occur in the sample.[21] This is given by:

$$A(t) = \lambda N(t) = A_o e^{-\lambda t} \tag{15}$$

where $A(t)$ is the total number of decays per unit time and A_o is the initial activity of the sample.[21]

In the case of NAA, stable nuclei are activated and their subsequent decay processes are measured. During irradiation, the production of radioactive nuclei is proportional to the microscopic cross-section of the neutron capture reaction of interest, the neutron flux, and the number of target atoms.[28] At the same time, the radioactive nuclei decay during the irradiation. The decay rate of the radioactive nuclei is given by:

$$A_2(t_{\text{irr}}) = N_{o,1}\sigma_1\phi\left(1 - e^{-\lambda_2 t_{\text{irr}}}\right) \tag{16}$$

where $A_2(t_{\text{irr}})$ is the decay rate of the radioactive nuclide for an irradiation time, t_{irr}, $N_{o,1}$ is the initial number of target nuclides, σ_1 is the microscopic cross-section for the neutron capture reaction of interest, ϕ is the neutron flux, and λ_2 is the decay constant of the radioactive nuclei.[28] The $1 - e^{-\lambda_2 t_{\text{irr}}}$ term is known as the saturation factor, S. In cases where the irradiation time is much longer than the half-life of the radionuclide, $e^{-\lambda_2 t_{\text{irr}}} \rightarrow 0$, and thus $S \rightarrow 1$.[28] At this point, $A_2(t_{\text{irr}})$ reaches a maximum. It should also be noted that the number of nuclides is indicative of the mass of the element in a sample as given by:

$$N_{o,1} = \frac{m_1 N_A}{M_1} \tag{17}$$

where m_1 is the mass of the target element in the sample, N_A is Avogadro's number, and M_1 is the atomic mass of the target element.[32]

It is usually necessary to correct for the decay during transport of the sample between the neutron source and the radiation detector using a decay correction factor given by:

$$D = e^{-\lambda_2 t_d} \tag{18}$$

where D is the decay correction factor and t_d is the decay time.[38] It is also necessary to apply a measurement correction factor to account for decay while the sample is counted on the detector. This factor is defined as follows:

$$C = \frac{1 - e^{-\lambda_2 t_m}}{\lambda_2 t_m} \tag{19}$$

where C is the measurement correction factor and t_m is the measurement time.[38] When all correction factors are applied, the decay rate of the radioactive nuclei in the sample can be calculated as follows:

$$A_2(t) = \frac{m_1 N_A}{M_1} \sigma_1 \phi SDC \tag{20}$$

where $A_2(t)$ is the decay rate of a radionuclide formed by neutron bombardment at a time, t after incorporation of all relevant correction factors.[39] This equation forms the basis of the relative method used to calculate elemental concentrations from NAA data.

The majority of NAA work uses the relative technique.[40] This method consists of simultaneously irradiating known masses of a comparator standard along with the unknown mass of a sample. If there are no variations in the nuclear parameters of the element or the neutron flux during irradiation, the activity per unit mass – called the specific activity – of the standard and the sample will be equal.[40] This relationship is given by:

$$\frac{A_2}{m_1} = \frac{N_A}{M_1}\sigma_1\phi SDC = \frac{A_2^*}{m_1^*} = \frac{N_A}{M_1^*}\sigma_1^*\phi^* S^* D^* C^* \tag{21}$$

where the asterisks refer to the comparator standard. Given the assumption that nuclear parameters and the neutron flux remain constant, this equation is further simplified to calculate the mass of the target element in an unknown sample. In addition, since irradiation occurs simultaneously, the saturation factor will be equal for the standard and the sample. The simplified form is given in Eq. (22). If the concentration of the target nuclide is desired, Eq. (23) may be used in lieu of Eq. (22).

$$m_1 = m_1^* \frac{A_2}{A_2^*}\frac{D}{D^*}\frac{C}{C^*} \tag{22}$$

$$\omega = \omega^* \frac{m^*}{m} \frac{A_2}{A_2^*} \frac{D}{D^*} \frac{C}{C^*} \tag{23}$$

Where ω is the concentration of the target nuclide in the sample, ω^* is the concentration of the target nuclide in the standard, m^* is the total mass of the standard, and m is the total mass of the unknown sample.

The relative method is simple to use, precise, and accurate if standards are available which are relatively similar in composition to the sample.[40,41] The technique also eliminates errors associated with the neutron flux, nuclear parameters, detector efficiency, gamma emission rates, isotopic abundances, and coincidence summing.[40]

Despite these advantages, the method has some drawbacks. One of the main drawbacks is that the quantity of unexpected elements that are present in the sample spectrum but not characterized by the standard cannot be determined.[41] Another disadvantage of the method is that the integrity of the standard must be maintained. In most NAA experiments, the validity of the standard – along with the experimental parameters and procedures – can be insured by incorporating a quality control material into the measurements. This is done by treating the material as an unknown sample and comparing the results to its certified elemental concentration. There are other techniques used to analyze results from NAA, most notably, the absolute and single comparator methods. Discussion of these methods is beyond the scope of this thesis; however, the description of these two methods is given by Girardi[39,42], and a comparison of all three techniques is provided by Kafala[40] and Bereznai.[41]

II.F. Discussion of select Genie™ 2000 algorithms

The Genie™ 2000 software is an integrated package designed to acquire and analyze spectra from a MCA. The software provides MCA control, spectral display and manipulation, basic spectrum analysis, and reporting of results.[43] In addition, expansion options are available that provide comprehensive analysis capabilities for alpha and gamma spectroscopy. This section is designed to provide a brief overview of the computational algorithms that were used in the course of this research. An exhaustive explanation of the features of Genie™ 2000 can be found in the *Genie™ 2000 Operations Manual* from Canberra Industries.[43] Detailed discussion of additional analysis algorithms available with the Genie™ 2000 software may be found in the *Genie™ 2000 Customization Tools Manual* from Canberra Industries.[44]

In order to find energy peaks and determine their area, the software must know what specific information to look for in the spectrum. This is accomplished with a statistical model containing unknown parameters that can be determined from physical measurements. In gamma spectroscopy with HPGe detectors, the expected peak shape is defined by a modified Gaussian distribution, given by:

$$F_i = \begin{cases} He^{-\frac{\left(x_i - C_p\right)^2}{2\sigma^2}} & x_i > C_p - T \\ He^{-\frac{T\left(2x_i - 2C_p + T\right)^2}{2\sigma^2}} & x_i < C_p - T \end{cases} \tag{24}$$

where F_i is the value of the peak model function at channel x_i, H is the height of the peak, C_p is the peak centroid channel, σ is the width of the Gaussian distribution, and T is the tail parameter.[44] The Gaussian width and the tail parameter are defined by Eqs. (25) and (26), respectively.

$$\sigma \approx \frac{FWHM}{2.355} \tag{25}$$

$$T = 0.7FWHM \tag{26}$$

Where the full-width at half-maximum (*FWHM*) is the width of the peak at half height after subtraction of the background continuum.[44]

The "Unidentified Second Difference" peak locate option in Genie™ 2000 uses a second difference peak locate algorithm to identify the presence of photopeaks in the spectrum given user-defined tolerance restrictions. The algorithm used by Genie™ 2000 is largely based on the PEAKFIND subroutine of the SAMPO80 computer program developed by Koskelo, et. al. in 1981.[45] The technique proposed by Koskelo was itself an expansion of work previously done by Mariscotti to determine a method for identifying peaks through numerical iteration using computers.[46] A detailed explanation of peak identification using the second difference method may be found in either reference.

The algorithm used in the Genie™ 2000 software defines the peak centroid channel as follows:

$$\text{centroid} = \frac{\sum_i i \cdot ss_i}{\sum_i ss_i} \tag{27}$$

where i is the channel number and the summation is done over the channels where the significance value, ss_i, is negative, thus the centroid is defined as the weighted average of those channels.[44] The significance value is defined by:

$$ss_i = \frac{dd_i}{sd_i} \tag{28}$$

where dd_i and sd_i are the generalized second difference and its standard deviation given by Eqs. (29) and (30), respectively.

$$dd_i = \sum_{j=-k}^{j=+k} c_j y_{i+j} \tag{29}$$

$$sd_i = \sqrt{\sum_{j=-k}^{j=+k} c_j^2 \left(y_{i+j}\right)} \tag{30}$$

Where y represents the number of counts per channel and the summation is conducted over $2k + 1$ channels, where k is dependent upon the calculated coefficients, c_j. The coefficients are calculated by:

$$c_j = \frac{100\left(j^2 - \sigma^2\right)}{\sigma^2} e^{-\left(\frac{j^2}{2\sigma^2}\right)} \tag{31}$$

where σ is the average Gaussian width of the peaks in the search interval. The algorithm is executed by setting c_0 equal to -100 and terminating the set of coefficients at k, such that $|c_{k+1}| \leq 0.01|c_0|$.[45] The second coefficient is then adjusted to make the sum of the coefficients equal to zero. The Gaussian width is automatically determined by the program based on the expected peak shape for the spectrum, and the coefficients are recalculated every 100 channels to ensure that the peak locate algorithm being used is appropriate for expected peaks.[44] The absolute value of the minimum of the significance value must be greater than the user-defined threshold value for the peaks to be "located" by the software.

The "Sum/Non-Linear Least Squares Fit Peak Area" option is designed to calculate the limits of the peak region and the area of a peak, along with its associated uncertainty. The net peak area for a single peak is calculated by:

$$S = G - B \tag{32}$$

where S is the net peak area, G is the sum of gross counts within the limits of the peak region, and B is the counts in the background continuum within the limits of the peak region.[44] Genie provides two different algorithms for determining the background continuum: linear or step. The linear algorithm should be used when the continuum is

approximately equal on either side of the peak region. The step algorithm is best used when the continuum is larger on one side of the peak. This research required the use of the step algorithm. For a step continuum, the parameter B may be calculated by:

$$B = \sum_{i=1}^{N}\left(\frac{B_1}{n} + \frac{B_2 - B_1}{nG}\sum_{j=1}^{i} y_j\right) \tag{33}$$

where N is the number of channels within the limits of the peak region, n is number continuum channels on either side of the peak region, B_1 is the number of counts in the continuum region to the left of the peak, B_2 is the number of counts in the continuum region on the right of the peak, G is the gross counts in the peak region, and y_i is the counts per channel in channel I.[44] The uncertainty for the net peak area with a step continuum is as follows:

$$\sigma_s = \sqrt{G + \frac{1}{(nG)^2}\left[\left(NG - \sum P_i\right)^2 B_1 + \left(\sum P_i\right)^2 B_2 + \left(B_2 - B_1\right)^2\left(\sum P_i\right)^2\left(\frac{1}{G} + \frac{1}{\sum P_i}\right)\right]} \tag{34}$$

where σ_S is the standard deviation of the net peak area and P_i is the combined summation of y_i.[44] If a peak area determination is subject to a critical level test, the net peak area must be greater than that of the critical level to be reported as a real peak. The critical level is determined by:

$$L_c = k_\alpha \sigma_0 \tag{35}$$

where L_c is the critical level, k_α is the maximum acceptable confidence level, and σ_0 is the standard deviation of a net background peak area.[44] The software will ignore any observed peak with an area below the critical level.

When measuring natural background of a sample, it is useful to perform a background subtraction in order to correct for background peaks that occur in the measurement environment. The "Standard Background Subtraction" option in Genie™ 2000 is designed for this purpose. The background corrected net peak area is given by Eq. (36).

$$S = (G - B) - I \tag{36}$$

Where I is the environmental background interference given by Eq. (37).[44]

$$I = \frac{T_s}{T_b} I_b \tag{37}$$

Where T_s is the live-time of the sample spectrum, T_b is the live-time of the background spectrum, and I_b is the net peak area of the corresponding peak in the background spectrum.[44] All peak identification and area calculations are done in the same manner

for the background spectrum as the sample spectrum. The uncertainty of a net peak area subject to an environmental background subtraction is calculated as follows:

$$\sigma_S = \sqrt{G + \left(\frac{N}{2n}\right)^2 (B_1 + B_2) + \left(\sigma_{I_b} \frac{T_s}{T_b}\right)^2} \tag{38}$$

where σ_{I_b} is the standard deviation of the net peak area corrected for environmental background.[44]

The "Efficiency Correction" calculation in Genie™ 2000 is used to obtain an efficiency and an associated uncertainty for each located peak using parameters established by the efficiency calibration. Genie™ 2000 supports four different efficiency curves: dual polynomial, linear polynomial, empirical polynomial, and interpolated. The interpolated curve uses a straight-line interpolation between two data points on either side of a requested energy. The empirical polynomial curve uses the natural logarithm of scaling-factor/E coefficients. The linear polynomial curve uses linear 1/E coefficients. The dual polynomial curve uses the natural logarithm of energies to establish separate curves on the low- and high-energy side of a crossover point. The dual efficiency curve was used for all efficiency correction calculations in this research because it provided the option of creating independent calibration curves for the low- and high-energy regions. The calculated efficiency and its associated uncertainty using a dual curve are shown by Eqs. (39) and (40), respectively.

$$\varepsilon = \exp\left[\sum_{i=0}^{n} b_i \left(\ln(E)\right)^i\right] \tag{39}$$

$$\sigma_\varepsilon = \varepsilon \sqrt{\sum_n \sum_m \left[\left(\ln(E)\right)^{n-1} \left(\ln(E)\right)^{m-1} \left(M^{-1}\right)_{n,m}\right]} \tag{40}$$

Where ε is the calculated efficiency, b_i are parameters defined for the curve during the initial efficiency calibration, and $(M^{-1})_{n,m}$ is the inverse of a matrix resulting from determination of the b_i efficiency calibration coefficients.[44]

The nuclide identification algorithm used by Genie™ 2000 uses a library of radionuclides and associated gamma ray energies to generate a matrix of possible identifications by comparing each nuclide in the analysis library to the observed peaks. The initial confidence index for each nuclide in the library is set to 1.0 and subsequently reduced through a series of three sequential penalty function calculations.[44] Nuclides are considered identified if they have a confidence index greater than the user-defined threshold. The activity of the identified nuclide is then calculated as follows:

$$A = \frac{S}{m\varepsilon' y T_i U_f DC} \tag{41}$$

where A is the activity of the nuclide per unit mass, S is the net peak area, m is the sample mass, ε' is the attenuation corrected efficiency, y is the branching ratio of the gamma ray associated with the energy peak, T_i is the live time of the acquisition, U_f is a

conversion factor to convert the result into units of μCi, *D* is the decay correction factor, and *C* is the measurement correction factor.[44]

II.G. Efficiency calibrations with ISOCS™

When measuring environmental background using gamma spectroscopy, it is essential to calibrate the efficiency of the detector as a mathematical function due to the wide range of gamma ray energies found in nature.[47] Efficiency calibrations can be done in a laboratory setting; however, these typically involve significant investment in calibration standards, hours of labor, and are only valid for a single source to detector geometry.[48] The ISOCS™ software is meant to reduce this burden by using mathematical techniques to determine the full energy peak efficiencies of a germanium detector in the 45 keV – 7 MeV energy range for almost any radiological source matrix or geometry.[49] The ISOCS™ calibration method consists of an HPGe detector characterized by Canberra, a user-defined source geometry, and the ISOCS™ software, which uses these to produce an efficiency calibration file. Validation of the software has been competed by Venkataraman et. al.[47]

Detector characterization is performed by Canberra Industries using MCNP. A MCNP model of the germanium detector is developed and independently validated using a National Institute of Standards and Technology (NIST) traceable point source. After validation, detector efficiencies are calculated using MCNP at a series of point locations distributed quasi-randomly around the detector. Response characteristics for the detector are created covering any point within a sphere 1,000 m in diameter, centered on the

detector, and over an energy range of 45 keV – 7 MeV.[48] The end result of the characterization is a series of mathematical equations describing the absolute efficiency as a function of angle, energy, and distance from the detector.[47]

The ISOCS™ software contains a set of geometry templates that simulate a variety of common shapes (e.g., boxes, cylinders, pipes, spheres, etc.). Each template has user-defined input parameters that describe the material, density, and dimensions of the source along with the position of the source relative to the detector. In order to calculate the efficiency, the ISOCS™ software divides the source region into 1,024 voxels, each containing a quasi-randomly determined point location. The efficiency of each voxel is calculated for a given energy, taking into consideration attenuation due to absorbers located within the source or the space between the source and detector.[47] The total efficiency is obtained by summing the voxels, and a second iteration is run with 2,048 voxels. If the results vary by less than the user-defined convergence criteria, the software will move to the next user-defined energy and repeat this process. If the convergence criterion is not met, the software will double the number of voxels and continue the calculations.[47]

II.H. Usage of MCNP

This section is meant to familiarize the reader with the advantages of MCNP and why the code was used for the simulations done in this research. An extensive description of the theory of the Monte Carlo method and the operation of the code itself can be found in *MCNP – A General Monte Carlo N-Particle Transport Code, Version 5, Volume I: Overview and Theory* by the X-5 Monte Carlo Team at Los Alamos National Laboratory (LANL). The MCNP version 5 code is available from the Radiation Safety Information Computational Center (RSICC). MCNP is a three-dimensional, general-purpose Monte Carlo transport code.[11] The code can be used for neutron, electron, photon, or coupled neutron, electron, photon calculations. It is also used for calculating the effective eigenvalue of fissile systems. In general, any physical shape defined by mathematics may be modeled using MCNP. Monte Carlo obtains answers for the transport equation by simulating and recording the specific behavior of individual particles.[50]

The MCNP transport code offers several advantages over codes that employ deterministic methods. One of the major advantages is that MCNP can be used to model complex, three-dimensional models that are impossible to describe with a deterministic model. MCNP also allows a large number of variance reduction techniques that can be used to lower the computational time and improve relative errors.[50] The code has built-in access to tens of thousands continuous-energy nuclear and atomic data libraries, which allows the user to call necessary information from a variety of sources. MCNP also contains a powerful source specification that can account for several different

source conditions without modification of the code.[50] It also allows independent probability distributions to be input for different source variables such as: time, energy, direction, and position. Another advantage of MCNP is the ability to tally current, flux, and energy normalized per starting particle. In the case of this research, MCNP was an ideal choice because it afforded the ability to create a complex, three-dimensional model consisting of a distributed source term with independent energy distribution probabilities and particle tallies over multiple volumes.

CHAPTER III

EXPERIMENTS AND SIMULATIONS

III.A. Gamma ray background measurements

Six core-drilled concrete cylinders were acquired from ORNL for the experimental measurements completed during the course of this research. Two samples each were drilled from three different composition concrete slabs. Each of the cylinders was marked with an identification number. The experimental samples are shown in Figure 7.

Figure 7. A picture of the six concrete samples used for this research.

The diameter and height of each sample were measured with a Neiko digital caliper, and the respective masses were measured using a Mettler-Toledo digital balance. The sample densities were subsequently calculated from these measurements. Since the heights of the samples were not uniform, an estimate of the average height was made using the following equation:

$$H = \frac{H_{\text{high}} + H_{\text{low}}}{2} \tag{42}$$

Where H is the estimated average height of the sample, H_{high} is the height of the sample at its highest point, and H_{low} is the height of the sample at its lowest point. Error propagations were done according to the standard error propagation formulas, given by:

$$r = s + t \tag{43}$$

$$r = s - t \tag{44}$$

$$\sigma_r = \sqrt{\sigma_s^2 + \sigma_t^2} \tag{45}$$

$$u = xy \tag{46}$$

$$u = \frac{x}{y} \tag{47}$$

$$\sigma_u = u\sqrt{\left(\frac{\sigma_x}{x}\right)^2 + \left(\frac{\sigma_y}{y}\right)^2} \tag{48}$$

where s, t, x, and y are measured values, r is the sum or difference of s and t, u is the product or quotient of x and y, and σ_s, σ_t, σ_r, σ_x, σ_y, and σ_u are the errors associated with s, t, r, x, y, and u, respectively.[15] The data obtained from the measurements is given in Table II.

Table II. Dimensional characteristics of experimental concrete samples.

Sample ID	Diameter ± σ (cm)	Height ± σ (cm)	Mass ± σ (g)	Density ± σ (g cm^{-3})
F1	5.92 ± 0.02	11.21 ± 0.03	709.98 ± 0.10	2.301 ± 0.007
F2	5.92 ± 0.02	11.38 ± 0.03	742.74 ± 0.10	2.371 ± 0.007
G1	5.91 ± 0.02	11.57 ± 0.03	725.05 ± 0.10	2.284 ± 0.007
G2	5.92 ± 0.02	8.85 ± 0.03	539.77 ± 0.10	2.216 ± 0.007
L1	5.92 ± 0.02	12.24 ± 0.03	763.48 ± 0.10	2.267 ± 0.007
L2	5.91 ± 0.02	12.54 ± 0.03	761.17 ± 0.10	2.213 ± 0.007

Gamma spectra measurements were taken in order to determine the radioisotopes present in each of the concrete samples. All measurements were done using a Canberra Industries closed-end coaxial P-type model GC2020 HPGe detector. The nominal FWHM energy resolution of this detector is 1.82 keV at 1,332 keV, and the relative efficiency is 24.4%. The gamma spectra were acquired using the Canberra Industries Genie™ 2000 software program and a Canberra model DSA-1000 MCA with 8,192 channels. The gamma spectrum energy range was set between 0.0 keV and 3,000 keV. The detector was then energy calibrated using 0.41 kBq ^{241}Am, and 37 kBq ^{137}Cs and ^{60}Co check sources. The sources were placed approximately 3.0 cm from the face of the detector and a 300 sec live-time spectrum was acquired. The appropriate channel number for each energy peak was calculated using the following:

$$x = E_\gamma \left(\frac{8{,}192}{3{,}000} \right) \tag{45}$$

where x is the desired channel number, E_γ is the select gamma ray energy from the check source, 8,192 is the number of channels in the MCA, and 3,000 is the energy range of the spectrum in keV. Information for the nuclides used during this energy calibration is shown in Table III.

Table III. Information on the nuclides used for the detector energy calibration.

Nuclide	Energy (keV)	Emission Rate (%)	Channel Number
^{60}Co	1,332.50	99.99	3,638.62
	1,173.24	99.97	3,203.73
^{137}Cs	661.66	85.10	1,806.77
^{241}Am	59.54	35.90	162.58

After energy calibration, the detector endcap was surrounded on the sides, top, bottom and front with approximately 5 cm thick lead bricks. The back of the endcap was not shielded due to the size of the liquid nitrogen dewar and the presence of necessary electrical connections. The distance between the center of the detector endcap and the bottom of the lead vault was measured to be 6.35 ± 0.02 cm. All gamma measurements were taken in a laboratory room containing several μCi-sized radiation standards. Prior to counting any samples, an 86,400 sec live-time background measurement was taken to account for possible background radiation from the room.

Following the background count, a sample was placed in the vault perpendicular to the bottom such that the surface of the concrete was approximately 3.0 cm from the face of the detector. The center of the concrete cylinder and the endcap were vertically aligned. In order to maintain geometric consistency between samples, a marker was placed on the bottom of the lead vault. The experimental geometry and lead vault are shown in Figure 8. The vault was sealed and an 86,400 sec live-time measurement was acquired. Following the measurement, the next concrete cylinder was placed in the vault and the process was repeated. All gamma spectra were saved locally and to disk for later analysis. Acquired gamma spectra for the 86,400 sec measurements are available in Appendix A.

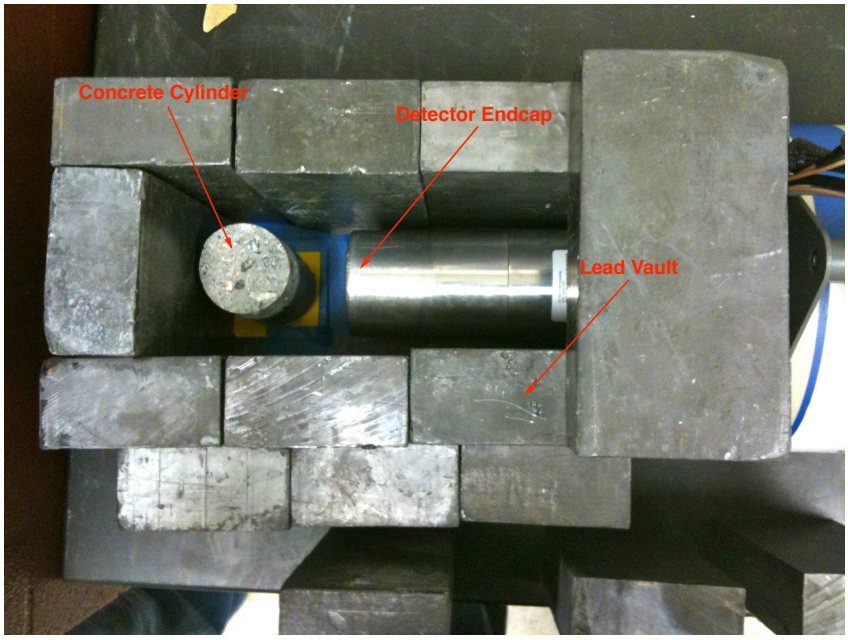

Figure 8. A picture of the lead vault and experimental geometry used for the gamma ray background activity measurements.

III.B. Instrumental neutron activation analysis

After the background gamma spectra were collected from each sample, the concrete was prepared for INAA measurements. Small, gram-sized portions of each sample were broken off with a chisel and ground into a powder using a diamonite mortar and pestle. The powdered samples were distributed into individual glass vials and placed in an oven for 24 hrs to remove moisture. The powders were then moved to a desiccator with an anhydrous calcium sulfate desiccant for an additional hour to ensure they remained dry prior to being weighed. A picture of the concrete powders is shown in Figure 9.

Figure 9. A picture of the powdered concrete samples used for NAA.

The thermal neutron source used for all INAA experiments was a 1 MW TRIGA research reactor located at the Texas A&M University Nuclear Science Center (NSC). All sample preparation and handling prior to and after irradiation was done wearing latex rubber gloves. A target mass of approximately 50 mg of one of the concrete samples

was measured out on a Mettler-Toledo digital balance. The mass was recorded and the powder was placed in a 1.48 ml (0.4 fluid dram) polyethylene vial, and the vial was heat-sealed with a soldering iron. A foam spacer was seated in the bottom of a 7.39 ml (2 fluid dram) polyethylene vial and the 1.48 ml vial was placed top-down on the spacer. The larger vial was closed and set aside for irradiation. Two separate vials were prepared for each concrete sample. A NIST standard reference material (SRM) 1633a fly ash sample was used as a multi-element standard. A National Bureau of Standards (NBS) SRM 688 basalt rock was used as both a quality control material for most elements and the comparator standard for calcium. Each of these samples was prepared in the same manner as the concrete.

The first series of irradiations for this experiment were done using the pneumatic delivery and retrieval system at the NSC. Samples were placed top-down in the delivery tube and sent pneumatically into the core. The neutron flux at the irradiation location was approximately 10^{13} cm^{-2} sec^{-1} for the duration of the experiment. The samples were irradiated for 30 sec, returned through the pneumatic system, and allowed to decay for 1,200 sec. The tops were then removed and the larger vial and foam spacer were discarded. The 1.48 ml vial was placed on a stand approximately 15 cm above the face of an HPGe detector and counted in live-time for 500 sec. The HPGe used for all pneumatic irradiation measurements was an EG&G Ortec closed-end coaxial P-type model GEM-50180-S detector. The nominal FWHM energy resolution of this detector is 1.78 keV at 1,332 keV, and the relative efficiency is 57%. The gamma spectra obtained from the counts were saved for later analysis.

After counting, the 1.48 ml vials were prepared for a longer irradiation in the reactor core. A single vial for each of the six concrete samples was placed vertically in an aluminum can, along with a duplicate vial for samples L1 and G2. Interspersed between the concrete samples were two vials containing the NIST SRM 1633a fly ash standard, one vial containing the NBS SRM 688 basalt rock quality control specimen, and one blank vial used to verify the absence of contaminants. The can was sealed and placed at the bottom of a "rotisserie" tube in the reactor core with a neutron flux of 10^{13} cm^{-2} sec^{-1}. The tube rotated in place during the irradiation to ensure a homogenous neutron flux to all samples in the can. The samples were continuously irradiated in the reactor for a period of 14 hrs.

Once the irradiation was complete, the samples were removed from the reactor and allowed to decay for approximately six days. During this time, they were transported to the Texas A&M University Center for Chemical Characterization and Analysis (CCCA) for the remainder of the gamma measurements. After allowing them to decay, the samples were counted in live-time for 2,000 sec on an HPGe detector. Once the samples were counted, they were set aside and allowed to decay for approximately three additional weeks. After three weeks, the samples were counted in live-time for 10,800 sec. Both sets of counts were done using a Canberra Industries closed-end coaxial P-type model GC4018 HPGe detector. The nominal FWHM energy resolution of this detector is 1.68 keV at 1,332 keV, and the relative efficiency is 41.3%. All gamma spectra were saved for later analysis. Acquired spectra for all INAA measurements can be seen in Appendix B.

III.C. Fast neutron activation analysis

Upon completion of the INAA measurements, the powdered concrete samples were prepared for FNAA. The FNAA experiment consisted of two separate measurements: one for silicon and one for oxygen. A 1.48 ml polyethylene vial was filled with concrete powder and the contents were weighed on a Mettler-Toledo digital balance. The mass was recorded and the powder was returned to the vial. This vial was placed in the bottom of a 7.39 ml polyethylene vial and an empty 2.5 ml vial was placed on top of the sample vial. The outer vial was then heat-sealed using a soldering iron. In contrast with the INAA measurements, only one preparation was done for each concrete sample. An Alfa Aesar® Puratronic® silicon (IV) oxide sample was used as the silicon comparator standard, and a United States Geological Survey (USGS) AGV-1 andesite sample was used as the silicon quality control material. The standard and quality control material were prepared in the same manner as the concrete.

The fast neutron source used for all FNAA experiments was a Kaman Sciences Corporation A-711 sealed-tube neutron generator located at the Texas A&M University Center for Chemical Characterization and Analysis (CCCA). For both the silicon and oxygen measurements, the neutron generator was operating at 140 kV with a mean current of 2.2 mA. The neutron beam intensity of the generator is typically between 10^9 and 10^{10} sec^{-1}; however, it was not specifically measured as part of the FNAA experiments.

The first FNAA experiment focused on measuring the silicon content of the samples. The 7.39 ml vials containing the concrete samples were sent pneumatically to

the neutron beam and irradiated for 300 sec. During irradiation, the number of neutrons detected by a BF_3 gas-filled proportional counter in the generator room was recorded. This information was used to monitor the neutron flux in the generator room and normalize the flux between subsequent irradiations. In each case, the decay time during transport from the generator to the detector was approximately 60 sec. The sample vials were then placed at the detector face and counted in live-time for 300 sec. The source-to-detector geometry for the silicon measurements can be seen in Figure 10.

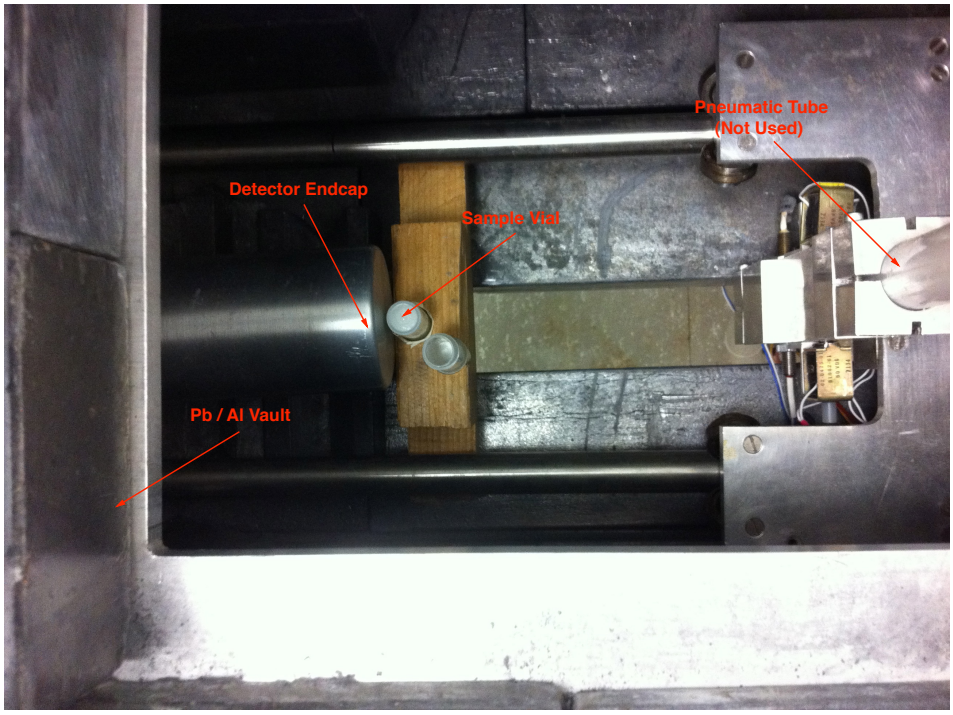

Figure 10. A picture of the source-to-detector geometry used for the silicon FNAA measurements.

Overall decay times for each sample prior to counting varied based on the dead time of the detector; however, in all cases the total decay time was less than 240 sec.

The detector used for the silicon measurements was an EG&G Ortec closed-end coaxial P-type model GEM-22170-S HPGe detector. The nominal FWHM energy resolution of this detector is 1.68 keV at 1,332 keV, and the relative efficiency is 21.2%. After counting, the gamma spectra were saved for later analysis and the sample vials were set aside for the oxygen measurements. All gamma spectra for the silicon measurements can be seen in Appendix C.

Prior to the oxygen measurements, the 7.39 ml vials were placed inside high-density, low oxygen content polyethylene containers. The containers were sealed under nitrogen gas to displace any oxygen in the ambient environment. A NIST SRM 136e potassium dichromate sample was used as the oxygen comparator standard. A Sigma-Aldrich® n-decyl alcohol sample and a NIST SRM 84k potassium hydrogen phthalate (KHP) sample were used as the oxygen quality control materials. The standard, quality control samples, and two blank containers were prepared in the same manner. The blank containers were used to correct the count rates in the samples. Due to the short half-life of ^{16}N ($t_{1/2}$ = 7.13 sec), the entire delivery, irradiation, recovery, and counting sequence for oxygen was automated using a Toshiba model T1-MDR40S programmable logic controller (PLC).

Each of the containers was placed into a loader connected to a pneumatic delivery system. The samples were sent into the neutron beam and irradiated for a period of 20 sec. After irradiation, the samples were sent to a detector system consisting of two 12.7 cm by 12.7 cm Bicron® end-well NaI(Tl) detectors. The detectors were

spaced approximately 10 cm apart with the sample delivery tube located in the middle. The source-to-detector geometry for these measurements is shown in Figure 11.

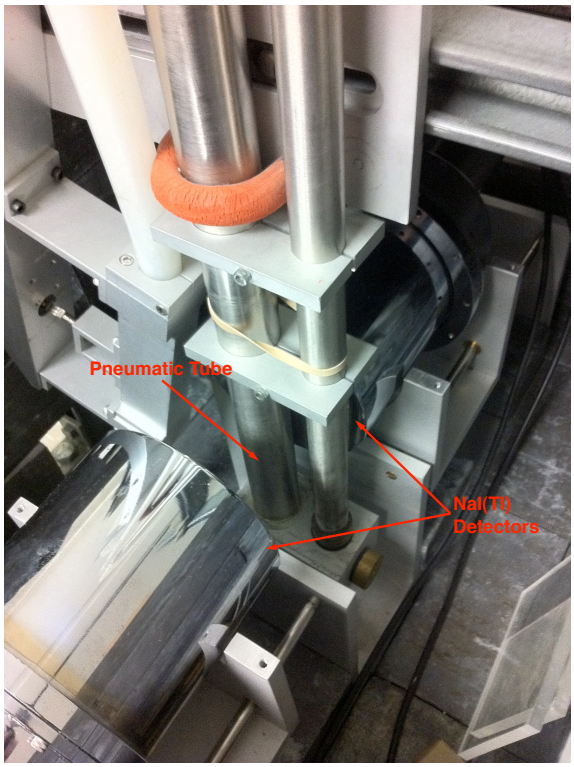

Figure 11. A picture of the source-to-detector geometry used for the oxygen FNAA measurements.

A MCS spectrum was collected throughout the measurement process for later analysis. In a MCS spectrum, the ordinate shows the number of counts whereas the abscissa represents time. The plot is a representation of either the summed counts from the NaI(Tl) detectors or the counts from the BF_3 tube. An example MCS spectrum from a n-decyl alcohol standard is shown in Figure 12. For this research, the MCS spectrum

consisted of 1,024 channels with an 80 msec dwell time on each channel for a total measurement time of approximately 82 sec.

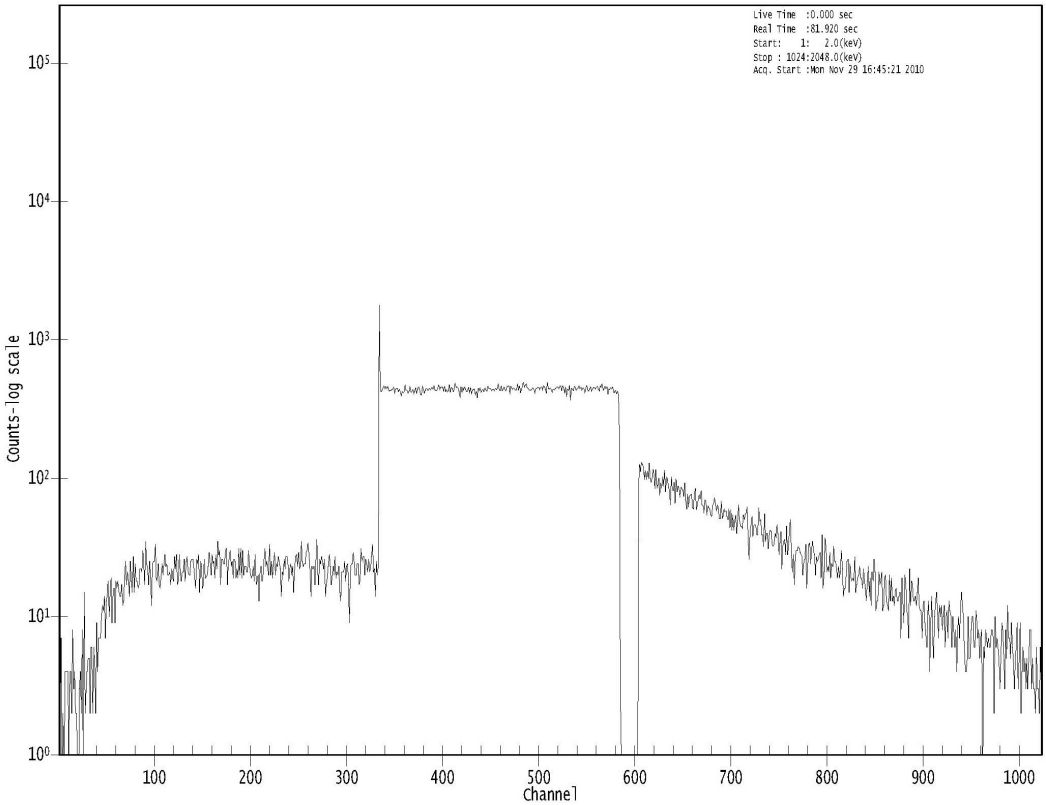

Figure 12. An example MCS spectrum from a n-decyl alcohol comparator standard.

Prior to and during delivery of the sample to the generator, the MCS spectrum consisted of counts from the NaI(Tl) detectors. Once the samples reached the generator, the PLC routed the signal from the BF_3 tube to the MCS analyzer. At this point, the computer was recording count data from the BF_3 tube in the generator room. After the 20 sec irradiation, the PLC routed the combined signals from the two NaI(Tl) detectors to the MCS analyzer. The delay between the end of irradiation and start of the gamma

count was 7.2 sec (90 channels). It should be noted that in order to only record gammas attributed to the $^{16}O(n, p)^{16}N$ reaction, the timing single channel analyzer (TSCA) of each detector was set to discriminate against energies below 4,500 keV. The logic signals from both TSCAs are summed and fed to the MCS analyzer, and the computer subsequently records count data based on the output signal from the MCS analyzer. The count from the NaI(Tl) detectors was collected for 21.2 sec (265 channels). At the completion of count, the sample was sent back to the neutron beam and the process was repeated four additional times for a total of five passes per sample. After the fifth pass, the PLC instructed the delivery system to transfer the sample container into a waste bin and drop the next container in the chute into the delivery system.

III.D. Determination of concrete composition

After acquiring the gamma and MCS spectra from the NAA measurements, the elemental composition of the concrete was determined using an AlphaVAX computer system running the VMS Genie software from Canberra Industries. All computer calculations were based on the relative method. The calculations for the INAA measurements relied on three known pieces of data: 1) the masses of the concrete, comparator standard, and quality control samples, 2) the certified concentration of a specific element in the standard, and 3) the area of the gamma ray energy peak corresponding to a product radionuclide indicative of the target atom of interest. It should be noted that the computer program subtracted the background counts from the total peak area, and this corrected peak area was used for the calculations. The mass of

the target element in the sample and its corresponding uncertainty was determined through the implementation of the relative method in a computer program.

Like the experiment, the FNAA calculations were completed in two parts. The silicon calculations were done using the same method described for the INAA calculations with one exception – the final concentration calculated by the computer program was corrected for variations in the neutron flux using counts from the BF_3 detector. The computer program calculates a constant for the standard that is representative of the number of counts from the ^{28}Al gamma ray due to the $^{28}Si(n, p)^{28}Al$ reaction per gram of silicon in the standard. This standard constant is normalized to the BF_3 counts in order to compensate for variations in the neutron flux between irradiations. In the case of this experiment, the standard constant was corrected for the standard samples using Eq. (46).

$$S_{\text{cor}}^{i} = S_i \frac{B_{\text{avg}}}{B_i} \tag{46}$$

Where S_{cor}^{i} is the corrected standard constant for standard number i, S_i is the standard constant calculated by the computer program for standard number i, B_{avg} is the average of the integrated BF_3 count across all sample, standard, and quality control irradiations, and B_i is the integrated BF_3 count for standard number i.[51] The average uncorrected standard constant and average corrected standard constant were calculated using Eqs. (47) and (48), respectively.

$$\overline{S}_i = \frac{\sum_{i=1}^{I} S_i}{I} \tag{47}$$

$$\overline{S}_{\text{cor}}^{i} = \frac{\sum_{i=1}^{I} S_{\text{cor}}^{i}}{I} \tag{48}$$

Where $\overline{S}_i$ is the average uncorrected standard constant, $\overline{S}_{\text{cor}}^{i}$ is the average corrected standard constant, and I is the number of standards irradiated.[51] The corrected silicon concentration was then calculated as follows:

$$\omega_{\text{cor}}^{x} = \omega_x \frac{\overline{S}_i}{\overline{S}_{\text{cor}}^{i}} \frac{B_{\text{avg}}}{B_x} \tag{49}$$

where ω_{cor}^{x} is the corrected concentration for sample x, ω_x is the uncorrected concentration of sample x, and B_x is the BF_3 count for sample x.[51]

The oxygen content calculations were conducted using the MCS spectra collected from the NaI(Tl) detectors. While the relative method was still used for the calculations, the total counts recorded by the detectors were used instead of specific gamma ray energy peak areas. A custom FORTRAN program was used to integrate a portion of the MCS spectrum during irradiation and the ^{16}N decay in order to determine a beam normalization value and the oxygen signal, respectively. The beam normalization value is the sum of all counts accumulated during irradiation, with each of

the counts decay corrected for the time remaining in the irradiation. The oxygen signal is the sum of the two discriminated NaI(Tl) detectors over the 21.2 sec count period. A constant representative of the ^{16}N counts due to the ^{16}O(n, p)^{16}N reaction per gram of oxygen in the standard during the count period was calculated for each standard run. The average standard constant was also calculated. The computer program then calculated the oxygen concentration in each sample run as follows:

$$\omega_O^x = \frac{N_x - N_{\text{blank}}}{m\bar{S}_i B_{\text{avg}}} \tag{50}$$

where ω_O^x is the oxygen concentration in sample x, N_x is the beam normalized value for the oxygen counts in sample x, N_{blank} is the beam normalized value for the oxygen counts in the blank vial, and m is the total mass of the sample.[51] Notice that a corrected standard constant was not calculated for the oxygen measurements. Since the irradiation time is short in comparison to the silicon measurements, it was assumed that there was not a significant variation in the neutron flux during irradiation.

III.E. Generation of efficiency calibration files using ISOCS™

After calculating the elemental composition, efficiency calibration files were generated for each concrete sample using the Canberra Industries ISOCS™ version 4.2.1 software package in conjunction with the detector characterization supplied by Canberra

for the model GC2020 HPGe detector. The simple cylinder template used to model the samples from this research is shown in Figure 13.

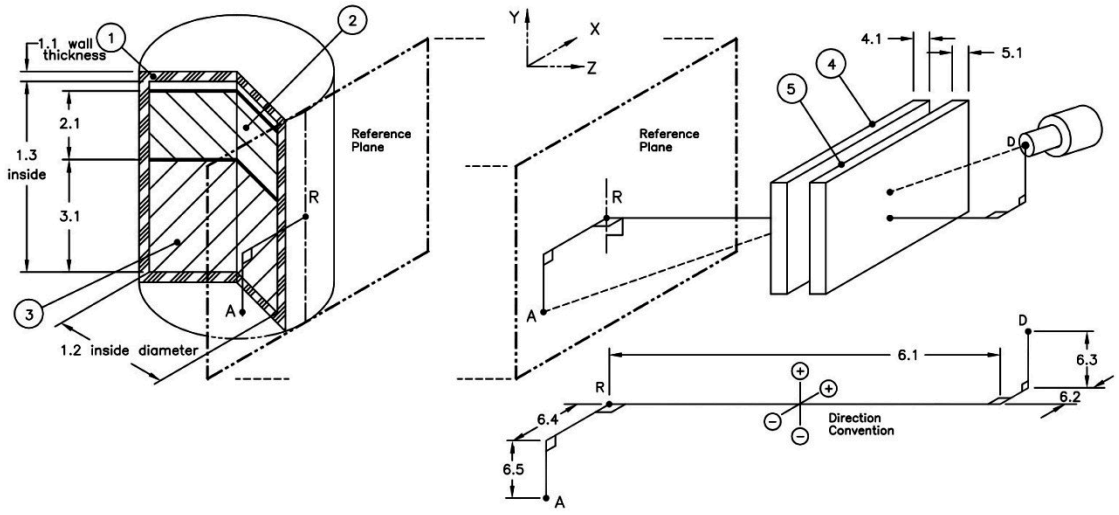

Figure 13. The ISOCS™ simple cylinder template used for generation of the efficiency calibration files.[52]

In this drawing, R refers to the source reference point – the center of the line where the source contacts the reference place, D is the detector reference point – the center point of the detector endcap, and A is the detector aiming point – which may be anywhere on the reference plane. Object 1 is the concrete cylinder itself. Dimension 1.1 – the thickness of the container – is a required input parameter since the template was designed for modeling radioactive material within a cylindrical container. This dimension was set to 10^{-5} cm for all samples so as not to significantly affect their attenuation characteristics. The diameter and height of each sample were input as dimensions 1.2 and 1.3, respectively. Object 2 is the radioactive source inside the

container. For this research, the entire sample was treated as the source, and the heights of the samples were input as dimension 2.1. Objects 3 and 4 are absorber plates between the detector and the source. Since no absorbers were used in the experimental geometry, these dimensions were left blank.

Object 6 defines the location of the source relative to point D. Dimension 6.1 is the distance between points D and R. This was set to 3.02 cm for all samples since the experimental geometry did not change between measurements. Dimensions 6.2 and 6.3 define the translation of the detector in the x- and y-directions, respectively. Dimensions 6.4 and 6.5 define the aiming point of the detector in the x- and y-directions, respectively. These dimensions are essential to accurately modeling the samples since the aiming point of the detector was never in line with the center point of the cylinders. By default, ISOCS™ aims the detector at the center of the sample. Since the x-position of the samples relative to the detector remained the same, dimensions 6.2 and 6.4 were left blank. In order to keep the source perpendicular to the face of the detector, dimensions 6.3 and 6.5 must be equal.[52] The y-direction translation for dimensions 6.3 and 6.5 was determined by:

$$d = d_{\text{vault}} - \frac{h_{\text{sample}}}{2} \tag{51}$$

where d is the y-direction translation for dimensions 6.3 and 6.5, h_{sample} is the height of the sample, and d_{vault} is the distance from the center of the detector endcap to the bottom of the lead vault (6.35 cm).

After adding the dimensions of the samples, the calculated densities were input for Objects 1 and 2. A new material was defined for each sample corresponding to the results from the NAA measurements. These material definitions were also used for Objects 1 and 2. All other material definitions and densities were left blank. The relative material concentration for object 2 was set to 1.0. The relative concentration for Object 3 was left blank. The input parameters for each sample are given in Appendix D.

Once the input parameters were defined, the file was saved and a geometry validation was run to ensure the cylinders were properly defined. A file containing a set of efficiency data points for the detector was the generated using the "Generate efficiency data points" command. The resultant files were used to determine the background activity of the concrete samples.

III.F. Determination of concrete background activity

After the efficiency calibration files were generated, it was possible to calculate the background activity for each of the concrete samples using the Genie™ 2000 software. The background spectra were analyzed prior to the spectra from the concrete cylinders. After opening a select background spectrum, a peak locate was conducted using the "Unidentified Second Differential" method. The peak significance threshold and energy tolerance were set to 7.00 and 1.00 keV, respectively. Once the peaks were

located, their areas were calculated using the "Sum/Non-Linear Least Squares Fit Peak Area" algorithm. For each set of spectra, the step continuum function was chosen with two channels on each side, the "Use fixed tail parameter" option was selected, and the "95% critical level test" was applied.

Once the peak areas were determined, the background data file was saved and the file for the first quadrant of the sample corresponding to the background was opened. Prior to analysis, the ISOCS™ efficiency calibration file for the sample was applied to the spectrum. The peak search and area determination for the sample spectrum were conducted in the same manner as the background spectrum. Once these were determined, the "Standard Background Subtract" algorithm was used to subtract the background peak areas from matching peak areas in the sample spectrum. The background file corresponding to the sample in question was chosen for the subtraction. The energy tolerance was set to 1.00 keV and the "95% critical level test" was applied. The dual curve "Efficiency Correction" algorithm was used to calculate the efficiency and associated uncertainty for each of the located peaks. After the efficiency correction was applied, the "NID with Interference Correction" algorithm was used to identify nuclides present in the sample and calculate their weighted mean activity. The energy tolerance and NID confidence threshold were set to 1.00 keV and 0.30, respectively. Once the analyses were completed, the spectrum data file was saved and the same procedure was repeated for the spectra from the remaining cylinders. It should also be noted that ^{40}K and ^{234}Th were the only isotopes identified independent of a radioactive decay chain. After analyzing the spectra it was determined that the remaining identified

nuclides were from either the thorium or radium decay series. Since the ^{232}Th and ^{226}Ra parent isotopes are much longer-lived than their daughter products, it was assumed that the entire chain was in secular equilibrium and that each daughter isotope possessed the same activity as the parent. For these cases, the calculations necessary to complete the radioactive source term were completed using the activity determined for parent.

III.G. Generation of radioactive source term for MCNP simulations

Once the background activity was determined, a source term calculation was completed for each sample for use in the MCNP simulations. All calculations were done using Microsoft® Excel® 2011. After creating a new file, the dimensions for one of the original concrete slabs from ORNL were entered, along with the density of the concrete sample in question. The volume and mass of the slab were calculated. The specific activity of all isotopes identified by the Genie™ 2000 software were listed, and the total activity of each nuclide in the slab and the total activity of the slab were determined using Eqs. (52) and (53), respectively.

$$A_{\text{tot},i} = mSA_i \tag{52}$$

$$A_{\text{tot}} = \sum_{i}^{I} A_{\text{tot},i} \tag{53}$$

Where $A_{\text{tot},i}$ is the total activity of nuclide *i* in the slab, m is the mass of the concrete slab, SA_i is the specific activity of nuclide *i* in the slab, and A_{tot} is the combined activity of all nuclides in the slab.

After determining the activity of each nuclide in the slab, the gamma emission rate was calculated. The gamma energies identified by the Genie™ 2000 software were listed along with their corresponding nuclide and respective yields. The emission rate for each gamma energy line, the total gamma emission rate, and fractional emission rates were calculated using Eqs. (54), (55), and (56), respectively.

$$\varepsilon_{\text{E},i} = y_{\text{E}} A_{\text{tot},i} \tag{54}$$

$$\varepsilon_{\text{tot}} = \sum_{i=1}^{I} \varepsilon_{\text{E},i} \tag{55}$$

$$f_{\text{E},i} = \frac{\varepsilon_{\text{E},i}}{\varepsilon_{\text{tot}}} \tag{56}$$

Where $\varepsilon_{\text{E},i}$ is the gamma emission rate at energy E for nuclide *i*, y_E is the radiative yield of the gamma ray at energy E, ε_{tot} is the total gamma emission rate of all nuclides in the slab, and $f_{\text{E},i}$ is the fractional emission rate of a specific gamma ray at energy E for nuclide *i* with the respect to the total emission rate.

III.H. MCNP simulations

After completing all experimental measurements, an MCNP simulation was conducted for each concrete sample. MCNP simulations were done in order to determine the contribution of the concrete slab to gamma ray background counts registered in the RPM detectors. The RPM geometry was based on a TSA Systems Ltd. model VM-250AG gamma vehicle portal monitor.[53] The concrete slab, RPM pillars, PVT scintillators, polymethyl methacrylate (PMMA) light pipes, and lead shielding were modeled as right parallelepiped macrobodies.

An individual deck was created for each of the six samples using the same portal geometry and material definitions, with the exception of the concrete. The MCNP decks for each sample are available in Appendix E. For each deck, the NAA results were used to define the material composition of the concrete in the slab. The appropriate density of for each concrete sample was entered into the corresponding cell card. The calculated source terms form the gamma background measurements were used to create a distributed radiological source throughout the volume of the slab. The energy distribution throughout the slab was created using the discrete energy lines from the concrete samples along with their corresponding fractional emission rates. The number of counts was measured through the use of F8 pulse height tallies over the volume of each PVT scintillator. Energy bins were used with each tally to monitor the count rate across the entire energy range and the 40 – 140 keV region. The tallies and energy bins remained consistent between decks. A total of 10^8 particles were started for each

simulation. After running each deck, the count rate registered by the RPM was determined by:

$$R_{\mathrm{RPM}} = \sum_{i=1}^{I} P_i A_{\mathrm{tot}} \tag{57}$$

where R_{RPM} is the total count rate for all PVT scintillators in the RPM, P_i is the pulse count for detector *i* obtained from the MCNP results, *I* is the total number of detectors in the RPM, and A_{tot} is the total activity of the concrete slab. The statistical variation corresponding to each value of P_i was calculated by:

$$\sigma_{P_i} = \eta P_i \tag{58}$$

where σ_{P_i} is the standard deviation of P_i and η is the relative error with respect to the mean from the MCNP output file.[50] The RPM count rate and standard deviation were calculated for the entire energy range and the 40 – 140 keV region. It should be noted that Eq. (59) is only a representation of the statistical error associated with MCNP. Since the code does not allow the user to define an uncertainty for any input value, a true estimate for the error associated with the model was not determined.

After determining the count rate in the RPM for each concrete sample, the accuracy of the model was investigated by comparing the MCNP results to count rates from slab G measured by the RPM at ORNL. The validity of the model was further

tested by recording the count rate of the RPM in the presence of 185, 370, 555, and 740 kBq ^{137}Cs check sources and comparing the results to the MCNP model. In MCNP, the ^{137}Cs check sources were modeled as point sources equidistant from each pillar and 10^8 particles were started for each source. An additional measurement was conducted moving the source approximately 130 cm away from the face of one of the pillars. This measurement was also simulated in MCNP.

After validating the model, two sensitivity analyses were conducted using the input decks created for the background measurement data. The first analysis was done to determine the sensitivity of the model to fluctuations in the concrete density. The deck for each sample was rerun twice with the concrete density set to $\pm 2\sigma$ from the measured value. The second sensitivity analysis was done to determine impact of the hydrogen and carbon content of the concrete on the count rate in the RPM. Each deck was rerun twice with the carbon content set 50% and 10% of its estimated value. For each run, the hydrogen content was increased in order to bring the total weight fraction back to unity and prevent MCNP from normalizing the concentrations of the other materials.

CHAPTER IV

RESULTS AND DISCUSSION

IV.A. Elemental composition of concrete samples

The masses of the concrete samples used during the NAA experiments are given in Table IV. In the case of the INAA measurements, sample masses for both preparations are provided. These masses were incorporated into the relative method used by the computer program to determine the elemental composition of each concrete cylinder.

Table IV. Concrete sample masses for NAA measurements.[a]

Sample	FNAA Mass (g)	INAA Mass (mg)
F1	2.570	50.85 50.32
F2	2.545	50.20 50.12
G1	2.377	50.09 50.01
G2	2.370	50.51 50.06
L1	2.716	50.21 50.58
L2	2.571	50.23 50.13

[a]Standard deviation for all masses is ± 1 μg.

The oxygen and silicon concentrations of the concrete samples determined by the FNAA experiment are shown in Table V. The oxygen and silicon concentrations of the

AGV-1, n-Decyl alcohol, and KHP quality control samples are given in Table VI along with their certified literature values.

Table V. Oxygen and silicon FNAA results for concrete samples.

Sample	Oxygen ± σ (w%)[a]	Silicon ± σ (w%)
F1	48.45 ± 1.57	1.51 ± 0.01
F2	48.72 ± 0.82	1.86 ± 0.02
G1	47.27 ± 0.56	26.62 ± 0.11
G2	47.31 ± 0.98	29.52 ± 0.14
L1	47.69 ± 2.10	4.75 ± 0.03
L2	48.21 ± 0.55	5.33 ± 0.03

[a]Averaged values for five irradiation and counting cycles.

Table VI. Oxygen and silicon FNAA results for quality control samples.

Sample	Oxygen ± σ (w%)	Silicon ± σ (w%)	Literature Value[54] (w%)
AGV-1	N/A	28.35 ± 0.11	27.67 ± 0.27
n-Decyl alcohol	10.69 ± 0.34[a]	N/A	10.11[b]
KHP	30.77 ± 3.04[a]	N/A	31.34[b]

[a]Averaged value for two sample preparations.
[b]Literature value based on stoichiometric ratio.

The oxygen and silicon concentrations of the concrete samples closely agree for samples from the same slab. In addition, the oxygen and silicon concentrations of the quality control specimens are within ±2σ of their accepted literature values; therefore, the results of the FNAA measurements are both accurate and precise.

The INAA experiment consisted of three measurements to account for isotopes of varying half-lives. The elemental concentrations obtained from the short-, intermediate-, and long-lived isotope measurements for samples F1 and F2 are given in Table VII. The results for samples G1 and G2 are given in Table VIII, and the results for samples F1 and F2 are given in Table IX. The elemental concentrations of the basalt quality control specimen are given in Table X along with the accepted literature values.

Table VII. Results of INAA measurements for concrete samples F1 and F2.

Element	Concentration ± σ	
	Sample F1	Sample F2
Short-Lived Isotopes[a]		
Al	4,440 ± 426 ppm	6,236 ± 498 ppm
Ca	31.01 ± 0.72 %	31.88 ± 0.74 %
Dy	BDL[b]	7.91 ± 4.85 ppm
Mg	1.19 ± 0.05 %	1.06 ± 0.05 %
Mn	304 ± 28 ppm	355 ± 9 ppm
Ti	606 ± 278 ppm	BDL[b]
V	14.59 ± 2.69 ppm	19.57 ± 3.41 ppm
Intermediate-Lived Isotopes[c]		
As	1.20 ± 0.15 ppm	1.56 ± 0.12 ppm
K	1,087 ± 325 ppm	1,683 ± 231 ppm
La	3.35 ± 0.08 ppm	4.25 ± 0.06 ppm
Lu	381 ± 90 ppb	658 ± 94 ppb
Na	260 ± 6 ppm	324 ± 5 ppm
Sm	6.14 ± 0.11 ppm	7.39 ± 0.08 ppm
U	1.16 ± 0.11 ppm	1.15 ± 0.07 ppm
Yb	2.79 ± 0.57 ppm	4.35 ± 0.56 ppm
Long-Lived Isotopes[c]		
Ba	35.10 ± 8.66 ppm	56.08 ± 8.33 ppm
Ce	6.47 ± 0.18 ppm	7.74 ± 0.14 ppm
Co	4.04 ± 0.16 ppm	1.05 ± 0.02 ppm
Cr	20.12 ± 0.34 ppm	26.09 ± 0.28 ppm
Cs	2.43 ± 0.34 ppm	2.85 ± 0.24 ppm
Eu	1.21 ± 0.08 ppm	1.41 ± 0.06 ppm
Fe	4,366 ± 36 ppm	5,406 ± 29 ppm
Hf	3.83 ± 0.25 ppm	5.06 ± 0.20 ppm
Nd	3.13 ± 0.50 ppm	4.75 ± 0.45 ppm
Rb	5.07 ± 0.80 ppm	6.22 ± 0.68 ppm
Sb	7.65 ± 0.50 ppm	1.04 ± 0.04 ppm
Sc	6.68 ± 0.05 ppm	8.88 ± 0.04 ppm
Sr	261 ± 20 ppm	326 ± 17 ppm
Ta	962 ± 148 ppb	1,059 ± 109 ppb
Tb	782 ± 177 ppb	1,108 ± 173 ppb
Th	710 ± 221 ppb	941 ± 181 ppb
Zn	64.16 ± 1.40 ppm	84.79 ± 1.19 ppm

[a]Averaged values for two sample preparations.
[b]Below detectable limits (BDL).
[c]F1 results are averaged values of two sample preparations.

Table VIII. Results of INAA measurements for concrete samples G1 and G2.

Element	Concentration ± σ	
	Sample G1	Sample G2
Short-Lived Isotopes[a]		
Al	6.18 ± 0.11 %	6.60 ± 0.06 %
Ca	10.06 ± 0.34 %	8.98 ± 0.26 %
Dy	3.74 ± 0.93 ppm	10.58 ± 1.11 ppm
Mg	3,781 ± 390 ppm	3,594 ± 408 ppm
Mn	785 ± 16 ppm	1,153 ± 21 ppm
Ti	2,514 ± 685 ppm	3,285 ± 815 ppm
V	75.15 ± 6.01 ppm	60.73 ± 5.77 ppm
Intermediate-Lived Isotopes[b]		
As	1.93 ± 0.36 ppm	1.61 ± 0.49 ppm
K	2.66 ± 0.17 %	3.27 ± 0.27 %
La	21.83 ± 0.21 ppm	27.43 ± 0.32 ppm
Lu	3.71 ± 0.33 ppm	2.46 ± 0.30 ppm
Na	1.87 ± 0.01 %	2.00 ± 0.02 %
Sm	3.46 ± 0.02 ppm	5.21 ± 0.35 ppm
U	2.75 ± 0.20 ppm	4.63 ± 0.32 ppm
Yb	3.06 ± 0.18 ppm	8.17 ± 0.38 ppm
Long-Lived Isotopes[b]		
Ba	442 ± 22 ppm	520 ± 32 ppm
Ce	37.42 ± 0.32 ppm	57.32 ± 0.52 ppm
Co	6.70 ± 0.05 ppm	5.77 ± 0.07 ppm
Cr	44.98 ± 0.56 ppm	37.10 ± 0.14 ppm
Cs	3.09 ± 0.08 ppm	3.46 ± 0.11 ppm
Eu	5.98 ± 0.14 ppm	3.70 ± 0.14 ppm
Fe	2.13 ± 0.01 %	1.91 ± 0.01 %
Hf	2.50 ± 0.06 ppm	3.20 ± 0.09 ppm
Nd	16.38 ± 0.97 ppm	39.06 ± 2.36 ppm
Rb	134 ± 3 ppm	164 ± 5 ppm
Sb	1.02 ± 0.07 ppm	9.52 ± 0.93 ppm
Sc	7.68 ± 0.01 ppm	7.27 ± 0.01 ppm
Sr	290 ± 25 ppm	253 ± 35 ppm
Ta	2.03 ± 0.05 ppm	8.71 ± 0.33 ppm
Tb	5.31 ± 0.41 ppm	3.36 ± 0.37 ppm
Th	10.02 ± 0.05 ppm	14.26 ± 0.09 ppm
Zn	104 ± 2 ppm	108 ± 3 ppm

[a]Averaged values for two sample preparations.

[b]G2 results are averaged values of two sample preparations.

Table IX. Results of INAA measurements for concrete samples L1 and L2.

Element	Concentration ± σ	
	Sample L1	Sample L2
Short-Lived Isotopes[a]		
Al	1.53 ± 0.06 %	1.74 ± 0.06 %
Ca	28.48 ± 0.68 %	29.46 ± 0.70 %
Dy	1.15 ± 0.69 ppm	1.06 ± 0.73 ppm
Mg	1.09 ± 0.05 %	0.89 ± 0.05 %
Mn	482 ± 10 ppm	501 ± 11 ppm
Ti	643 ± 500 ppm	909 ± 507 ppm
V	32.29 ± 3.80 ppm	35.31 ± 3.70
Intermediate-Lived Isotopes		
As	2.54 ± 0.16 ppm	2.74 ± 0.17 ppm
K	6,900 ± 513 ppm	7,705 ± 518 ppm
La	6.56 ± 0.08 ppm	8.19 ± 0.10 ppm
Lu	731 ± 129 ppb	956 ± 139 ppb
Na	732 ± 8 ppm	1,022 ± 10 ppm
Sm	1.15 ± 0.01 ppm	1.34 ± 0.01 ppm
U	1.54 ± 0.08 ppm	1.35 ± 0.09 ppm
Yb	5.46 ± 0.59 ppm	7.43 ± 0.83 ppm
Long-Lived Isotopes		
Ba	56.30 ± 9.82 ppm	90.09 ± 10.54 ppm
Ce	13.29 ± 0.18 ppm	15.05 ± 0.20 ppm
Co	2.47 ± 0.03 ppm	2.87 ± 0.03 ppm
Cr	34.38 ± 0.36 ppm	38.85 ± 0.39 ppm
Cs	7.53 ± 0.42 ppm	9.23 ± 0.31 ppm
Eu	2.33 ± 0.09 ppm	2.87 ± 0.10 ppm
Fe	0.909 ± 0.003 %	1.057 ± 0.004 %
Hf	9.23 ± 0.29 ppm	9.83 ± 0.31 ppm
Nd	6.13 ± 0.50 ppm	6.76 ± 0.61 ppm
Rb	19.05 ± 1.10 ppm	21.76 ± 1.30 ppm
Sb	1.06 ± 0.05 ppm	1.40 ± 0.05 ppm
Sc	2.19 ± 0.01 ppm	2.42 ± 0.01 ppm
Sr	317 ± 19 ppm	455 ± 24 ppm
Ta	1.63 ± 0.15 ppm	2.17 ± 0.14 ppm
Tb	1.38 ± 0.19 ppm	1.92 ± 0.14 ppm
Th	1.89 ± 0.02 ppm	2.25 ± 0.03 ppm
Zn	80.56 ± 1.26 ppm	110 ± 2 ppm

[a]Averaged values for two sample preparations.

Table X. Results of INAA measurements for SRM 688 quality control sample.

Element	Concentration ± σ	
	Experimental	Literature[54]
Short-Lived Isotopes[a]		
Al	9.17 ± 0.12 %	9.18 ± 0.05 %
Ca[b]	N/A	8.79 ± 0.36 %
Dy	3.75 ± 0.39 ppm	3.40 ± 0.20 ppm
Mg	1.18 ± 0.06 %	N/A[c]
Mn	1,281 ± 48 ppm	1,210 ± 60 ppm
Ti	7,721 ± 303 ppm	7,090 ± 190 ppm
V	258 ± 10 ppm	242 ± 8 ppm
Intermediate-Lived Isotopes		
As	2.38 ± 0.42 ppm	2.40 ± 0.30 ppm
K	BDL[d]	1,550 ± 60 ppm
La	5.32 ± 0.13 ppm	5.17 ± 0.05 ppm
Lu	BDL[d]	304 ± 6 ppb
Na	1.53 ± 0.01 %	1.59 ± 0.03 %
Sm	2.33 ± 0.02 ppm	2.40 ± 0.03 ppm
U	BDL[d]	320 ± 180 ppb
Yb	2.28 ± 0.17 ppm	2.03 ± 0.03 ppm
Long-Lived Isotopes		
Ba	BDL[d]	154 ± 49 ppm
Ce	11.01 ± 0.41 ppm	11.95 ± 0.15 ppm
Co	49.00 ± 0.16 ppm	48.50 ± 0.40 ppm
Cr	322 ± 2 ppm	329 ± 3 ppm
Cs	BDL[d]	< 100 ppb
Eu	1.02 ± 0.03 ppm	0.98 ± 0.02 ppm
Fe	7.10 ± 0.01 %	7.21 ± 0.08 %
Hf	1.65 ± 0.08 ppm	1.55 ± 0.03 ppm
Nd	5.58 ± 1.32 ppm	8.40 ± 1.00 ppm
Rb	BDL[d]	3.80 ± 1.20 ppm
Sb	BDL[d]	97 ± 16 ppb
Sc	36.68 ± 0.03 ppm	37.00 ± 0.30 ppm
Sr	27.20 ± 41.13 ppm	172 ± 17 ppm
Ta	167 ± 36 ppb	269 ± 11 ppb
Tb	985 ± 94 ppb	499 ± 11 ppb
Th	BDL[d]	282 ± 19 ppb
Zn	99.39 ± 3.83 ppm	84.00 ± 10.00 ppm

[a]Averaged values for three sample preparations.
[b]SRM 688 was used as comparator standard for calcium.
[c]Quality control sample does not have a literature concentration for this element.
[d]Below detectable limits (BDL).

The elemental concentrations of the short- and intermediated-lived isotopes in the basalt quality control samples closely correspond to the literature values. The concentrations for most of the long-lived isotopes are also consistent with their literature values; however, some elemental concentrations (e.g., Sr, Ta, Tb, and Zn) vary greatly. Many of these elements are only present in trace amounts, and their literature values are generally not well known. Major constituent elements of the quality control material (e.g., Al, Mg, Ti, Na, and Fe) are within $\pm 2\sigma$ of their literature values; therefore the INAA results are considered accurate and precise.

Generally, samples from the same concrete slabs have similar concentrations; however, in some instances there is a significant difference. This is possibly due to the inherent non-homogeneity of the original slab. Certain aggregate materials may not be evenly dispersed in the concrete, thereby creating regions in the slab where one or more elements are more or less concentrated than in the surrounding area. Thoroughly mixing the concrete prior to pouring may reduce this problem, but it is unlikely to eliminate it entirely. In addition, the concentrations determined for the short-lived isotopes were averaged values from two sample preparations. For the intermediate- and long-lived isotope concentrations, only measurements for samples F1 and G2 were duplicated. The error propagation corresponding to the averaged value may have caused a discrepancy in concentrations for some elements. The total weight percentage determined by both NAA methods is given in Table XI.

Table XI. Total weight percentage determined by INAA and FNAA.

Sample ID	Total Determined ± σ (w%)
F1	83.28 ± 1.73
F2	84.97 ± 1.11
G1	97.63 ± 0.70
G2	100.54 ± 1.09
L1	85.39 ± 2.21
L2	87.79 ± 0.90

Two major constituent elements of concrete not characterized through either NAA technique used in this research are carbon and hydrogen. While both of these elements may be determined using PGNAA,[55-58] cost limitations and time constraints prevented this method from being employed as part of the elemental characterization. Several assumptions were made in order to determine the amount of carbon and hydrogen present in the samples. For samples from slabs F and L, the NAA results show large amounts (> 0.10 w%) of O, Ca, Si, Mg, Al, and K. The samples from slab G contained large amounts of O, Si, Ca, Al, K, Fe, Na, and Mg. The approximate elemental compositions for different varieties of concrete and a granite rock are given in Table XII. A comparison of the values from the table and the concentrations determined through NAA led to the assumption that the primary aggregate materials for slabs F, G, and L are: limestone, granite, and limestone-silicate, respectively. In addition, slab G has a similar elemental composition to the type 04 concrete.

Table XII. Approximate elemental composition of four concrete materials.[59]

Element	Limestone (w%)	Granite (w%)	Type 04 (w%)	Limestone-Silicate (w%)
H	0.51	0.13	0.56	0.63
C	10.03	0.03		17.73
O	48.53	47.12	49.88	40.34
Na		2.88	1.72	0.03
Mg	0.17	2.13	0.26	3.30
Al	0.51	8.20	4.58	1.11
Si	1.20	28.03	31.54	3.48
K		2.64	1.92	0.11
Ca	38.26	3.68	8.29	32.50
Fe	0.81	5.17	1.23	0.77

The next assumption – based on the precision of the NAA measurements and the elemental compositions of the aggregate materials from Table XIII – was that the unaccounted for weight percentage in the samples was comprised of carbon and hydrogen. Since the hydrogen content of the concrete varieties listed in Table XIII did not vary by a large amount, 0.50 w% of hydrogen was added to each sample. The difference between this assumed total and 100 w% was filled with carbon. No modifications were made to sample G2 since it had been fully characterized with NAA. A sensitivity analysis was run after validation of the MCNP model to evaluate the impact of this assumption on the overall results.

IV.B. Calculated background activity

The specific activities of isotopes identified by the Genie™ 2000 software are given in Tables XIII – XV. It should be noted that ^{234}Th and ^{226}Ra are both members of the same decay chain, which stems from a natural ^{238}U parent. They are separated in

Tables XIII – XV for two reasons: 1) To help understand the approximately 2σ difference between ^{232}Th specific activities in samples from slab G, and 2) To validate the assumption that the identified isotopes – with the exception of ^{40}K – are in secular equilibrium with a parent nuclide. In each case, the specific activity of ^{234}Th is within at least ±2σ of the value calculated for ^{226}Ra. This distinction has been primarily made for the convenience of the reader and does not impact the results.

Table XIII. Specific activities of background isotopes in slab F.

Isotope	Specific Activity ± σ (Bq kg^{-1})	
	Sample F1	Sample F2
^{40}K	42.27 ± 4.69	36.58 ± 4.63
^{226}Ra[a]	10.67 ± 0.50	10.55 ± 0.52
^{232}Th[a]	4.97 ± 0.37	4.65 ± 0.38
^{234}Th	12.74 ± 2.28	13.34 ± 2.33

[a]The isotope is assumed to be in secular equilibrium with its daughter nuclides.

Table XIV. Specific activities of background isotopes in slab G.

Isotope	Specific Activity ± σ (Bq kg^{-1})	
	Sample G1	Sample G2
^{40}K	696 ± 30	735 ± 32
^{226}Ra[a]	64.34 ± 1.84	67.70 ± 2.05
^{232}Th[a]	80.21 ± 1.56	74.56 ± 1.56
^{234}Th	48.21 ± 5.15	85.56 ± 9.17

[a]The isotope is assumed to be in secular equilibrium with its daughter nuclides.

Table XV. Specific activities of background isotopes in slab L.

Isotope	Specific Activity ± σ (Bq kg^{-1})	
	Sample L1	Sample L2
^{40}K	170 ± 9	151 ± 8
^{226}Ra[a]	13.08 ± 0.61	12.70 ± 0.62
^{232}Th[a]	9.58 ± 0.53	7.87 ± 0.46
^{234}Th	15.47 ± 2.50	18.43 ± 2.68

[a]The isotope is assumed to be in secular equilibrium with its daughter nuclides.

The data indicates that samples from the same slab have approximately the same specific activities. Generally, between samples from the same slab, the specific activities of the identified isotopes are within ±2σ of each other. One exception to this is the ^{234}Th activity in samples from slab G. The calculated ^{234}Th activity in sample G2 is approximately 44% larger than the activity calculated for sample G1. Typically, this result would be unexpected, but the results from the INAA experiment explain this variation. As can be seen in Table IX, the uranium and thorium concentrations of sample G2 are approximately 41% and 30% greater, respectively, than that of sample G1. Also, the specific activity of the ^{232}Th parent nuclide is approximately 7% larger in sample G1, indicating that although sample G2 has a greater overall concentration of thorium, sample G1 contains more of the naturally occurring ^{232}Th isotope. Since sample G1 contains a greater amount of ^{232}Th, and natural uranium is composed primarily of the ^{234}Th parent nuclide, ^{238}U, the greater specific activity of ^{234}Th in sample G2 is a result of the larger overall uranium content of the sample.

IV.C. Contribution of concrete to gamma ray background

Count rates and their associated uncertainties were calculated based on tally data from the MCNP simulations. The average count rate per detector for each sample based on both sets of background measurement data is given in Table XVI.

Table XVI. Gamma ray count rate in the RPM due to concrete.

Sample ID	Average Count Rate ± σ (counts sec^{-1} $detector^{-1}$)[a]	
	0.0 – 3.0 MeV	40 – 140 keV
F1	84.29 ± 0.60	11.17 ± 0.22
F2	80.08 ± 0.58	10.71 ± 0.21
G1	950 ± 6	120 ± 2
G2	951 ± 6	120 ± 2
L1	164 ± 1	19.92 ± 0.39
L2	146 ± 1	17.83 ± 0.35

[a]Error represents statistical uncertainty from MCNP only.

The count rates determined by MCNP are consistent with the results from the specific activity measurements. Slab G had the highest total activity, followed by slabs L and F. It is expected that the larger activity would lead to a higher count rate in the RPM. It is worth noting that sample L1 has a count rate approximately 10% higher than that of sample L2. The results given in Table XV show that sample L1 has a total activity approximately 9% higher than that of sample L2. The higher total activity for sample L1 indicates that more gammas will be emitted from the slab and subsequently detected by the RPM.

A chart with a comparison of the count rate data from the RPM and the simulated count rate from MCNP for slab G is given in Figure 14. The count rates for each

detector were obtained by taking a 24 hr average from a RPM data printout. The error bars for all count rates are given at ±1σ. In addition, the error associated with the MCNP data is attributed only to the statistical error from MCNP.

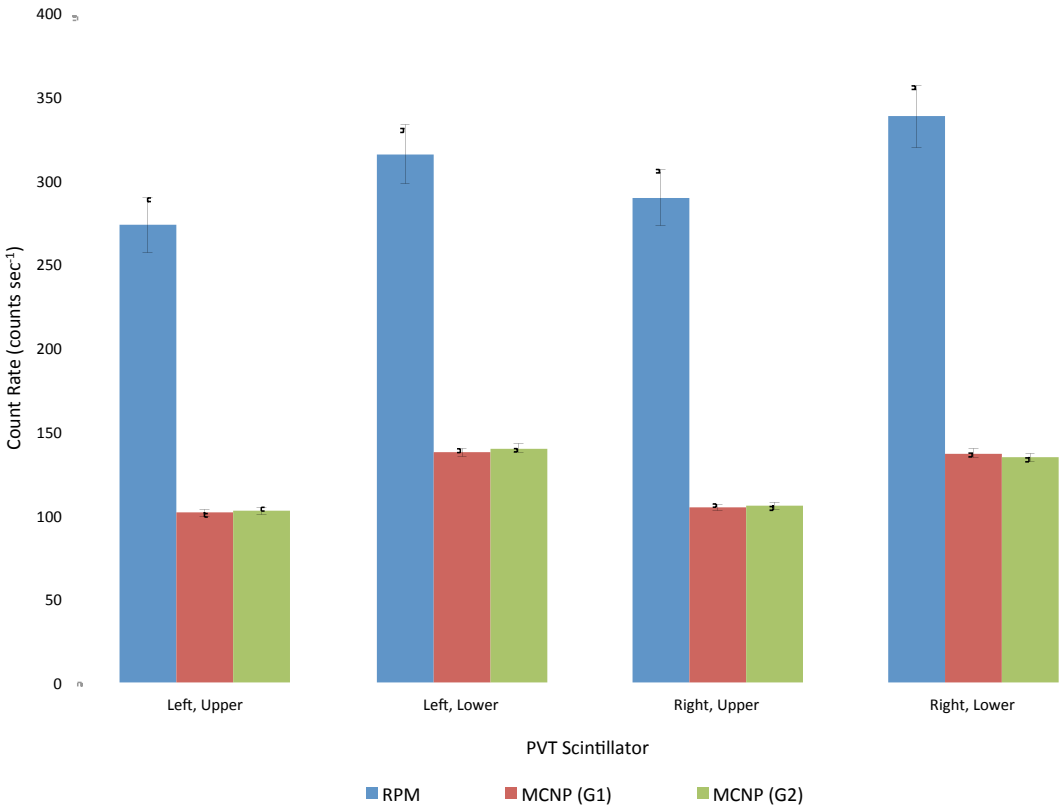

Figure 14. A comparison of actual and simulated RPM count rates from slab G.

The count rates in the upper detectors are less than those in the lower detectors. This is expected because the lower detectors are closer to the concrete slab, and therefore closer to the source of the gamma rays. The data also shows that the MCNP results are consistent between samples G1 and G2. This is important to note because the larger amount of uranium and thorium in sample G2 did not impact the overall count rate. Since the highest yield gamma rays from the decay of ^{234}Th are 63 and 93 keV, it is possible that they do not reach any of the PVT scintillators due to attenuation in the slab, the surrounding air, or the RPM structural material.

The actual count rates from the RPM could include signals from environmental background, the concrete slab, or electronic noise. These extraneous sources of radioactivity make it difficult to determine the validity of the MCNP model, which only considers gamma rays generated from the concrete slab. A 12 hr average was taken from a RPM data printout for a time period where no concrete slab was present. This value was subtracted from the actual data in Figure 14 to form an estimated count rate for the RPM in the absence of a concrete slab. A comparison of the estimated values and the simulated counts rates is shown in Figure 15.

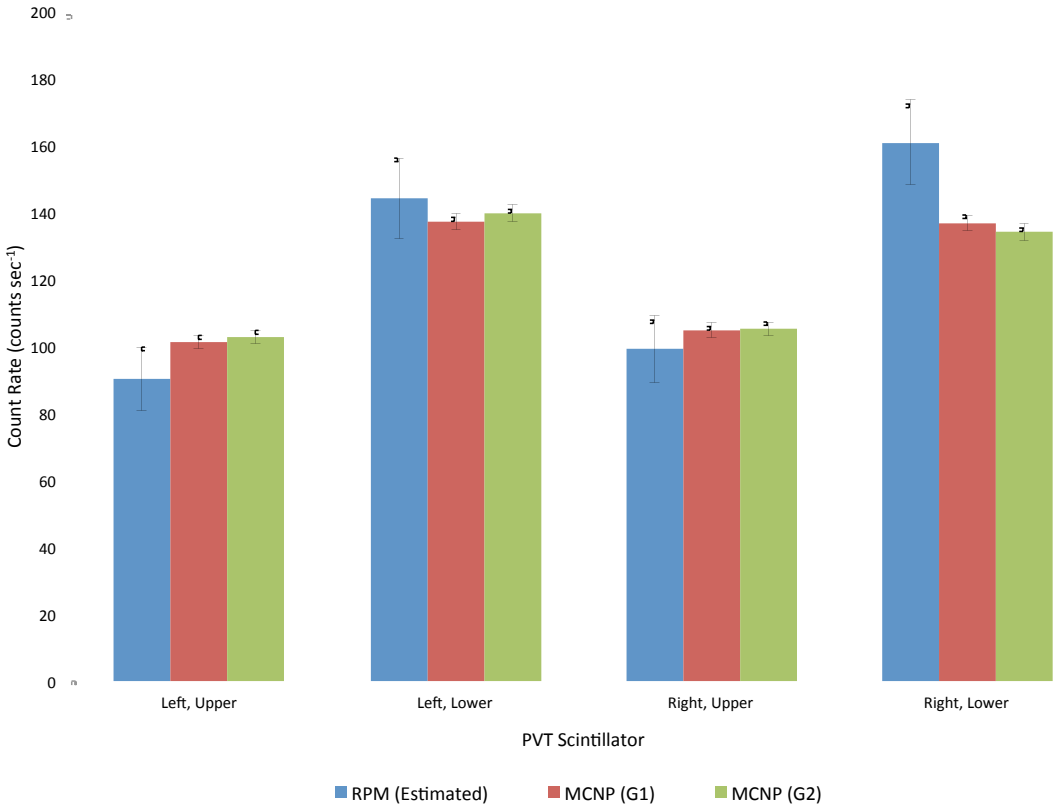

Figure 15. A comparison of estimated and simulated RPM count rates from slab G.

The chart shows that it is possible to obtain a reasonable estimate of the gamma ray contribution from the concrete using MCNP. Even though the estimated and simulated results are within ±1σ for three detectors and ±2σ for all four detectors, it is necessary to note a few issues that could still influence the results from the RPM. In the case of the data presented in both Figures 14 and 15, it was assumed that the physical RPM was properly discriminated between 40 and 140 keV. The count rates in the RPM could be higher or lower if incorrect discrimination settings were applied. There may also be interference from electronic noise, which is not considered in the MCNP model. Subtracting the 12 hr averaged data from a different 24 hr data set could also impact the

results. Since environmental background can vary based on any number of external factors, the estimated RPM count rate may not be an accurate representation of the count rate from only the concrete.

IV.D. Model validation and sensitivity analysis

The MCNP model was tested by measuring the response of the RPM to different strength ^{137}Cs check sources and comparing the count rates to those obtained from MCNP. A plot of this comparison, along with a ratio of the MCNP and RPM count rates, is shown in Figure 16.

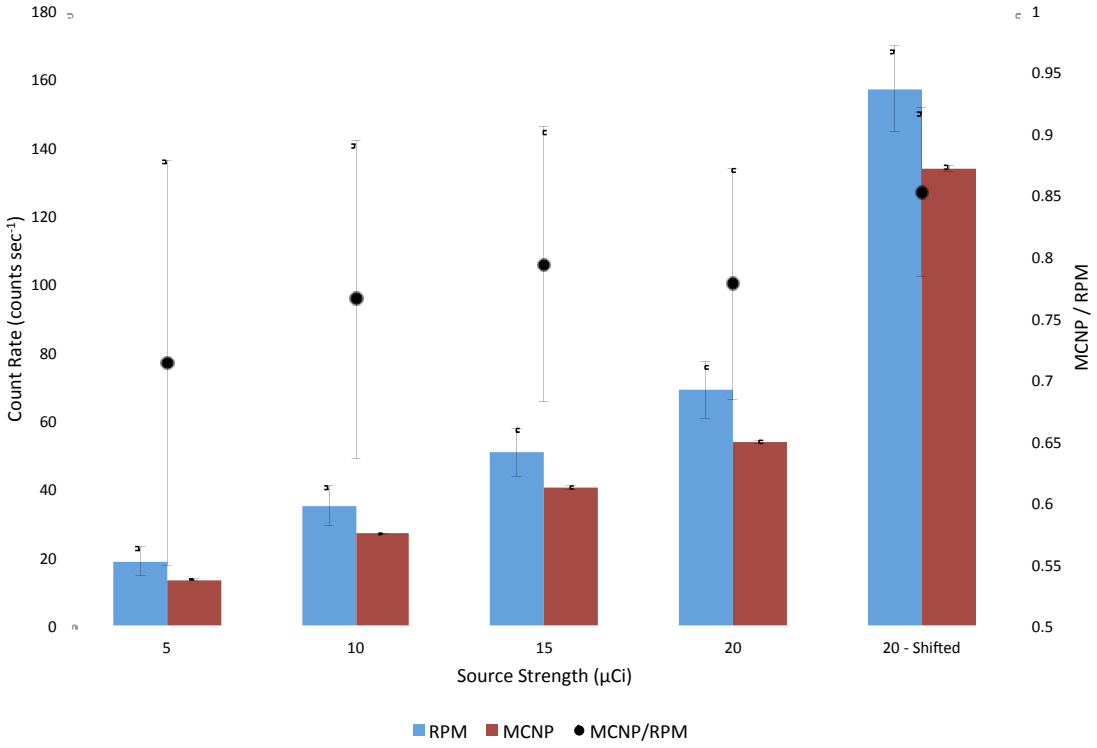

Figure 16. A comparison of actual and simulated count rates for a single PVT scintillator in a RPM.

Figure 16 shows that the count rate in the physical detector exceeded the count rate simulated in the MCNP model; however, the ratio of the simulated and measured data is statistically the same for all measurements. The first four data points represent check sources placed approximately 183 cm above the center of the slab. The last data point represents a source placed approximately 183 cm above the slab and 130 cm from the face of a portal. These distances were measured on the actual RPM using a tape measure, and therefore a particular amount of uncertainty is present in the exact placement of the sources. The validation was also limited by the size of the sources available. While larger sources or longer count times would have led to less statistical variation in the physical data, radiation handling and transport policies prevented examination with a stronger source.

The validation case indicates there is a certain amount of bias in the model. The ratio of the simulated and measured data shows that the MCNP model under-predicts the RPM by 21 – 29% for sources placed at the center of the slab and 15% when the source is placed closer to one pillar. As previously stated for the results from slab G, another potential cause of the higher physical count rate is electronic noise in the system. Since the detector volume is large and the discriminated energy range is low, it is possible that extraneous counts were introduced to the system. Research previously completed by Siciliano, et. al. indicates that the lower level discriminator setting is important because a majority of the low energy signals in the PVT scintillator are caused by Compton scattering.[60] If the setting is too low, electronic noise can affect the count rates, but if the discriminator is set too high, some desired gamma rays may not be counted at all. In

addition, Siciliano's work suggests that given the same discrimination settings, the simulated count rate in MCNP could be lower than the actual count rate in the RPM when subjected to a source emitting high-energy (> 600 keV) gamma rays, such as ^{60}Co or ^{137}Cs.[60]

A sensitivity analysis was completed with MCNP to determine the effect of concrete density on the simulated results. The decks for each sample were rerun with density variations of ±2σ from the measured value. A plot of the results from slab F is shown in Figure 17. Plots of the results for slabs G and L can be seen in Appendix F.

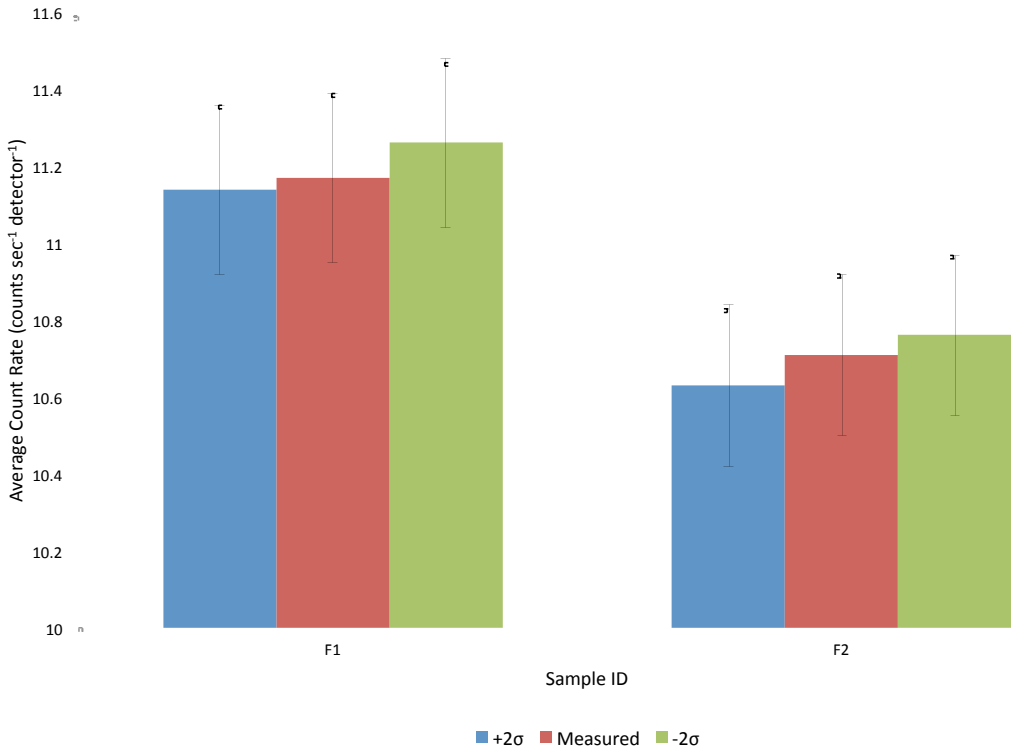

Figure 17. A plot of the impact of variations in concrete density on the simulated average count rates in a RPM.

Figure 17 indicates that variations in the density will have a minor impact on the overall results. For the cases examined in this research, the average count rates remained well within statistical variation at ±2σ. Even though this did not adversely impact the results in this case, it proves that the density of the concrete will have some impact on the number of gamma rays reaching the detector. Concretes with a higher density are more likely to attenuate a gamma ray, thus decreasing its probability of reaching one of the detectors in the RPM. Higher density concretes are available on the market, but none were at hand for this research. Additionally, the value of σ was low in this case because the measurement equipment was precise. Less precise equipment will lead to larger uncertainties and subsequently cause the count rates at ±σ to increase.

A second sensitivity analysis was conducted to test the impact of the carbon and hydrogen content on the average count rate in the RPM. The concentrations of carbon and hydrogen were assumed since the elemental concentration of both elements was not determined from the NAA methods used in this research. The carbon concentration was set at 50% and 10% of the assumed value and the difference between the total weight percentage and unity was filled with hydrogen. A plot of the results from slab F is shown in Figure 18. Plots of the results for slabs G and L are in Appendix G.

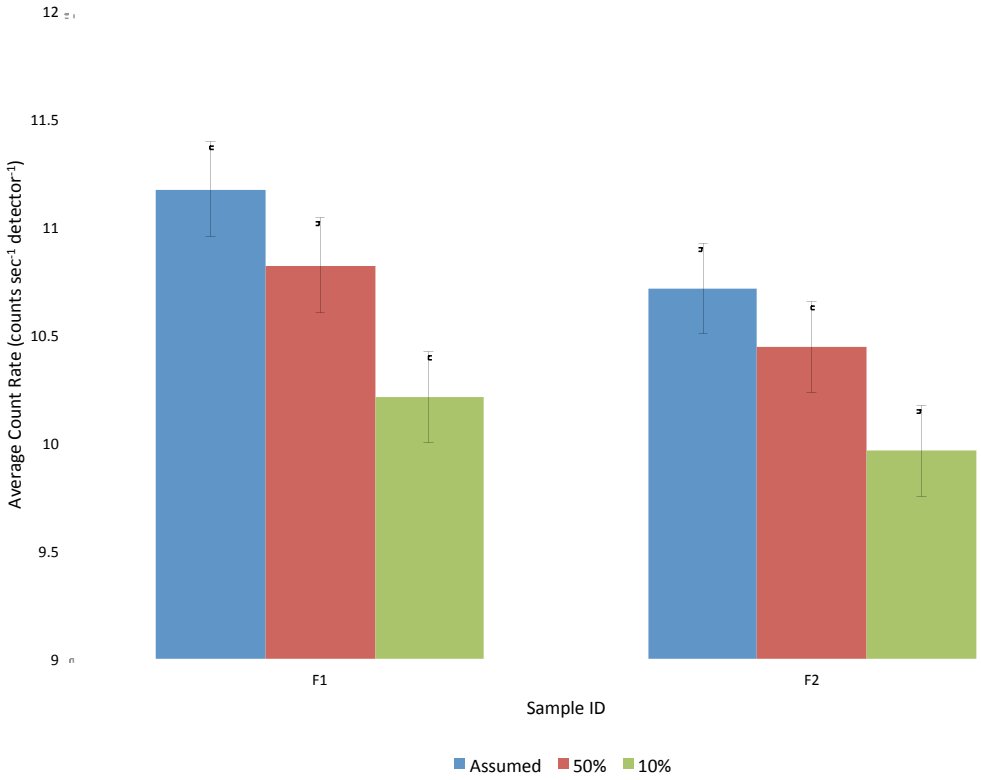

Figure 18. A plot of the impact of variations in carbon and hydrogen concentration on the average count rate in a RPM from concrete slab F.

The data shows that carbon content has an impact on the average count rate in the RPM, but these results were unexpected. Since hydrogen has a lower *Z* than carbon, it was assumed that there would be less gamma attenuation in the slab and the count rate would increase as the carbon content decreased. Instead, the count rate decreased as the carbon content decreased and the hydrogen content increased. This is caused by a larger number of electrons available for interactions with a gamma ray. Since the density of concrete did not change, the mass of carbon was replaced with the same mass of hydrogen. Carbon is a heavier element, thus a larger atom density of hydrogen is required to replace the mass of the carbon. The larger density of hydrogen atoms in the

concrete compared to the carbon atoms means that there are more electrons available to interact with the gamma rays. Since the missing weight percentage from carbon was replaced with hydrogen in the model, it follows that the count rate should decrease because there is more attenuation in the slab due to the increased amount of hydrogen. In addition, the mass attenuation coefficient for hydrogen is larger than that of carbon at energies above 25 keV. A plot of the total mass attenuation coefficient for carbon and hydrogen with respect to the energy of the incident gamma ray is given in Figure 19.

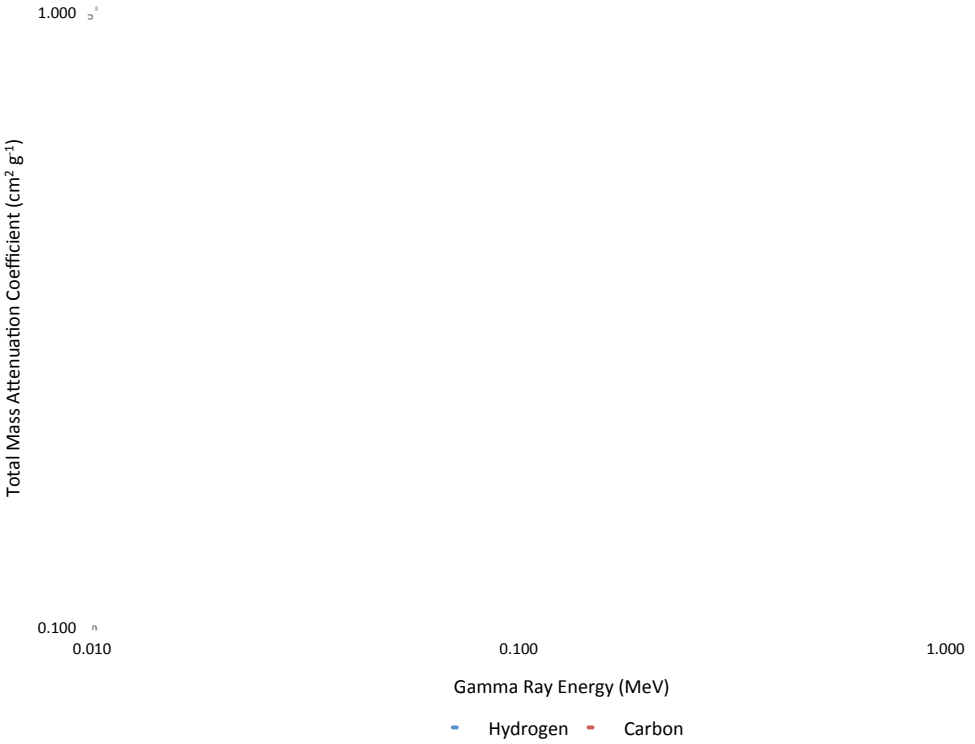

Figure 19. The total mass attenuation coefficient of hydrogen and carbon with respect to incident gamma ray energy.[61]

CHAPTER V

SUMMARY AND CONCLUSIONS

V.A. Summary and conclusions

The consequences of illicit RN material being transported undetected across international borders are very severe. To ensure our safety, it is important that RPMs deployed around the world be able to discern gamma rays emitted from RN material from those emitted by the environmental background. This research relied on a combination of physical experiments and computer simulations to provide a methodology for determining the contribution of concrete to the gamma ray background in a RPM. A flowchart describing the general process used for this research is shown in Figure 20.

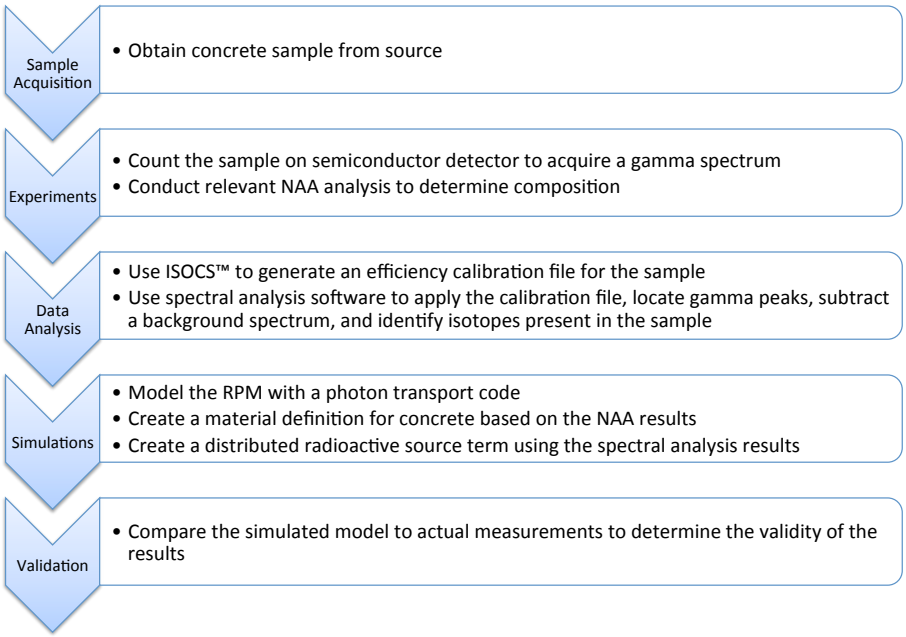

Figure 20. A flowchart describing the general process used for this research.

The concrete used in this research was provided by ORNL. The samples were subjected to an environmental background measurement using an HPGe detector. Small portions of the samples were also used for thermal neutron INAA and FNAA experiments in order to determine their respective elemental compositions. The Canberra Industries ISOCS™ software was used to generate efficiency calibration files for the HPGe detector based on a validated mathematical model. The Canberra Industries Genie™ 2000 software was used to analyze the energy spectra from the HPGe detector and determine the activity of radioactive isotopes in the concrete sample. Finally, the MCNP version 5 transport code was used to model a physical RPM system and estimate the counts in the PVT scintillators due to the radioactivity in the concrete slab. The model was validated using ^{137}Cs check sources and comparing actual count rates from the RPM to simulated count rates from the MCNP model. Additionally, count rates from concrete slab G at ORNL were compared to simulated count rates from MCNP. Two sensitivity analyses were also completed to determine the impact of the concrete density and the concentrations of carbon and hydrogen on the average count rate in the RPM.

The environmental background measurements of the concrete were conducted in a lead vault. While the vault did a reasonable job at shielding the detector from check sources and concrete walls in the laboratory, it had the unintended consequence of contributing lead x-rays to the gamma spectra. Vaults with laminate shields capable of attenuating the x-rays were available; however, none of the HPGe detectors occupying the vaults were characterized for the ISOCS™ software. In addition, a portable HPGe

detector was used for the measurements. Placing it in a laminate-shielded vault would have required removing the current detector and constructing an apparatus to hold the detector vertically. A background subtraction was completed to eliminate x-rays from the concrete spectra; however, it is preferable that they not be allowed to interact with the detector to prevent possible interference with gamma rays of similar energies.

It was assumed when comparing the actual and simulated data that the RPM was correctly discriminated between 40 and 140 keV. The actual discrimination settings were unknown. If the RPM was incorrectly discriminated, the count rates registered by the detectors would be higher or lower than the real value. In addition, there could also be electronic noise in the system contributing to extraneous counts in the RPM. The noise is not quantified by MCNP; therefore, in a direct comparison of actual and simulated count rates, the value from the RPM could be higher than the one from MCNP.

The density sensitivity analysis showed that variations of $\pm 2\sigma$ do not have a significant impact on the average count rate. The instruments used to measure the mass and exterior dimensions of the concrete cylinders had a high degree of precision. If less precise instruments are used, the value of σ will increase, and there will be an adverse impact on the uncertainty in the count rates. The carbon and hydrogen concentration sensitivity analysis showed that the model is slightly sensitive to large variations in the concentrations of these two elements. The initial results were unexpected, but subsequent study of the attenuation characteristics of carbon and hydrogen proved that gammas with energy above 25 keV will attenuate more in hydrogen than in carbon.

A comparison of the actual and simulated count rates for slab G indicated that a quantitative estimate of the gamma ray background contribution of concrete is achievable; however, other sources of radiation in the vicinity of the RPM need to be identified and characterized. The comparison of estimated and simulated RPM count rates from slab G indicates that the user can successfully determine the gamma ray contribution of a particular concrete if the environmental background is well known.

V.B. Recommendations

Over the course of this research, several instances were noted where the model used might be improved for those interested in expanding on this work. When conducting gamma ray measurements, it is important to count the samples long enough to obtain a statistically significant number of counts. Optimal counting time will vary based on the activity of both the sample and the radiological background in the counting area. In this research, a lead vault was built around the HPGe detector; however, this made it difficult to distinguish lead x-rays from the low-energy gamma rays of some isotopes. A laminate shield consisting of lead, aluminum, and copper would not only help reduce lead x-rays, but other sources of background radiation.

Many roadways contain a matrix of reinforcing bars typically made of carbon steel, called rebar. If desired, the user may adapt the methods used to include the additional material. This requires conducting NAA on the reinforcing bars to determine their chemical composition and modeling them in both ISOCS™ and MCNP. Since the bars are approximately three times denser than the concrete itself, it is likely that they

will contribute to the attenuation of gamma rays from the slab. While the concrete used for this research contained a small amount of rebar, it was ultimately not considered because attempts to determine the rebar content were unsuccessful. Crushing the concrete would allow the user to calculate volume of rebar in the sample; however, this is problematic because the user no longer knows the location of the rebar within the concrete sample. This prevents the rebar from being incorporated into the ISOCS™ model because the accuracy of the efficiency calibration relies on the input parameters.

As shown in Chapter IV section D, the carbon and hydrogen content has a slight impact on the overall count rate. It is possible to determine the concentration of both elements in the concrete using PGNAA. As in this research, the user may employ INAA and FNAA to determine an accurate and precise value for many other elements in the concrete. If the concrete is well characterized using these techniques, a value of the carbon and hydrogen content can be estimated with a good deal of certainty. Even though the sensitivity analysis showed that variations in carbon content did not have a significant impact on the results, it is possible to measure a more accurate value.

It was determined that for the concrete used in this research, variations in the density did not adversely impact the average count rate; however, higher density concrete may offer additional gamma attenuation. If higher density concretes are used, the attenuation of gamma rays should be considered. Likewise, if less precise tools are used to determine the density of the concrete, the larger uncertainties will give rise to larger variations in the simulated count rates. Precise instruments should be used to limit the impact of any uncertainties on the overall results.

While a majority of the results presented in the research are focused on total count rate, it should be noted that the MCNP simulations are based on an ideal scenario. In the physical measurements, there are uncertainties in the detection and counting process. There is also electronic noise in the system that is not accounted for in the MCNP model. This noise may come from the electronic components themselves or external influences such as wind, ground vibrations, or fluctuations in temperature and humidity. While noise does not alter the size of a signal, it can have a major impact on the precision with which it is measured. The user should make sure that the energy range of interest in correctly discriminated so that most of the electronic noise is eliminated. If a low energy range is required, the user may choose to either accept a certain level of electronic noise in the system or find a way to quantify it and include it in the calculations.

It is necessary to eliminate bias when comparing physical data to the MCNP simulation. Each detector has different internal defects, an independent intrinsic efficiency, and different electronic components connecting it to the rest of the system. Each of these characteristics has uncertainties that will propagate once the detectors are summed together to give a total count rate for the RPM. In order to eliminate this bias, the user should choose one detector and compare the count rates obtained from the MCNP simulation and the measured data.

In conclusion, the research presented in this thesis establishes a model capable of providing RPM customers and users a way to qualitatively determine whether one particular type of concrete will contribute less gamma ray background to their system. It

also provides the foundations for a quantitative estimate of the background contribution of the roadway to the gamma counts registered by a specific RPM. The methods used are also adaptable based on the particular needs and budgetary requirements of the consumer. In addition, several areas have been mentioned where these methods may be improved, but further investigation is left to the reader.

REFERENCES

1. R. T. KOUZES, "Detecting Illicit Nuclear Materials," *Am. Sci.*, **93**, *5*, 422-427 (2005).

2. U.S. General Accounting Office, "Nuclear Nonproliferation: U.S. Efforts to Combat Nuclear Smuggling," GAO-02-989T, July 2002. http://www.gao.gov/new.items/d02989t.pdf (accessed 16 January 2011)

3. National Nuclear Security Administration, "Fact Sheet: NNSA's Second Line of Defense Program," 2010. http://nnsa.energy.gov/mediaroom/factsheets/nnsassecondlineofdefenseprogram (accessed 16 January 2011)

4. M. MARCHESANO, "Funding Analysis of FY09 International WMD Security Programs," (April 2009). http://partnershipforglobalsecurity.presstools.org/node/33516 (accessed 16 January 2011)

5. Nuclear Threat Initiative, "Interdicting Nuclear Smuggling: International Counterproliferation Program," 2002. http://www.nti.org/e_research/cnwm/interdicting/icp.asp (accessed on 16 January 2011)

6. Defense Threat Reduction Agency, "Fiscal Year (FY) 2009 Budget Estimates," February 2008. http://comptroller.defense.gov/defbudget/fy2009/budget_justification/pdfs/01_Operation_and_Maintenance/O_M_VOL_1_PARTS/DTRA%20OP-5%20FY%202009%20PB.pdf (accessed 16 January 2011)

7. Department of State, "The Export Control and Related Border Security Assistance (EXBS) Program," 2006. http://www.exportcontrol.org/links/1371c.aspx (accessed 16 January 2011)

8. G. I. BALATSKY, S. L. EATON, and W. R. SEVERE, "Illicit Trafficking of Nuclear and Radiological Materials," in *Nuclear Safeguards, Security, and Nonproliferation: Achieving Security with Technology and Policy*, edited by J. E. DOYLE, Butterworth-Heinemann, Oxford, UK (2008).

9. A. A. SOLODOV and R. J. LIVESAY, private communication, Oak Ridge National Laboratory, Oak Ridge, TN. November 2009.

10. R. KNAPP, "Building Networks of Trust through Collaborative Science," *Science and Technology Review*, Los Alamos National Laboratory (March 2005). https://www.llnl.gov/str/March05/Knapp.html (accessed 16 January 2011)

11. MCNP X-5 Monte Carlo Team, "MCNP—A General Purpose Monte Carlo N-Particle Transport Code, Version 5," LA UR 03 1987, Los Alamos National Laboratory, April 2003, The MCNP5 code can be obtained from the Radiation Safety Information Computational Center (RSICC), P. O. Box 2008. Oak Ridge, TN, 37831-6362.

12. T.F. SANQUIST, P. DOCTOR, and R. PARASURAMAN, "Designing Effective Alarms for Radiation Detection in Homeland Security Screening," *IEEE Trans. Syst., Man, Cybern. C, Appl. Reviews*, **38**, *6*, 856-860 (2008).

13. TSA Systems, Ltd., "Vehicle and Pedestrian Monitor: VM-250AGN / VM-700AGN, Operations & Service Manual," Document #5000, Revision A (January 2006).

14. L. A. CURRIE, "Limits for Qualitative Detection and Quantitative Determination: Application to Radiochemistry," *Anal. Chem.* **40**, *3*, 586-593 (1968).

15. G. F. KNOLL, *Radiation Detection and Measurement*, 3rd Edition, John Wiley & Sons, Inc., New York City, NY (2000).

16. A. B. REYNOLDS, *Bluebells and Nuclear Energy*, Cogito Books, Madison, WI (1996).

17. Portland Cement Association, "Aggregate," 2010. http://www.cement.org/basics/concretebasics_aggregate.asp (accessed 17 January 2011)

18. M. TSUTSUMI, T. OISHI, N. KINOUCHI, R. SAKAMOTO, and M. YOSHIDA, "Simulation of the Background for Gamma Detection System in the Indoor Environments of Concrete Buildings," *J. Nucl. Sci. Technol.* **38**, *12*, 1109-1114 (2001).

19. R. A. TIPLER and P. A. LLEWELLYN, *Modern Physics*, 4th Edition, W.H. Freeman and Company, New York City, NY (2003).

20. G. GILMORE, *Practical Gamma-ray Spectrometry*, 2nd Edition, John Wiley & Sons, Ltd., West Sussex, UK (2008).

21. K. S. KRANE, *Introductory Nuclear Physics*, John Wiley & Sons, Inc., New York City, NY (1988).

22. D. REILLY, N. ENSSLIN, H. SMITH, JR., and S. KREINER, *Passive Nondestructive Assay of Nuclear Materials*, U.S. Nuclear Regulatory Commission, Wahington, DC (1991).

23. G. HEVESY and H. LEVI, "The Action of Neutrons on the Rare Earth Elements," *Dansk. Videnskap. Selsk. Math. Fys. Medd.* **14**, *5*, 3-34 (1936).

24. G. HEVESY and H. LEVI, "Artificial Radioactivity of Dysprosium and other Rare Earth Elements," *Nature* **136**, 103, (1935).

25. R. H. FILBY, "Isotopic and Nuclear Analytical Techniques in Biological Systems: A Critical Study – IX. Neutron Activation Analysis (Technical Report)," *Pure Appl. Chem.* **67**, *11*, 1929-1941 (1995).

26. M. B. CHADWICK, P. OBLOZINSKY, M. HERMAN, et. al., "ENDF/B-VII.0: Next Generation Evaluated Nuclear Data Library for Nuclear Science and Technology," *Nucl. Data Sheets* **107**, 2931-3060 (2006).

27. M. G. VENTURA, V. STIBILJ, M. FREITAS, and A. PACHECO, "Determination of ultratrace levels of selenium in fruit and vegetable samples grown and consumed in Portugal," *Food Chem.* **115**, 200-206 (2009).

28. D. DE SOETE, R. GIJBELS, and J. HOSTE, *Neutron Activation Analysis*, John Wiley & Sons, Ltd., New York City, NY (1972).

29. P. BODE, "Detectors and detection limits in INAA – I. General theoretical relationships between detector specifications and detection limits," *J. Radioanal. Nucl. Chem.* **222**, *1*, 117-125 (1997).

30. N. EBY, "Instrumental Neutron Activation Analysis (INAA) Trace Element Analysis," University of Massachusetts – Lowell. Personal Website. http://faculty.uml.edu/Nelson_Eby/Analytical%20Methods/INAA/trace_element_analysis_trace_ele.htm#Instrumental%20Neutron%20Activation%20Analysis%20(INAA):%20Practice%20and%20Potential%20Forensic%20Applications (accessed 17 January 2011).

31. J. N. BECK and C. M. LAMBERTY, "Thermal Neutron Activation Analysis – An Important Analytical Tool," *Appl. Spectrosc. Rev.* **37**, *1*, 19-55 (2002).

32. O. OLDENBERG and N. C. RASMUSSEN, *Modern Physics for Engineers*, Techbooks, Marietta, OH (1996).

33. E. M. BAUM, H. D. KNOX, and T. R. MILLER (eds.), *Chart of the Nuclides*, 16th Edition, Knolls Atomic Power Laboratory, Schenectady, NY (2002).

34. S. S. NARGOLWALLA and E. P. PRZYBYLOWICZ, *Activation Analysis with Neutron Generators*, John Wiley & Sons, Inc., New York City, NY (1973).

35. J. W. MORGAN and W. D. EHMANN, "Precise Determination of Oxygen and Silicon in Chondritic Meteorites by 14-MeV Neutron Activation with a Single Transfer System," *Anal. Chim. Acta.* **49**, 287-299 (1970).

36. W. D. EHMANN and B. F. NI, "A 14-MeV FNAA System for Oxygen Analysis Using a PC Microcomputer and Multiscaling," *J. Radioanal. Nucl. Chem.* **160**, *1*, 169-179 (1992).

37. W. D. JAMES, "Fast Neutron Activation Analysis at Texas A&M University," *J. Radioanal. Nucl. Chem.* **219**, *2*, 187-190 (1997).

38. T. BEREZNAI, "Determination of Antimony in Tin by Radiochemical Neutron Activation Analysis," *Anal. Chim. Acta.* **119**, 175-178 (1980).

39. F. GIRARDI, G. GUZZI, and J. PAULY, "Activation Analysis by Absolute Gamma-Ray Counting and Direct Calculation of Weights from Nuclear Constants," *Anal. Chem.* **36**, *8*, 1588-1594 (1964).

40. S. I. KAFALA and T. D. MACMAHON, "Comparison of Neutron Activation Analysis Methods," *J. Radioanal. Nucl. Chem.* **271**, *2*, 507-516 (2007).

41. T. BEREZNAI, "Methods, Problems and Trends of Standardization in Multielement Reactor Neutron Activation Analysis," *Fresenius Z. Anal. Chem.* **302**, 353-363 (1980).

42. F. GIRARDI, G. GUZZI, and J. PAULY, "Reactor Neutron Activation Analysis by the Single Comparator Method," *Anal. Chem.* **37**, *9*, 1085-1092 (1965).

43. Canberra Industries, Inc., "Genie™ 2000 Spectroscopy Software: Operations," Version 3.2, Canberra Industries, Meridian, CT (2009).

44. Canberra Industries, Inc., "Genie™ 2000 Spectroscopy Software: Customization Tools," Version 3.2, Canberra Industries, Meridian, CT (2009).

45. M. J. KOSKELO, P. A. AARNIO, and J. T. ROUTTI, "SAMPO80: Minicomputer Program for Gamma Spectrum Analysis with Nuclide Identification," *Comput. Phys. Commun.* **24**, 11-35 (1981).

46. M. A. MARISCOTTI, "A Method for Automatic Identification of Peaks in the Presence of Background and its Application to Spectrum Analysis," *Nucl. Instrum. Methods.* **50**, 309-320 (1967).

47. R. VENKATARAMAN, F. BRONSON, V. ALRASHKEVICH, B. M. YOUNG, and M. FIELD, "Validation of In Situ Object Counting System (ISOCS) Mathematical Efficiency Calibration Software," *Nucl. Instrum. Meth. A.* **422**, 450-454 (1999).

48. Canberra Industries, Inc. "In Situ Gamma Spectroscopy with ISOCS, an In Situ Object Counting System," Application Note, 2008. http://www.canberra.com/pdf/Literature/M2352-InSitu-ISOCS-AN.pdf (accessed 19 January 2011)

49. R. VENKATARAMAN, F. BRONSON, V. ALRASHKEVICH, M. FIELD, and B. M. YOUNG, "Improved Detector Response Characterization Method in ISOCS and LabSOCS," presented at the Methods and Applications of Radioanalytical Chemistry (MARC VI) conference, Kailua-Kona, HI, 7-11 April 2003.

50. X-5 Monte Carlo Team, "MCNP – A General Monte Carlo N-Particle Transport Code, Version 5," Volume I, LA-UR-03-1987, Los Alamos National Laboratory, Los Alamos, NM (2003).

51. W. D. JAMES, private communication, Center for Chemical Characterization and Analysis, Texas A&M University, College Station, TX. January 2011.

52. Canberra Industries, Inc. "Model S573 ISOCS Calibration Software: Technical Reference Manual," Version 4.2, Canberra Industries, Meridian, CT (2009).

53. TSA Systems, Ltd., "Vehicle Portal Monitors," Data Sheet. June 2008. http://tsasystems.com/library/data_sheets/VPM250AG-AGN_6-08.pdf (accessed 20 January 2011)

54. M. D. GLASCOCK, *Tables for Neutron Activation Analysis*, University of Missouri Research Rector Facility, Columbia, MO (March 1991).

55. R. M. LINDSTROM, R. L. PAUL, D. H. VINCENT, and R. R. GREENBURG, "Measuring Hydrogen by Cold-Neutron Prompt-Gamma Activation Analysis," *J. Radioanal. Nucl. Chem.* **180**, *2*, 271-275 (1994).

56. S. YAMAZAKI, Y. OURA, and M. EBIHARA, "Determination of Hydrogen in Rock Samples by Neutron-Induced Prompt Gamma-Ray Analysis," *J. Radioanal. Nucl. Chem.* **272**, *2*, 353-357 (2007).

57. R. L. PAUL and R. M. LINDSTROM, "Prompt Gamma-Ray Activation: Fundamentals and Applications," *R. Radioanal. Nucl. Chem.* **243**, *1*, 181-189 (2000).

58. D. J. DORSEY, R. HEBNER, and W. S. CHARLTON, "Non-Destructive Evaluation of Carbon Fiber Reinforcement Content," *J. Compos. Mater.* **38**, *17*, 1505-1519 (2004).

59. R. G. WILLIAMS III, C. J. GESH, and R. T. PAGH, "Compendium of Material Composition Data for Radiation Transport Modeling," PNNL-15870. Pacific Northwest National Laboratory, Richland, WA (April 2006).

60. E. R. SICILIANO, J. H. ELY, R. T. KOUZES, B.D. MILBRATH, J.E. SCHWEPPE, and D. C. STROMSWOLD, "Comparison of PVT and NaI(Tl) Scintillators for Vehicle Portal Monitor Applications," *Nucl. Instrum. Meth. A*. **550**, 647-674 (2005).

61. National Institute of Standards and Technology, "X-Ray Mass Attenuation Coefficients" Table 3. http://physics.nist.gov/PhysRefData/XrayMassCoef/tab3.html (accessed 17 February 2011).

APPENDIX A

HPGe gamma ray spectra for concrete cylinders

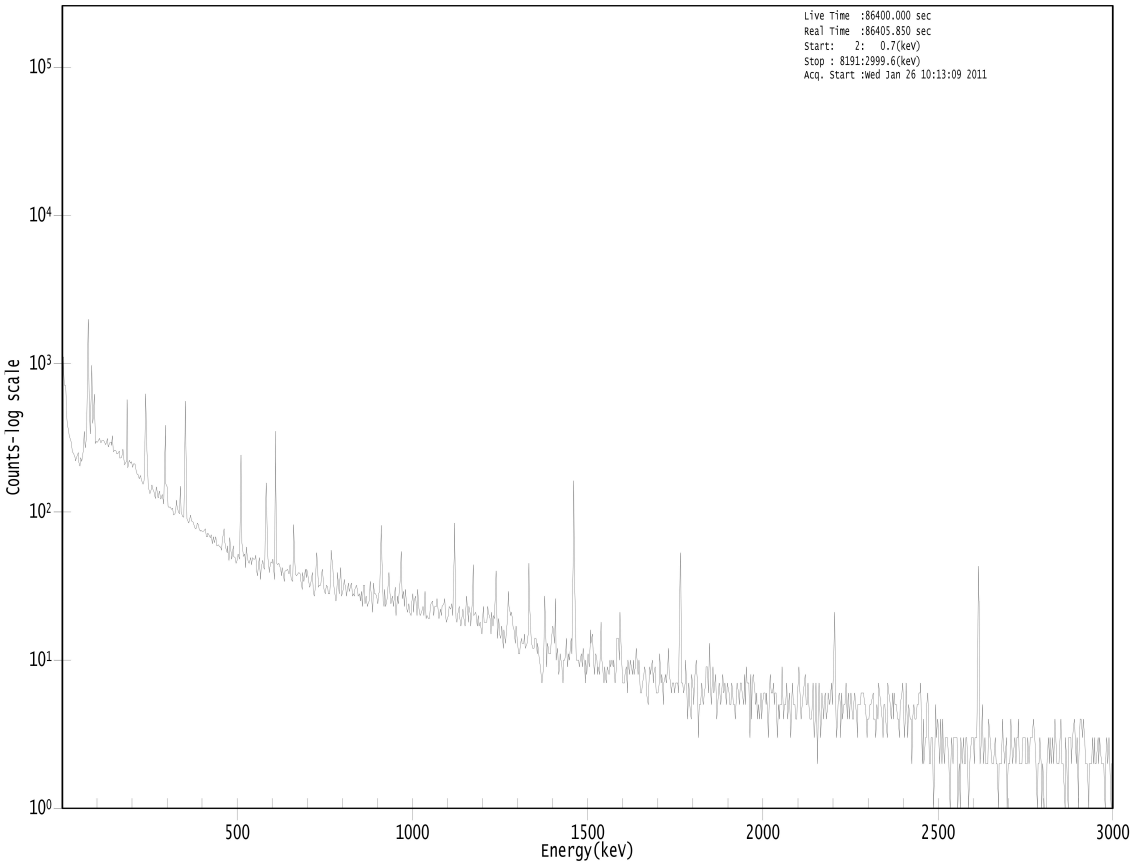

Figure A.1. HPGe gamma spectrum for sample F1.

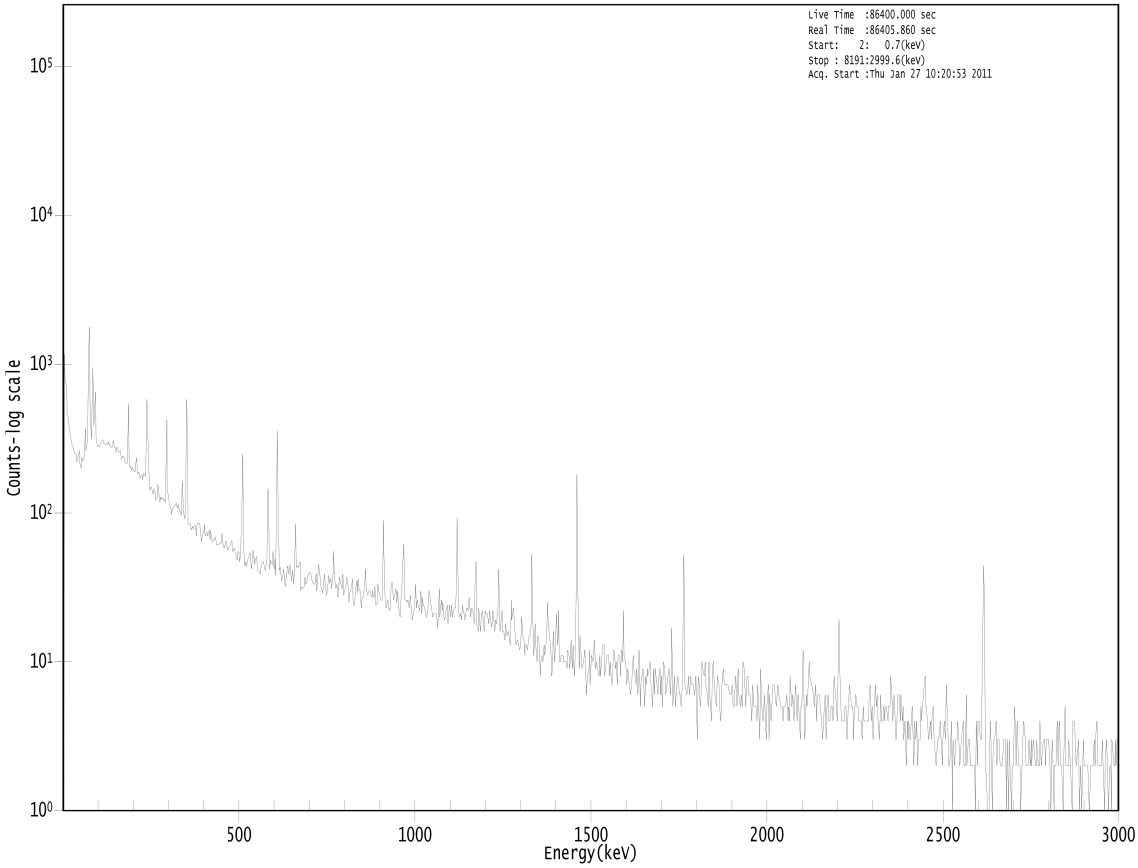

Figure A.2. HPGe gamma spectrum for sample F2.

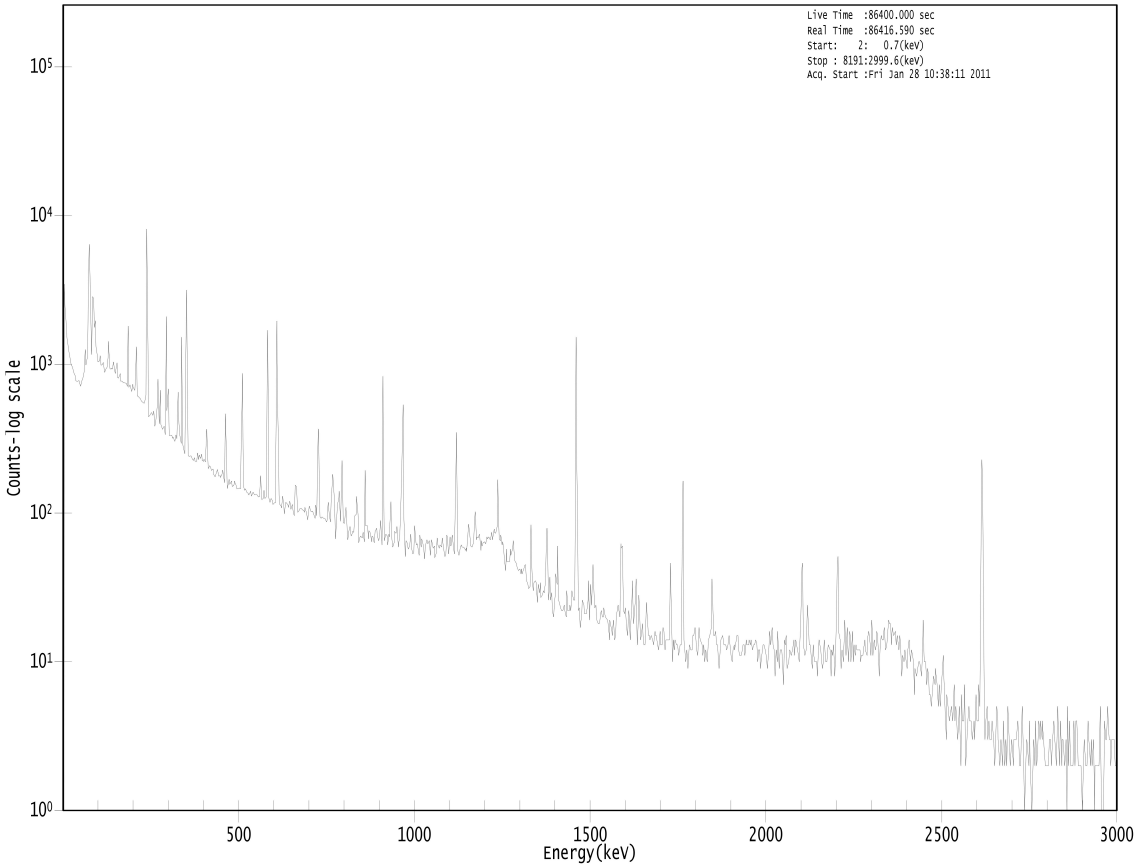

Figure A.3. HPGe gamma spectrum for sample G1.

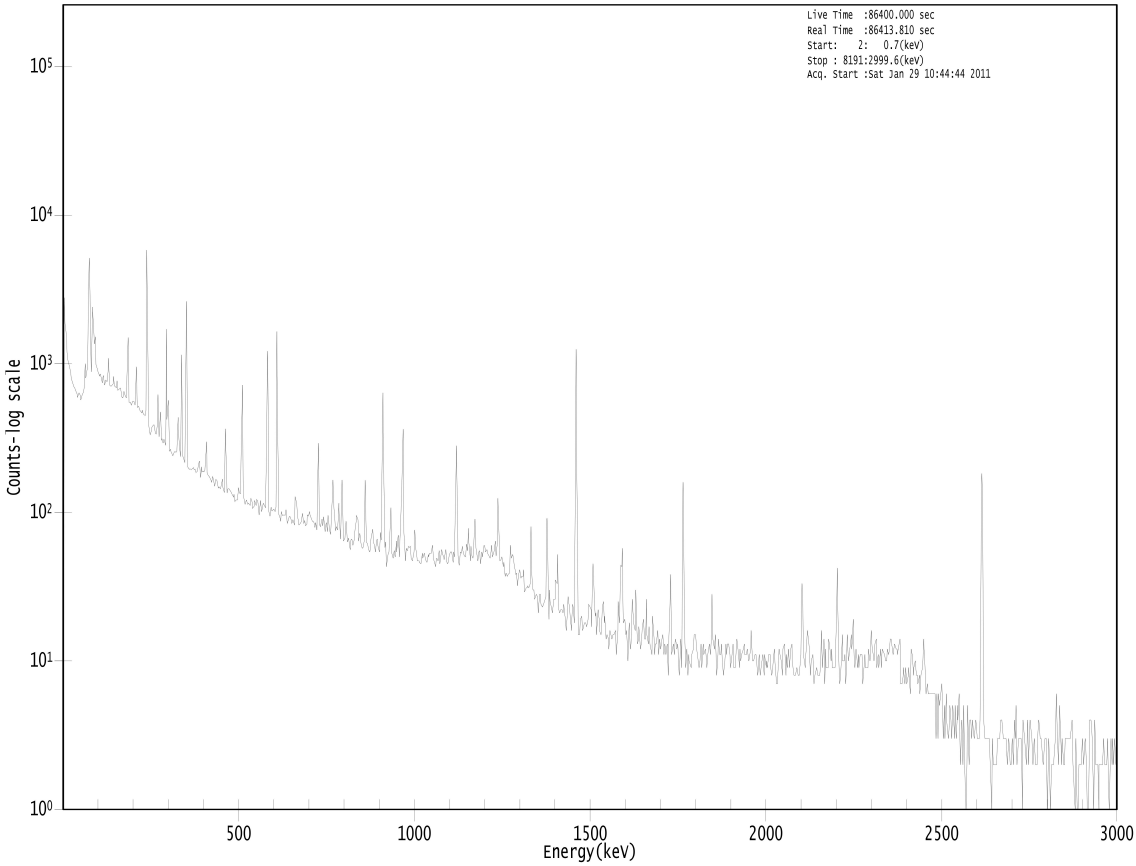

Figure A.4. HPGe gamma spectrum for sample G2.

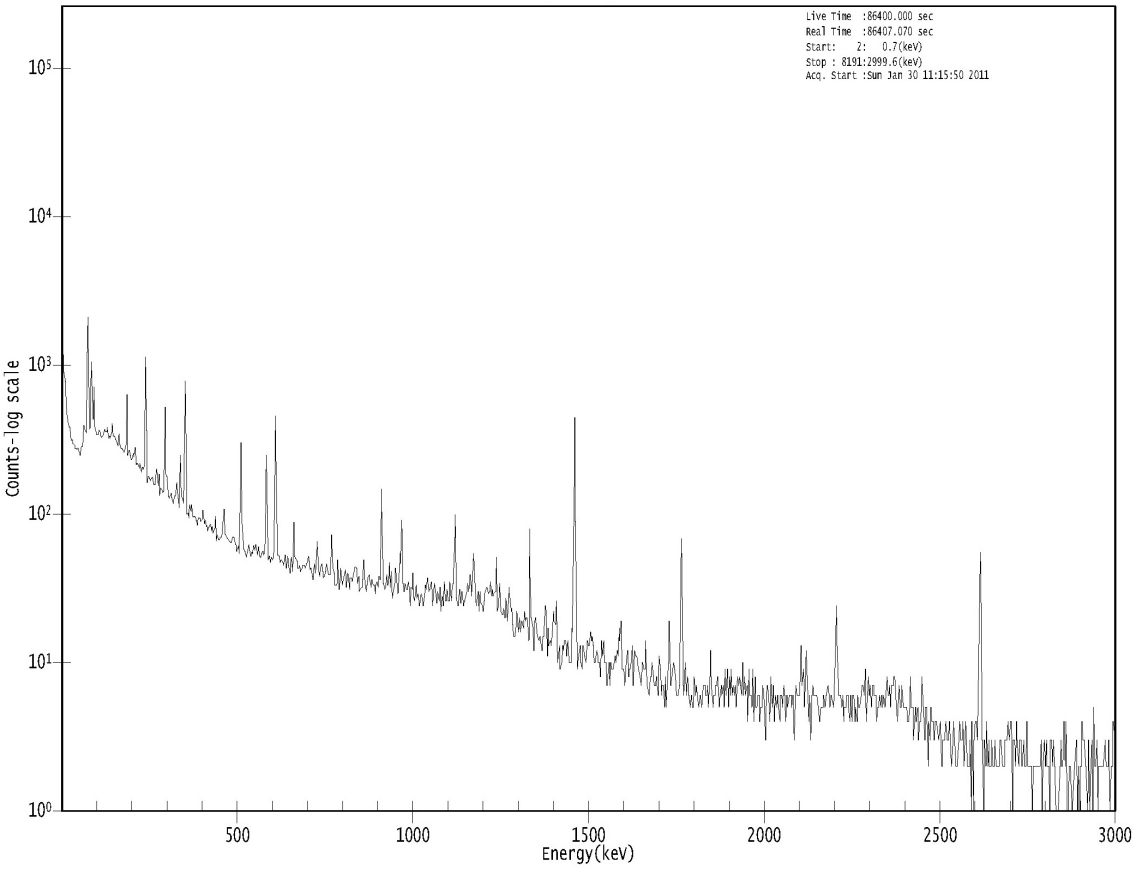

Figure A.5. HPGe gamma spectrum for sample L1.

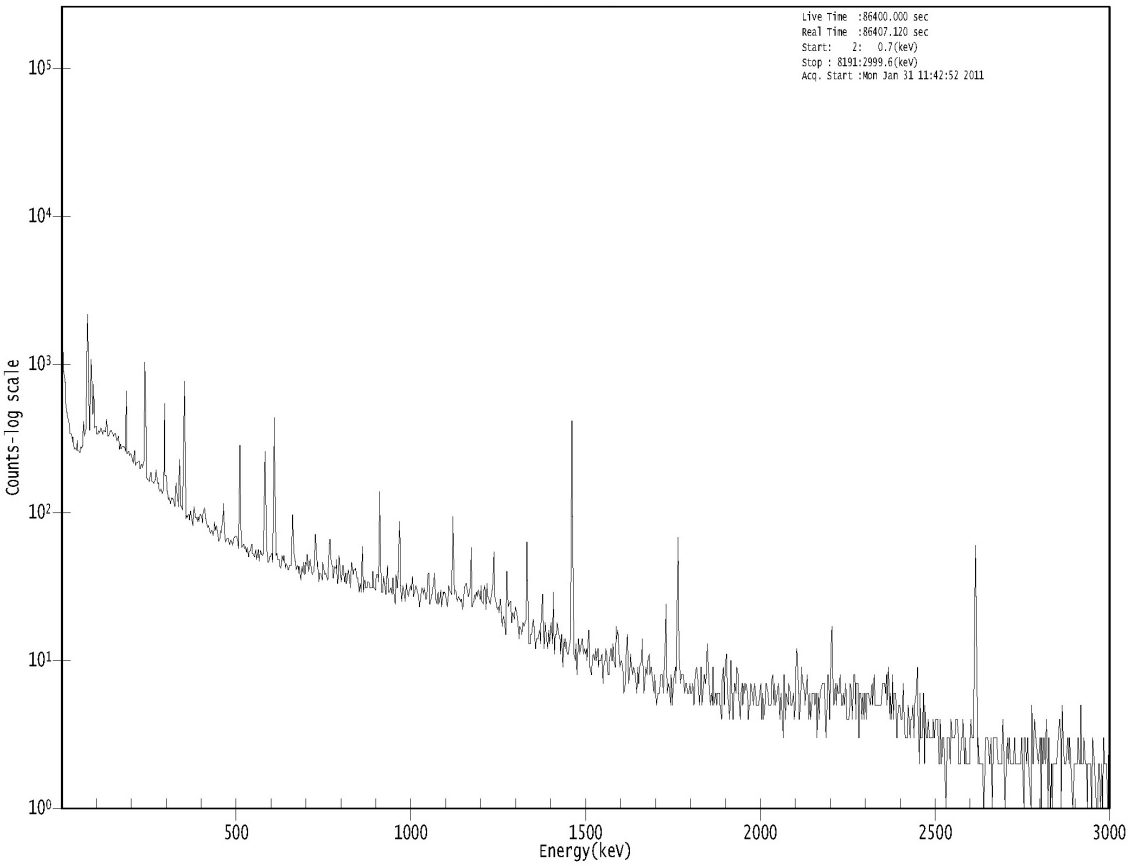

Figure A.6. HPGe gamma spectrum from sample L2.

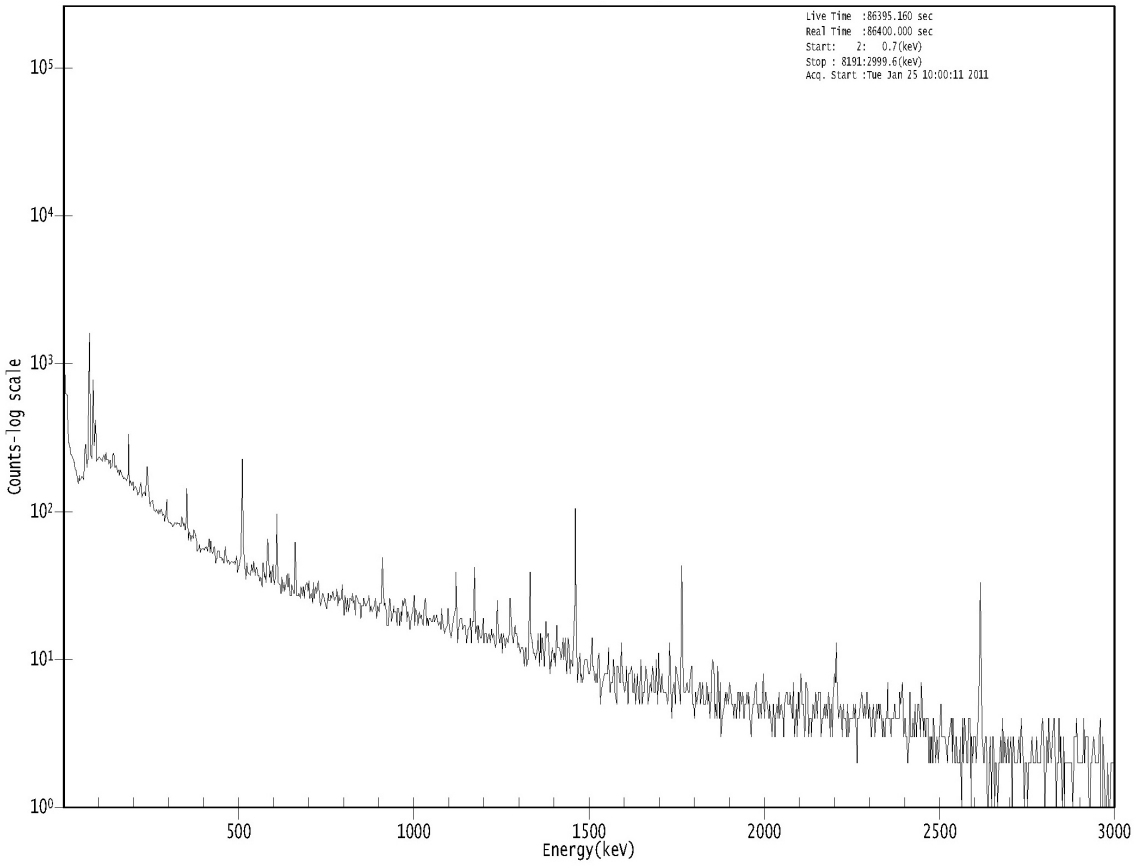

Figure A.7. HPGe gamma spectrum for background measurement.

APPENDIX B

HPGe gamma ray spectra for short half-life INAA measurements

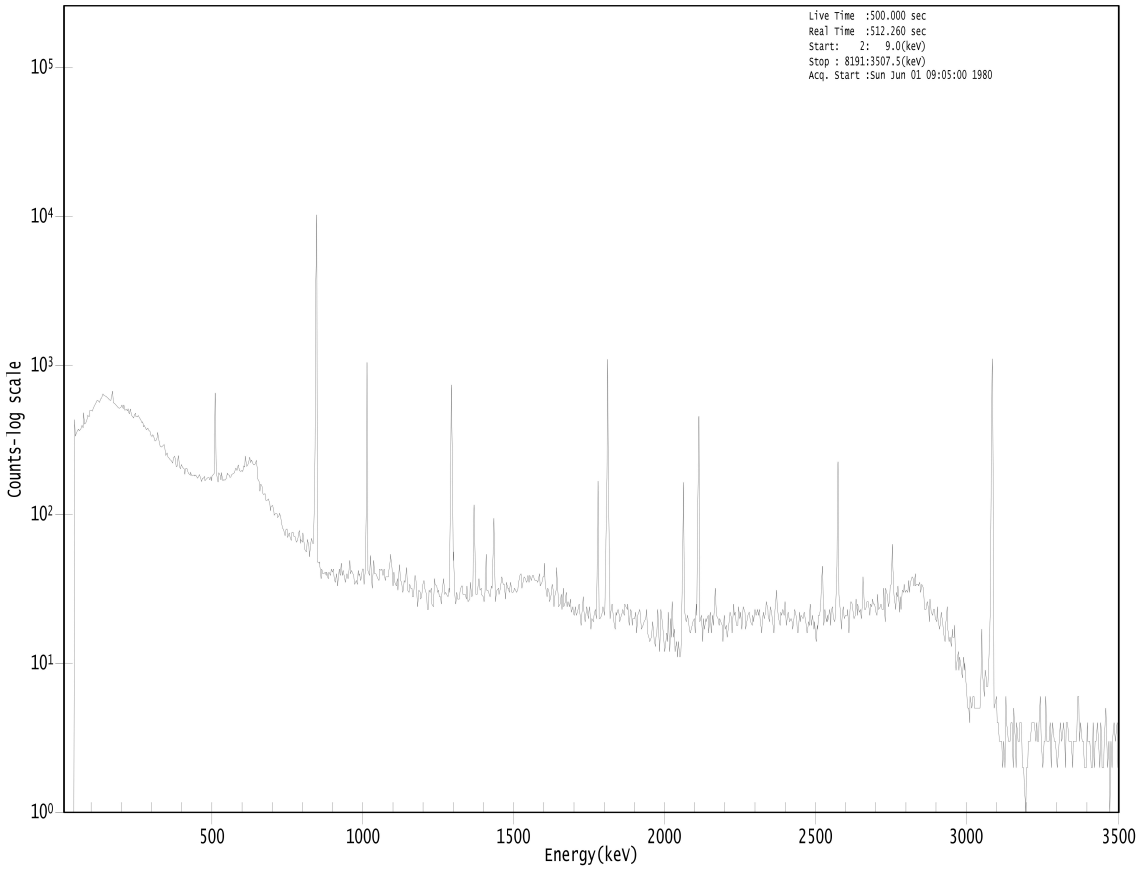

Figure B.1. HPGe gamma ray spectrum for first F1 INAA measurement.

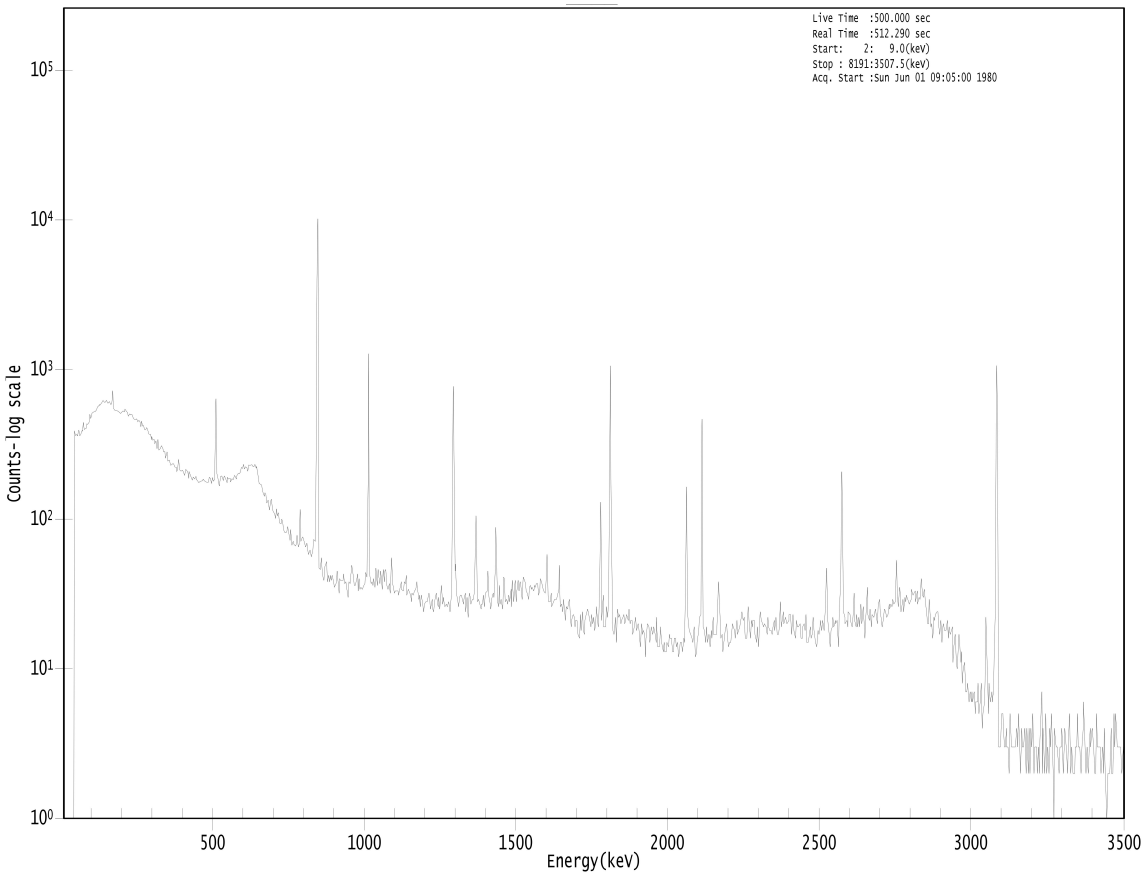

Figure B.2. HPGe gamma ray spectrum for second F1 INAA measurement.

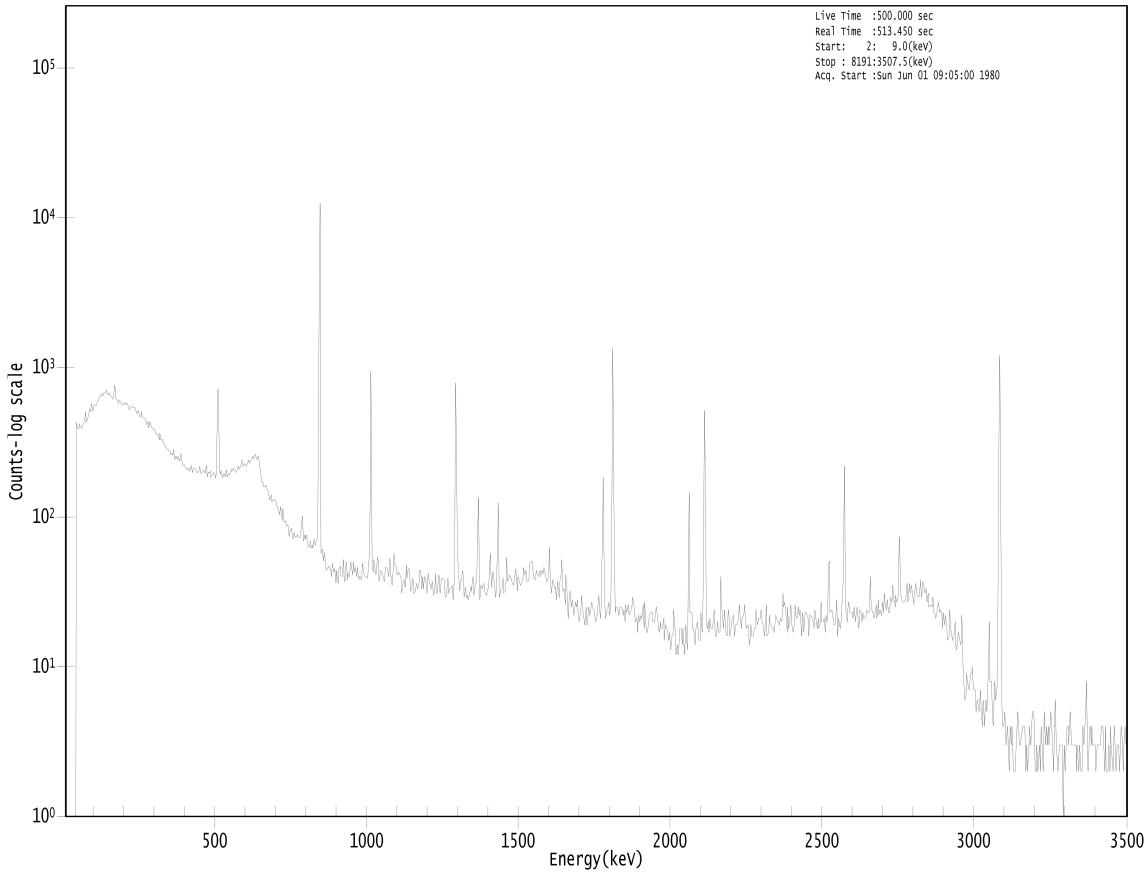

Figure B.3. HPGe gamma ray spectrum for first F2 INAA measurement.

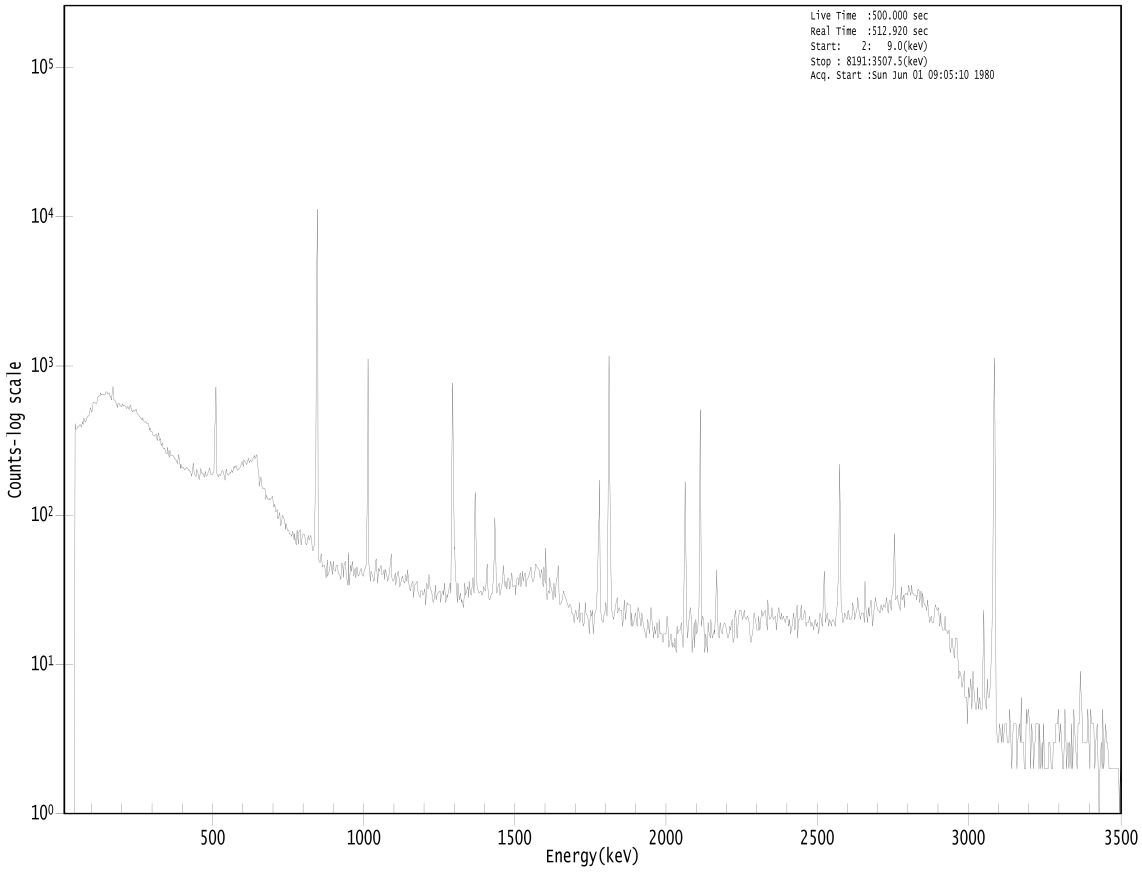

Figure B.4. HPGe gamma ray spectrum for second F2 INAA measurement.

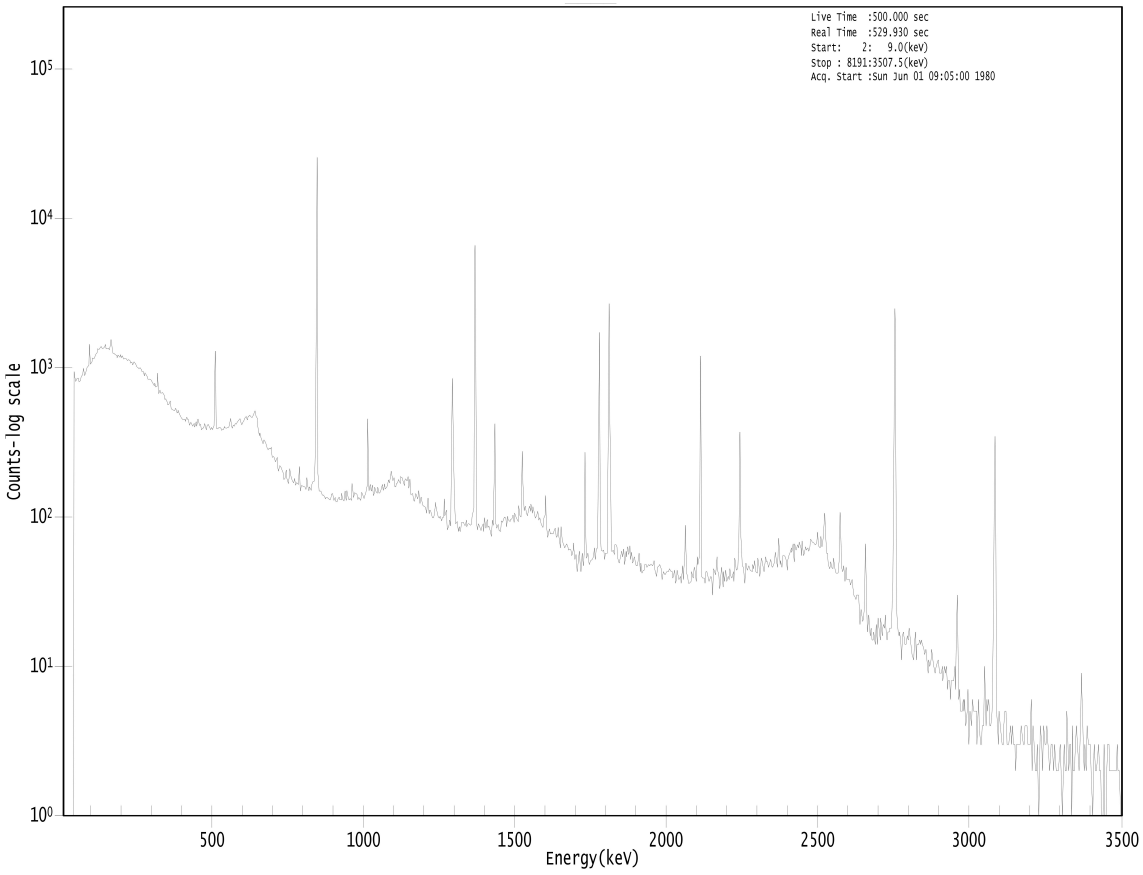

Figure B.5. HPGe gamma ray spectrum for first G1 INAA measurement.

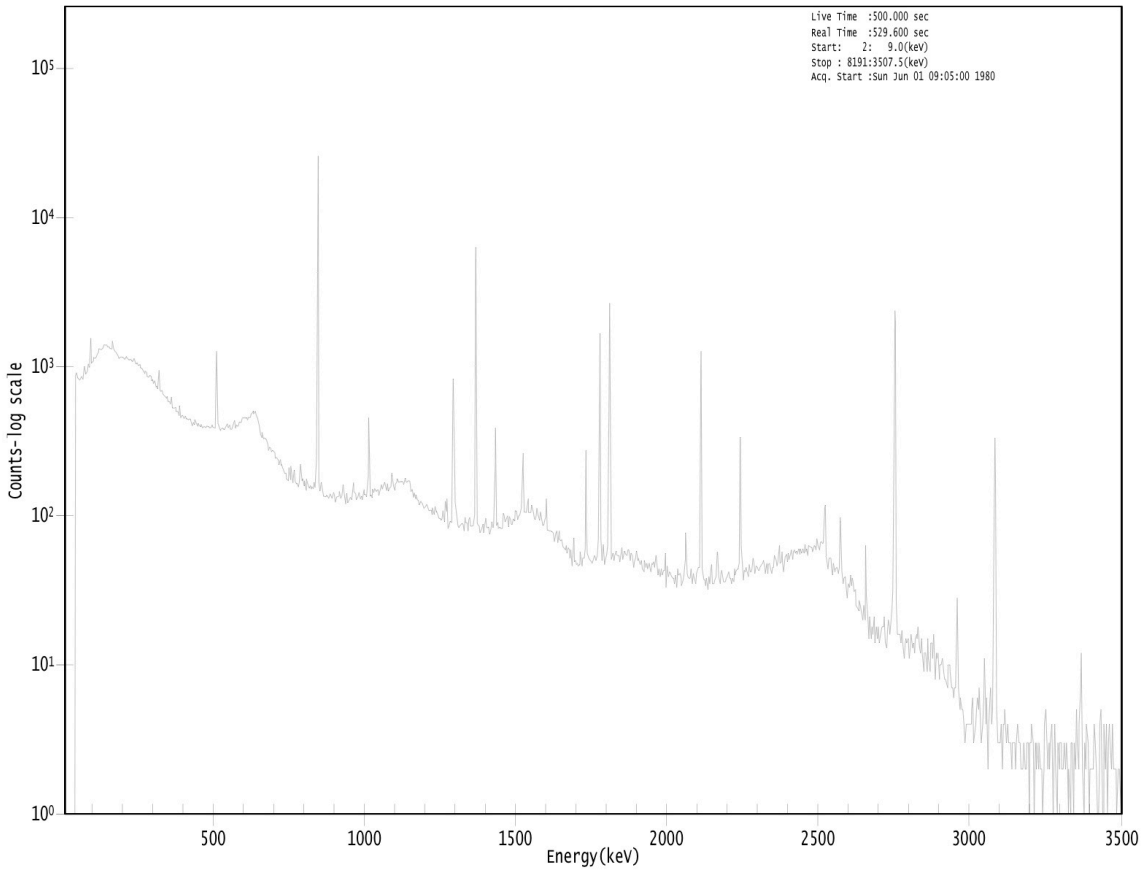

Figure B.6. HPGe gamma ray spectrum for second G1 INAA measurement.

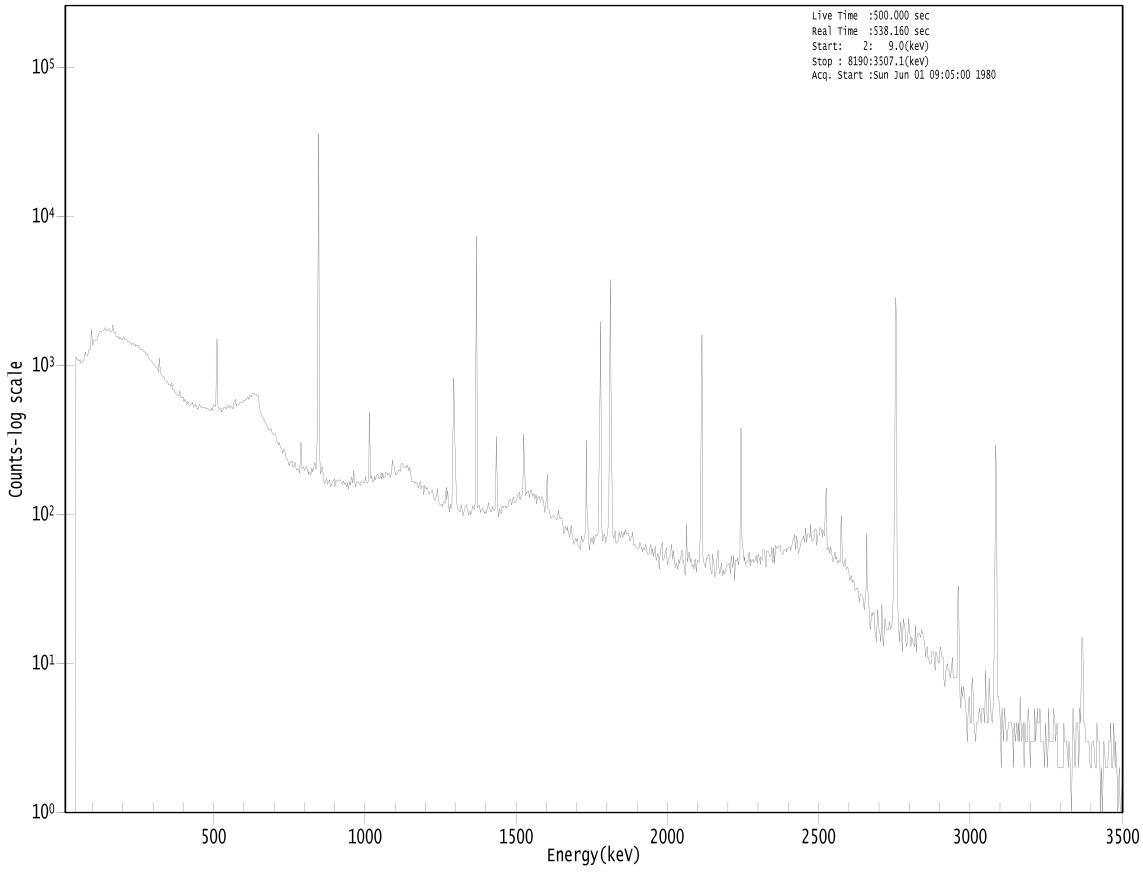

Figure B.7. HPGe gamma ray spectrum for first G2 INAA measurement.

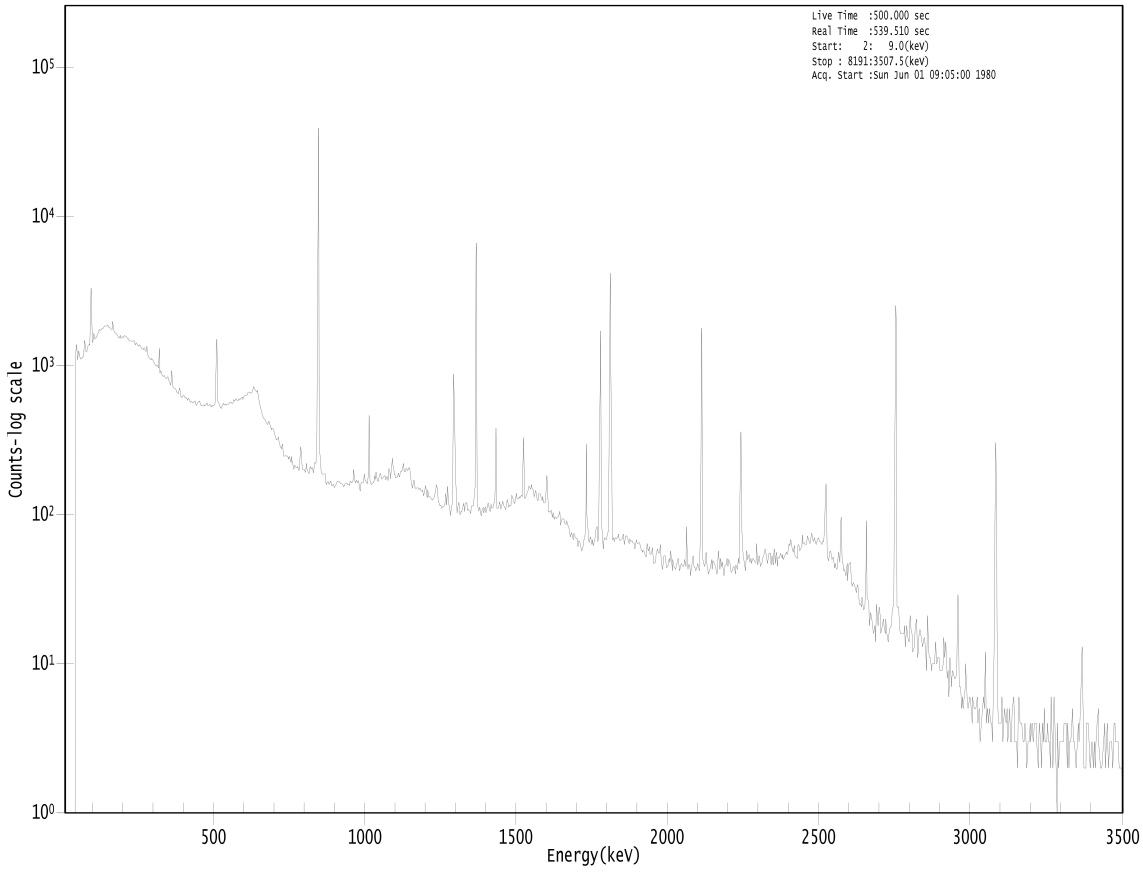

Figure B.8. HPGe gamma ray spectrum for second G2 INAA measurement.

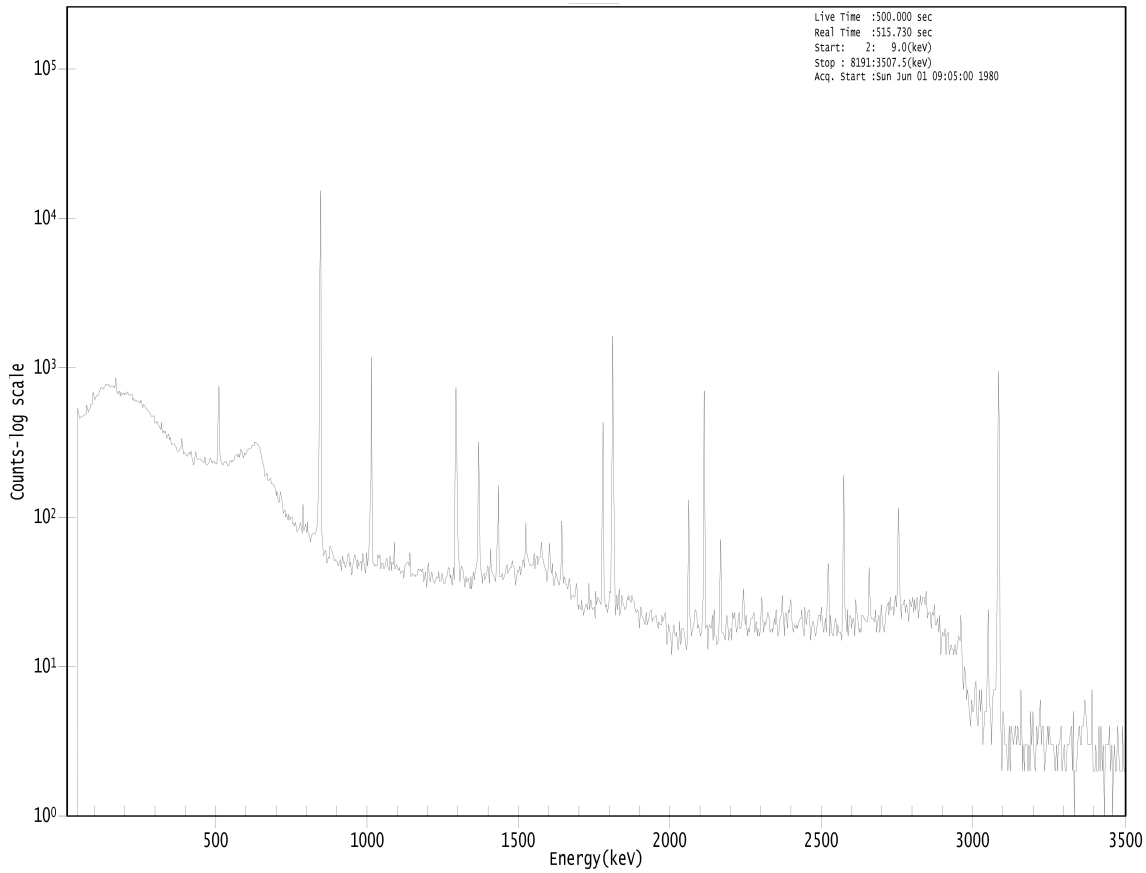

Figure B.9. HPGe gamma ray spectrum for first L1 INAA measurement.

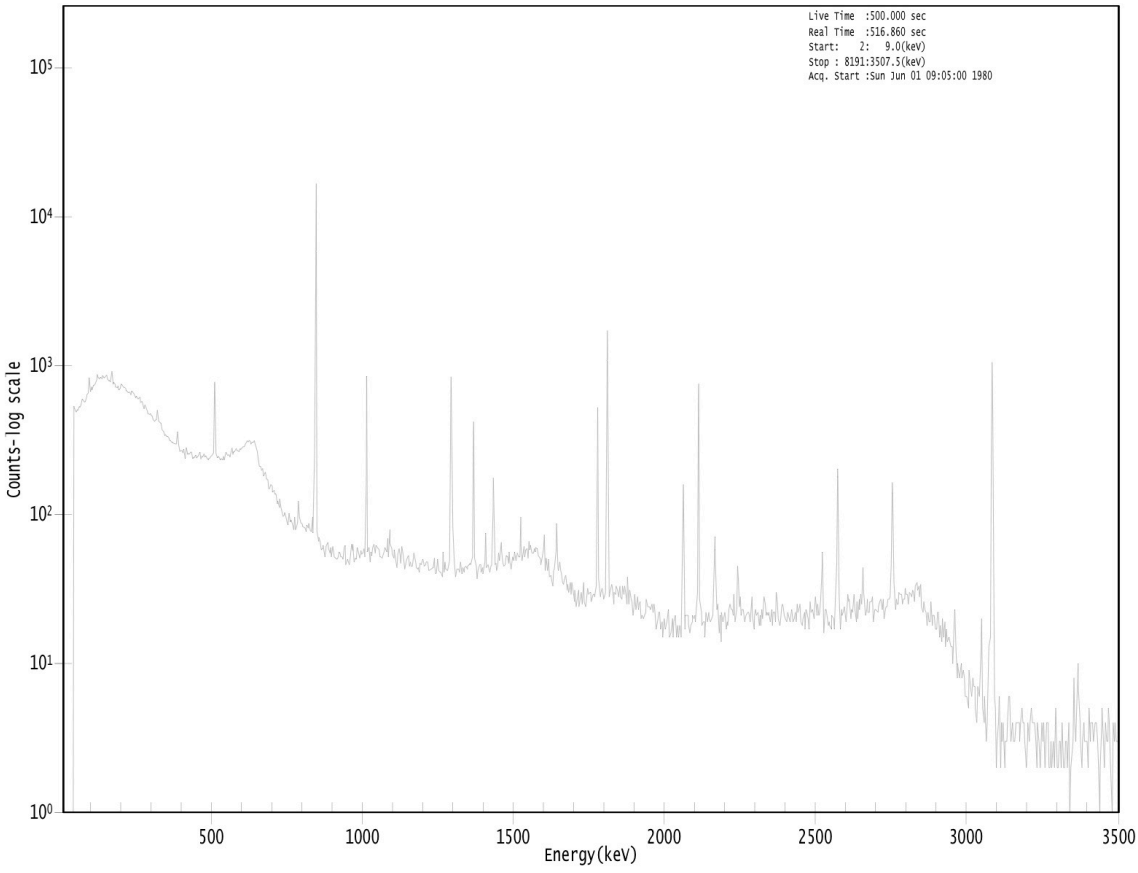

Figure B.10. HPGe gamma ray spectrum for second L1 INAA measurement.

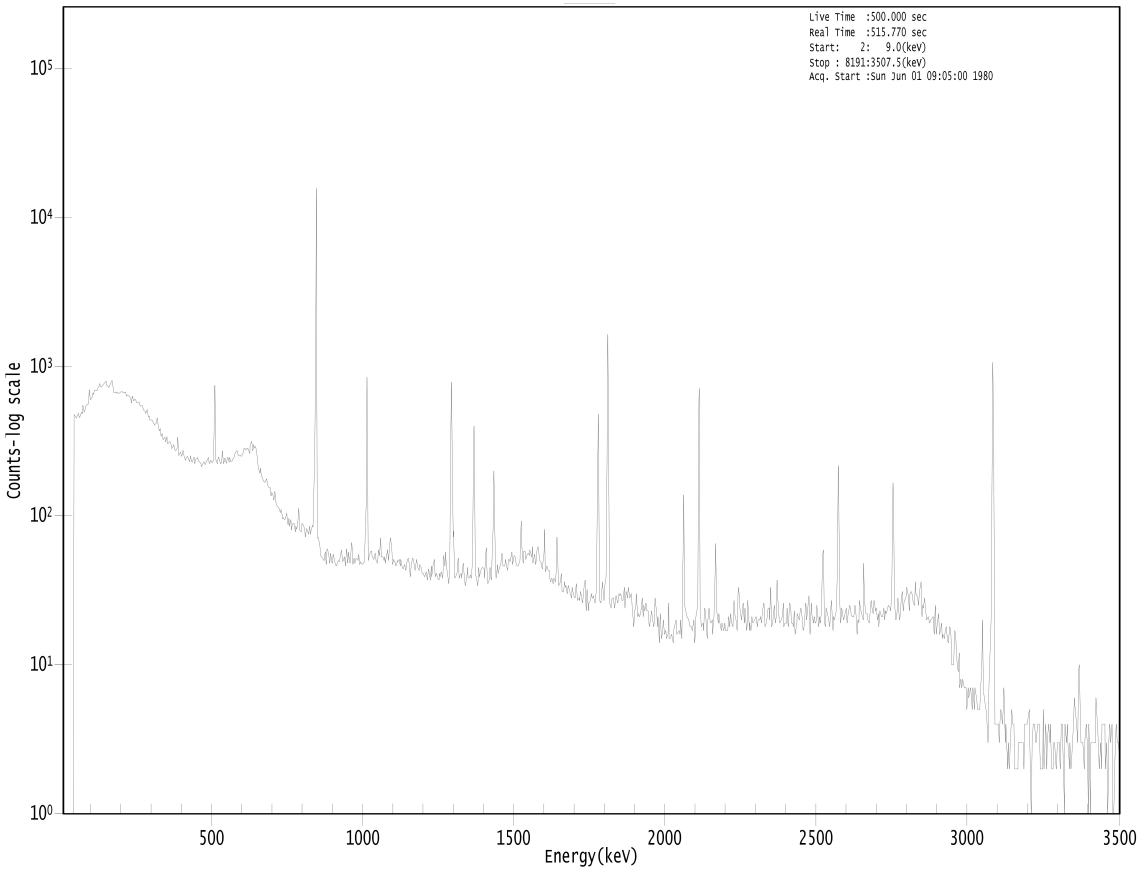

Figure B.11. HPGe gamma ray spectrum for first L2 INAA measurement.

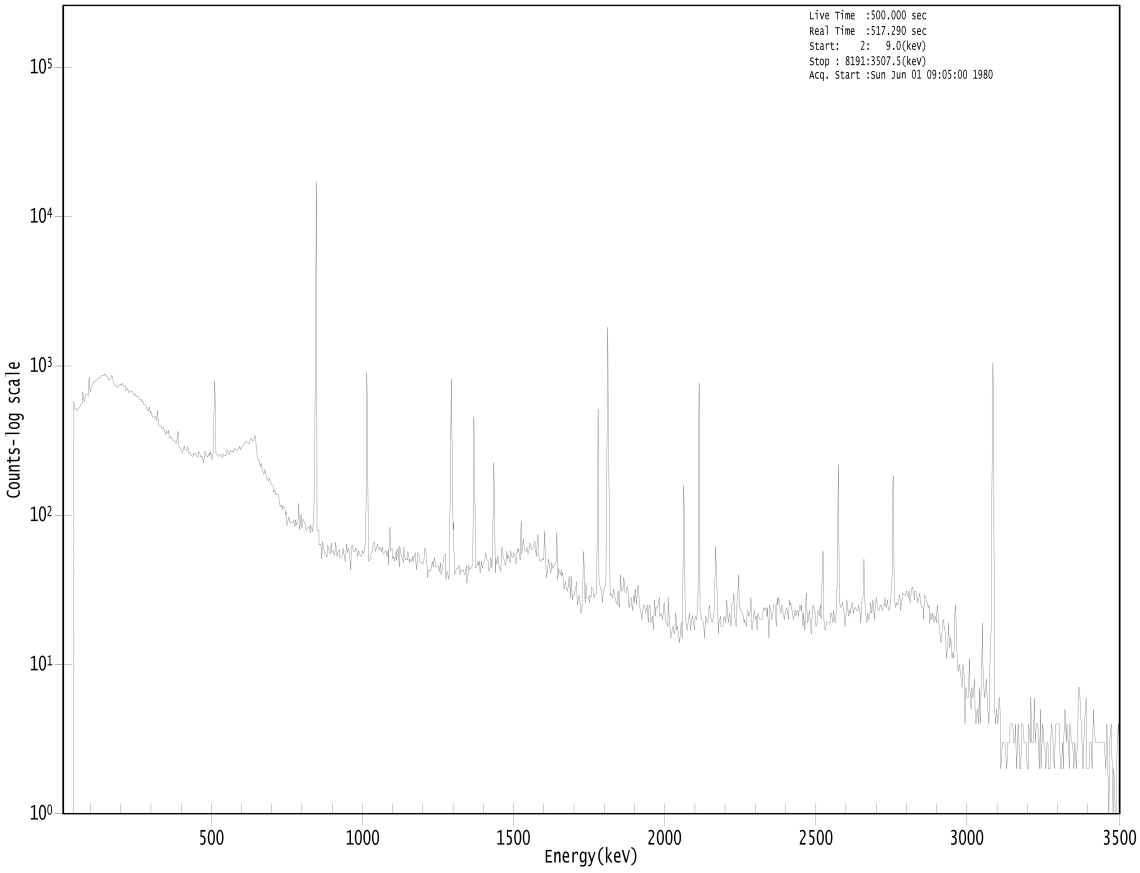

Figure B.12. HPGe gamma ray spectrum for second L2 INAA measurement.

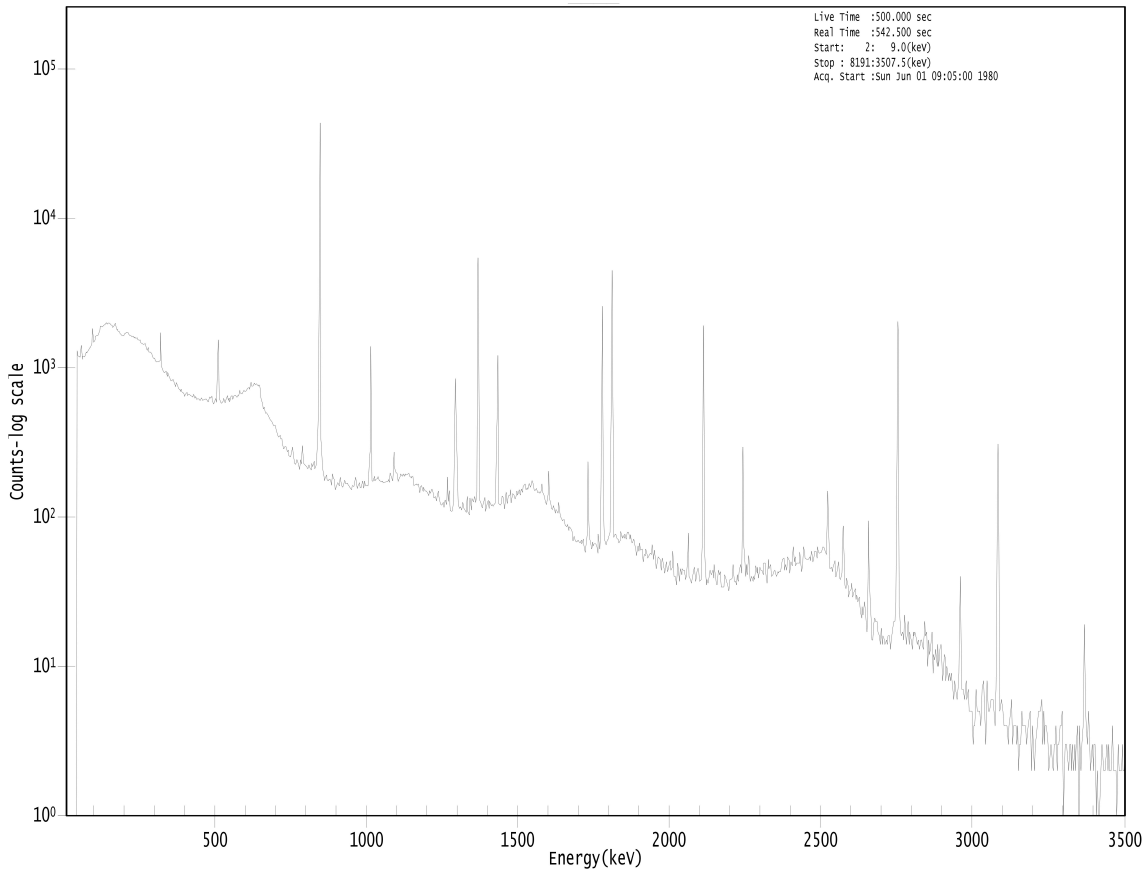

Figure B.13. HPGe gamma ray spectrum for first SRM 688 quality control sample.

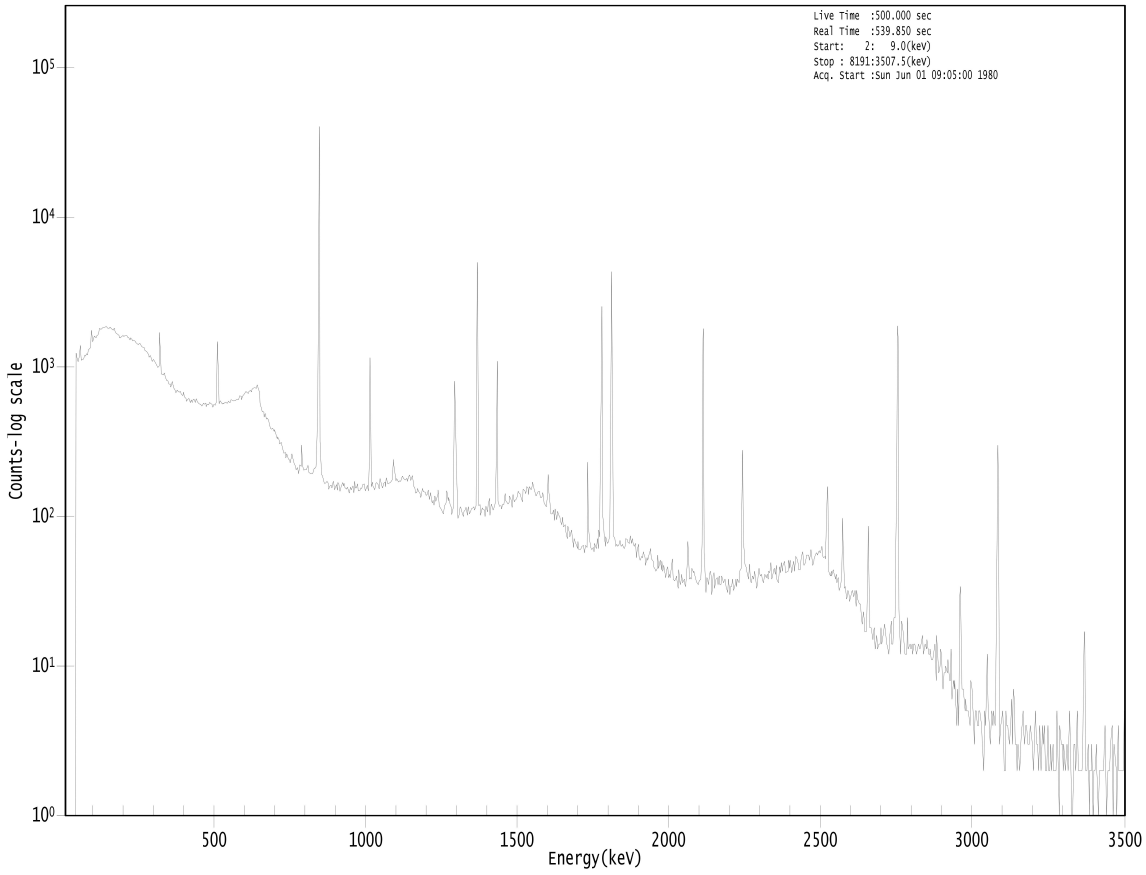

Figure B.14. HPGe gamma ray spectrum for second SRM 688 quality control sample.

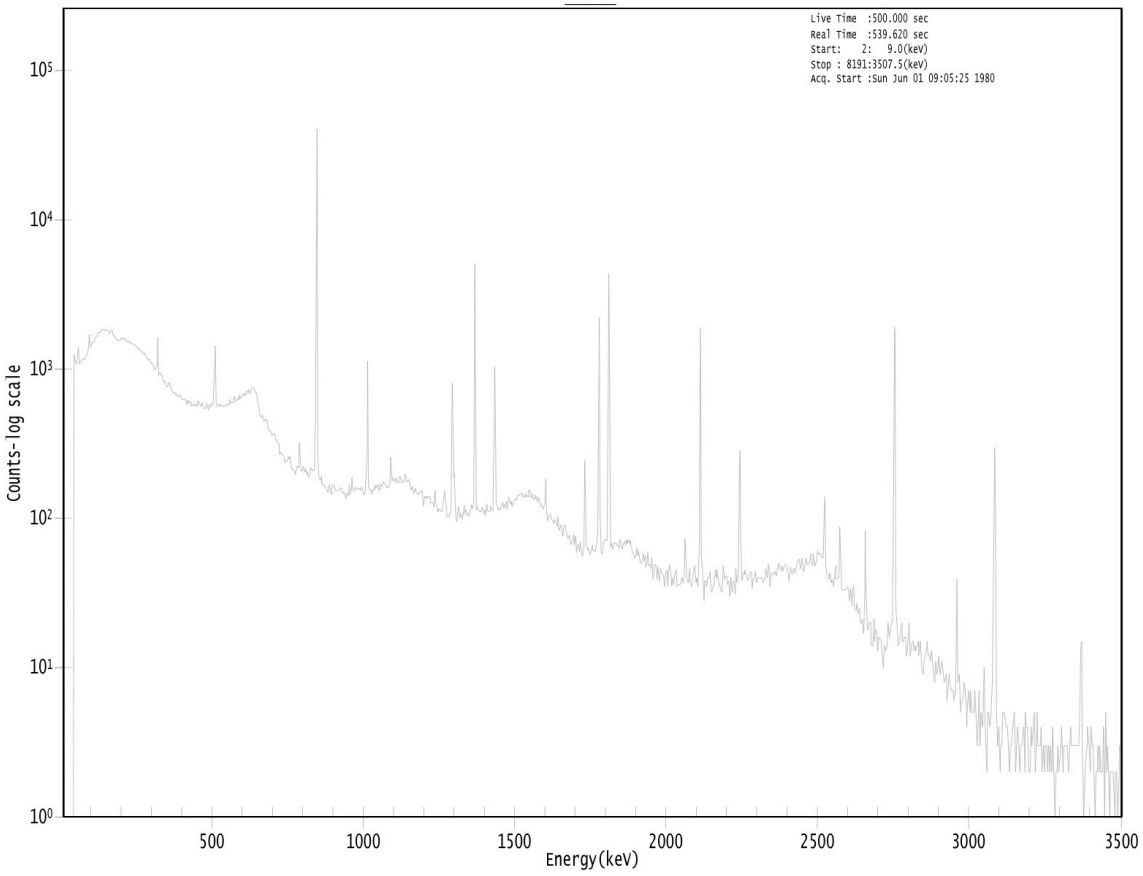

Figure B.15. HPGe gamma ray spectrum for third SRM 688 quality control sample.

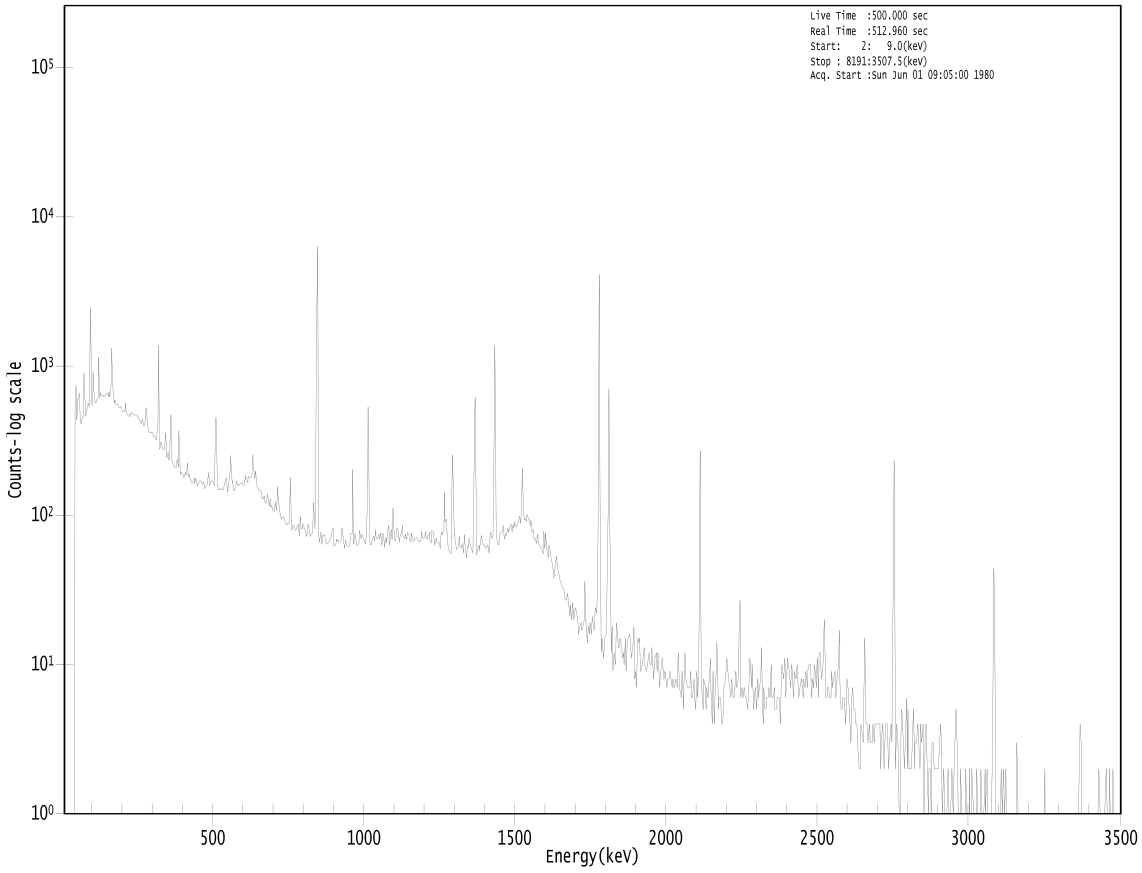

Figure B.16. HPGe gamma ray spectrum for first SRM 1633a comparator standard.

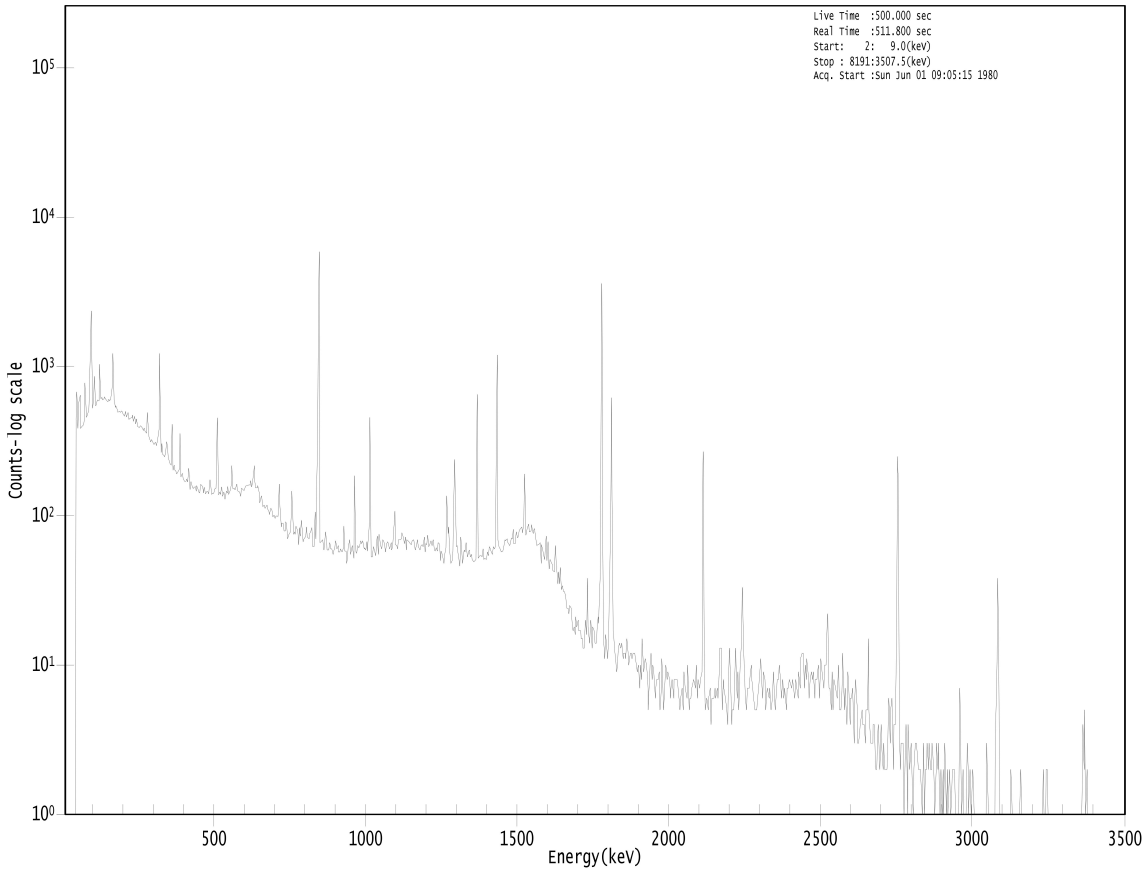

Figure B.17. HPGe gamma ray spectrum for second SRM 1633a comparator standard.

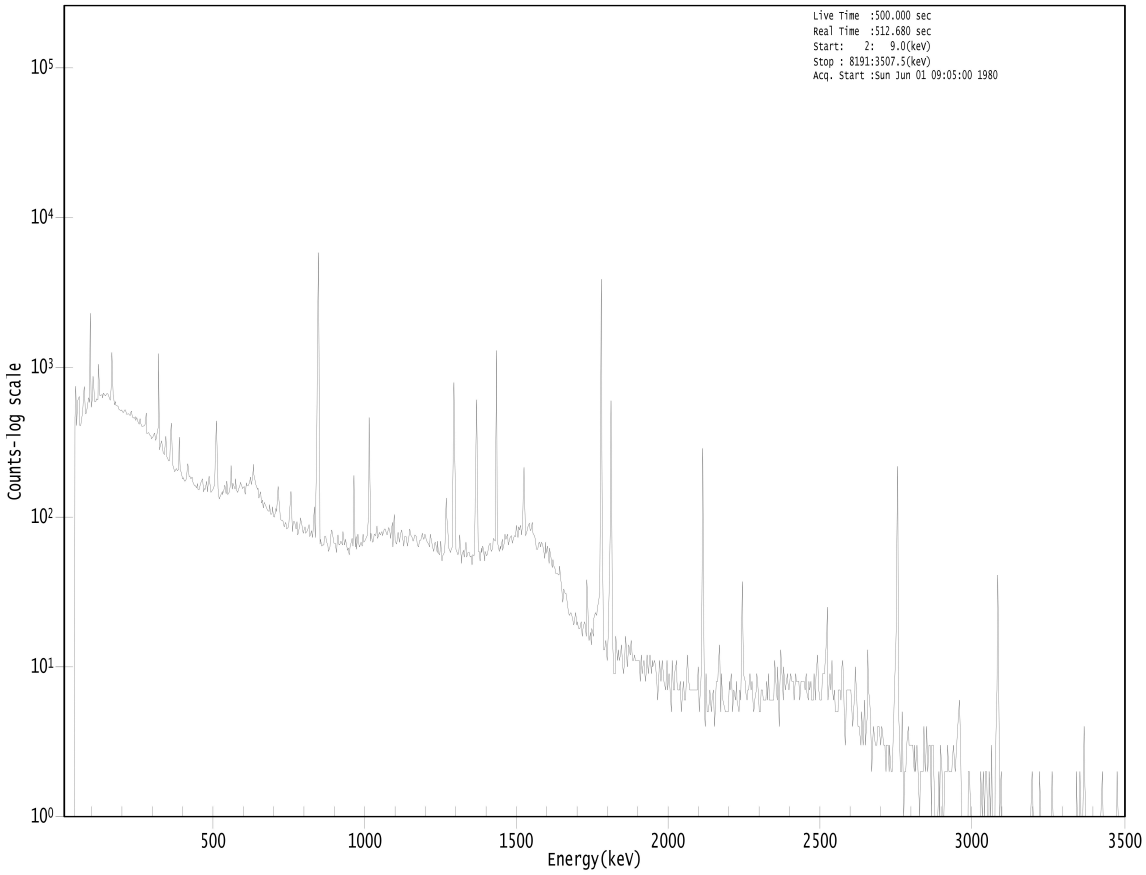

Figure B.18. HPGe gamma ray spectrum for third SRM 1633a comparator standard.

HPGe gamma ray spectra for intermediate half-life INAA measurements

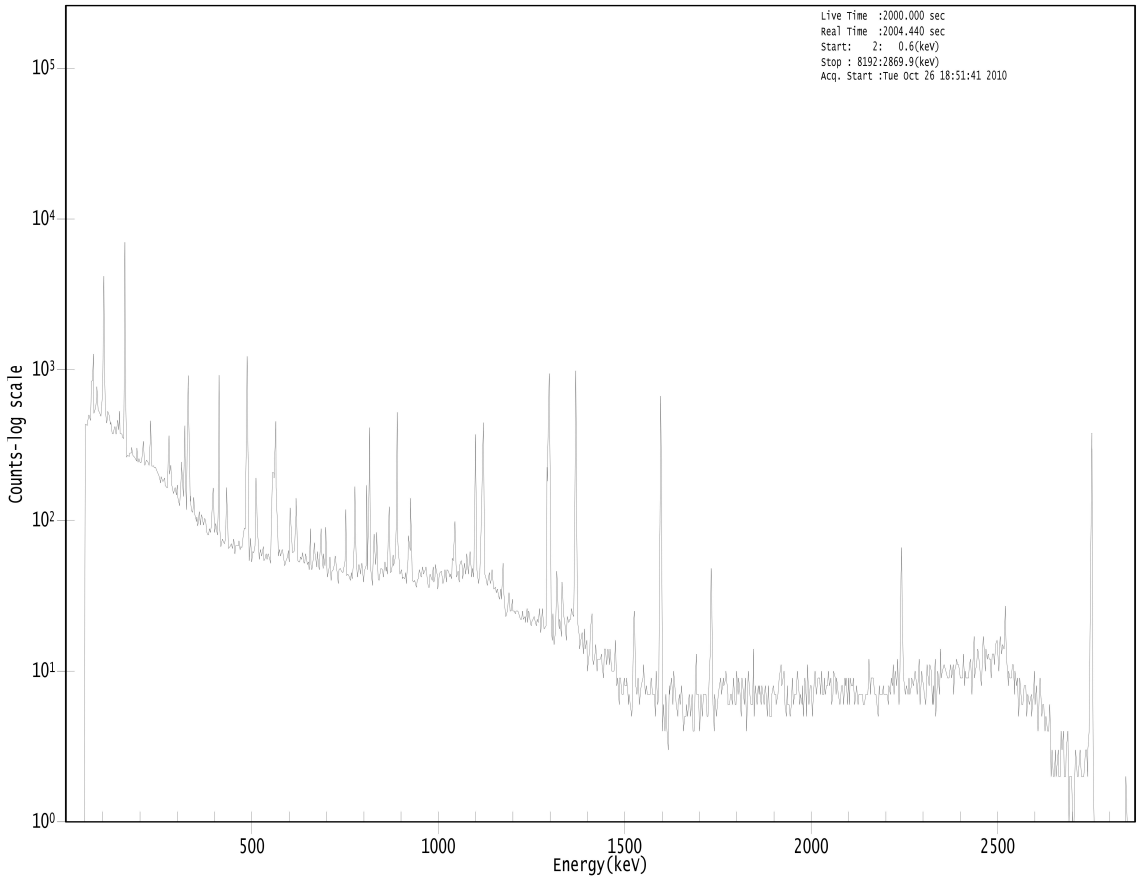

Figure B.19. HPGe gamma ray spectrum for first F1 INAA measurement.

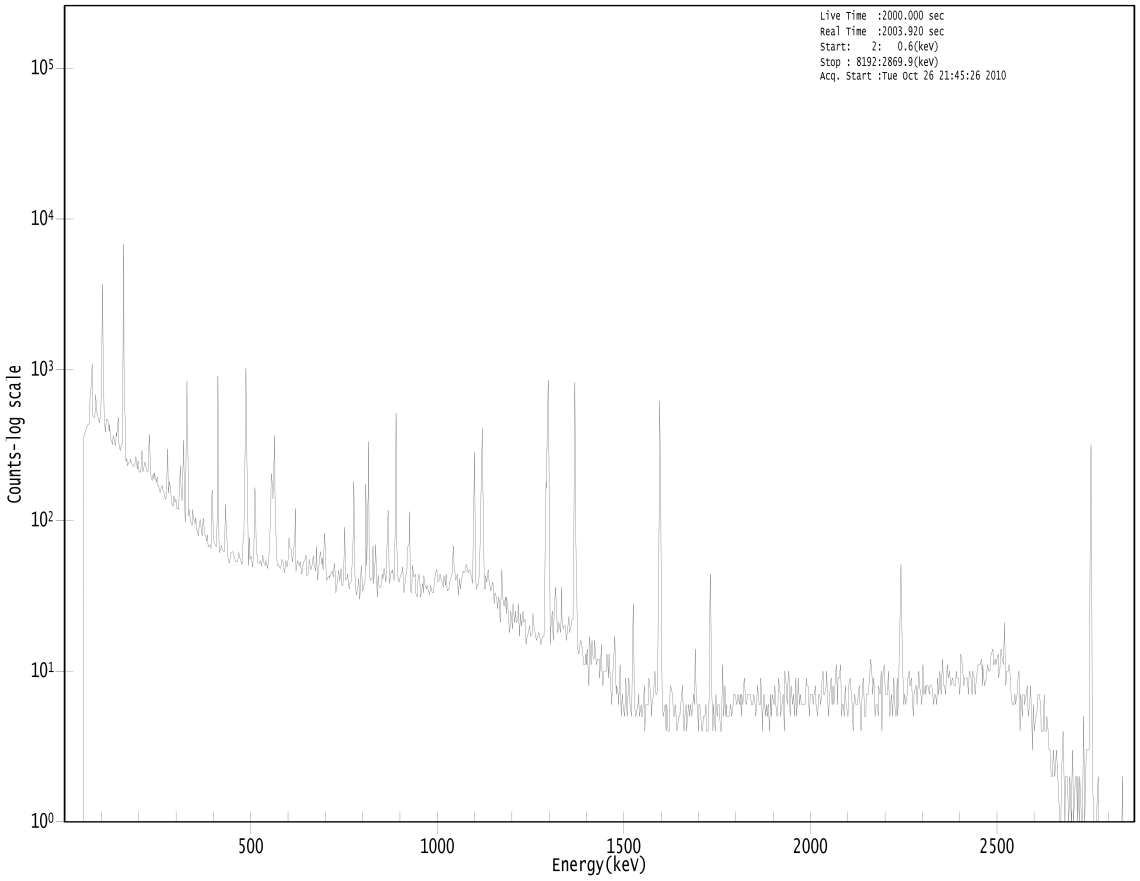

Figure B.20. HPGe gamma ray spectrum for second F1 INAA measurement.

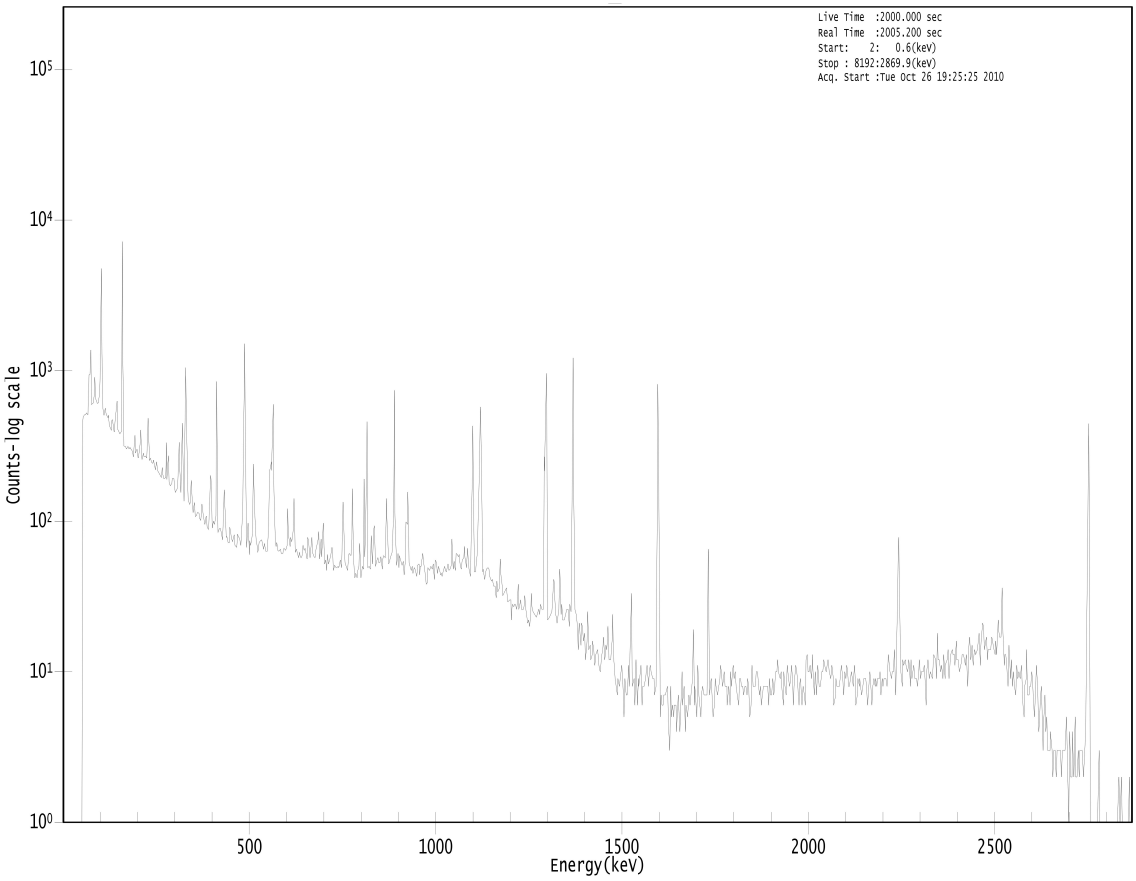

Figure B.21. HPGe gamma ray spectrum for F2 INAA measurement.

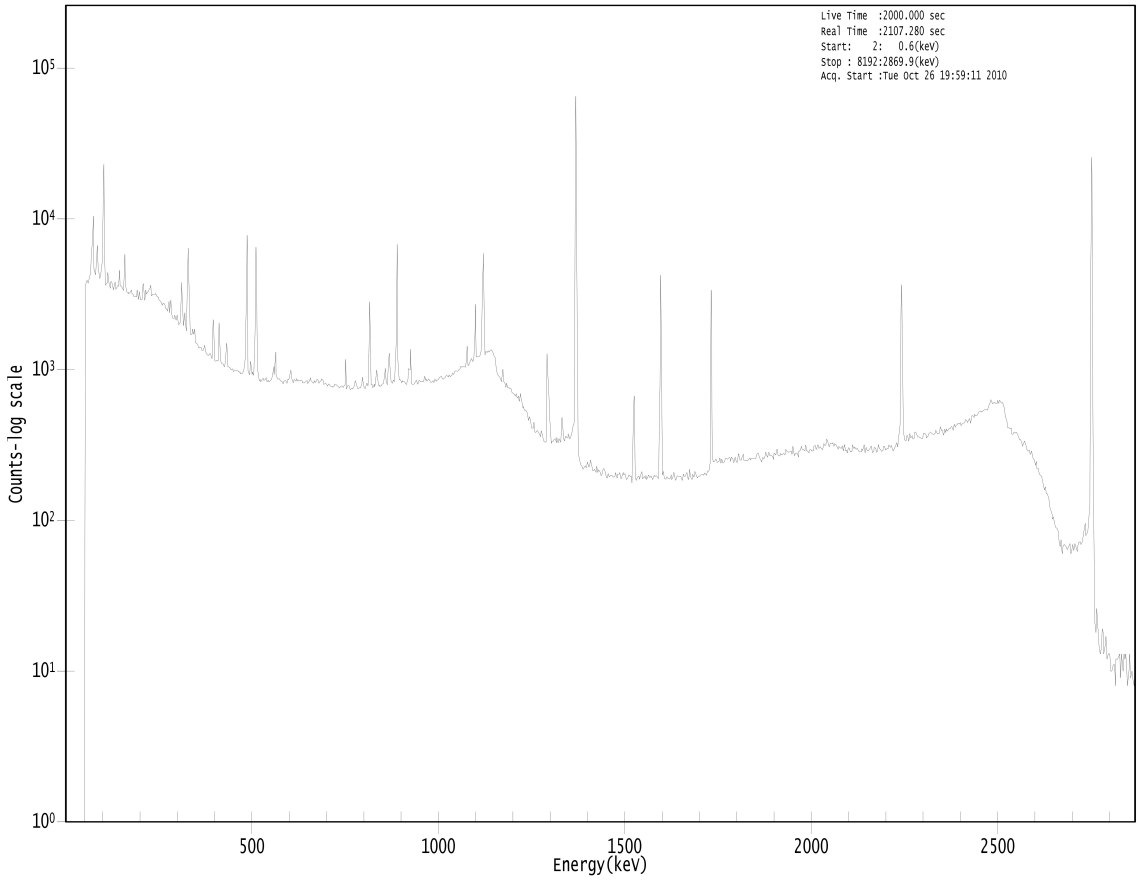

Figure B.22. HPGe gamma ray spectrum for G1 INAA measurement.

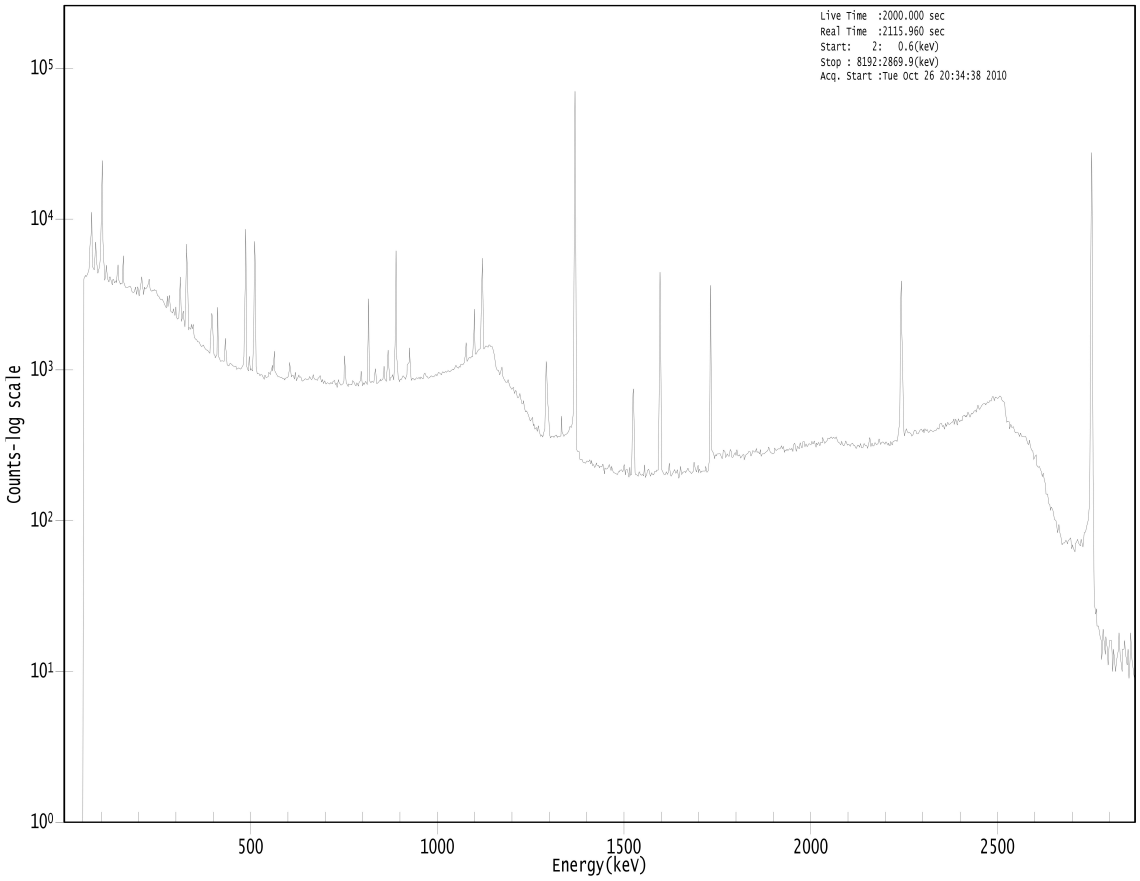

Figure B.23. HPGe gamma ray spectrum for first G2 INAA measurement.

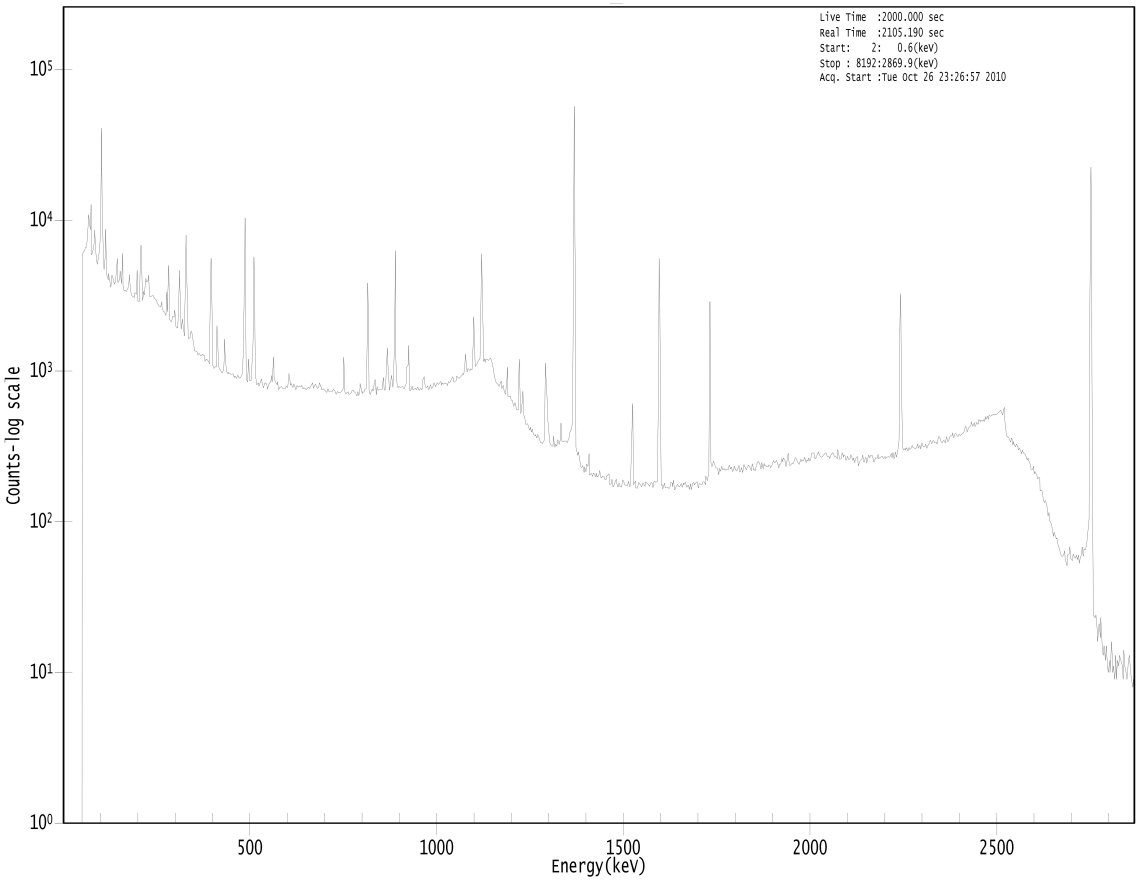

Figure B.24. HPGe gamma ray spectrum for second G2 INAA measurement.

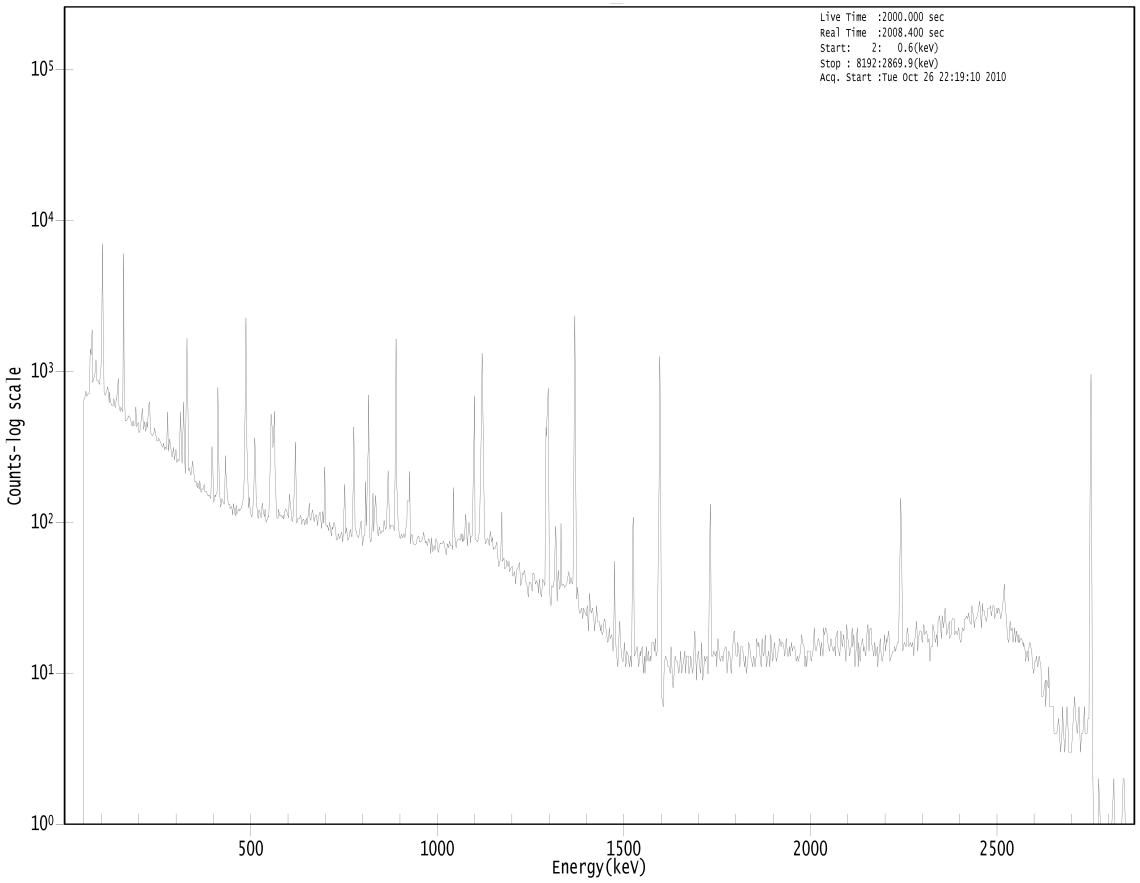

Figure B.25. HPGe gamma ray spectrum for L1 INAA measurement.

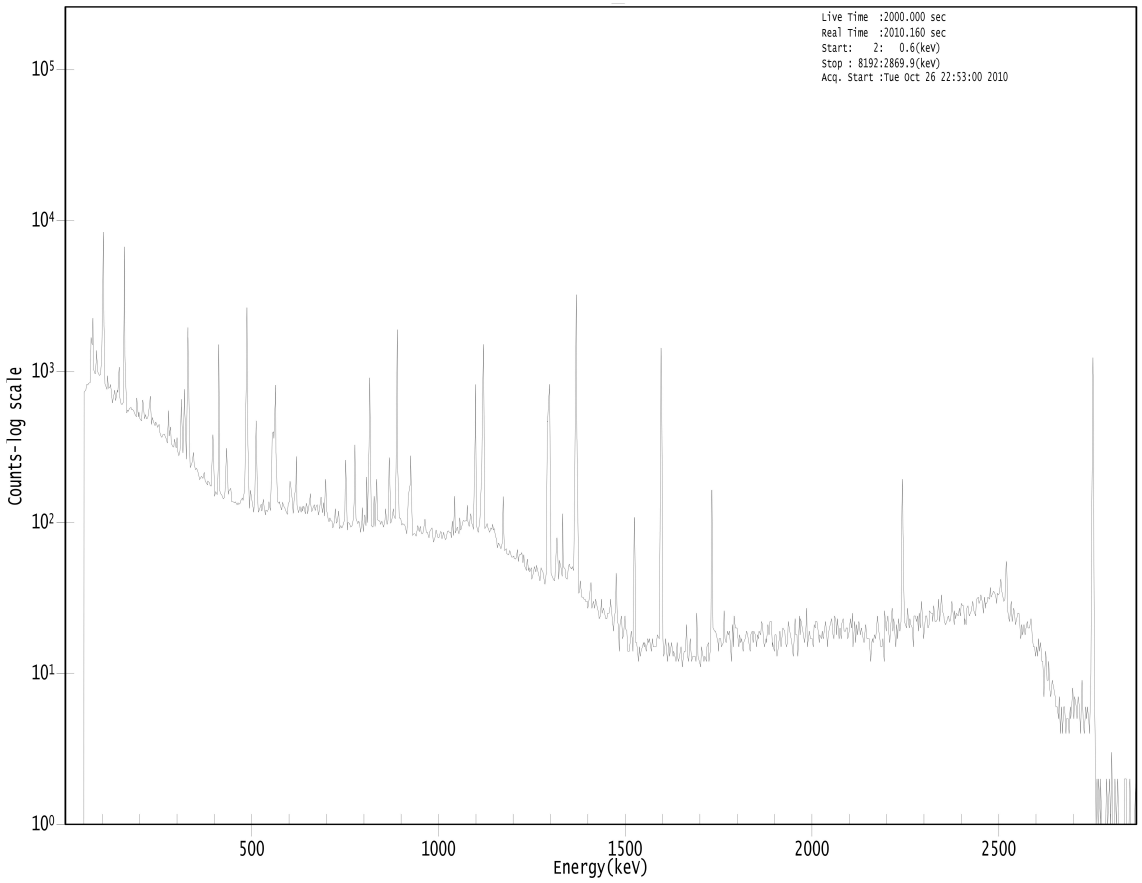

Figure B.26. HPGe gamma ray spectrum for L2 INAA measurement.

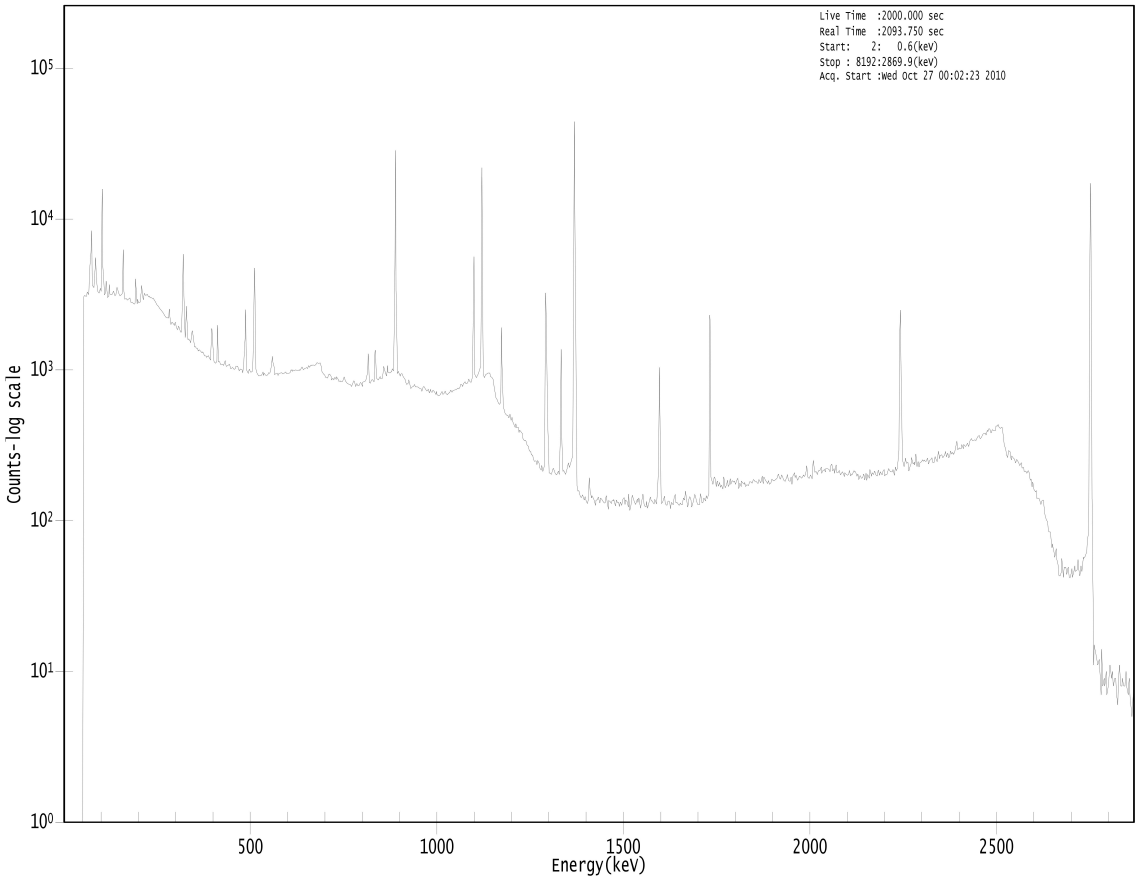

Figure B.27. HPGe gamma ray spectrum for SRM 688 quality control sample.

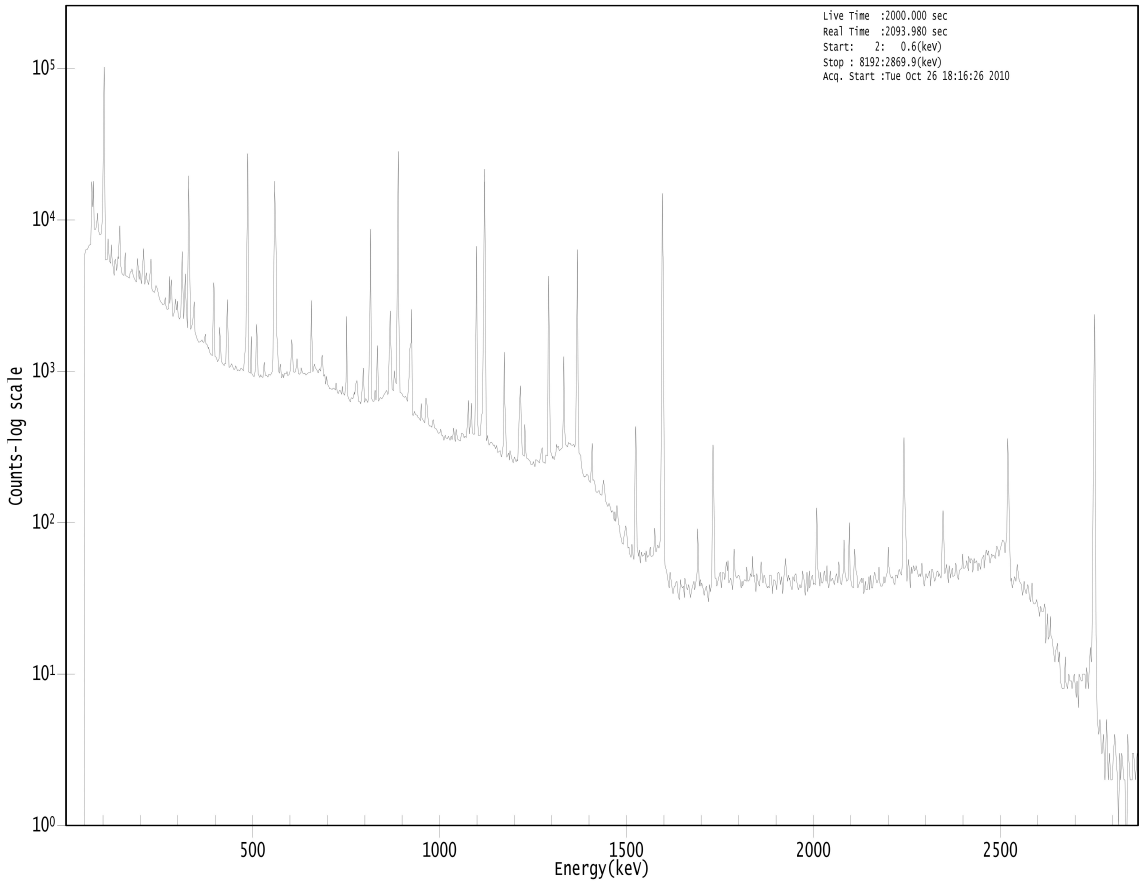

Figure B.28. HPGe gamma ray spectrum for first SRM 1633a comparator standard.

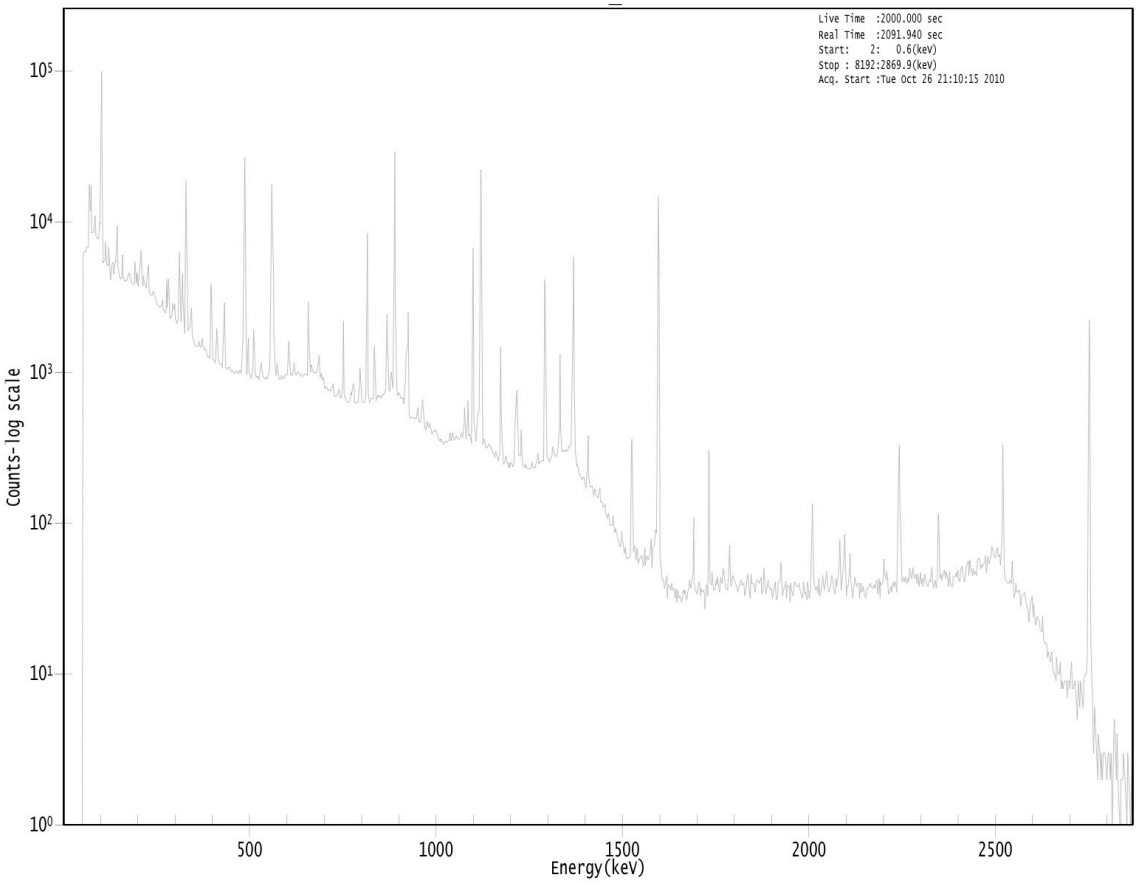

Figure B.29. HPGe gamma ray spectrum for second SRM 1633a comparator standard.

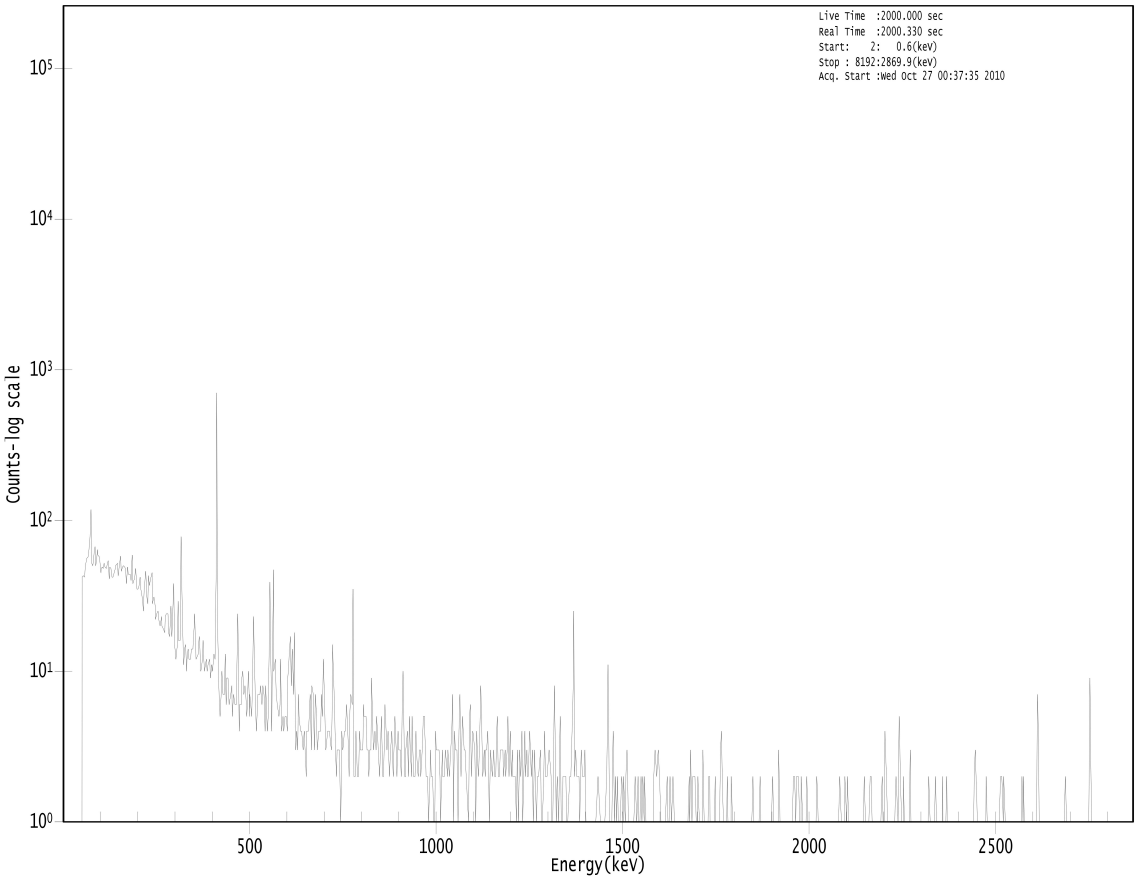

Figure B.30. HPGe gamma ray spectrum for blank vial.

HPGe gamma ray spectra for long half-life INAA measurements

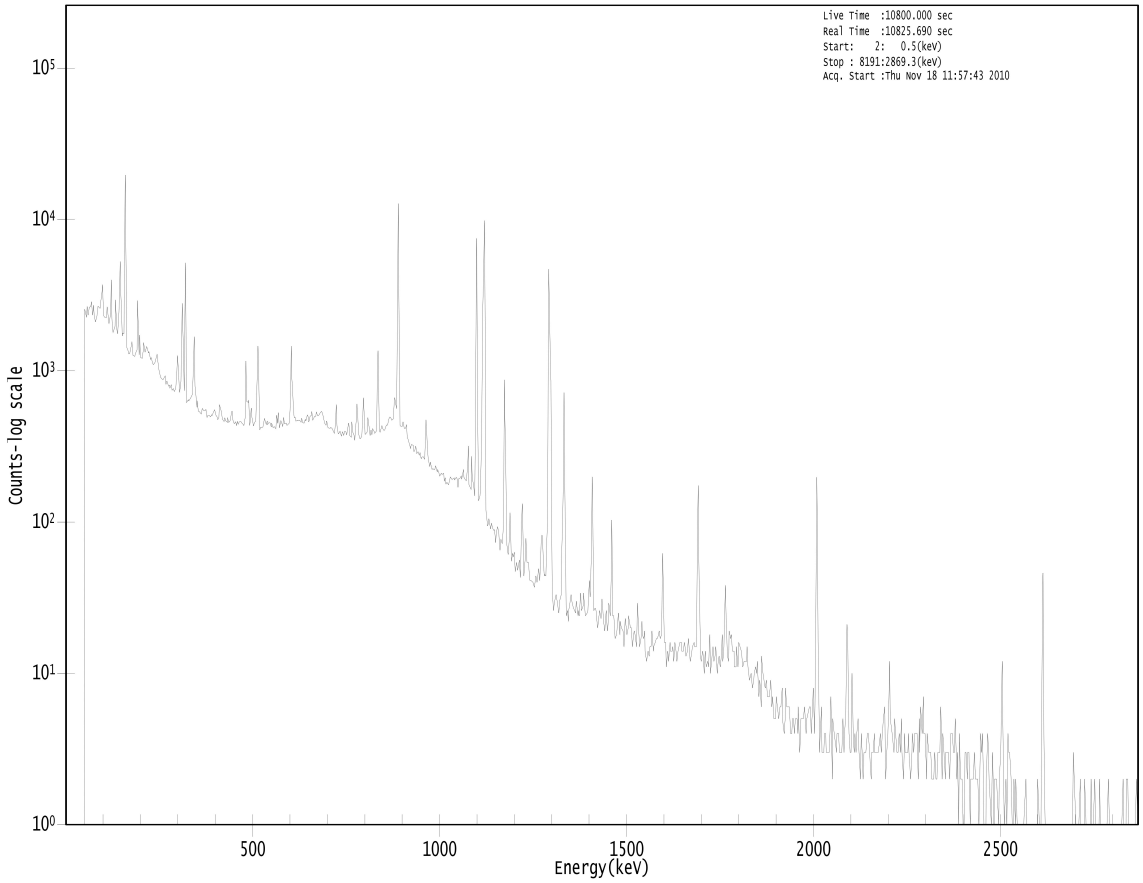

Figure B.31. HPGe gamma ray spectrum for first F1 INAA measurement.

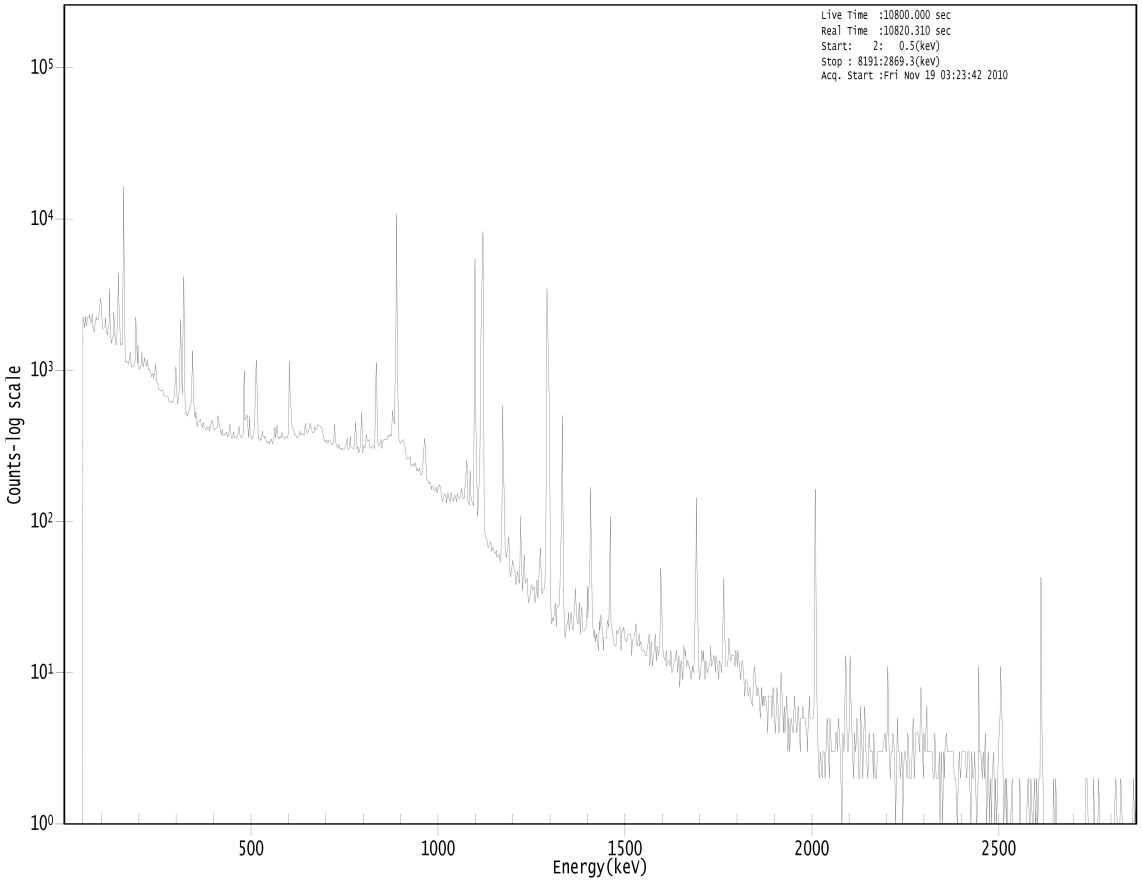

Figure B.32. HPGe gamma ray spectrum for second F1 INAA measurement.

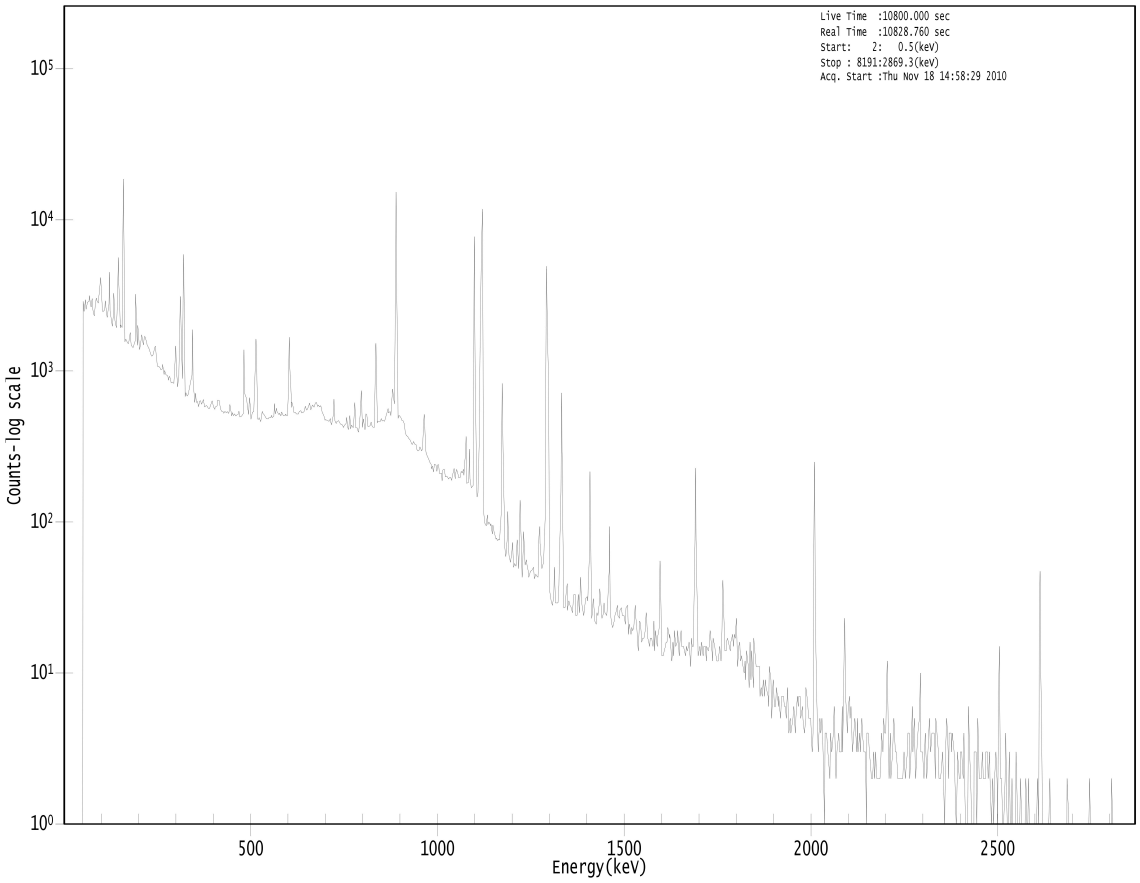

Figure B.33. HPGe gamma ray spectrum for F2 INAA measurement.

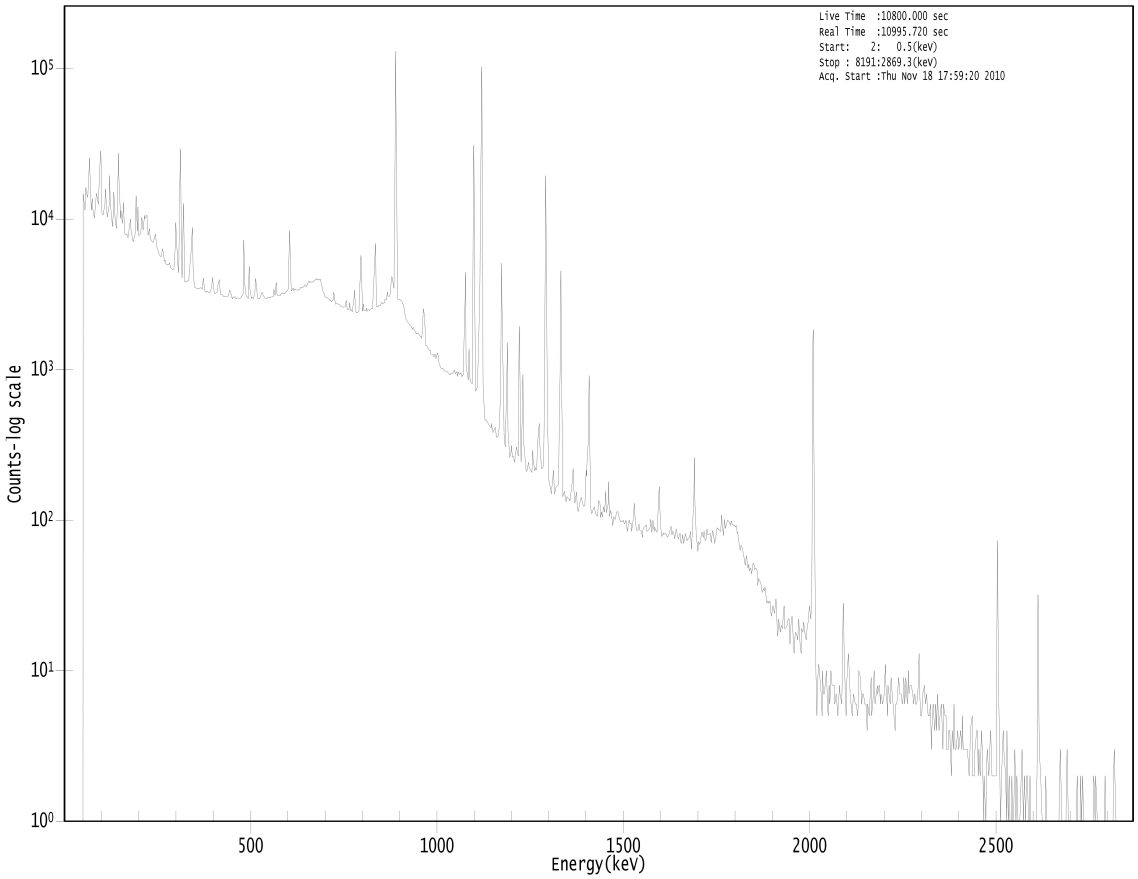

Figure B.34. HPGe gamma ray spectrum for G1 INAA measurement.

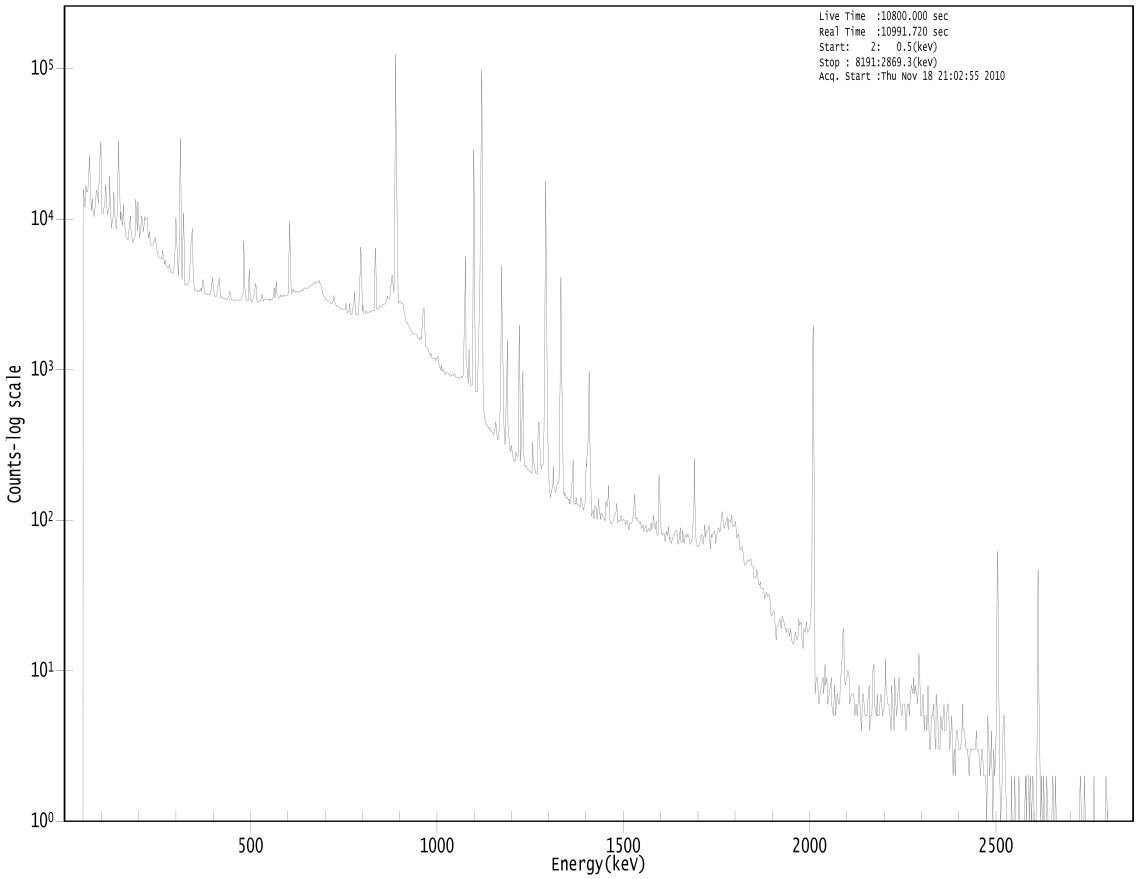

Figure B.35. HPGe gamma ray spectrum for first G2 INAA measurement.

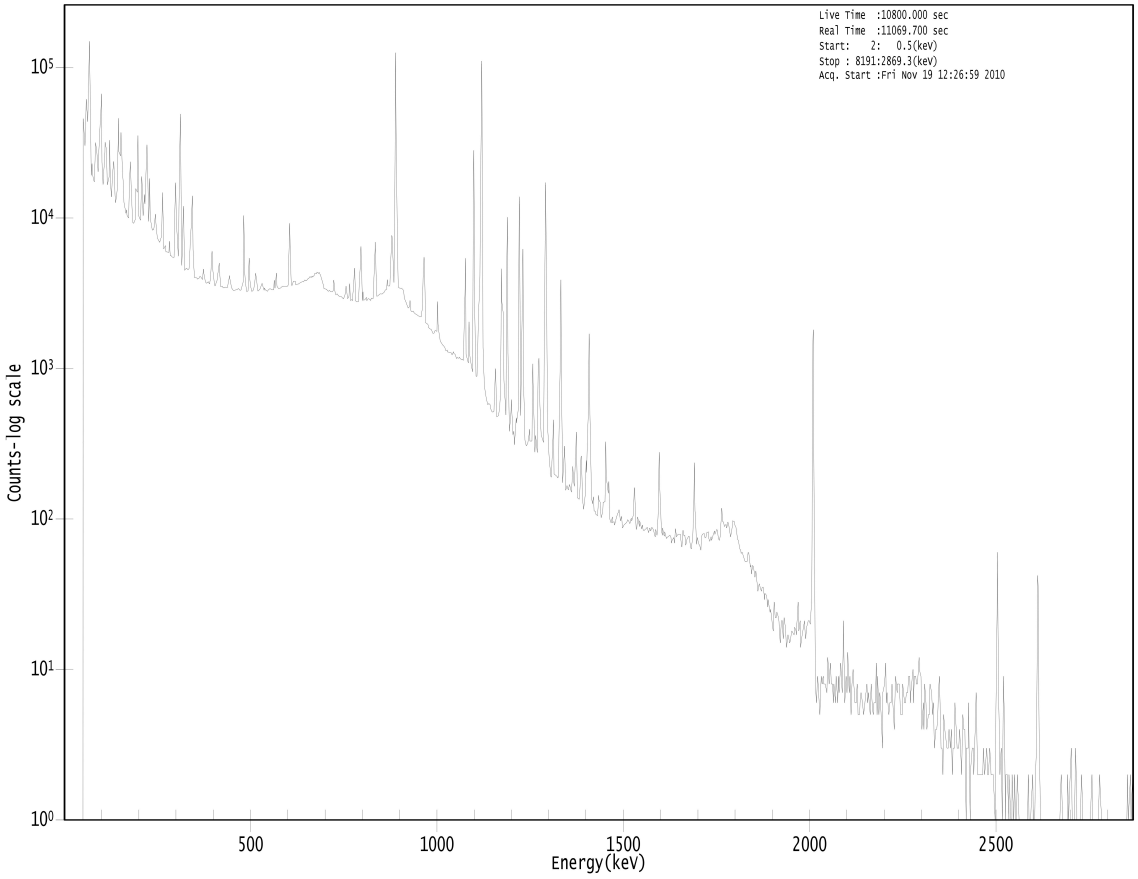

Figure B.36. HPGe gamma ray spectrum for second G2 INAA measurement.

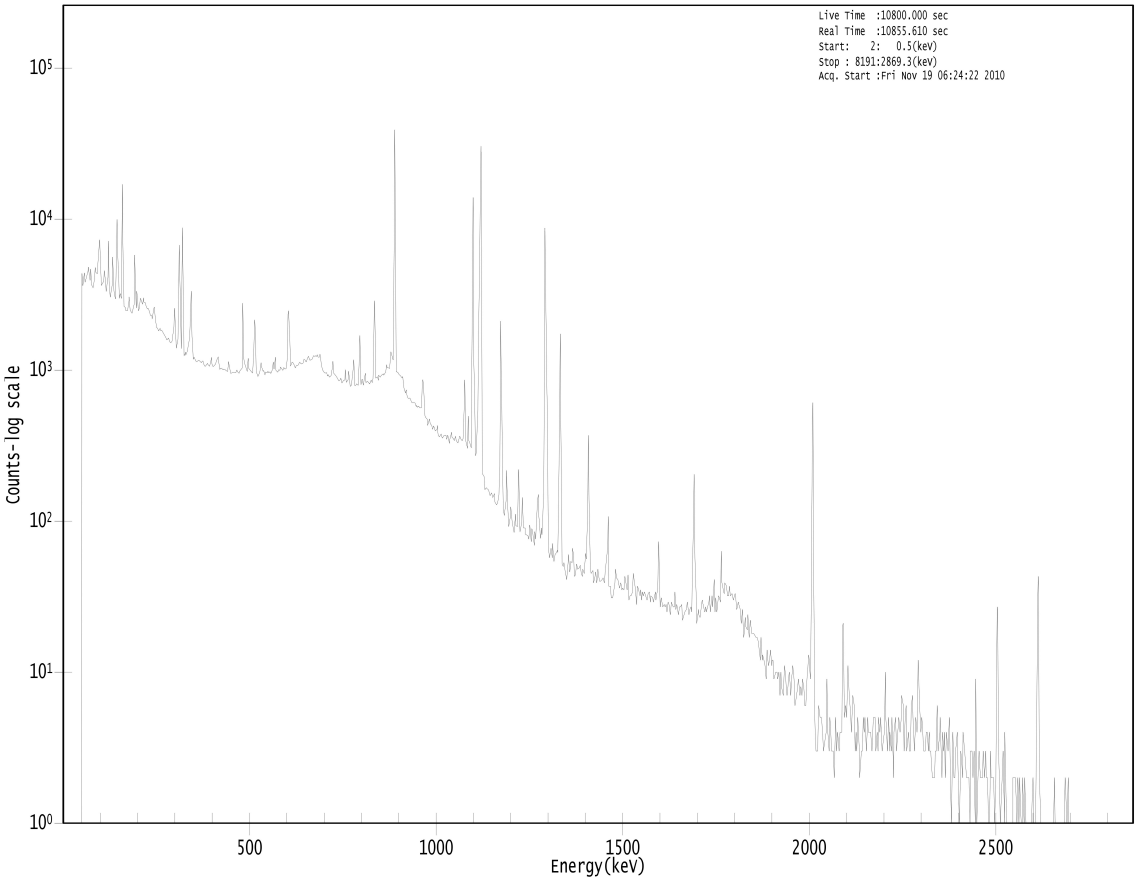

Figure B.37. HPGe gamma ray spectrum for L1 INAA measurement.

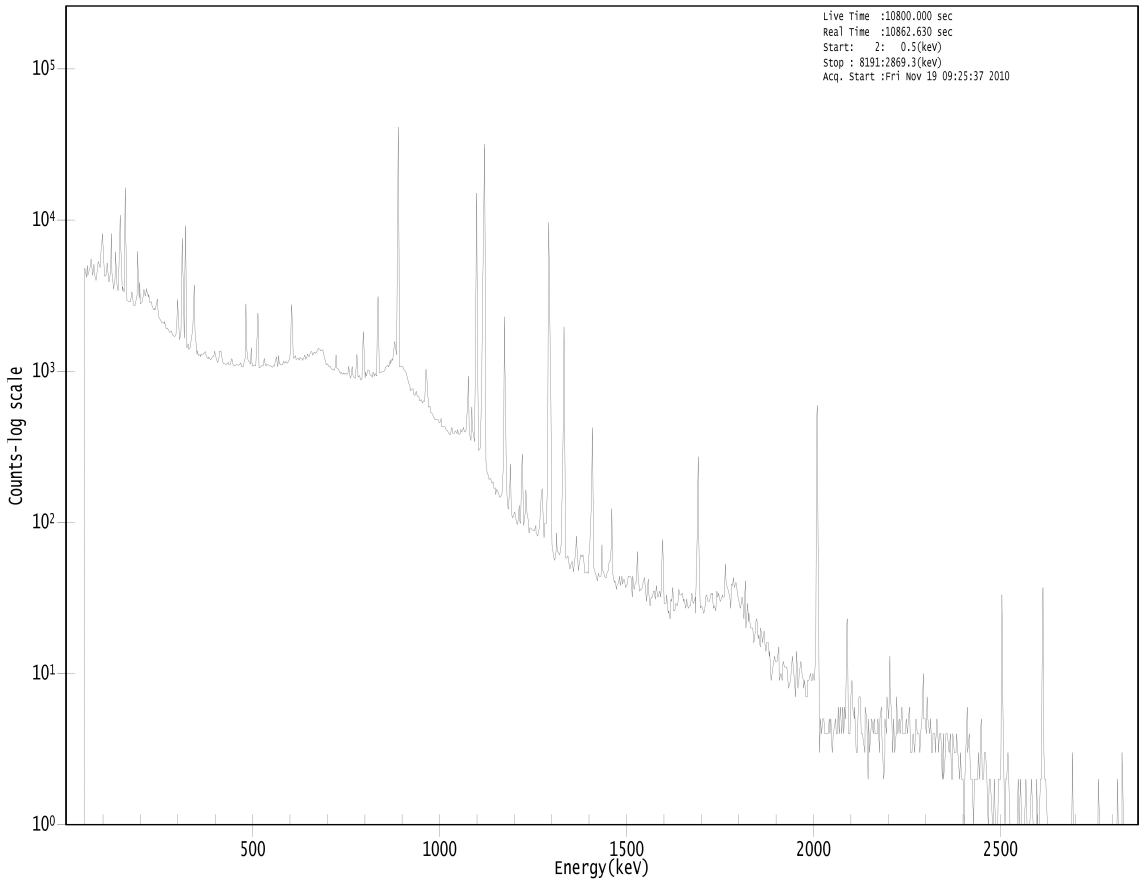

Figure B.38. HPGe gamma ray spectrum for L2 INAA measurement.

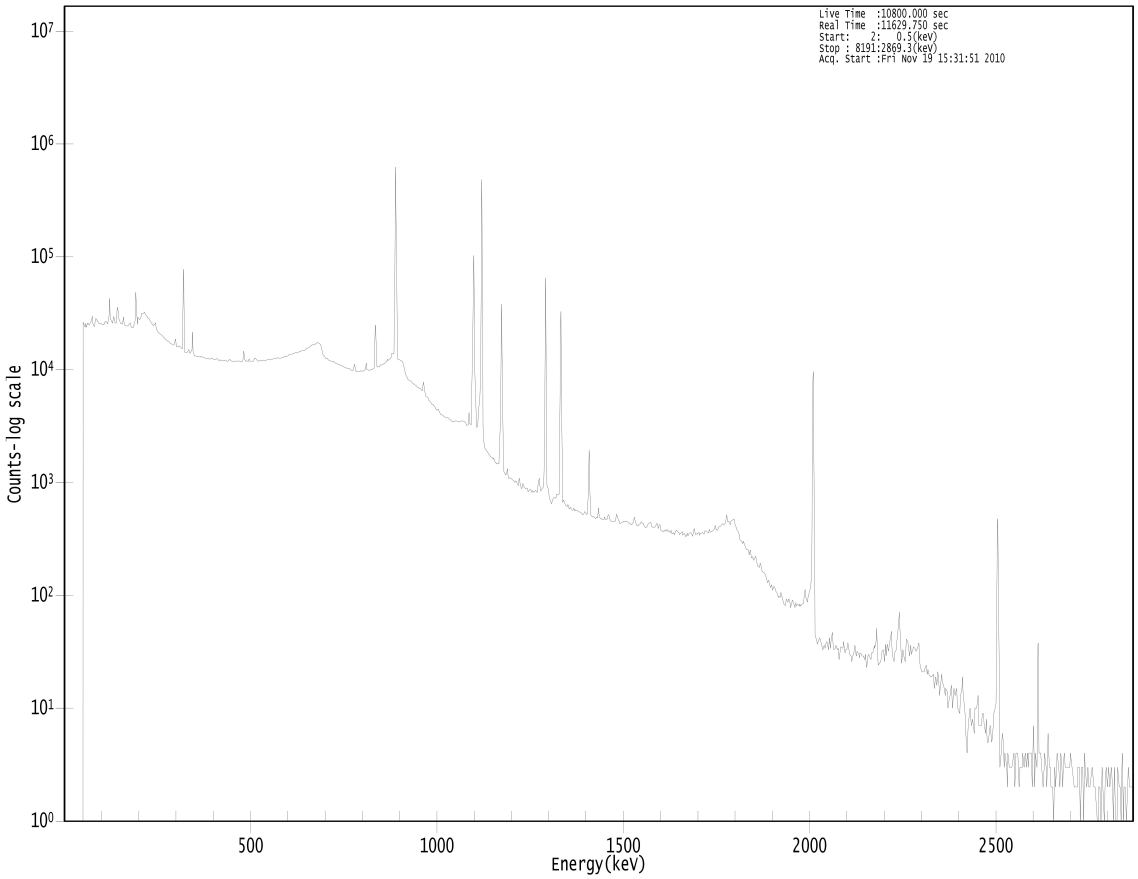

Figure B.39. HPGe gamma ray spectrum for SRM 688 quality control sample.

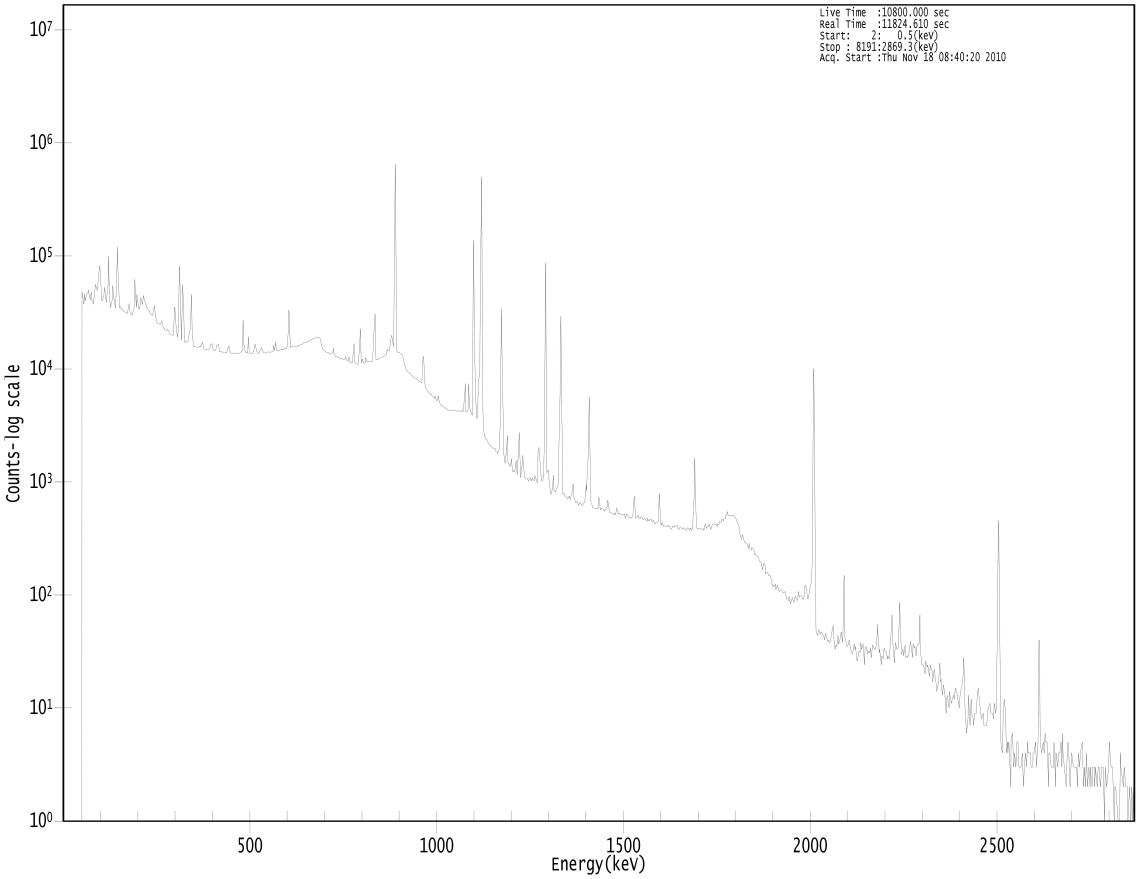

Figure B.40. HPGe gamma ray spectrum for first SRM 1633a comparator standard.

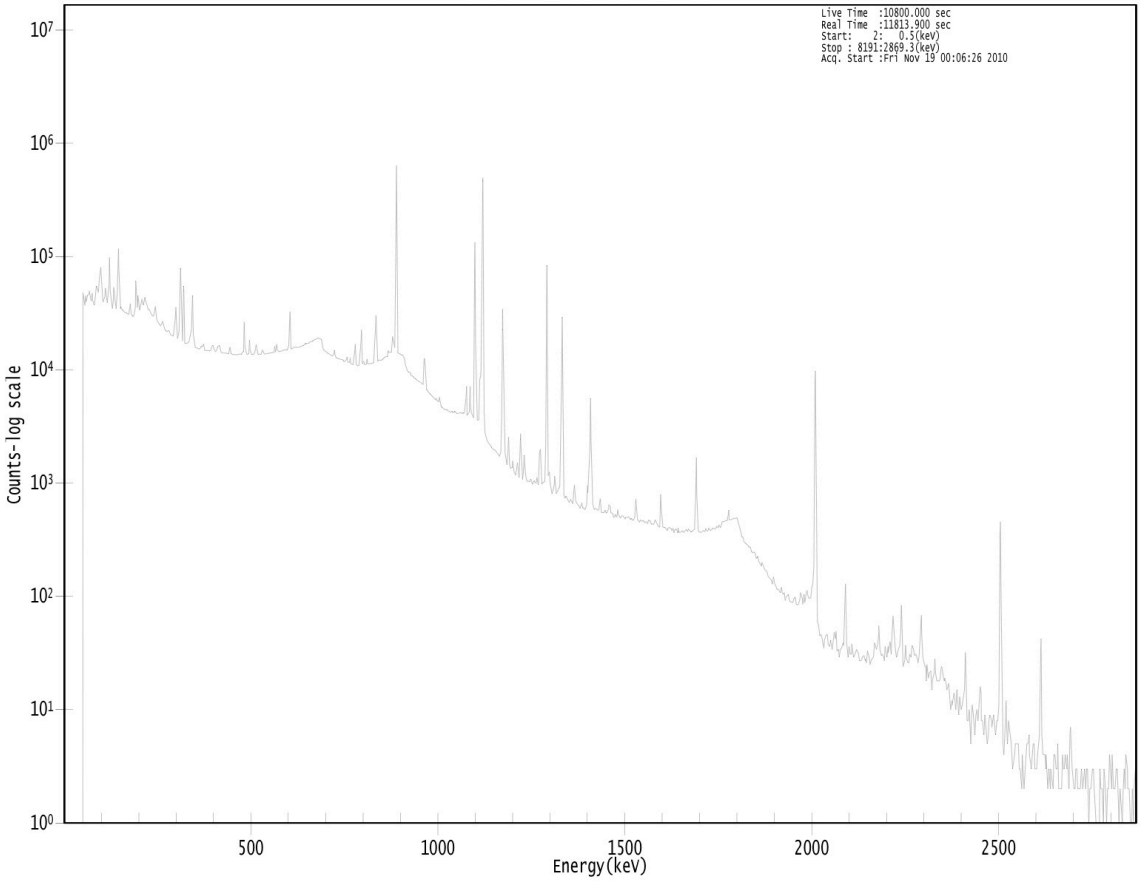

Figure B.41. HPGe gamma ray spectrum for second SRM 1633a comparator standard.

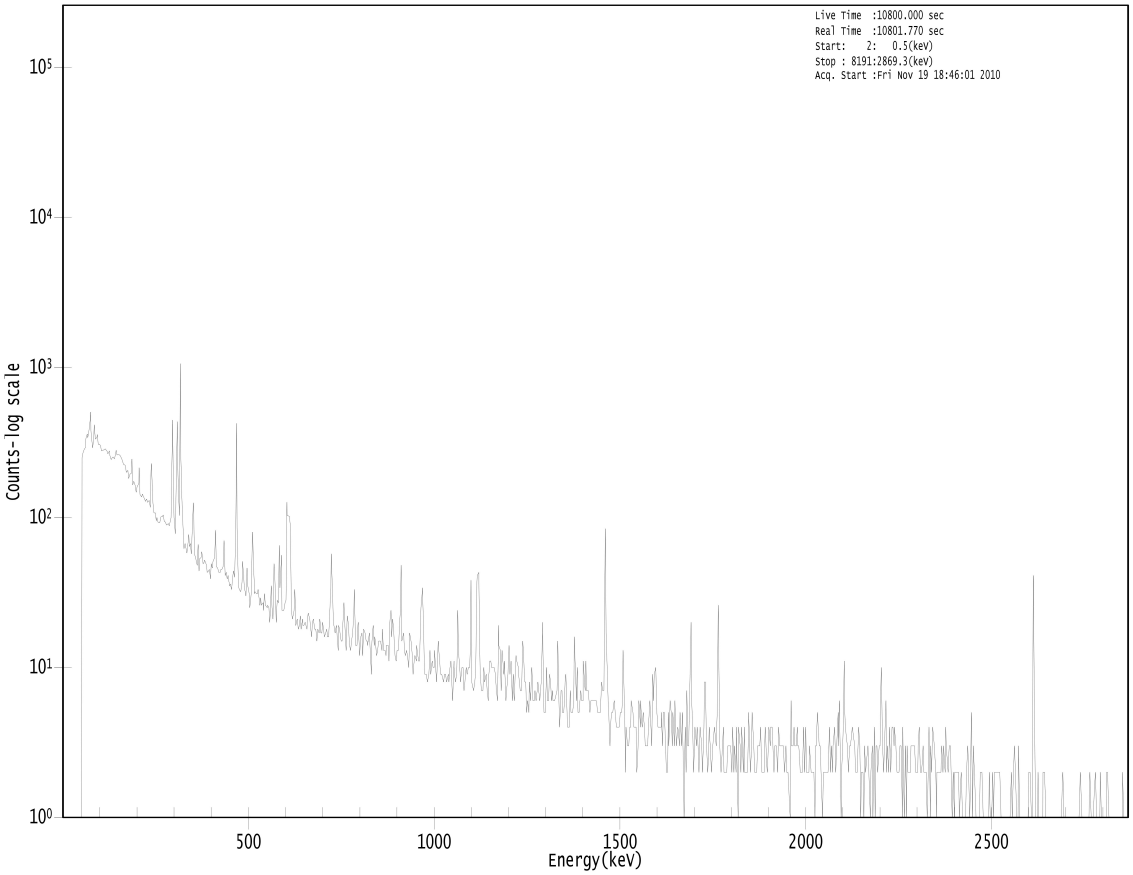

Figure B.42. HPGe gamma ray spectrum for blank vial.

APPENDIX C

HPGe gamma ray spectra for silicon FNAA measurements

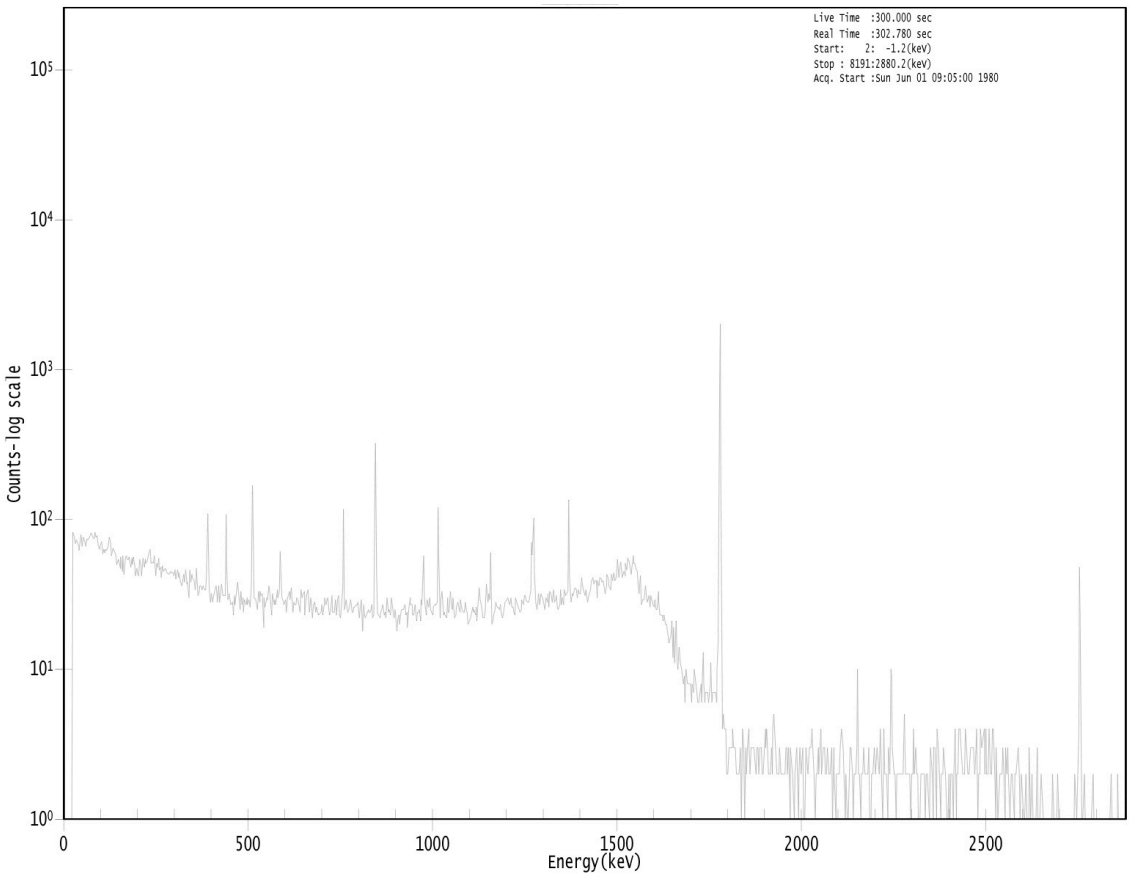

Figure C.1. HPGe gamma ray spectrum for F1 silicon FNAA measurement.

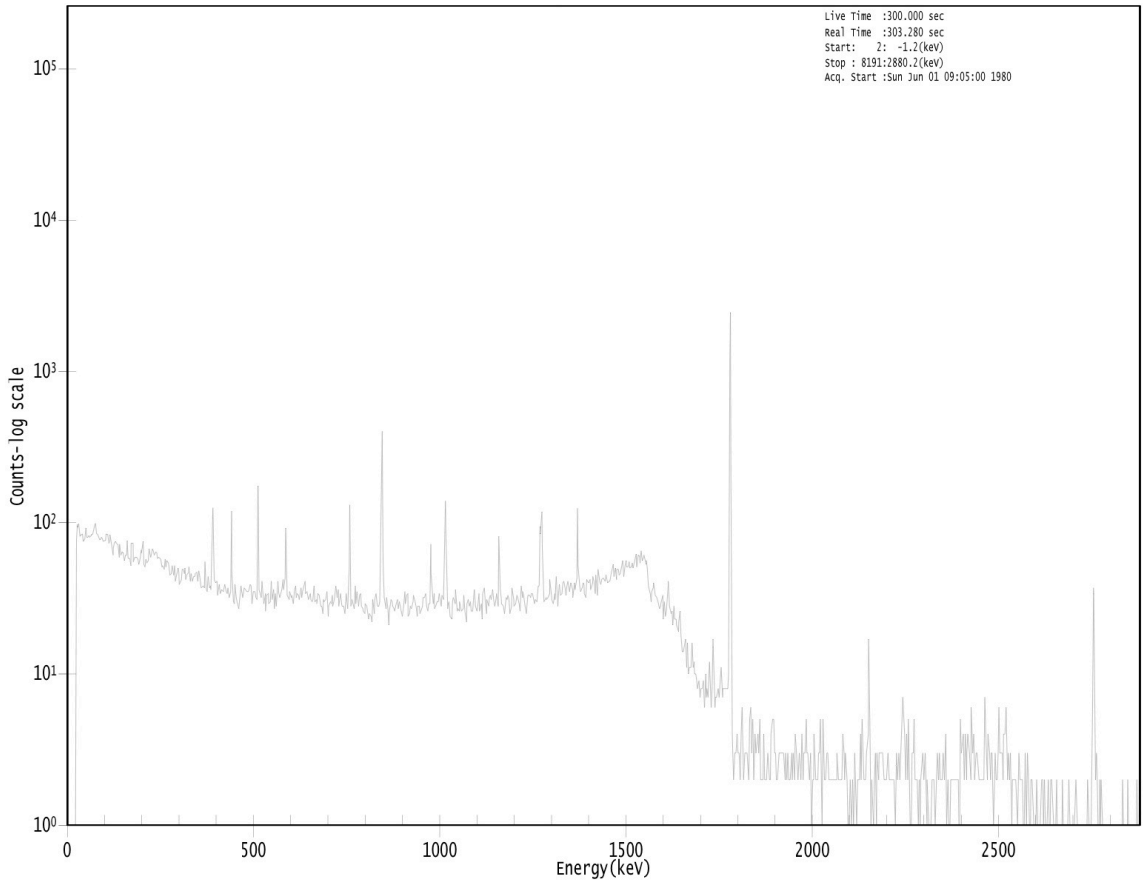

Figure C.2. HPGe gamma ray spectrum for F2 silicon FNAA measurement.

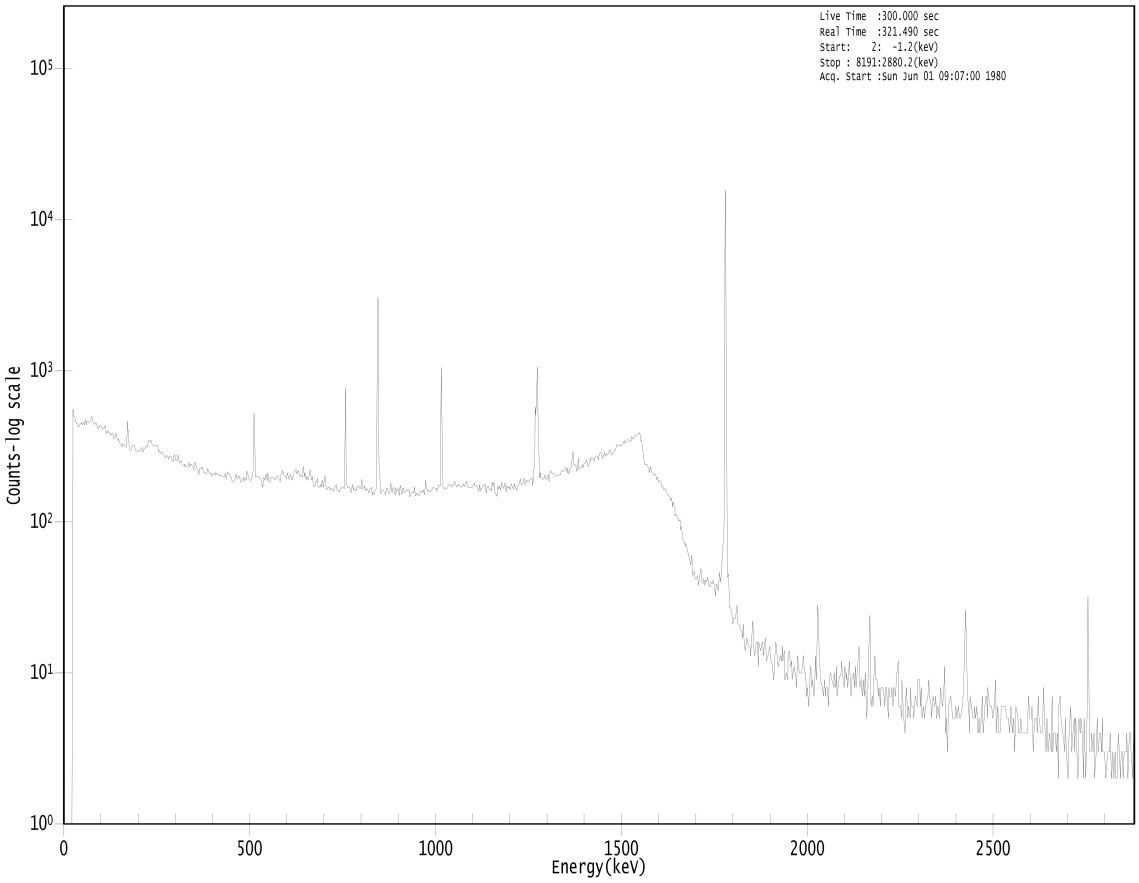

Figure C.3. HPGe gamma ray spectrum for G1 silicon FNAA measurement.

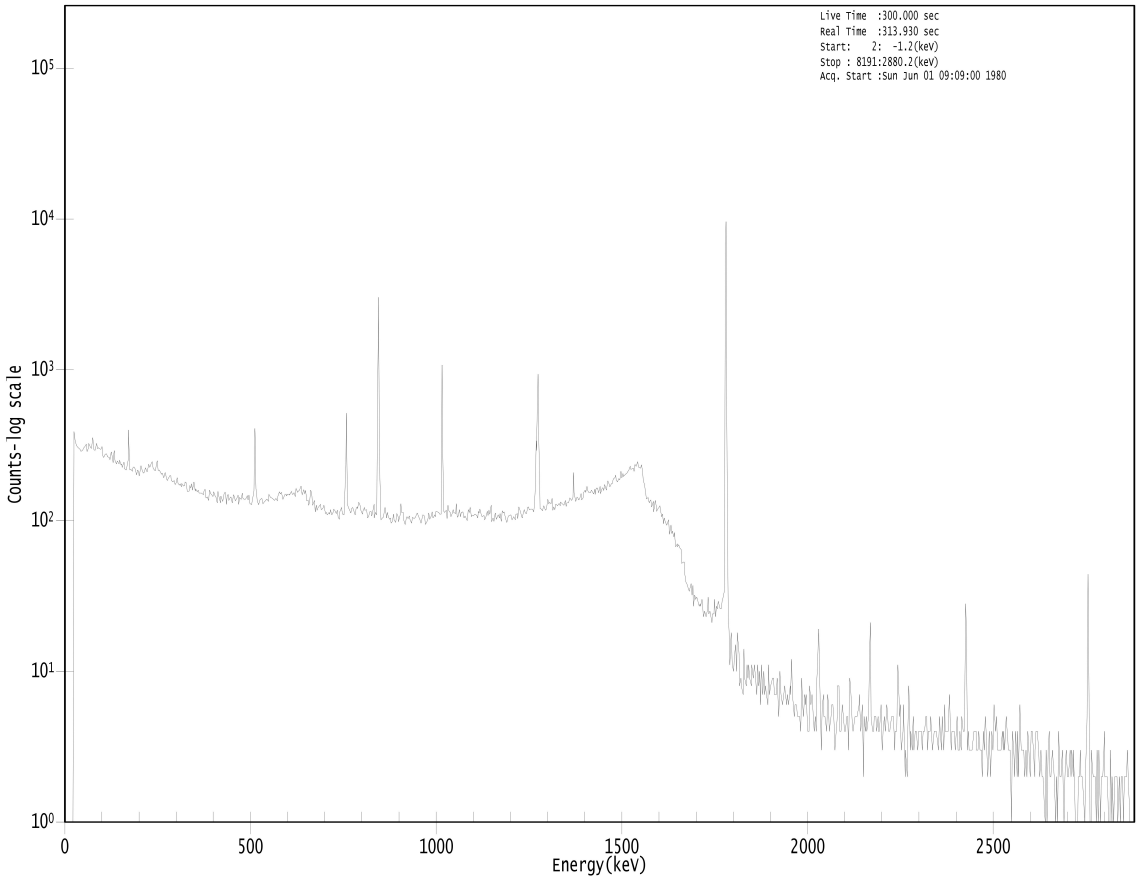

Figure C.4. HPGe gamma ray spectrum for G2 silicon FNAA measurement.

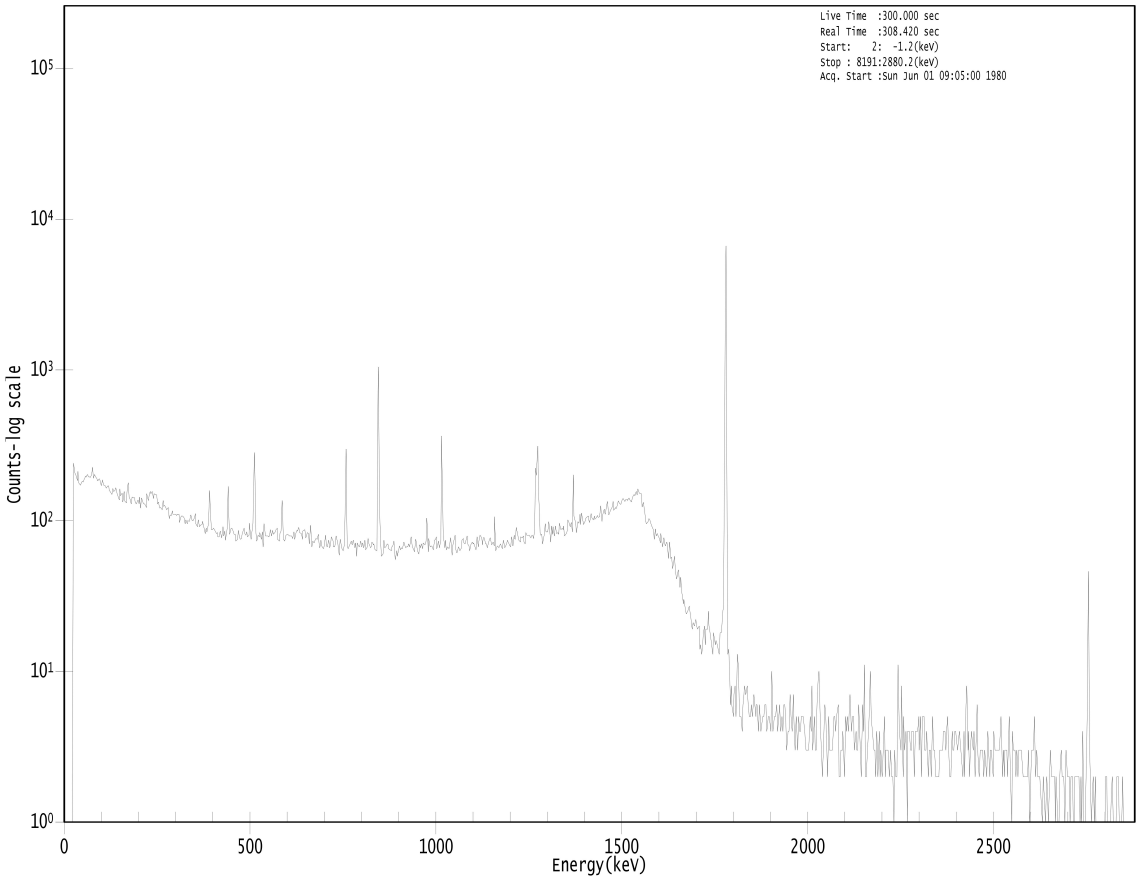

Figure C.5. HPGe gamma ray spectrum for L1 silicon FNAA measurement.

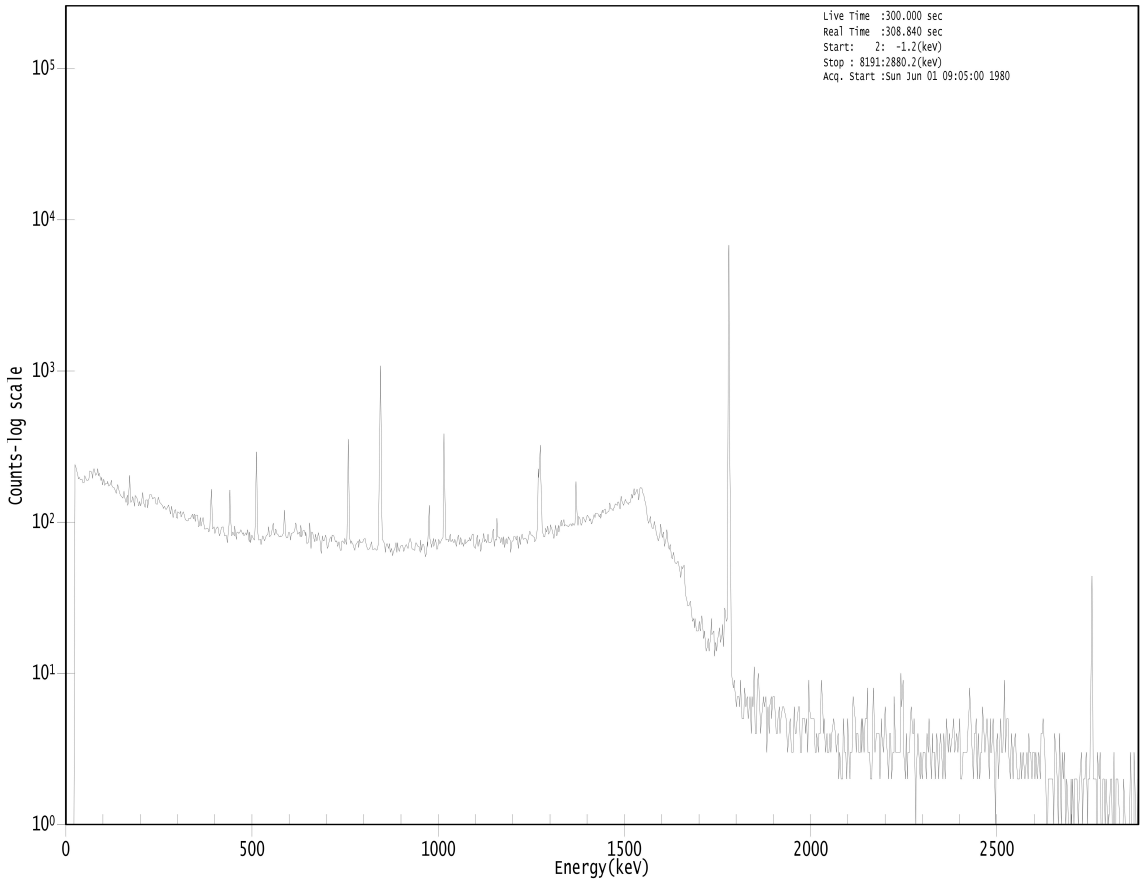

Figure C.6. HPGe gamma ray spectrum for L2 silicon FNAA measurement.

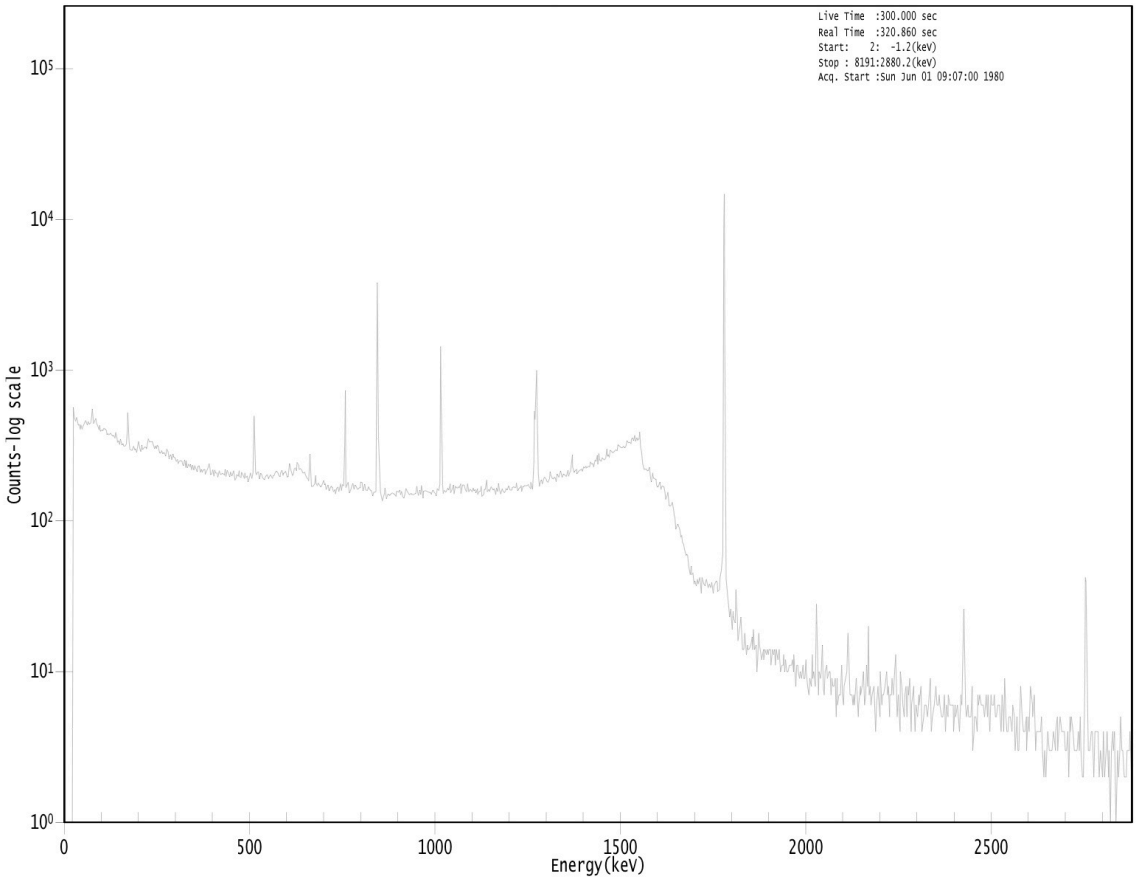

Figure C.7. HPGe gamma ray spectrum for AGV-1 quality control sample.

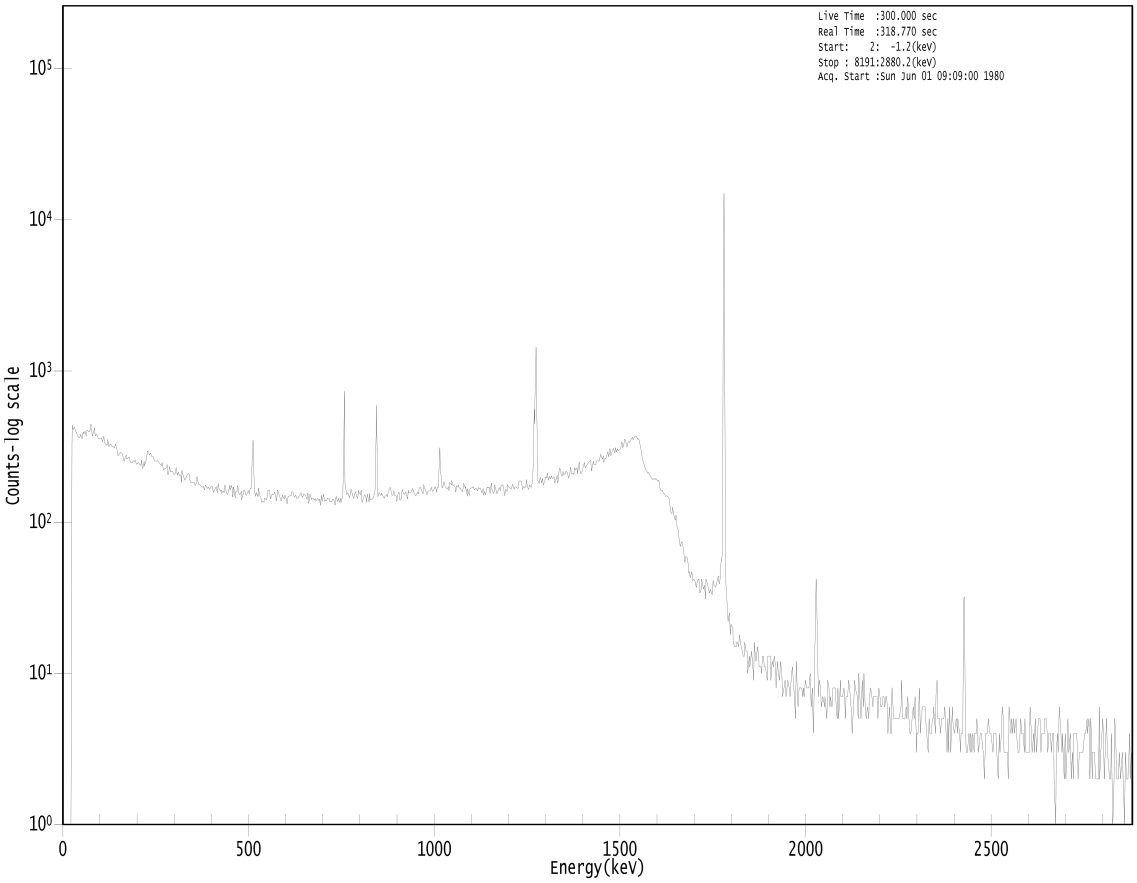

Figure C.8. HPGe gamma ray spectrum for first SiO_2 comparator standard.

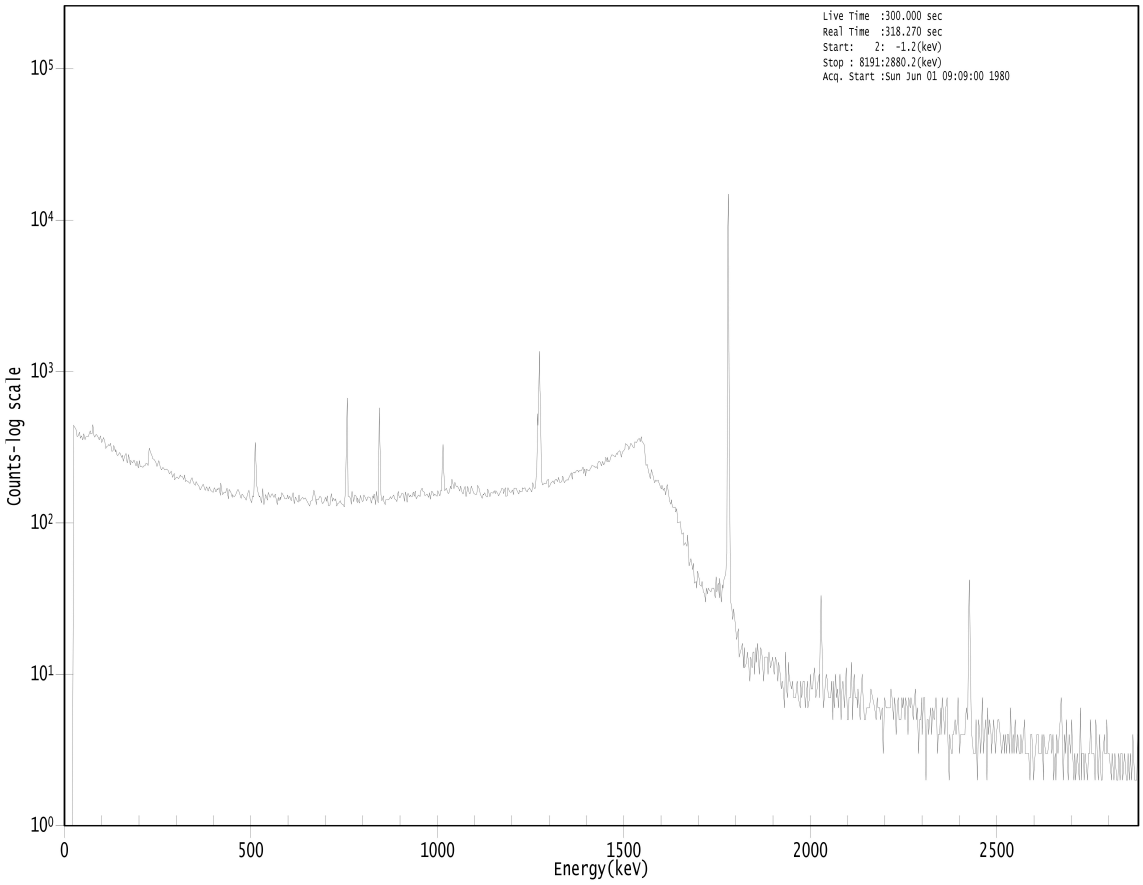

Figure C.9. HPGe gamma ray spectrum for second SiO_2 comparator standard.

APPENDIX D

Input parameters for ISOCS™ efficiency calibration files

Table D.I. Input parameters for sample F1 ISOCS™ efficiency calibration file.[a]

Object	Dimensions (cm)					Material	Density ($g\ cm^{-3}$)	Rel.
	d.1	d.2	d.3	d.4	d.5			
1	0.00001	5.92	11.21	N/A	N/A	f1_naa	2.301	N/A
2	11.21	N/A	N/A	N/A	N/A	f1_naa	2.301	1.00
3	0.00	N/A	N/A	N/A	N/A	(none)	N/A	N/A
4	0.00	N/A	N/A	N/A	N/A	(none)	N/A	N/A
5	0.00	N/A	N/A	N/A	N/A	(none)	N/A	N/A
6	3.02	0.00	0.745	0.00	0.745	N/A	N/A	N/A

[a]N/A means the particular input parameter is not applicable to the object.

Table D.II. Input parameters for sample F2 ISOCS™ efficiency calibration file.[a]

Object	Dimensions (cm)					Material	Density ($g\ cm^{-3}$)	Rel.
	d.1	d.2	d.3	d.4	d.5			
1	0.00001	5.92	11.38	N/A	N/A	f2_naa	2.371	N/A
2	11.38	N/A	N/A	N/A	N/A	f2_naa	2.371	1.00
3	0.00	N/A	N/A	N/A	N/A	(none)	N/A	N/A
4	0.00	N/A	N/A	N/A	N/A	(none)	N/A	N/A
5	0.00	N/A	N/A	N/A	N/A	(none)	N/A	N/A
6	3.02	0.00	0.660	0.00	0.660	N/A	N/A	N/A

[a]N/A means the particular input parameter is not applicable to the object.

Table D.III. Input parameters for sample G1 ISOCS™ efficiency calibration file.[a]

Object	Dimensions (cm)					Material	Density ($g\ cm^{-3}$)	Rel.
	d.1	d.2	d.3	d.4	d.5			
1	0.00001	5.91	11.57	N/A	N/A	g1_naa	2.284	N/A
2	11.57	N/A	N/A	N/A	N/A	g1_naa	2.284	1.00
3	0.00	N/A	N/A	N/A	N/A	(none)	N/A	N/A
4	0.00	N/A	N/A	N/A	N/A	(none)	N/A	N/A
5	0.00	N/A	N/A	N/A	N/A	(none)	N/A	N/A
6	3.02	0.00	0.565	0.00	0.565	N/A	N/A	N/A

[a]N/A means the particular input parameter is not applicable to the object.

Table D.IV. Input parameters for sample G2 ISOCS™ efficiency calibration file.[a]

Object	Dimensions (cm)					Material	Density ($g\ cm^{-3}$)	Rel.
	d.1	d.2	d.3	d.4	d.5			
1	0.00001	5.92	8.85	N/A	N/A	g2_naa	2.216	N/A
2	8.85	N/A	N/A	N/A	N/A	g2_naa	2.216	1.00
3	0.00	N/A	N/A	N/A	N/A	(none)	N/A	N/A
4	0.00	N/A	N/A	N/A	N/A	(none)	N/A	N/A
5	0.00	N/A	N/A	N/A	N/A	(none)	N/A	N/A
6	3.02	0.00	1.925	0.00	1.925	N/A	N/A	N/A

[a]N/A means the particular input parameter is not applicable to the object.

Table D.V. Input parameters for sample L1 ISOCS™ efficiency calibration file.[a]

Object	Dimensions (cm)					Material	Density ($g\ cm^{-3}$)	Rel.
	d.1	d.2	d.3	d.4	d.5			
1	0.00001	5.92	12.24	N/A	N/A	l1_naa	2.267	N/A
2	12.24	N/A	N/A	N/A	N/A	l1_naa	2.267	1.00
3	0.00	N/A	N/A	N/A	N/A	(none)	N/A	N/A
4	0.00	N/A	N/A	N/A	N/A	(none)	N/A	N/A
5	0.00	N/A	N/A	N/A	N/A	(none)	N/A	N/A
6	3.02	0.00	0.230	0.00	0.230	N/A	N/A	N/A

[a]N/A means the particular input parameter is not applicable to the object.

Table D.VI. Input parameters for sample L2 ISOCS™ efficiency calibration file.[a]

Object	Dimensions (cm)					Material	Density ($g\ cm^{-3}$)	Rel.
	d.1	d.2	d.3	d.4	d.5			
1	0.00001	5.92	12.54	N/A	N/A	l2_naa	2.213	N/A
2	12.54	N/A	N/A	N/A	N/A	l2_naa	2.213	1.00
3	0.00	N/A	N/A	N/A	N/A	(none)	N/A	N/A
4	0.00	N/A	N/A	N/A	N/A	(none)	N/A	N/A
5	0.00	N/A	N/A	N/A	N/A	(none)	N/A	N/A
6	3.02	0.00	0.080	0.00	0.080	N/A	N/A	N/A

[a]N/A means the particular input parameter is not applicable to the object.

APPENDIX E

MCNP input decks for concrete samples based on 86,400 sec measurement data

MCNP input deck for sample F1

```
c Portal Monitor Environmental Gamma Background Study
c Created by Alexander Solodov, GNSTD, Oak Ridge National Laboratory
c Modified by Christopher Ryan, NSSPI, Texas A&M University
c Version 2.0 Lead around detectors, steel back and Al front for portals
c Version 3.0 Activities from Greek paper
c Version 4.0 Added Light Pipe
c
c * CELL CARDS *
1   1  -2.301     -100                                        imp:p=1 $ Concrete Slab
2   2  -2.700     -109:-119                                   imp:p=1 $ Aluminum
3   5  -7.920     (-110 +111):(-120 +121)                     imp:p=1 $ SS304
10  4  -1.032     -112                                        imp:p=1 $ PVT, Right Lower
11  4  -1.032     -113                                        imp:p=1 $ PVT, Right Upper
20  4  -1.032     -122                                        imp:p=1 $ PVT, Left Lower
21  4  -1.032     -123                                        imp:p=1 $ PVT, Left Upper
5   3  -1.205E-3  (-111 +112 +113 +114 +115 +116 +117): &
                 (-121 +122 +123 +124 +125 +126 +127)    imp:p=1 $ Air (Portal Interior)
6   6  -11.35     (-114 +112 +116):(-115 +113 +117): &
                 (-124 +122 +126):(-125 +123 +127)       imp:p=1 $ Shielding, Lead
7   7  -1.19      -116:-117:-126:-127                         imp:p=1 $ PMMA
8   3  -1.205E-3  -99 +100 +109 +110 +119 +120                imp:p=1 $ Air (Universe
Interior)
9   0             +99                                         imp:p=0 $ The edge of the
universe...
c * END CELL CARDS *

c * SURFACE CARDS *
100 RPP -198.0000  198.0000 -228.2500 228.2500 -30.4800   0.0000  $ Concrete Slab
109 RPP  254.0000  254.3175  -33.0000  33.0000   0.0000 304.0000  $ Right Portal (Front
Face)
110 RPP  254.3175  277.0000  -33.0000  33.0000   0.0000 304.0000  $ Right Portal (Outer
Surface)
111 RPP  254.3175  276.6825  -32.6825  32.6825   0.3175 303.6825  $ Right Portal (Inner
Surface)
112 RPP  269.5000  273.5000  -24.5000  -9.5000  23.0000  99.0000  $ Right Lower Detector
113 RPP  269.5000  273.5000  -24.5000  -9.5000 214.0000 290.0000  $ Right Upper Detector
114 RPP  269.5000  274.4525  -25.4525  -8.5475  22.0475 112.0000  $ Lead, Right Lower
Detector
115 RPP  269.5000  274.4525  -25.4525  -8.5475 201.0000 290.9525  $ Lead, Right Upper
Detector
116 RPP  269.5000  273.5000  -24.5000  -9.5000  99.0000 112.0000  $ PMMA, Right Lower
Detector
117 RPP  269.5000  273.5000  -24.5000  -9.5000 201.0000 214.0000  $ PMMA. Right Upper
Detector
119 RPP -254.3175 -254.0000  -33.0000  33.0000   0.0000 304.0000  $ Left Portal (Front
Face)
120 RPP -277.0000 -254.3175  -33.0000  33.0000   0.0000 304.0000  $ Left Portal (Outer
Surface)
121 RPP -276.6830 -254.3175  -32.6825  32.6825   0.3175 303.6825  $ Left Portal (Inner
Surface)
122 RPP -273.5000 -269.5000  -24.5000  -9.5000  23.0000  99.0000  $ Left Lower Detector
123 RPP -273.5000 -269.5000  -24.5000  -9.5000 214.0000 290.0000  $ Left Upper Detector
```

```
124 RPP -274.4525 -269.5000  -25.4525  -8.5475  22.0475 112.0000  $ Lead, Left Lower
Detector
125 RPP -274.4525 -269.5000  -25.4525  -8.5475 201.0000 290.9525  $ Lead, Left Upper
Detector
126 RPP -273.5000 -269.5000  -24.5000  -9.5000  99.0000 112.0000  $ PMMA, Left Lower
Detector
127 RPP -273.5000 -269.5000  -24.5000  -9.5000 201.0000 214.0000  $ PMMA, Left Upper
Detector
99 so    500.0000                                                 $ Universe Sphere
c * END SURFACE CARDS *

c * DATA CARDS *
c   -- Source Specifications --
c
MODE p
SDEF PAR 2 X D1 Y D2 Z D3 ERG D4 CEL 1
SI1 -198 198
SP1 0 1
SI2 -228.50 228.50
SP2 0 1
SI3 -30.48 0
SP3 0 1
SI4     L 0.06329 0.09260 0.12907 0.18621 0.23863 0.24200
          0.27024 0.27736 0.29522 0.30009 0.32803 0.33832
          0.35193 0.40946 0.46300 0.58319 0.60931 0.72733
          0.76836 0.79495 0.86056 0.91120 0.93406 0.96477
          0.96897 1.12039 1.23811 1.37767 1.46081 1.76449
          2.20421 2.61453
SP4     D 0.01800 0.02088 0.00354 0.01128 0.06332 0.02335
          0.00506 0.00332 0.06065 0.00480 0.00431 0.01648
          0.11815 0.00281 0.00643 0.04441 0.14486 0.01502
          0.01552 0.00621 0.00652 0.03773 0.00952 0.00730
          0.02310 0.04745 0.01819 0.01257 0.13276 0.04839
          0.01596 0.05211
NPS 1.00E8
c
c   -- Material Specifications --
c
c   -- Concrete --
c
m1    01000 -0.005000  $ Hydrogen in Concrete
      06000 -0.162900  $ Carbon in Concrete
      08000 -0.484500  $ Oxygen in Concrete
      11000 -0.000260  $ Sodium in Concrete
      12000 -0.011900  $ Magnesium in Concrete
      13000 -0.004440  $ Aluminum in Concrete
      14000 -0.015100  $ Silicon in Concrete
      19000 -0.001087  $ Potassium in Concrete
      20000 -0.310100  $ Calcium in Concrete
      25000 -0.000304  $ Manganese in Concrete
      26000 -0.004366  $ Iron in Concrete
c
c   -- Aluminum, Structural 6061 --
c
m2    13000 -0.9685    $ Aluminum
      26000 -0.0070    $ Iron
      29000 -0.0025    $ Copper
      14000 -0.0060    $ Silicon
      12000 -0.0110    $ Magnesium
      24000 -0.0035    $ Chromium
      25000 -0.0015    $ Manganese
c
c   -- Air (suitable for breathing!) --
c
m3    06000 -0.000124  $ Carbon in Air
      07000 -0.755268  $ Nitrogen in Air
      08000 -0.231781  $ Oxygen in Air
      18000 -0.012827  $ Argon in Air
c
```

```
c   -- PVT Scintillator --
c
m4    01000 -0.085000   $ Hydrogen in PVT
      06000 -0.915000   $ Carbon in PVT
c
c   -- Germanium Detector --
c m4    32000 -1.000000   $ Germanium Detector
c
c   -- Steel, Stainless 304 --
c
m5    24000 -0.190000   $ Chromium in Steel
      25000 -0.020000   $ Manganese in Steel
      26000 -0.695000   $ Iron in Steel
      28000 -0.095000   $ Nickel in Steel
c
c   -- Lead --
c
m6    82000 -1.000000   $ Pure lead
c
c   -- PMMA (Light Pipe Lucite) --
c
m7    01000 -0.080538   $ Hydrogen in PMMA
      06000 -0.599848   $ Carbon in PMMA
      08000 -0.319614   $ Oxygen in PMMA
c
c   -- Tallies --
c
F18:P 10                                $ Pulse Height Tally (RL)
E18   0.0 0.00001 0.040 0.140 1.0 3.0   $ Energy Bin
F28:P 11                                $ Pulse Height Tally (RU)
E28   0.0 0.00001 0.040 0.140 1.0 3.0   $ Energy Bins
F38:P 20                                $ Pulse Height Tally (LL)
E38   0.0 0.00001 0.040 0.140 1.0 3.0   $ Energy Bins
F48:P 21                                $ Pulse Height Tally (LU)
E48   0.0 0.00001 0.040 0.140 1.0 3.0   $ Energy Bins
c
c * END OF FILE *
```

MCNP input deck for sample F2

```
c Portal Monitor Environmental Gamma Background Study
c Created by Alexander Solodov, GNSTD, Oak Ridge National Laboratory
c Modified by Christopher Ryan, NSSPI, Texas A&M University
c Version 2.0 Lead around detectors, steel back and Al front for portals
c Version 3.0 Activities from Greek paper
c Version 4.0 Added Light Pipe
c
c * CELL CARDS *
1   1  -2.371     -100                                    imp:p=1 $ Concrete Slab
2   2  -2.700     -109:-119                               imp:p=1 $ Aluminum
3   5  -7.920     (-110 +111):(-120 +121)                 imp:p=1 $ SS304
10  4  -1.032     -112                                    imp:p=1 $ PVT, Right Lower
11  4  -1.032     -113                                    imp:p=1 $ PVT, Right Upper
20  4  -1.032     -122                                    imp:p=1 $ PVT, Left Lower
21  4  -1.032     -123                                    imp:p=1 $ PVT, Left Upper
5   3  -1.205E-3  (-111 +112 +113 +114 +115 +116 +117): &
                  (-121 +122 +123 +124 +125 +126 +127)    imp:p=1 $ Air (Portal Interior)
6   6  -11.35     (-114 +112 +116):(-115 +113 +117): &
                  (-124 +122 +126):(-125 +123 +127)       imp:p=1 $ Shielding, Lead
7   7  -1.19      -116:-117:-126:-127                     imp:p=1 $ PMMA
8   3  -1.205E-3  -99 +100 +109 +110 +119 +120            imp:p=1 $ Air (Universe
Interior)
9   0             +99                                     imp:p=0 $ The edge of the
universe...
c * END CELL CARDS *

c * SURFACE CARDS *
100 RPP -198.0000  198.0000 -228.2500 228.2500 -30.4800   0.0000  $ Concrete Slab
109 RPP  254.0000  254.3175  -33.0000  33.0000   0.0000 304.0000  $ Right Portal (Front
Face)
110 RPP  254.3175  277.0000  -33.0000  33.0000   0.0000 304.0000  $ Right Portal (Outer
Surface)
111 RPP  254.3175  276.6825  -32.6825  32.6825   0.3175 303.6825  $ Right Portal (Inner
Surface)
112 RPP  269.5000  273.5000  -24.5000  -9.5000  23.0000  99.0000  $ Right Lower Detector
113 RPP  269.5000  273.5000  -24.5000  -9.5000 214.0000 290.0000  $ Right Upper Detector
114 RPP  269.5000  274.4525  -25.4525  -8.5475  22.0475 112.0000  $ Lead, Right Lower
Detector
115 RPP  269.5000  274.4525  -25.4525  -8.5475 201.0000 290.9525  $ Lead, Right Upper
Detector
116 RPP  269.5000  273.5000  -24.5000  -9.5000  99.0000 112.0000  $ PMMA, Right Lower
Detector
117 RPP  269.5000  273.5000  -24.5000  -9.5000 201.0000 214.0000  $ PMMA. Right Upper
Detector
119 RPP -254.3175 -254.0000  -33.0000  33.0000   0.0000 304.0000  $ Left Portal (Front
Face)
120 RPP -277.0000 -254.3175  -33.0000  33.0000   0.0000 304.0000  $ Left Portal (Outer
Surface)
121 RPP -276.6830 -254.3175  -32.6825  32.6825   0.3175 303.6825  $ Left Portal (Inner
Surface)
122 RPP -273.5000 -269.5000  -24.5000  -9.5000  23.0000  99.0000  $ Left Lower Detector
123 RPP -273.5000 -269.5000  -24.5000  -9.5000 214.0000 290.0000  $ Left Upper Detector
124 RPP -274.4525 -269.5000  -25.4525  -8.5475  22.0475 112.0000  $ Lead, Left Lower
Detector
125 RPP -274.4525 -269.5000  -25.4525  -8.5475 201.0000 290.9525  $ Lead, Left Upper
Detector
126 RPP -273.5000 -269.5000  -24.5000  -9.5000  99.0000 112.0000  $ PMMA, Left Lower
Detector
127 RPP -273.5000 -269.5000  -24.5000  -9.5000 201.0000 214.0000  $ PMMA, Left Upper
Detector
99 so    500.0000                                          $ Universe Sphere
c * END SURFACE CARDS *

c * DATA CARDS *
c   -- Source Specifications --
c
```

```
MODE p
SDEF PAR 2 X D1 Y D2 Z D3 ERG D4 CEL 1
SI1 -198 198
SP1 0 1
SI2 -228.50 228.50
SP2 0 1
SI3 -30.48 0
SP3 0 1
SI4     L 0.06329 0.09260 0.12907 0.18621 0.23863 0.24200
          0.27024 0.27736 0.29522 0.30009 0.32803 0.33832
          0.35193 0.40946 0.46300 0.58319 0.60931 0.72733
          0.76836 0.79495 0.86056 0.91120 0.93406 0.96477
          0.96897 1.12039 1.23811 1.37767 1.46081 1.76449
          2.20421 2.61453
SP4     D 0.01966 0.02282 0.00345 0.01163 0.06181 0.02408
          0.00494 0.00324 0.06255 0.00468 0.00421 0.01609
          0.12186 0.00274 0.00628 0.04335 0.14940 0.01466
          0.01601 0.00607 0.00637 0.03683 0.00982 0.00712
          0.02255 0.04894 0.01876 0.01296 0.11988 0.04991
          0.01646 0.05087
NPS 1.00E8
c
c   -- Material Specifications --
c
c   -- Concrete --
c
m1    01000 -0.005000  $ Hydrogen in Concrete
      06000 -0.146100  $ Carbon in Concrete
      08000 -0.487200  $ Oxygen in Concrete
      11000 -0.000324  $ Sodium in Concrete
      12000 -0.010600  $ Magnesium in Concrete
      13000 -0.006236  $ Aluminum in Concrete
      14000 -0.018600  $ Silicon in Concrete
      19000 -0.001683  $ Potassium in Concrete
      20000 -0.318800  $ Calcium in Concrete
      25000 -0.000355  $ Manganese in Concrete
      26000 -0.005406  $ Iron in Concrete
c
c   -- Aluminum, Structural 6061 --
c
m2    13000 -0.9685    $ Aluminum
      26000 -0.0070    $ Iron
      29000 -0.0025    $ Copper
      14000 -0.0060    $ Silicon
      12000 -0.0110    $ Magnesium
      24000 -0.0035    $ Chromium
      25000 -0.0015    $ Manganese
c
c   -- Air (suitable for breathing!) --
c
m3    06000 -0.000124  $ Carbon in Air
      07000 -0.755268  $ Nitrogen in Air
      08000 -0.231781  $ Oxygen in Air
      18000 -0.012827  $ Argon in Air
c
c   -- PVT Scintillator --
c
m4    01000 -0.085000   $ Hydrogen in PVT
      06000 -0.915000   $ Carbon in PVT
c
c   -- Germanium Detector --
c m4    32000 -1.000000   $ Germanium Detector
c
c   -- Steel, Stainless 304 --
c
m5    24000 -0.190000   $ Chromium in Steel
      25000 -0.020000   $ Manganese in Steel
      26000 -0.695000   $ Iron in Steel
      28000 -0.095000   $ Nickel in Steel
```

```
c
c   -- Lead --
c
m6    82000 -1.000000   $ Pure lead
c
c   -- PMMA (Light Pipe Lucite) --
c
m7    01000 -0.080538   $ Hydrogen in PMMA
      06000 -0.599848   $ Carbon in PMMA
      08000 -0.319614   $ Oxygen in PMMA
c
c   -- Tallies --
c
F18:P 10                                $ Pulse Height Tally (RL)
E18   0.0 0.00001 0.040 0.140 1.0 3.0  $ Energy Bin
F28:P 11                                $ Pulse Height Tally (RU)
E28   0.0 0.00001 0.040 0.140 1.0 3.0  $ Energy Bins
F38:P 20                                $ Pulse Height Tally (LL)
E38   0.0 0.00001 0.040 0.140 1.0 3.0  $ Energy Bins
F48:P 21                                $ Pulse Height Tally (LU)
E48   0.0 0.00001 0.040 0.140 1.0 3.0  $ Energy Bins
c
c * END OF FILE *
```

MCNP input deck for sample G1

```
c Portal Monitor Environmental Gamma Background Study
c Created by Alexander Solodov, GNSTD, Oak Ridge National Laboratory
c Modified by Christopher Ryan, NSSPI, Texas A&M University
c Version 2.0 Lead around detectors, steel back and Al front for portals
c Version 3.0 Activities from Greek paper
c Version 4.0 Added Light Pipe
c
c * CELL CARDS *
1   1  -2.284     -100                                    imp:p=1 $ Concrete Slab
2   2  -2.700     -109:-119                               imp:p=1 $ Aluminum
3   5  -7.920     (-110 +111):(-120 +121)                 imp:p=1 $ SS304
10  4  -1.032     -112                                    imp:p=1 $ PVT, Right Lower
11  4  -1.032     -113                                    imp:p=1 $ PVT, Right Upper
20  4  -1.032     -122                                    imp:p=1 $ PVT, Left Lower
21  4  -1.032     -123                                    imp:p=1 $ PVT, Left Upper
5   3  -1.205E-3  (-111 +112 +113 +114 +115 +116 +117): &
                  (-121 +122 +123 +124 +125 +126 +127)    imp:p=1 $ Air (Portal Interior)
6   6  -11.35     (-114 +112 +116):(-115 +113 +117): &
                  (-124 +122 +126):(-125 +123 +127)       imp:p=1 $ Shielding, Lead
7   7  -1.19      -116:-117:-126:-127                     imp:p=1 $ PMMA
8   3  -1.205E-3  -99 +100 +109 +110 +119 +120            imp:p=1 $ Air (Universe
Interior)
9   0             +99                                     imp:p=0 $ The edge of the
universe...
c * END CELL CARDS *

c * SURFACE CARDS *
100 RPP -198.0000  198.0000 -228.2500 228.2500 -30.4800   0.0000  $ Concrete Slab
109 RPP  254.0000  254.3175  -33.0000  33.0000   0.0000 304.0000  $ Right Portal (Front
Face)
110 RPP  254.3175  277.0000  -33.0000  33.0000   0.0000 304.0000  $ Right Portal (Outer
Surface)
111 RPP  254.3175  276.6825  -32.6825  32.6825   0.3175 303.6825  $ Right Portal (Inner
Surface)
112 RPP  269.5000  273.5000  -24.5000  -9.5000  23.0000  99.0000  $ Right Lower Detector
113 RPP  269.5000  273.5000  -24.5000  -9.5000 214.0000 290.0000  $ Right Upper Detector
114 RPP  269.5000  274.4525  -25.4525  -8.5475  22.0475 112.0000  $ Lead, Right Lower
Detector
115 RPP  269.5000  274.4525  -25.4525  -8.5475 201.0000 290.9525  $ Lead, Right Upper
Detector
116 RPP  269.5000  273.5000  -24.5000  -9.5000  99.0000 112.0000  $ PMMA, Right Lower
Detector
117 RPP  269.5000  273.5000  -24.5000  -9.5000 201.0000 214.0000  $ PMMA. Right Upper
Detector
119 RPP -254.3175 -254.0000  -33.0000  33.0000   0.0000 304.0000  $ Left Portal (Front
Face)
120 RPP -277.0000 -254.3175  -33.0000  33.0000   0.0000 304.0000  $ Left Portal (Outer
Surface)
121 RPP -276.6830 -254.3175  -32.6825  32.6825   0.3175 303.6825  $ Left Portal (Inner
Surface)
122 RPP -273.5000 -269.5000  -24.5000  -9.5000  23.0000  99.0000  $ Left Lower Detector
123 RPP -273.5000 -269.5000  -24.5000  -9.5000 214.0000 290.0000  $ Left Upper Detector
124 RPP -274.4525 -269.5000  -25.4525  -8.5475  22.0475 112.0000  $ Lead, Left Lower
Detector
125 RPP -274.4525 -269.5000  -25.4525  -8.5475 201.0000 290.9525  $ Lead, Left Upper
Detector
126 RPP -273.5000 -269.5000  -24.5000  -9.5000  99.0000 112.0000  $ PMMA, Left Lower
Detector
127 RPP -273.5000 -269.5000  -24.5000  -9.5000 201.0000 214.0000  $ PMMA, Left Upper
Detector
99 so    500.0000                                           $ Universe Sphere
c * END SURFACE CARDS *

c * DATA CARDS *
c   -- Source Specifications --
c
```

```
MODE p
SDEF PAR 2 X D1 Y D2 Z D3 ERG D4 CEL 1
SI1 -198 198
SP1 0 1
SI2 -228.50 228.50
SP2 0 1
SI3 -30.48 0
SP3 0 1
SI4     L 0.06329 0.09260 0.12907 0.18621 0.23863 0.24200
          0.27024 0.27736 0.29522 0.30009 0.32803 0.33832
          0.35193 0.40946 0.46300 0.58319 0.60931 0.72733
          0.76836 0.79495 0.86056 0.91120 0.93406 0.96477
          0.96897 1.12039 1.23811 1.37767 1.46081 1.76449
          2.20421 2.61453
SP4     D 0.00656 0.00761 0.00550 0.00655 0.09843 0.01355
          0.00787 0.00516 0.03519 0.00746 0.00671 0.02562
          0.06856 0.00436 0.01000 0.06904 0.08405 0.02335
          0.00901 0.00966 0.01014 0.05865 0.00552 0.01134
          0.03592 0.02753 0.01056 0.00729 0.21047 0.02808
          0.00926 0.08102
NPS 1.00E8
c
c   -- Material Specifications --
c
c   -- Concrete --
c
m1    01000 -0.005000  $ Hydrogen in Concrete
      06000 -0.023300  $ Carbon in Concrete
      08000 -0.472700  $ Oxygen in Concrete
      11000 -0.018700  $ Sodium in Concrete
      12000 -0.003781  $ Magnesium in Concrete
      13000 -0.061800  $ Aluminum in Concrete
      14000 -0.266200  $ Silicon in Concrete
      19000 -0.026600  $ Potassium in Concrete
      20000 -0.100600  $ Calcium in Concrete
      25000 -0.000785  $ Manganese in Concrete
      26000 -0.021300  $ Iron in Concrete
c
c   -- Aluminum, Structural 6061 --
c
m2    13000 -0.9685    $ Aluminum
      26000 -0.0070    $ Iron
      29000 -0.0025    $ Copper
      14000 -0.0060    $ Silicon
      12000 -0.0110    $ Magnesium
      24000 -0.0035    $ Chromium
      25000 -0.0015    $ Manganese
c
c   -- Air (suitable for breathing!) --
c
m3    06000 -0.000124  $ Carbon in Air
      07000 -0.755268  $ Nitrogen in Air
      08000 -0.231781  $ Oxygen in Air
      18000 -0.012827  $ Argon in Air
c
c   -- PVT Scintillator --
c
m4    01000 -0.085000   $ Hydrogen in PVT
      06000 -0.915000   $ Carbon in PVT
c
c   -- Germanium Detector --
c m4    32000 -1.000000   $ Germanium Detector
c
c   -- Steel, Stainless 304 --
c
m5    24000 -0.190000   $ Chromium in Steel
      25000 -0.020000   $ Manganese in Steel
      26000 -0.695000   $ Iron in Steel
      28000 -0.095000   $ Nickel in Steel
```

```
c
c   -- Lead --
c
m6    82000 -1.000000   $ Pure lead
c
c   -- PMMA (Light Pipe Lucite) --
c
m7    01000 -0.080538   $ Hydrogen in PMMA
      06000 -0.599848   $ Carbon in PMMA
      08000 -0.319614   $ Oxygen in PMMA
c
c   -- Tallies --
c
F18:P 10                                $ Pulse Height Tally (RL)
E18   0.0 0.00001 0.040 0.140 1.0 3.0  $ Energy Bin
F28:P 11                                $ Pulse Height Tally (RU)
E28   0.0 0.00001 0.040 0.140 1.0 3.0  $ Energy Bins
F38:P 20                                $ Pulse Height Tally (LL)
E38   0.0 0.00001 0.040 0.140 1.0 3.0  $ Energy Bins
F48:P 21                                $ Pulse Height Tally (LU)
E48   0.0 0.00001 0.040 0.140 1.0 3.0  $ Energy Bins
c
c * END OF FILE *
```

MCNP input deck for sample G2

```
c Portal Monitor Environmental Gamma Background Study
c Created by Alexander Solodov, GNSTD, Oak Ridge National Laboratory
c Modified by Christopher Ryan, NSSPI, Texas A&M University
c Version 2.0 Lead around detectors, steel back and Al front for portals
c Version 3.0 Activities from Greek paper
c Version 4.0 Added Light Pipe
c
c * CELL CARDS *
1   1  -2.216     -100                                    imp:p=1 $ Concrete Slab
2   2  -2.700     -109:-119                               imp:p=1 $ Aluminum
3   5  -7.920     (-110 +111):(-120 +121)                 imp:p=1 $ SS304
10  4  -1.032     -112                                    imp:p=1 $ PVT, Right Lower
11  4  -1.032     -113                                    imp:p=1 $ PVT, Right Upper
20  4  -1.032     -122                                    imp:p=1 $ PVT, Left Lower
21  4  -1.032     -123                                    imp:p=1 $ PVT, Left Upper
5   3  -1.205E-3  (-111 +112 +113 +114 +115 +116 +117): &
                  (-121 +122 +123 +124 +125 +126 +127)    imp:p=1 $ Air (Portal Interior)
6   6  -11.35     (-114 +112 +116):(-115 +113 +117): &
                  (-124 +122 +126):(-125 +123 +127)       imp:p=1 $ Shielding, Lead
7   7  -1.19      -116:-117:-126:-127                     imp:p=1 $ PMMA
8   3  -1.205E-3  -99 +100 +109 +110 +119 +120            imp:p=1 $ Air (Universe
Interior)
9   0             +99                                     imp:p=0 $ The edge of the
universe...
c * END CELL CARDS *

c * SURFACE CARDS *
100 RPP -198.0000  198.0000 -228.2500 228.2500 -30.4800   0.0000  $ Concrete Slab
109 RPP  254.0000  254.3175  -33.0000  33.0000   0.0000 304.0000  $ Right Portal (Front
Face)
110 RPP  254.3175  277.0000  -33.0000  33.0000   0.0000 304.0000  $ Right Portal (Outer
Surface)
111 RPP  254.3175  276.6825  -32.6825  32.6825   0.3175 303.6825  $ Right Portal (Inner
Surface)
112 RPP  269.5000  273.5000  -24.5000  -9.5000  23.0000  99.0000  $ Right Lower Detector
113 RPP  269.5000  273.5000  -24.5000  -9.5000 214.0000 290.0000  $ Right Upper Detector
114 RPP  269.5000  274.4525  -25.4525  -8.5475  22.0475 112.0000  $ Lead, Right Lower
Detector
115 RPP  269.5000  274.4525  -25.4525  -8.5475 201.0000 290.9525  $ Lead, Right Upper
Detector
116 RPP  269.5000  273.5000  -24.5000  -9.5000  99.0000 112.0000  $ PMMA, Right Lower
Detector
117 RPP  269.5000  273.5000  -24.5000  -9.5000 201.0000 214.0000  $ PMMA. Right Upper
Detector
119 RPP -254.3175 -254.0000  -33.0000  33.0000   0.0000 304.0000  $ Left Portal (Front
Face)
120 RPP -277.0000 -254.3175  -33.0000  33.0000   0.0000 304.0000  $ Left Portal (Outer
Surface)
121 RPP -276.6830 -254.3175  -32.6825  32.6825   0.3175 303.6825  $ Left Portal (Inner
Surface)
122 RPP -273.5000 -269.5000  -24.5000  -9.5000  23.0000  99.0000  $ Left Lower Detector
123 RPP -273.5000 -269.5000  -24.5000  -9.5000 214.0000 290.0000  $ Left Upper Detector
124 RPP -274.4525 -269.5000  -25.4525  -8.5475  22.0475 112.0000  $ Lead, Left Lower
Detector
125 RPP -274.4525 -269.5000  -25.4525  -8.5475 201.0000 290.9525  $ Lead, Left Upper
Detector
126 RPP -273.5000 -269.5000  -24.5000  -9.5000  99.0000 112.0000  $ PMMA, Left Lower
Detector
127 RPP -273.5000 -269.5000  -24.5000  -9.5000 201.0000 214.0000  $ PMMA, Left Upper
Detector
99 so    500.0000                                          $ Universe Sphere
c * END SURFACE CARDS *

c * DATA CARDS *
c   -- Source Specifications --
c
```

```
MODE p
SDEF PAR 2 X D1 Y D2 Z D3 ERG D4 CEL 1
SI1 -198 198
SP1 0 1
SI2 -228.50 228.50
SP2 0 1
SI3 -30.48 0
SP3 0 1
SI4     L 0.06329 0.09260 0.12907 0.18621 0.23863 0.24200
          0.27024 0.27736 0.29522 0.30009 0.32803 0.33832
          0.35193 0.40946 0.46300 0.58319 0.60931 0.72733
          0.76836 0.79495 0.86056 0.91120 0.93406 0.96477
          0.96897 1.12039 1.23811 1.37767 1.46081 1.76449
          2.20421 2.61453
SP4     D 0.01157 0.01343 0.00509 0.00685 0.09098 0.01418
          0.00727 0.00477 0.03682 0.00689 0.00620 0.02368
          0.07174 0.00403 0.00925 0.06381 0.08795 0.02158
          0.00942 0.00893 0.00937 0.05421 0.00578 0.01049
          0.03320 0.02881 0.01105 0.00763 0.22105 0.02938
          0.00969 0.07489
NPS 1.00E8
c
c   -- Material Specifications --
c
c   -- Concrete --
c
m1    06000 -0.000500  $ Carbon in Concrete
      08000 -0.473100  $ Oxygen in Concrete
      11000 -0.020000  $ Sodium in Concrete
      12000 -0.003594  $ Magnesium in Concrete
      13000 -0.066000  $ Aluminum in Concrete
      14000 -0.295200  $ Silicon in Concrete
      19000 -0.032700  $ Potassium in Concrete
      20000 -0.089800  $ Calcium in Concrete
      25000 -0.001153  $ Manganese in Concrete
      26000 -0.019100  $ Iron in Concrete
c
c   -- Aluminum, Structural 6061 --
c
m2    13000 -0.9685    $ Aluminum
      26000 -0.0070    $ Iron
      29000 -0.0025    $ Copper
      14000 -0.0060    $ Silicon
      12000 -0.0110    $ Magnesium
      24000 -0.0035    $ Chromium
      25000 -0.0015    $ Manganese
c
c   -- Air (suitable for breathing!) --
c
m3    06000 -0.000124  $ Carbon in Air
      07000 -0.755268  $ Nitrogen in Air
      08000 -0.231781  $ Oxygen in Air
      18000 -0.012827  $ Argon in Air
c
c   -- PVT Scintillator --
c
m4    01000 -0.085000   $ Hydrogen in PVT
      06000 -0.915000   $ Carbon in PVT
c
c   -- Germanium Detector --
c m4    32000 -1.000000   $ Germanium Detector
c
c   -- Steel, Stainless 304 --
c
m5    24000 -0.190000   $ Chromium in Steel
      25000 -0.020000   $ Manganese in Steel
      26000 -0.695000   $ Iron in Steel
      28000 -0.095000   $ Nickel in Steel
c
```

```
c   -- Lead --
c
m6    82000 -1.000000   $ Pure lead
c
c   -- PMMA (Light Pipe Lucite) --
c
m7    01000 -0.080538   $ Hydrogen in PMMA
      06000 -0.599848   $ Carbon in PMMA
      08000 -0.319614   $ Oxygen in PMMA
c
c   -- Tallies --
c
F18:P 10                                $ Pulse Height Tally (RL)
E18   0.0 0.00001 0.040 0.140 1.0 3.0  $ Energy Bin
F28:P 11                                $ Pulse Height Tally (RU)
E28   0.0 0.00001 0.040 0.140 1.0 3.0  $ Energy Bins
F38:P 20                                $ Pulse Height Tally (LL)
E38   0.0 0.00001 0.040 0.140 1.0 3.0  $ Energy Bins
F48:P 21                                $ Pulse Height Tally (LU)
E48   0.0 0.00001 0.040 0.140 1.0 3.0  $ Energy Bins
c
c * END OF FILE *
```

MCNP input deck for sample L1

```
c Portal Monitor Environmental Gamma Background Study
c Created by Alexander Solodov, GNSTD, Oak Ridge National Laboratory
c Modified by Christopher Ryan, NSSPI, Texas A&M University
c Version 2.0 Lead around detectors, steel back and Al front for portals
c Version 3.0 Activities from Greek paper
c Version 4.0 Added Light Pipe
c
c * CELL CARDS *
1   1  -2.267     -100                                    imp:p=1 $ Concrete Slab
2   2  -2.700     -109:-119                               imp:p=1 $ Aluminum
3   5  -7.920     (-110 +111):(-120 +121)                 imp:p=1 $ SS304
10  4  -1.032     -112                                    imp:p=1 $ PVT, Right Lower
11  4  -1.032     -113                                    imp:p=1 $ PVT, Right Upper
20  4  -1.032     -122                                    imp:p=1 $ PVT, Left Lower
21  4  -1.032     -123                                    imp:p=1 $ PVT, Left Upper
5   3  -1.205E-3  (-111 +112 +113 +114 +115 +116 +117): &
                  (-121 +122 +123 +124 +125 +126 +127)    imp:p=1 $ Air (Portal Interior)
6   6  -11.35     (-114 +112 +116):(-115 +113 +117): &
                  (-124 +122 +126):(-125 +123 +127)       imp:p=1 $ Shielding, Lead
7   7  -1.19      -116:-117:-126:-127                     imp:p=1 $ PMMA
8   3  -1.205E-3  -99 +100 +109 +110 +119 +120            imp:p=1 $ Air (Universe
Interior)
9   0             +99                                     imp:p=0 $ The edge of the
universe...
c * END CELL CARDS *

c * SURFACE CARDS *
100 RPP -198.0000  198.0000 -228.2500 228.2500 -30.4800   0.0000  $ Concrete Slab
109 RPP  254.0000  254.3175  -33.0000  33.0000   0.0000 304.0000  $ Right Portal (Front
Face)
110 RPP  254.3175  277.0000  -33.0000  33.0000   0.0000 304.0000  $ Right Portal (Outer
Surface)
111 RPP  254.3175  276.6825  -32.6825  32.6825   0.3175 303.6825  $ Right Portal (Inner
Surface)
112 RPP  269.5000  273.5000  -24.5000  -9.5000  23.0000  99.0000  $ Right Lower Detector
113 RPP  269.5000  273.5000  -24.5000  -9.5000 214.0000 290.0000  $ Right Upper Detector
114 RPP  269.5000  274.4525  -25.4525  -8.5475  22.0475 112.0000  $ Lead, Right Lower
Detector
115 RPP  269.5000  274.4525  -25.4525  -8.5475 201.0000 290.9525  $ Lead, Right Upper
Detector
116 RPP  269.5000  273.5000  -24.5000  -9.5000  99.0000 112.0000  $ PMMA, Right Lower
Detector
117 RPP  269.5000  273.5000  -24.5000  -9.5000 201.0000 214.0000  $ PMMA. Right Upper
Detector
119 RPP -254.3175 -254.0000  -33.0000  33.0000   0.0000 304.0000  $ Left Portal (Front
Face)
120 RPP -277.0000 -254.3175  -33.0000  33.0000   0.0000 304.0000  $ Left Portal (Outer
Surface)
121 RPP -276.6830 -254.3175  -32.6825  32.6825   0.3175 303.6825  $ Left Portal (Inner
Surface)
122 RPP -273.5000 -269.5000  -24.5000  -9.5000  23.0000  99.0000  $ Left Lower Detector
123 RPP -273.5000 -269.5000  -24.5000  -9.5000 214.0000 290.0000  $ Left Upper Detector
124 RPP -274.4525 -269.5000  -25.4525  -8.5475  22.0475 112.0000  $ Lead, Left Lower
Detector
125 RPP -274.4525 -269.5000  -25.4525  -8.5475 201.0000 290.9525  $ Lead, Left Upper
Detector
126 RPP -273.5000 -269.5000  -24.5000  -9.5000  99.0000 112.0000  $ PMMA, Left Lower
Detector
127 RPP -273.5000 -269.5000  -24.5000  -9.5000 201.0000 214.0000  $ PMMA, Left Upper
Detector
99 so    500.0000                                          $ Universe Sphere
c * END SURFACE CARDS *

c * DATA CARDS *
c   -- Source Specifications --
c
```

```
MODE p
SDEF PAR 2 X D1 Y D2 Z D3 ERG D4 CEL 1
SI1 -198 198
SP1 0 1
SI2 -228.50 228.50
SP2 0 1
SI3 -30.48 0
SP3 0 1
SI4     L 0.06329 0.09260 0.12907 0.18621 0.23863 0.24200
          0.27024 0.27736 0.29522 0.30009 0.32803 0.33832
          0.35193 0.40946 0.46300 0.58319 0.60931 0.72733
          0.76836 0.79495 0.86056 0.91120 0.93406 0.96477
          0.96897 1.12039 1.23811 1.37767 1.46081 1.76449
          2.20421 2.61453
SP4     D 0.01208 0.01402 0.00377 0.00764 0.06745 0.01581
          0.00539 0.00354 0.04106 0.00511 0.00460 0.01756
          0.07999 0.00299 0.00685 0.04731 0.09807 0.01600
          0.01051 0.00662 0.00695 0.04019 0.00645 0.00777
          0.02461 0.03212 0.01232 0.00851 0.29564 0.03276
          0.01081 0.05552
NPS 1.00E8
c
c   -- Material Specifications --
c
c   -- Concrete --
c
m1    01000 -0.005000  $ Hydrogen in Concrete
      06000 -0.142900  $ Carbon in Concrete
      08000 -0.476900  $ Oxygen in Concrete
      11000 -0.000732  $ Sodium in Concrete
      12000 -0.010900  $ Magnesium in Concrete
      13000 -0.015300  $ Aluminum in Concrete
      14000 -0.047500  $ Silicon in Concrete
      19000 -0.006900  $ Potassium in Concrete
      20000 -0.284800  $ Calcium in Concrete
      25000 -0.000482  $ Manganese in Concrete
      26000 -0.009090  $ Iron in Concrete
c
c   -- Aluminum, Structural 6061 --
c
m2    13000 -0.9685    $ Aluminum
      26000 -0.0070    $ Iron
      29000 -0.0025    $ Copper
      14000 -0.0060    $ Silicon
      12000 -0.0110    $ Magnesium
      24000 -0.0035    $ Chromium
      25000 -0.0015    $ Manganese
c
c   -- Air (suitable for breathing!) --
c
m3    06000 -0.000124  $ Carbon in Air
      07000 -0.755268  $ Nitrogen in Air
      08000 -0.231781  $ Oxygen in Air
      18000 -0.012827  $ Argon in Air
c
c   -- PVT Scintillator --
c
m4    01000 -0.085000   $ Hydrogen in PVT
      06000 -0.915000   $ Carbon in PVT
c
c   -- Germanium Detector --
c m4    32000 -1.000000   $ Germanium Detector
c
c   -- Steel, Stainless 304 --
c
m5    24000 -0.190000   $ Chromium in Steel
      25000 -0.020000   $ Manganese in Steel
      26000 -0.695000   $ Iron in Steel
      28000 -0.095000   $ Nickel in Steel
```

```
c
c   -- Lead --
c
m6    82000 -1.000000   $ Pure lead
c
c   -- PMMA (Light Pipe Lucite) --
c
m7    01000 -0.080538   $ Hydrogen in PMMA
      06000 -0.599848   $ Carbon in PMMA
      08000 -0.319614   $ Oxygen in PMMA
c
c   -- Tallies --
c
F18:P 10                                $ Pulse Height Tally (RL)
E18   0.0 0.00001 0.040 0.140 1.0 3.0  $ Energy Bin
F28:P 11                                $ Pulse Height Tally (RU)
E28   0.0 0.00001 0.040 0.140 1.0 3.0  $ Energy Bins
F38:P 20                                $ Pulse Height Tally (LL)
E38   0.0 0.00001 0.040 0.140 1.0 3.0  $ Energy Bins
F48:P 21                                $ Pulse Height Tally (LU)
E48   0.0 0.00001 0.040 0.140 1.0 3.0  $ Energy Bins
c
c * END OF FILE *
```

MCNP input deck for sample L2

```
c Portal Monitor Environmental Gamma Background Study
c Created by Alexander Solodov, GNSTD, Oak Ridge National Laboratory
c Modified by Christopher Ryan, NSSPI, Texas A&M University
c Version 2.0 Lead around detectors, steel back and Al front for portals
c Version 3.0 Activities from Greek paper
c Version 4.0 Added Light Pipe
c
c * CELL CARDS *
1   1  -2.213     -100                                    imp:p=1 $ Concrete Slab
2   2  -2.700     -109:-119                               imp:p=1 $ Aluminum
3   5  -7.920     (-110 +111):(-120 +121)                 imp:p=1 $ SS304
10  4  -1.032     -112                                    imp:p=1 $ PVT, Right Lower
11  4  -1.032     -113                                    imp:p=1 $ PVT, Right Upper
20  4  -1.032     -122                                    imp:p=1 $ PVT, Left Lower
21  4  -1.032     -123                                    imp:p=1 $ PVT, Left Upper
5   3  -1.205E-3  (-111 +112 +113 +114 +115 +116 +117): &
                  (-121 +122 +123 +124 +125 +126 +127)    imp:p=1 $ Air (Portal Interior)
6   6  -11.35     (-114 +112 +116):(-115 +113 +117): &
                  (-124 +122 +126):(-125 +123 +127)       imp:p=1 $ Shielding, Lead
7   7  -1.19      -116:-117:-126:-127                     imp:p=1 $ PMMA
8   3  -1.205E-3  -99 +100 +109 +110 +119 +120            imp:p=1 $ Air (Universe
Interior)
9   0             +99                                     imp:p=0 $ The edge of the
universe...
c * END CELL CARDS *

c * SURFACE CARDS *
100 RPP -198.0000  198.0000 -228.2500 228.2500 -30.4800   0.0000  $ Concrete Slab
109 RPP  254.0000  254.3175  -33.0000  33.0000   0.0000 304.0000  $ Right Portal (Front
Face)
110 RPP  254.3175  277.0000  -33.0000  33.0000   0.0000 304.0000  $ Right Portal (Outer
Surface)
111 RPP  254.3175  276.6825  -32.6825  32.6825   0.3175 303.6825  $ Right Portal (Inner
Surface)
112 RPP  269.5000  273.5000  -24.5000  -9.5000  23.0000  99.0000  $ Right Lower Detector
113 RPP  269.5000  273.5000  -24.5000  -9.5000 214.0000 290.0000  $ Right Upper Detector
114 RPP  269.5000  274.4525  -25.4525  -8.5475  22.0475 112.0000  $ Lead, Right Lower
Detector
115 RPP  269.5000  274.4525  -25.4525  -8.5475 201.0000 290.9525  $ Lead, Right Upper
Detector
116 RPP  269.5000  273.5000  -24.5000  -9.5000  99.0000 112.0000  $ PMMA, Right Lower
Detector
117 RPP  269.5000  273.5000  -24.5000  -9.5000 201.0000 214.0000  $ PMMA. Right Upper
Detector
119 RPP -254.3175 -254.0000  -33.0000  33.0000   0.0000 304.0000  $ Left Portal (Front
Face)
120 RPP -277.0000 -254.3175  -33.0000  33.0000   0.0000 304.0000  $ Left Portal (Outer
Surface)
121 RPP -276.6830 -254.3175  -32.6825  32.6825   0.3175 303.6825  $ Left Portal (Inner
Surface)
122 RPP -273.5000 -269.5000  -24.5000  -9.5000  23.0000  99.0000  $ Left Lower Detector
123 RPP -273.5000 -269.5000  -24.5000  -9.5000 214.0000 290.0000  $ Left Upper Detector
124 RPP -274.4525 -269.5000  -25.4525  -8.5475  22.0475 112.0000  $ Lead, Left Lower
Detector
125 RPP -274.4525 -269.5000  -25.4525  -8.5475 201.0000 290.9525  $ Lead, Left Upper
Detector
126 RPP -273.5000 -269.5000  -24.5000  -9.5000  99.0000 112.0000  $ PMMA, Left Lower
Detector
127 RPP -273.5000 -269.5000  -24.5000  -9.5000 201.0000 214.0000  $ PMMA, Left Upper
Detector
99 so    500.0000                                           $ Universe Sphere
c * END SURFACE CARDS *

c * DATA CARDS *
c   -- Source Specifications --
c
```

```
MODE p
SDEF PAR 2 X D1 Y D2 Z D3 ERG D4 CEL 1
SI1 -198 198
SP1 0 1
SI2 -228.50 228.50
SP2 0 1
SI3 -30.48 0
SP3 0 1
SI4     L 0.06329 0.09260 0.12907 0.18621 0.23863 0.24200
          0.27024 0.27736 0.29522 0.30009 0.32803 0.33832
          0.35193 0.40946 0.46300 0.58319 0.60931 0.72733
          0.76836 0.79495 0.86056 0.91120 0.93406 0.96477
          0.96897 1.12039 1.23811 1.37767 1.46081 1.76449
          2.20421 2.61453
SP4     D 0.01591 0.01846 0.00342 0.00820 0.06127 0.01697
          0.00490 0.00321 0.04408 0.00464 0.00417 0.01595
          0.08588 0.00272 0.00623 0.04297 0.10530 0.01453
          0.01128 0.00601 0.00631 0.03651 0.00692 0.00706
          0.02236 0.03449 0.01323 0.00914 0.29068 0.03518
          0.01160 0.05043
NPS 1.00E8
c
c   -- Material Specifications --
c
c   -- Concrete --
c
m1    01000 -0.005000  $ Hydrogen in Concrete
      06000 -0.119400  $ Carbon in Concrete
      08000 -0.482100  $ Oxygen in Concrete
      11000 -0.001022  $ Sodium in Concrete
      12000 -0.008900  $ Magnesium in Concrete
      13000 -0.017400  $ Aluminum in Concrete
      14000 -0.053300  $ Silicon in Concrete
      19000 -0.007705  $ Potassium in Concrete
      20000 -0.294600  $ Calcium in Concrete
      25000 -0.000501  $ Manganese in Concrete
      26000 -0.001507  $ Iron in Concrete
c
c   -- Aluminum, Structural 6061 --
c
m2    13000 -0.9685    $ Aluminum
      26000 -0.0070    $ Iron
      29000 -0.0025    $ Copper
      14000 -0.0060    $ Silicon
      12000 -0.0110    $ Magnesium
      24000 -0.0035    $ Chromium
      25000 -0.0015    $ Manganese
c
c   -- Air (suitable for breathing!) --
c
m3    06000 -0.000124  $ Carbon in Air
      07000 -0.755268  $ Nitrogen in Air
      08000 -0.231781  $ Oxygen in Air
      18000 -0.012827  $ Argon in Air
c
c   -- PVT Scintillator --
c
m4    01000 -0.085000   $ Hydrogen in PVT
      06000 -0.915000   $ Carbon in PVT
c
c   -- Germanium Detector --
c m4    32000 -1.000000   $ Germanium Detector
c
c   -- Steel, Stainless 304 --
c
m5    24000 -0.190000   $ Chromium in Steel
      25000 -0.020000   $ Manganese in Steel
      26000 -0.695000   $ Iron in Steel
      28000 -0.095000   $ Nickel in Steel
```

```
c
c   -- Lead --
c
m6    82000 -1.000000   $ Pure lead
c
c   -- PMMA (Light Pipe Lucite) --
c
m7    01000 -0.080538   $ Hydrogen in PMMA
      06000 -0.599848   $ Carbon in PMMA
      08000 -0.319614   $ Oxygen in PMMA
c
c   -- Tallies --
c
F18:P 10                                $ Pulse Height Tally (RL)
E18   0.0 0.00001 0.040 0.140 1.0 3.0  $ Energy Bin
F28:P 11                                $ Pulse Height Tally (RU)
E28   0.0 0.00001 0.040 0.140 1.0 3.0  $ Energy Bins
F38:P 20                                $ Pulse Height Tally (LL)
E38   0.0 0.00001 0.040 0.140 1.0 3.0  $ Energy Bins
F48:P 21                                $ Pulse Height Tally (LU)
E48   0.0 0.00001 0.040 0.140 1.0 3.0  $ Energy Bins
c
c * END OF FILE *
```

APPENDIX F

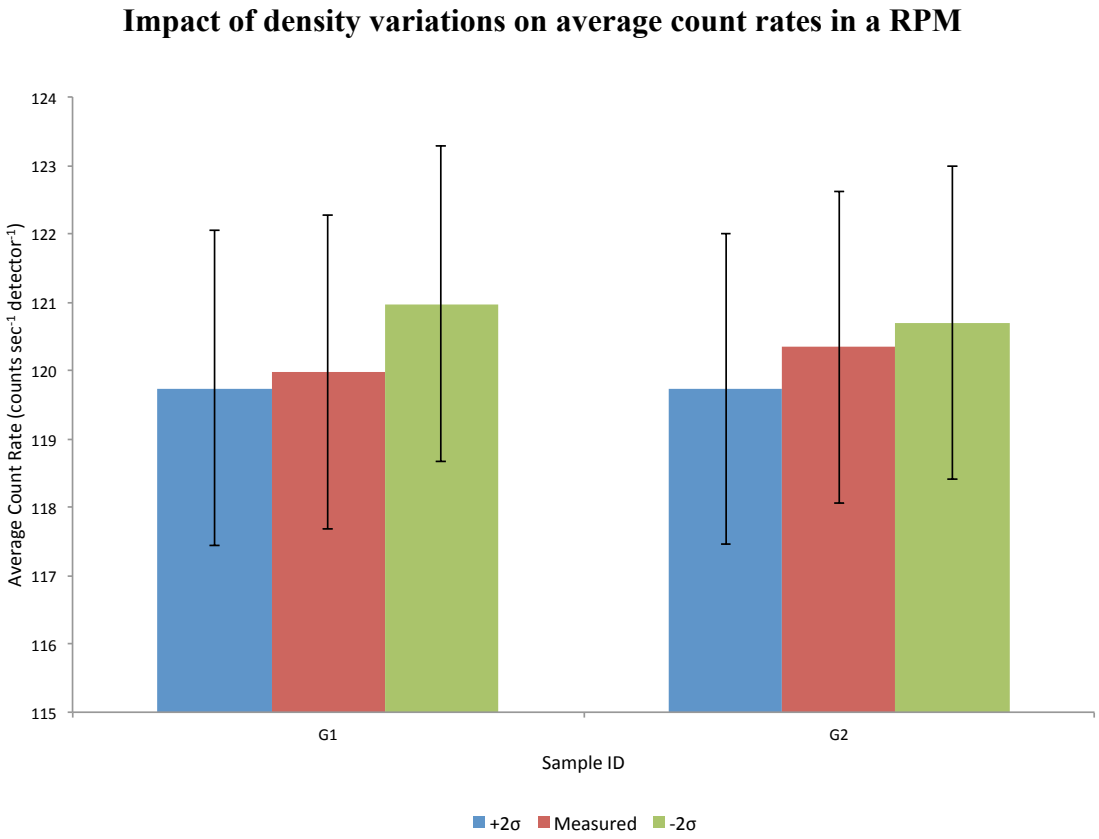

Figure F.1. Plot of the impact of density variations on the average count rate in a RPM from concrete slab G.

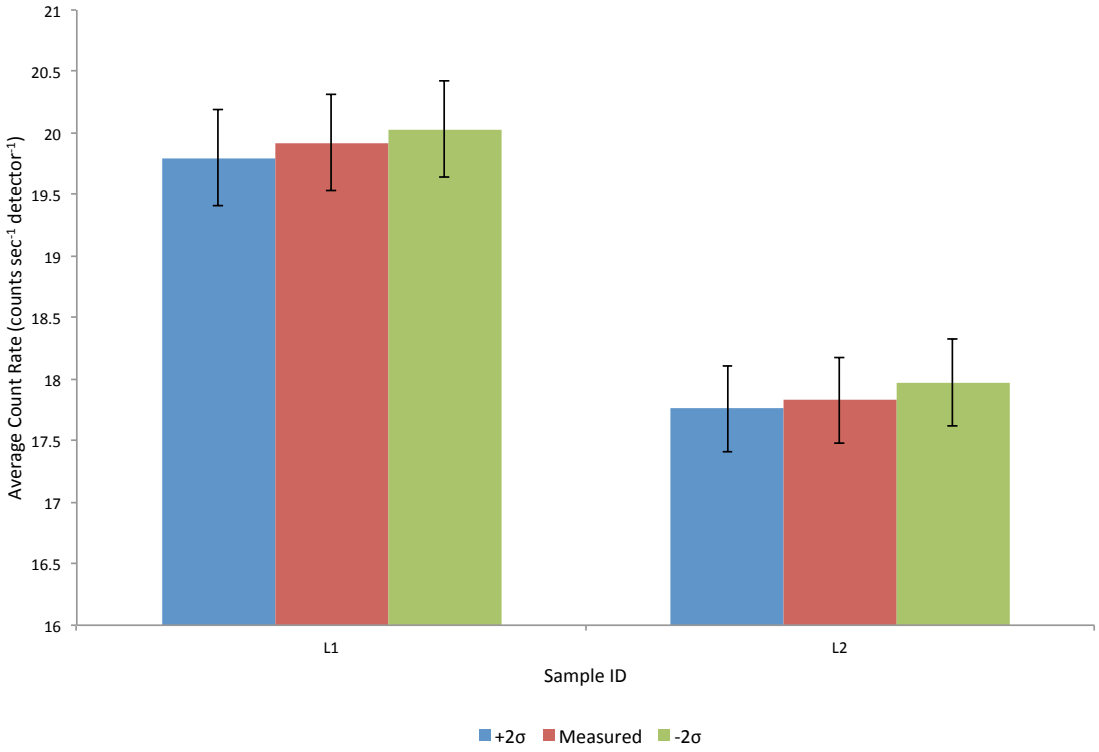

Figure F.2. Plot of the impact of density variations on the average count rate in a RPM from concrete slab L.

APPENDIX G

Impact of variations of carbon and hydrogen content on average count rates in a RPM

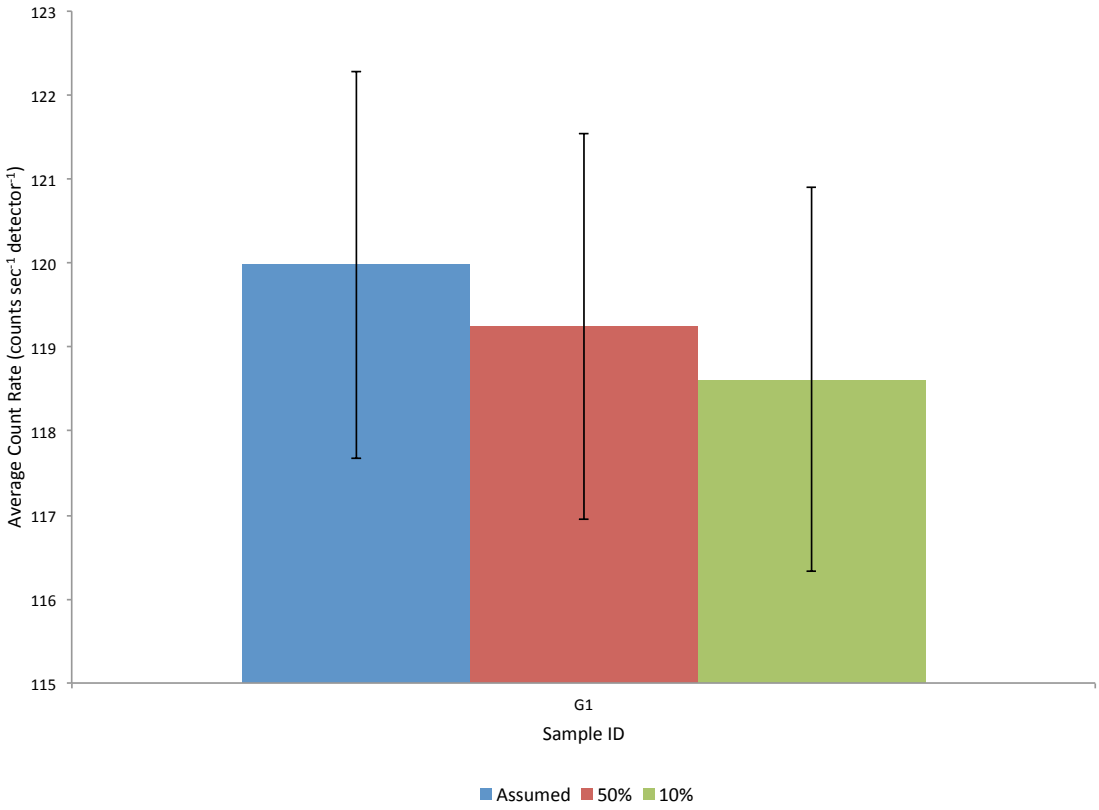

Figure G.1. Plot of the impact of variations in carbon and hydrogen concentration on the average count rate in a RPM from concrete slab G.

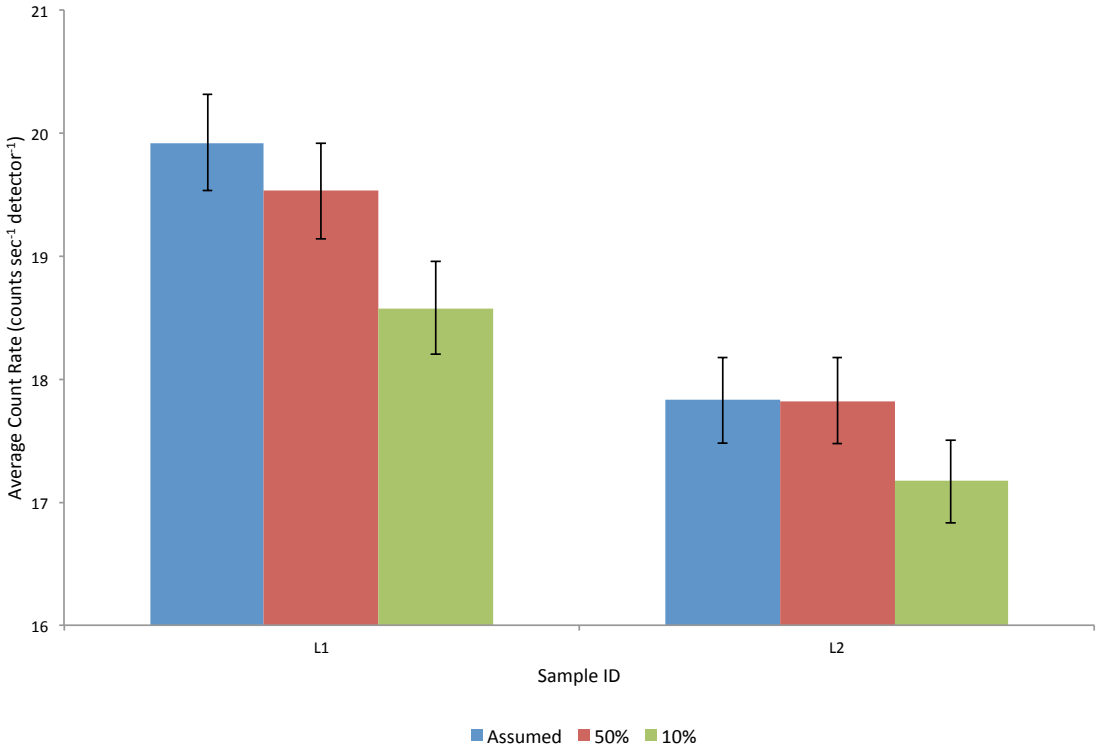

Figure G.2. Plot of the impact of variations in carbon and hydrogen concentration on the average count rate in a RPM from concrete slab L.

VITA

Name: Christopher Michael Ryan

Address: Texas A&M University
Department of Nuclear Engineering
Nuclear Security Science and Policy Institute
3473 TAMU
College Station, TX 77843-3473

Email Address: cmryan07@gmail.com

Education: B.S., Nuclear Engineering, Texas A&M University, 2007
M.S., Nuclear Engineering, Texas A&M University, 2011